Rossana Schipani, B.Eng, M.Sc.

3D BIOPRINTING OF CARTILAGE-MIMETIC IMPLANTS FOR BIOLOGICAL JOINT RESURFACING

Trinity College Dublin, 2020

A thesis submitted to the University of Dublin in partial fulfilment of the requirements for the degree of

Doctor in Philosophy

Supervisor: Prof. Daniel J. Kelly
Internal Examiner: Prof. David Taylor
External Examiner: Prof. Matthew B. Fisher

Declaration

I declare that this thesis has not been submitted as an exercise for a degree at this or any other university and it is entirely my own work.

I agree to deposit this thesis in the University's open access institutional repository or allow the library to do so on my behalf, subject to Irish Copyright Legislation and Trinity College Library conditions of use and acknowledgement.

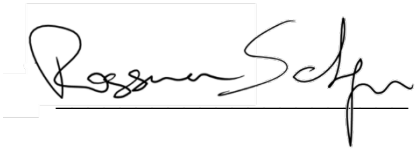

Rossana Schipani

Summary

Osteoarthritis (OA) is a chronic degenerative joint disease, which typically affects articular cartilage and the underlying subchondral bone. Total joint replacement using a synthetic prosthesis is the only surgical treatment option for end-stage OA. While this procedure is well established, complications and failures are not uncommon, which typically results in a more complex revision surgery. This has led to increased interest in tissue engineering strategies that combine biomaterials, cells and/or signalling molecules to regenerate damaged tissues. The overall goal of this thesis is to combine 3D bioprinting with computational modelling and tissue engineering strategies to fabricate regenerative implants for biological joint resurfacing. To realize such an ambitious goal, the implant must be mechanically functional to support the load immediately upon implantation, and to provide cells with appropriate biochemical and biophysical cues to stimulate functional tissue formation. In particular, strategies capable of engineering different tissue phenotypes in a spatially defined manner within the implant are required. The engineered cartilage layer should stimulate the production of phenotypically stable articular cartilage, with depth-dependent anisotropic properties similar to those of the native tissue. The osseous layer should facilitate osseointegration with the host bone and vascularization to ensure stability of the implant.

This thesis began by developing a finite element modelling (FEM) strategy to design 3D printed polymeric networks with defined mechanical properties prior to their fabrication (Chapter 3). Considering geometric discrepancies between scaffold designs pre- and post-fabrication was found to be critical to developing predictive finite element

(FE) models. These FE models were then used to tune structural and mechanical properties of 3D printed polycaprolactone (PCL) scaffolds, obtaining constructs covering a large range of compressive properties.

In Chapter 4, PCL networks (designed in Chapter 3) were combined with an alginate-gelatin methacryloyl (GelMA) interpenetrating network (IPN) hydrogel to develop 3D bioprinted constructs that are both mechanically functional and supportive of mesenchymal stromal cells (MSCs) chondrogenesis for cartilage tissue engineering. When the IPN hydrogels were reinforced with a PCL network characterized by relatively high tension-compression nonlinearity, the resulting composites possessed equilibrium and dynamic properties matching or approaching those of native cartilage. FE models of these composites revealed that such PCL networks reduced the radial expansion and increased the hydrostatic pressure generated within the IPN under compression. *In vitro*, such biomimetic composites were able to support robust chondrogenesis when a co-culture of bone marrow-derived stromal cells (BMSCs) and chondrocytes (CCs) was encapsulated within the IPN.

The next stage of this thesis (Chapter 5) explored the use of 3D bioprinting to fabricate mechanically reinforced bi-layered constructs, consisting of spatially defined hyaline and hypertrophic cartilage-like layers for osteochondral tissue engineering. To generate hypertrophic cartilage in the osseous (or endochondral) region of the constructs, BMSCs were encapsulated in an RGD-γ irradiated alginate hydrogel bioink. To engineer phenotypically stable articular cartilage in the chondral region two different approaches were explored: 1) a co-culture of BMSCs and CCs was loaded in an alginate-GelMA IPN bioink or 2) dynamic compression was applied to constructs containing only BMSCs. Both approaches showed promise, although further work is needed to identify the

appropriate loading regime to produce spatially distinct tissue phenotypes. Conversely, printing a co-culture of BMSCs and CCs was found to be an effective approach to engineer phenotypically stable cartilage in the chondral layer of osteochondral constructs *in vitro*.

Finally, a novel multiple-tool biofabrication strategy was established to produce 'off-the-shelf' implants through the accurate deposition of growth factors-containing bioinks within specific areas of a bi-layered PCL network (Chapter 6). The performance of such implants was evaluated *in vivo* either for the treatment of large osteochondral defects in the knee condyle of goats or for resurfacing the whole shoulder joint of rabbits. Although animal-to-animal variability was observed, the quality of repair in the osteochondral defects created in goats was comparable between defects treated with the 3D printed bi-layered constructs and empty controls, pointing to areas for improvement especially in terms of osseointegration of the implant. In rabbits, the implant was scaled-up and the design was refined to ensure anatomical accuracy and stability. However, the prosthesis failed mechanically, affecting the healing process.

To conclude, this thesis describes a novel multiple-tool biofabrication framework for engineering biological joint resurfacing implants. By integrating FEM and bioprinting technology it was possible to design cell-laden constructs with cartilage-mimetic biomechanical properties and to spatially direct the formation of phenotypically stable articular cartilage and hypertrophic cartilage within bi-layered osteochondral constructs. This work lays the foundation for new tissue engineering strategies that could ultimately be used to provide new regenerative treatments for joint diseases such as OA.

Acknowledgements

First and foremost, I would like to express my gratitude to Prof. Danny Kelly who has been the most wonderful and supportive supervisor. He has never failed to provide constant guidance and positivity throughout this often stormy journey. Above all, I would like to thank him for being key to my huge professional as well as personal growth during my time in Trinity College Dublin, which has been amazing.

I would like to thank my funding European Research Council (ERC) for making this work possible. I would like to thank my examiners Prof. David Taylor and Prof. Matthew Fisher for taking the time to read my thesis and for making the Viva itself unexpectedly enjoyable.

Thanks also to Tríona and Dave Nolan who have always been there for me when I needed them – you both have been key to the development of my FEA skills.

I would like to thank every single member of the TCBE family for making the past 4+ years a memorable part of my life – each one of you holds a special place in my heart. Special thanks go to Mathieu, Pierluca, Paola, Ian and Farhad for supporting me and, above all, putting up with me. I will never forget the chats, the laughs, the awesome trips, the countless pints and nights out - I certainly know I have found lifelong friends.

Grá, thank you for your precious friendship and for understanding me like very few people do. Above all, thanks for pushing me to always be my best self - cannot wait to plan another Spa weekend together.

Thanks to the Japan crew (Jess, Ollie and Pedro) and the Greece crew (Julia, Matteo, Stefan, Pierluca and Dinorath) for having shared with me two of the most amazing adventures I have ever had. Jess, Olwyn, Julia and Pedro we have started this journey together and I would have so many memories to mention – I am so grateful for the bond we have created.

Outside the lab, I would like to thank my best friend Antonio whose positivity and encouragement have made my days brighter in many occasions – despite the distance, you never failed to be constantly present in my life.

I would finally like to thank Mum, Dad, Saverio, Arianna, Yasmin and Dylan – my family -for being my biggest fans and for their love throughout. Your unwavering support has made it possible to achieve my goals and I hope I will always be able to make you proud.

Table of Contents

List of Figures

List of Tables

Nomenclature

3D	Three-dimensional
3DP	3D printed
ACI	Autologous chondrocyte implantation
ANOVA	Analysis of variance
BMP	Bone morphogenetic protein
BMSCs	Bone marrow-derived stromal cells
BV	Bone volume
$CaCl_2$	Calcium chloride
CAD	Computer-aided design
$CaSO_4$	Calcium sulfate
CCs	Chondrocytes
CFD	Computational fluid dynamics
CTGF	Connective tissue growth factor
DCC	Dicyclohexylcarbodiimide
DMEM	Dulbecco's Modified Eagle Medium
DMF	Dimethylformamide
DMMB	Dimethyl methylene blue-binding assay
E	Young's modulus
ECM	Extracellular matrix
EDTA	Ethylene-diamine-tetracetic acid
EtO	Ethylene oxyde
FBS	Foetal bovine serum
FCD	Fixed charged density
FDM	Fused deposition modelling
FE	Finite element
FEA	Finite element analysis
FEM	Finite element modelling
FGF	Fibroblast growth factor
GAG	Glycosaminoglycan
GelMA	Gelatin methacryloyl
H_2SO_4	Sulfuric acid
H_A	Aggregate modulus
HA	Hydroxyapatite
Hep	Heparin

hgDMEM	High glucose Dulbecco's Modified Eagle Medium
HPRA	Health Products Regulatory Authority
IGF	Insuline-like growth factor
IPN	Interpenetrating network
k	Permeability
Micro CT	Micro computed tomography
MSCs	Mesenchymal stromal cells
NaOH	Sodium hydroxide
nHA	Nano-sized hydroxyapatite
OA	Osteoarthritis
PA	Polyamide
PBS	Phosphate buffered saline
PCL	Polycaprolactone
PD	Permanent deformation
PEG	Polyethylene glycol
PEO	Polyethylene oxide
PGA	Poly (glycolic acid)
PLA	Poly (lactic acid)
PLGA	Poly (lactic-co-glycolic acid)
PLM	Polarized light microscopy
PVA	Polyvinyl alcohol
RGD	Arg-Gly-Asp
SAS	Subarticular spongiosa
SBP	Subchondral bone plate
SEM	Scanning electron microscopy
ß-TCB	Beta-tricalcium phosphate
TBA	Tributylamine
TCP	Tricalcium phosphate
TGF-ß3	Transforming growth factor-beta 3
TKA	Total knee arthroplasty
TV	Total volume
VEGF	Vascular endothelial growth factor
ν	Poisson's ratio

Publications

Articles

Schipani, R., Scheurer, S., Florentin, R., Critchley S. E., & Kelly, D. J. Reinforcing interpenetrating network hydrogels with 3D printed polymer networks to engineer cartilage mimetic composites. *Biofabrication*, doi.org/10.1088/1758-5090/ab8708.

Schipani, R., Nolan, D. R., Lally, C., & Kelly, D. J. (2019). Integrating finite element modelling and 3D printing to engineer biomimetic polymeric scaffolds for tissue engineering. *Connective tissue research*, 1-16.

Conferences

Schipani, R., Scheurer, S., Lally, C., Kelly, D. J. *Integrating 3D bioprinting and finite element analysis to engineer biomimetic implants for cartilage tissue engineering.* Gordon Research Conference on Biomaterials and Tissue Engineering. July 28 - August 2, 2019, Barcelona, Spain.

Schipani, R., Critchely, S. E., Nolan, D. R., Alsberg, E., Lally, C., Kelly, D.J. *A combined design and fabrication strategy to engineer biomimetic implants for osteochondral tissue engineering.* Tissue Engineering and Regenerative Medicine International Society (TERMIS) European Chapter Meeting. May 27-31, 2019, Rhodes, Greece.

Schipani, R., Critchley, S. E., Nolan, D. R., Pitacco, P., Aprile, P., Alsberg, E., Lally, C., Kelly, D. J. *Integrating finite element modelling and 3D bioprinting to engineer biologically functional implants for osteochondral tissue engineering*. 25th Bioengineering in Ireland Conference. January 18-19, 2019, Limerick, Ireland.

Schipani, R., Scheurer, S., Florentin, R., Rathan, S., Lally, C., Kelly, D.J. *Reinforcing IPN hydrogels with 3D-printed polymeric frames to engineer cartilage mimetic scaffolds*. Tissue Engineering and Regenerative Medicine International Society (TERMIS) World Congress. September 4-7, 2018, Kyoto, Japan.

Schipani, R., Nolan, D. R., Lally, C., Kelly, D. J. *Tailoring the geometry of 3D-printed polycaprolactone scaffolds to develop biomimetic constructs with mechanical properties comparable to articular cartilage.* 8th World Congress of Biomechanics. July 8-12, 2018, Dublin, Ireland.

Schipani, R., Scheurer, S., Florentin, R., Rathan, S., Lally, C., Kelly, D.J. *Reinforcing interpenetrating network hydrogels with 3D printed polymeric networks leads to synergistic increase in mechanical properties.* 8th World Congress of Biomechanics. July 8-12, 2018, Dublin, Ireland.

Schipani, R., Nolan, D. R., Lally, C., Kelly, D. J. *Modulating the design of 3D printed polycaprolactone scaffolds to engineer cartilage-mimetic constructs.* 24th Bioengineering in Ireland Conference. January 26-27, 2018, Dublin, Ireland.

Schipani, R., Nolan, D. R., Lally, C., Kelly, D. J. *A combined experimental and numerical analysis of structure-function relations in 3D printed scaffolds.* European Society of Biomechanics (ESB) Conference. July 2-4, 2017, Sevilla, Spain.

Schipani, R., Kelly, D. J. *A computational modelling approach for investigating mechanical properties of 3D printed polycaprolactone scaffolds*. 23rd Bioengineering in Ireland Conference. January 20-21, 2017, Belfast, Ireland.

Schipani, R., Kelly, D. J. *Computer modelling and pre-clinical evaluation of 3D printed constructs designed to treat degenerative joint disease.* 22nd Bioengineering in Ireland Conference. January 22-23, 2016, Galway, Ireland.

Chapter 1
Introduction

1.1 Osteoarthritis

Osteoarthritis (OA) is a disease of the whole joint that causes structural alterations to the articular cartilage, subchondral bone, ligaments, capsule, synovium and periarticular muscles (Hunter et al., 2019). The symptoms include inflammation, stiffness and loss of mobility which are often associated with significant functional impairment. The number of individuals affected by OA is expected to double by 2030 mainly due to aging of the worldwide population, along with the increase in obesity (Loeser et al., 2017). When a joint is severely compromised, the current gold standard treatment is total joint arthroplasty, where the entire joint is replaced with a polymer or metal prosthesis. Although the procedure is well established, there are several limitations such as loosening of the implant and a lifespan of about 15 years, which necessitates a more complicated revision surgery if and when the original implant fails (Schiavone Panni et al., 2009; Seil et al., 2011).

The anatomical progression of OA begins with thinning of the articular cartilage leading to narrowing of the joint space. The articular surface plays a key role in withstanding high loads while maintaining a frictionless articulating interface between the bones (Lepage et al., 2019). Understanding the dynamic relationship between cartilage and the underlying subchondral bone, which together form the osteochondral unit, is fundamental when determining new treatment strategies. This has led to increased interest in tissue engineering to develop functional cartilage and bone tissue

replacements, often combined to create regenerative osteochondral implants to treat joint defects and prevent the progression of OA.

1.2 3D bioprinting for joint tissue engineering

Tissue engineering therapies are promising treatments as they offer the potential to repair damaged cartilage and bone in a joint by using a combination of biomaterials, cells and bioactive factors. This concept has already been applied mainly to treat focal chondral lesions. For example, autologous chondrocyte implantation (ACI) is a two-stage procedure currently used in the clinic where cells are first isolated from a non-load bearing location of the joint, expanded *in vitro* and then implanted in the defect beneath a collagen membrane or a periosteal flap (Brittberg et al., 1994). Although patients experience improvements in mobility and pain, a more fibrocartilaginous tissue is generally formed (Nehrer et al., 1999). Additionally, although ACI does not involve direct intervention into the bone, it has been deemed responsible for complications in the subchondral bone such as intralesional osteophytes, subchondral bone plate advancement and cysts formation (Henderson et al., 2005; Lepage et al., 2019; Minas et al., 2009). Most of the existing tissue engineering products are not designed to treat both the injured articular cartilage and subchondral bone, and more importantly are not suitable for treating osteoarthritic joints. Realising tissue engineering strategies capable of biologically resurfacing diseased joint surfaces will require addressing multiple challenges, including the development of mechanical functional materials that are capable of supporting spatially defined and tissue-specific differentiation of stem/progenitor cells.

A central challenge when engineering functional osteochondral tissue is recapitulating the complex environment of the cartilage to bone interface. Both cartilage and bone layers must be mechanically competent to provide immediate support upon implantation and stimulate native-like tissue formation. To this end, the engineered cartilage should mimic the anisotropy of the native tissue which is believed to be fundamental to its mechanical functionality. On the other side, the bone layer should promote vascularization and osseointegration with the host tissue. 3D bioprinting is an emerging technology with the potential to enable the engineering of such complex tissues as it enables the spatial patterning of biomaterials, cells and biological factors (Daly et al., 2017a; Kang et al., 2016; Mouser et al., 2016; Murphy et al., 2014a). Thermoplastic polymers can be printed alongside cell-laden hydrogels (bioinks), resulting in composite constructs with controlled internal and external architectures and mechanical properties tuned to specific applications (Castilho et al., 2019; Kang et al., 2016; Kundu et al., 2015; Visser et al., 2015). Moreover, 3D bioprinting can be integrated with patient-specific computed tomography (CT) data to develop scaled-up, anatomically accurate implants for joint regeneration.

Key to engineering functional bioprinted constructs for osteochondral tissue regeneration is the choice of suitable hydrogel bioinks, cell types and reinforcing materials which, when combined together, provide a biomimetic environment able to stimulate tissue specific extracellular matrix (ECM) deposition. Hydrogels are water swollen materials that have been extensively investigated in cartilage tissue engineering. A number of hydrogel parameters such as polymer chemistry, crosslinking density, mechanical properties, degradation and release rate of biochemical factors, can be tuned to improve their performance in tissue repair (Ahadian et al., 2018; Drury et al., 2003;

Spiller et al., 2011). Traditional hydrogels used for cartilage tissue engineering applications are characterized by single polymer networks which are mechanically inferior compared to native cartilage. Recently, more complex hydrogel systems, often characterized by the combination of two or more independent polymer networks, have been explored. These systems can offer superior mechanical and biological properties better mimicking the properties of native tissues (Ahadian et al., 2018; Cooper et al., 2016; Jeon et al., 2017b; Moffat et al., 2018). Using bioprinting, such hydrogels combined with cells and specific biological factors can be precisely deposited to form heterogeneous constructs to mimic the composition and/or structural organization of the native tissue.

To further improve the mechanical properties of cell-laden bioinks for load-bearing applications (e.g. osteochondral defect repair), they can be reinforced with 3D printed porous polymer networks (Bas et al., 2017c; Castilho et al., 2018; Visser et al., 2015). The geometry features of such polymer networks can be tailored to obtain functional constructs that are both conducive to tissue formation and mimetic of the mechanical properties of a specific tissue. Recently, finite element modelling (FEM) has been increasingly used to aid on the optimization of such tissue engineered constructs (Boccaccio et al., 2016; Hendrikson et al., 2017; Lacroix et al., 2009). FEM could be used for the design of scaffolds *a priori* with optimized mechanical and structural properties that could promote a specific cell function or phenotype. Such approaches have yet to be used to design and produce composite constructs that mimic the complex mechanical properties of articular cartilage.

Mesenchymal stromal cells (MSCs) are commonly used for cartilage and bone tissue engineering as they can differentiate along multiple pathways. Numerous studies have

demonstrated that bone marrow-derived stromal cells (BMSCs) can produce cartilage-like tissue if supplemented with growth factors such as transforming growth factor – beta 3 (TGF-ß3) (Johnstone et al., 1998; Vinardell et al., 2012). A limitation with this approach is that the resulting cartilaginous tissue is phenotypically unstable and tends to undergo endochondral ossification, expressing hypertrophic markers such as collagen type X and generating a calcified tissue *in vivo* (Vinardell et al., 2012). This endochondral ossification process can be used as a strategy for bone tissue engineering, as it replicates the developmental process by which long bones are formed (Scotti et al., 2010). To engineer stable articular cartilage, alternative strategies and/or additional cues will likely be required. For example, co-cultures of MSCs and chondrocytes (CCs) have been explored with the aim of suppressing hypertrophy and generating stable articular cartilage using a relatively small number of CCs (Acharya et al., 2012; Bian et al., 2011; Fischer et al., 2010). Altering the biochemical and/or physical environment of MSC-laden constructs may be another route that can be employed to generate phenotypically stable articular cartilage (Buckley et al., 2010; Burke et al., 2013; Critchley et al., 2018b; Daly et al., 2018; Hung et al., 2004; Mauck et al., 2007; O'Conor et al., 2013).

1.3 Thesis objectives

The overall goal of this thesis was to use FEM-aided 3D bioprinting to develop biomimetic, osteochondral implants to repair large load bearing defects. Therefore, the specific objectives of the thesis are:

Objective 1: ***To develop a computationally efficient FEM approach to design 3D printed polymeric networks with user-defined mechanical properties.*** This thesis will

first investigate discrepancies between the designed and final geometry of 3D printed polycaprolactone (PCL) scaffolds due to the fabrication process. Novel CAD-based finite element (FE) models, that account for such discrepancies, will then be used in combination with fused deposition modelling (FDM) to accurately design 3D printed porous PCL constructs with user-defined mechanical properties for cartilage tissue engineering.

Objective 2: ***To 3D bioprint cell-laden composites with articular cartilage-like mechanical properties and assess their ability to provide an environment conducive to MSC chondrogenesis.*** Motivated by the need to develop engineered tissues that are both biomechanically functional and supportive of MSC chondrogenesis, PCL networks (designed in Objective 1) will be combined with interpenetrating network (IPN) hydrogels consisting of alginate and gelatin methacryloyl (GelMA). FE models and experimental mechanical tests are used to characterize the mechanical behaviour of the resulting composites. Finally, 3D bioprinting is used to encapsulate a co-culture of BMSCs and CCs within the fibre-reinforced IPN bioink to assess the constructs capacity to support the development of stable cartilage-like tissue *in vitro*.

Objective 3: ***To investigate the influence of specific cell types and mechanical stimulation on ECM deposition within 3D bioprinted bi-layered composites with depth-dependent mechanical properties.*** Co-cultures and the application of appropriate biophysical cues are two strategies that can be utilized to engineer phenotypically stable articular cartilage. Building on the outputs from Objective 1 and 2, the 3rd objective of this thesis is to 3D print bi-layered networks with hyaline and hypertrophic cartilage-like mechanical properties in each layer. Next, cell-laden and layer-specific bioinks will be bioprinted within each region of the construct. The ability to engineer both phenotypically

stable articular cartilage (top layer) and hypertrophic cartilage (bottom layer) within such bi-layered constructs *in vitro* is explored using two different strategies: 1) using a co-culture of BMSCs and CCs in the chondral layer and BMSCs only in the osseous layer, or 2) applying dynamic compression stimulation when only BMSCs are encapsulated throughout the construct.

Objective 4: ***To explore the capacity of 3D bioprinted biphasic constructs containing bioinks functionalized with specific growth factors to regenerate 1) critically sized osteochondral defects in the knee condyle of goats and 2) the entire glenohumeral joint of rabbits.*** The final objective of this thesis is to evaluate *in vivo* the performance of the engineered bi-layered PCL-reinforced bioinks for osteochondral tissue regeneration. To develop 'off-the-shelf' products that do not require *in vitro* maturation prior to *in vivo* implantation, BMSCs and/or specific growth factors will be incorporated into each layer of the construct to promote chondrogenesis in the chondral layer and osteogenesis and vascularization in the osseous layer. Finally, the bi-layered constructs will be 1) evaluated in a caprine model to treat large osteochondral defects in the knee condyle or 2) scaled-up to resurface the whole shoulder joint in a lapine model.

Chapter 2
Literature review

2.1 Introduction

Regenerating the osteochondral unit within a synovial joint requires the engineering of functional cartilage and bone and the complex interface that integrates these unique tissues. Therefore, this literature review will discuss about the developmental processes that determine the formation of the osteochondral unit, with special attention to the composition and structural organization of each tissue. This will provide insights into the key aspects that should be taken into account when engineering cartilage and bone replacements. Next, the review will focus on advances in osteochondral tissue engineering, highlighting how several fabrication methods, cell sources, biomaterials and biological signals have been explored to identify potential approaches for treating cartilage and/or osteochondral defects. In particular, this review will describe how 3D bioprinting technology enables the spatial positioning of materials, cells and bioactive cues in 3D. The use of multi-material bioprinting will be summarized, which could potentially be used to engineer functional osteochondral tissue replacements with mechanical properties compatible with high load bearing applications. Furthermore, advances in computational modelling and bioreactor systems will be reviewed; this will demonstrate the advantage of using computational approaches for the optimal design of tissue engineering constructs, while bioreactor systems are necessary for providing physiological mechanical stimuli to enhance new tissue formation.

2.2 The osteochondral complex

In articulating joints, articular cartilage and subchondral bone form a highly organized composite system referred to as the osteochondral unit, which is responsible for the transmission of load during joint motion (Goldring et al., 2016; Hoemann et al., 2012a; Lepage et al., 2019; Tamaddon et al., 2018). Articular cartilage lines the ends of the long bones and is capable of withstanding high loads by maintaining a compliant articulating surface with negligible friction. The transferred load is shared with the subchondral bone plate. The bone-cartilage relationship is crucial to maintaining joint health and functionality. The hyaline cartilage present in the osteochondral unit is connected to the subchondral bone through a zone of calcified cartilage. Hyaline and calcified cartilage are separated by a distinct histological boundary known as the tidemark (Lepage et al., 2019). The mature osteochondral complex is the result of the endochondral ossification process that turns the foetal cartilage "anlagen" into stable articular cartilage at the ends of fully developed long bones (Hoemann et al., 2012a; Lepage et al., 2019). Bone tissue develops first in the primary ossification centre (diaphysis) and then in the secondary ossification centres (epiphysis). Following proliferation, mesenchymal cells condensate before differentiating into cartilage cells, named chondrocytes and secrete collagenous matrix, giving rise to cartilage templates. Next, chondrocytes stop proliferating and undergo hypertrophy, expressing collagen type X, angiogenic factors and alkaline phosphatase that determine calcification of the surrounding matrix (Kronenberg et al., 2003; Long et al., 1995; Mackie et al., 2008; Shen et al., 2005). The developing tissue is invaded by blood vessels that deliver osteoblasts and osteoprogenitor cells that promote the expression of osteogenic factors, turning the transient cartilage into bone (Chen et al., 2014a; Clarkin et al., 2010; Provot et al., 2005). The newly formed bone is anchored to

the stable articular cartilage thanks to a thin layer of calcified cartilage present at the distal ends of the long bones after ossification has occurred (Figure 2.1). During joint development, differentiated chondrocytes convert into non-chondrogenic cells in between the continuously forming cartilage templates leading to the formation of a three-layered interzone (Archer et al., 1995). Two outer interzone layers participate in the initial lengthening of long bones, whereas cells in the intermediate layer of the interzone develop into the layers of articular cartilage found in mature joints (Ito et al., 2000; Koyama et al., 2008; Lamb et al., 2003; Pacifici et al., 2006).

Lesions or repetitive overloading to the joint could result in cartilage deterioration that could affect adjacent structures such as subchondral bone, causing mechanical instability of the joints as well as loss of joint function (Goldring et al., 2016; Lepage et al., 2019; Temenoff et al., 2000; Yousefi et al., 2015). Therefore, it is essential to understand the composition, structure and function of the entire osteochondral unit, in order to develop efficient treatment strategies.

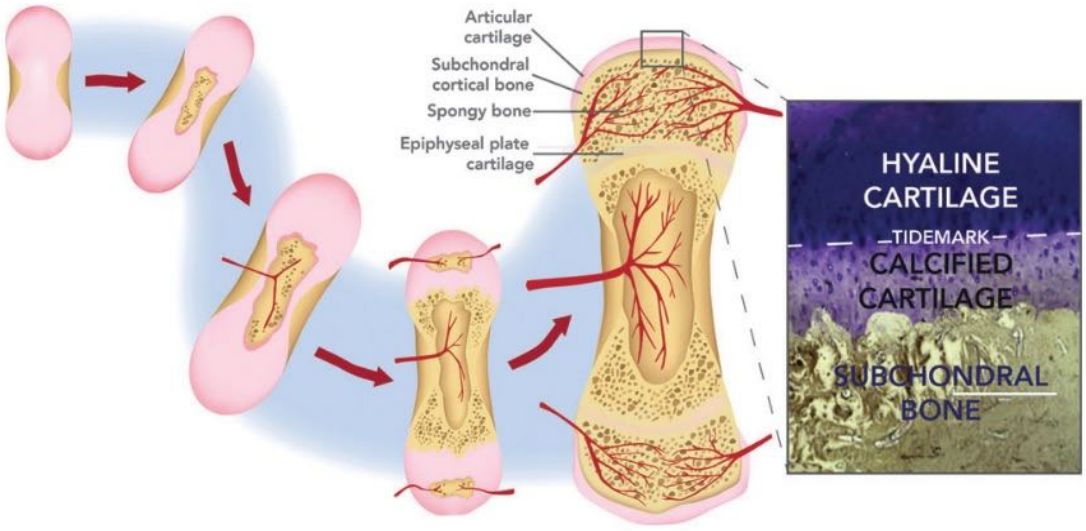

Figure 2-1 Schematic representation of the endochondral ossification process leading to the formation of the osteochondral unit. Histological section of the osteochondral tissue obtained by staining with Toluidine Blue and von Kossa is shown on the right-hand side. (Lepage et al., 2019).

2.2.1 Articular cartilage composition and structure

Articular cartilage is a multiphasic tissue composed of an organic solid matrix that is saturated with water and mobile ions (Mow et al., 2002). It is a thin layer of connective tissue that covers the ends of articulating bones providing a low-friction load bearing surface that is key to the overall function of the osteochondral unit. Articular cartilage has limited regenerative capacities. This is due, at least in part, to the fact that it is an avascular tissue with no connection to the nervous system, meaning that regenerative cells cannot enter into a damaged part of the tissue from the vascular network and that nutrients transfer occurs by diffusion through the surrounding synovial fluid or the underlying bone (Hoemann et al., 2012b; Magill et al., 2011). Chondrocytes are the main cell type of articular cartilage, responsible for secreting and maintaining the cartilage extracellular matrix (ECM). Chondrocytes are surrounded by their own ECM, therefore they do not experience direct cell-to-cell contact.

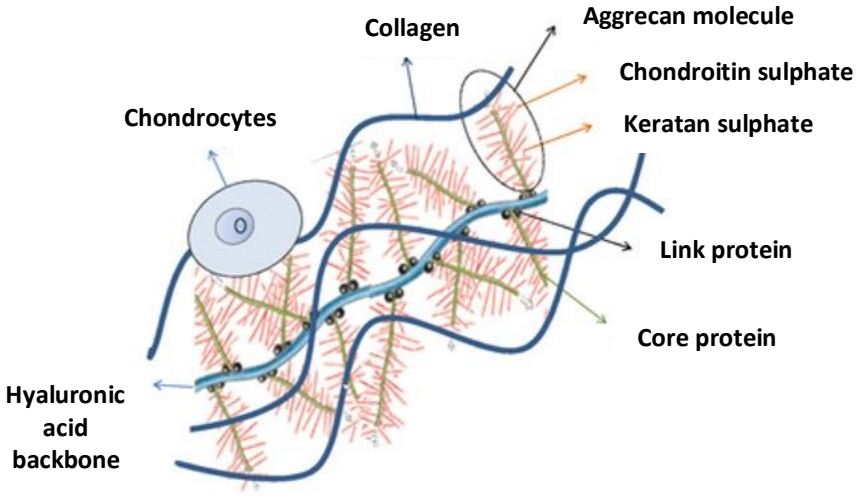

Figure 2-2 Schematic of proteoglycan structures aggregated to a backbone of hyaluronic acid. Adapted from (Izadifar et al., 2012).

The cartilage ECM consists primarily of fluid (70%) and an organic component (30%), whilst no mineral constituents are present in the healthy tissue (Darling et al., 2003; Schlichting et al., 2008). The interstitial water is distributed non-uniformly within the tissue and represents an important constituent in regulating many physical properties (Mow et al., 1993; Mow et al., 2002). The organic component of the ECM comprises of collagens (60%), proteoglycans (25%) and other matrix proteins (15%) (Buckwalter et al., 1998; Cohen et al., 1998; Eyre et al., 2002). Collagen type II is the most abundant type of collagen present in cartilage (95%) whereas collagen types I, IV, V, VI and IX are found in smaller amounts (Mow et al., 1992). Overall, collagen fibres are responsible for the tensile stiffness and strength of the tissue. This is due to the triple helix arrangement of polypeptides of the amino acid alpha chains, which are characterized by a high length to thickness ratio resulting into weak compressive properties (Mow et al., 1992). The most abundant proteoglycan is aggrecan, characterized by its ability to interact with hyaluronan to form large proteoglycan aggregates through a link protein (Figure 2.2) (Izadifar et al., 2012; Mow et al., 2002). Aggrecan occupies the interfibrillar space of the cartilage ECM, where the link protein prevents their escape from the tissue. A single aggrecan is composed of a protein core to which several glycosaminoglycan (GAG) side chains are covalently attached (Figure 2.2). Such GAG chains (i.e. keratan sulphate and chondroitin sulphate) consists of at least one negatively charged group such as carboxyl and/or sulphate (Hardingham et al., 1992; Schaefer et al., 2010). The negatively charged groups give rise to a fixed charged density (FCD), which exerts an internal swelling pressure known as the Donnan osmotic fluid pressure (Gannon et al., 2015a; Mow et al., 2002; Mow et al., 1980). This is responsible for governing the tissue hydration, the rate of fluid transport and various electromechanical effects (Mow et al.,

2002). When an external compressive load is applied to a joint, the intrinsic swelling pressure is increased causing the fluid to move through the cartilage matrix. Because

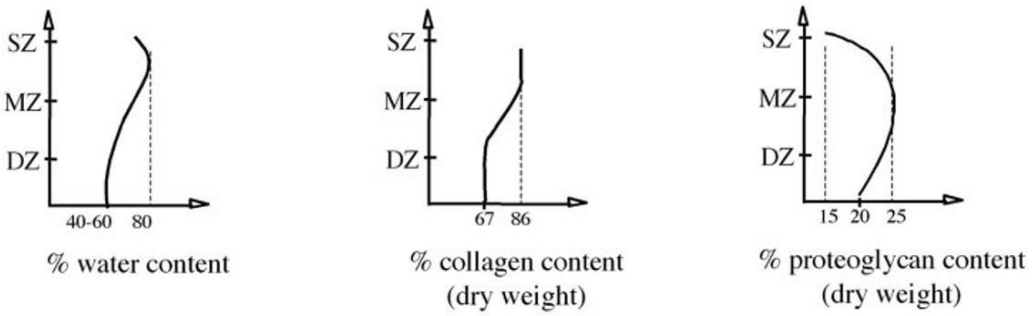

Figure 2-3 Graphs showing how the articular cartilage ECM components content varies in each region determining the depth-dependent properties of the tissue. (Mow et al., 2002).

cartilage ECM components are densely packed, the GAG negative charge generates repulsion forces, but they are restrained by the collagen network, providing the tissue with resistance to compressive forces (Mow et al., 2002).

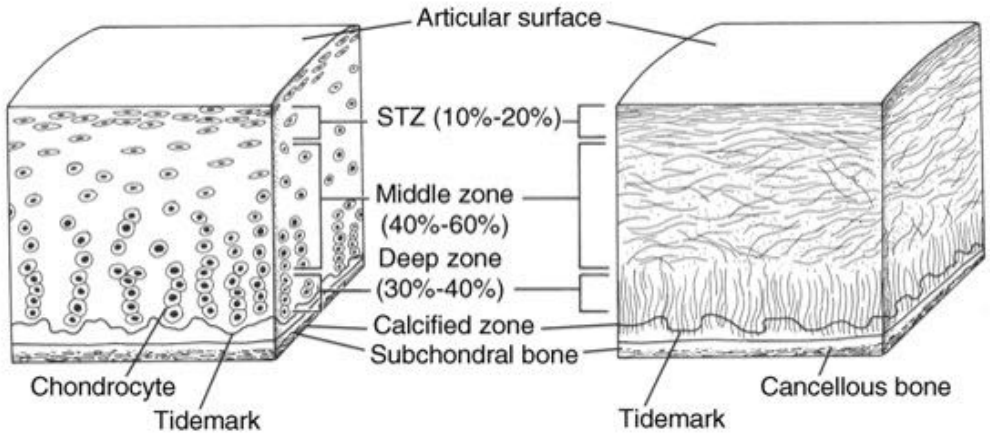

Figure 2-4 Schematic diagram of the structural organization of chondrocytes and collagen fibres within the three zones of articular cartilage. Adapted from (Buckwalter et al., 1994).

The unique zonal structure and composition of articular cartilage plays a key role in determining its mechanical functionality (Gannon et al., 2015a; Musumeci et al., 2016). Spatial changes in the amount and organization of the two dominant ECM components, proteoglycan and collagen, give rise to inhomogeneous (depth-dependent) mechanical properties (Figure 2.3) (Mow et al., 2002). Cartilage can be divided into four zones: superficial (or tangential), middle (or intermediate), deep (or radial) and calcified zones (Figure 2.4). The uppermost superficial zone has high collagen and water content which decreases progressively with depth, while the aggrecan content increases showing a maximum peak in the deep zone (Figure 2.3). The superficial region makes up 10-20% of the overall tissue thickness and contains a high number of chondrocytes that show a flattened morphology and follow the collagen fibres orientation. Chondrocytes in the superficial zone produce a boundary lubricant called lubricin or PRG-4 which reduces friction within the joint during articulation (Jay et al., 2014; Schumacher et al., 1994). While the proteoglycan concentration is low, there is a high content of collagen fibres that are densely packed and arranged parallel to the articular surface, providing high resistance to shear and transverse expansion (Buckwalter et al., 1994a). The middle zone is a transitional region between superficial and deep zones, where chondrocytes appear more rounded in shape and randomly distributed. The middle region is characterized by the highest proteoglycan content that provides the tissue with compressive resistance, while collagen fibres are larger and less dense in order to entrap the proteoglycan molecules (Buckwalter et al., 1994a). Moreover, collagen fibres are randomly oriented as they transition from the parallel form in the superficial zone to perpendicular. In the deep zone, chondrocytes are distributed in a columnar fashion as thick collagen fibres and are arranged perpendicular to the surface, anchoring the cartilage to the underlying

subchondral bone (Buckwalter et al., 1994a). The matrix anisotropy through the thickness of the tissue results in depth-dependent mechanical properties that are essential to cartilage functionality.

2.2.2 Articular cartilage mechanical properties

Diarthrodial joints are subjected to physiological loading daily, causing the deforming cartilage to increase contact areas and local joint congruence (Mow et al., 2002). As a result, articular cartilage experiences a combination of compressive, tensile and shear stresses. The tissue is viscoelastic, as can be observed during creep and stress-relaxation experiments (Figure 2.5). The viscoelastic behaviours are determined by flow-dependent and flow-independent dissipative mechanisms in response to loading. The former derives from the frictional drag force generated by the interstitial fluid flowing through the porous-permeable solid matrix, the latter is due to the time-dependent deformations of the solid macromolecules (Mow et al., 2002). Understanding how fluid can flow through the cartilage solid matrix helps understanding the cartilage deformational behaviour. When cartilage undergoes compressive loading, the interstitial fluid will flow within the tissue or will be exuded from the tissue as a result of the formation of a pressure gradient. As the fluid passes through the matrix, high drag forces are generated giving rise to the frictional dissipation mechanisms that contribute to the viscoelastic properties of the tissue in compression (Lu et al., 2008) (Soltz et al., 2000). Because articular cartilage is composed by a solid collagen and proteoglycan phase and an interstitial fluid phase, the cartilage viscoelastic behaviour is best described by the biphasic theory developed by Mow and colleagues (Mow et al., 1980). According to this theory, three main internal forces are developed within the tissue in the presence of an external load: 1) the pressure generated within the fluid phase, 2) the stress created within the deformed solid matrix

and 3) the frictional resistance determined by the solid and fluid phases when they flow past each other (Lu et al., 2008). The viscoelastic effect is a result of the three aforementioned forces acting in synergy to balance out the externally applied load. Furthermore, as the permeability of cartilage is very small, the interstitial fluid pressure and dissipation mechanisms occurring within the tissue provide an efficient method to protect the solid matrix components as well as the embedded chondrocytes from the high stresses and strains associated with the complex loading experienced by the joint daily (Soltz et al., 1998) (Soltz et al., 2000).

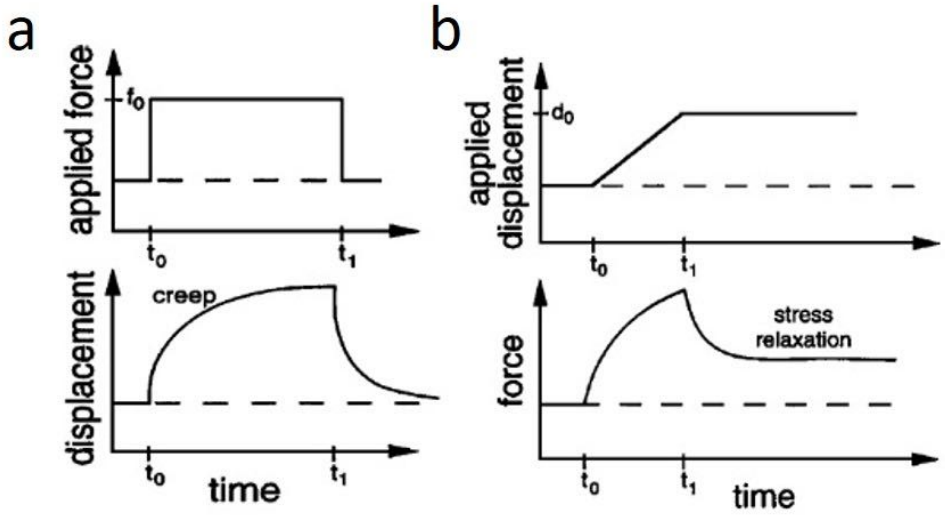

Figure 2-5 Schematics representing the (a) creep and (b) stress-relaxation test curves that describe the load-deformation viscoelastic behaviours of articular cartilage. (Mow et al., 2002).

2.2.2.1 Compressive properties

As the dominant force experienced by articular cartilage is compression, the most used testing protocols to evaluate the tissue compressive properties are confined compression, unconfined compression and indentation tests (Figure 2.6a). When subjected to compressive loading, the interstitial fluid moves through the tissue

generating frictional drag forces and high pressures within the matrix. Therefore, articular cartilage will undergo stress-relaxation if a constant displacement (or strain) is applied and will creep in response to an applied constant force (or stress) (Figure 2.5a, b) (Mow et al., 2002). Fluid nearest the surface is exuded first, followed by movement of the deeper sections. Upon removal of the load or displacement, the solid matrix begins to redistribute the fluid back into the depths of the tissue recovering its initial dimensions. At the end of the ramp phase of a stress-relaxation test (Figure 2.5b), the stress in the cartilage decreases exponentially until an equilibrium phase is reached, in which the applied stress is balanced by the stress in the matrix, there is no pressure gradients nor fluid flow, therefore the intrinsic compressive modulus can be quantified (Soltz et al., 1998).

In a creep or stress-relaxation test under uniaxial confined compression (Figure 2.6 a – top), a cartilage plug is placed in an impermeable chamber with matching diameter in order to prevent the bulging of the specimen in the radial direction. The fluid is forced to escape the tissue only in the vertical direction as the sample is compressed using a porous platen. Two intrinsic material properties can be determined: 1) equilibrium confined compressive aggregate modulus (H_A) and 2) hydraulic permeability (k). The aggregate modulus of articular cartilage has been shown to range from 0.1 - 2.0 MPa, whereas the permeability was reported to be (1.2 - 6.2) x 10^{-16} $m^4/N \cdot s$ (Armstrong et al., 1984; Mow et al., 2002; Mow et al., 1980). In unconfined compression configuration (Figure 2.6 a – middle), the cartilage sample is placed between two non-porous platens. The tissue is compressed with one of the platens and is allowed to bulge, as it is not constrained on the sides. The properties that can be determined from unconfined compression tests are: 1) equilibrium Young's modulus (E), 2) Poisson's ratio (ν) and 3) hydraulic permeability (k). The intrinsic Young's modulus was quantified to be approximately 0.41 - 0.85 MPa,

whereas the Poisson's ratio ranged from 0.06 - 0.18 (Athanasiou et al., 1991; Jurvelin et al., 1997; Kempson et al., 1970).

Indentation test (Figure 2.6a – bottom) is another relevant testing technique used to measure articular cartilage compressive properties. Advantages include minimal disruption of the tissue sample as well as higher accuracy when assessing the mechanical properties *in situ* or of specimen with curved surfaces (Athanasiou et al., 1994; Lyyra-Laitinen et al., 1999; Lyyra et al., 1999). The set-up involves the use of an appropriate stage to keep the sample in place, while a constant load is applied via a porous/non-porous platen of variable diameter. Using the biphasic theory for articular cartilage, the equilibrium aggregate modulus (H_A), Poisson's ration (ν) and hydraulic permeability (k) have been quantified as follows: H_A = 0.4 – 0.9 MPa; ν = 0.13 – 0.45; k = (4 – 10) x 10^{-16} $m^4/N \cdot s$, falling in the range measured by the techniques mentioned above (Kempson et al., 1970; Mow et al., 2002).

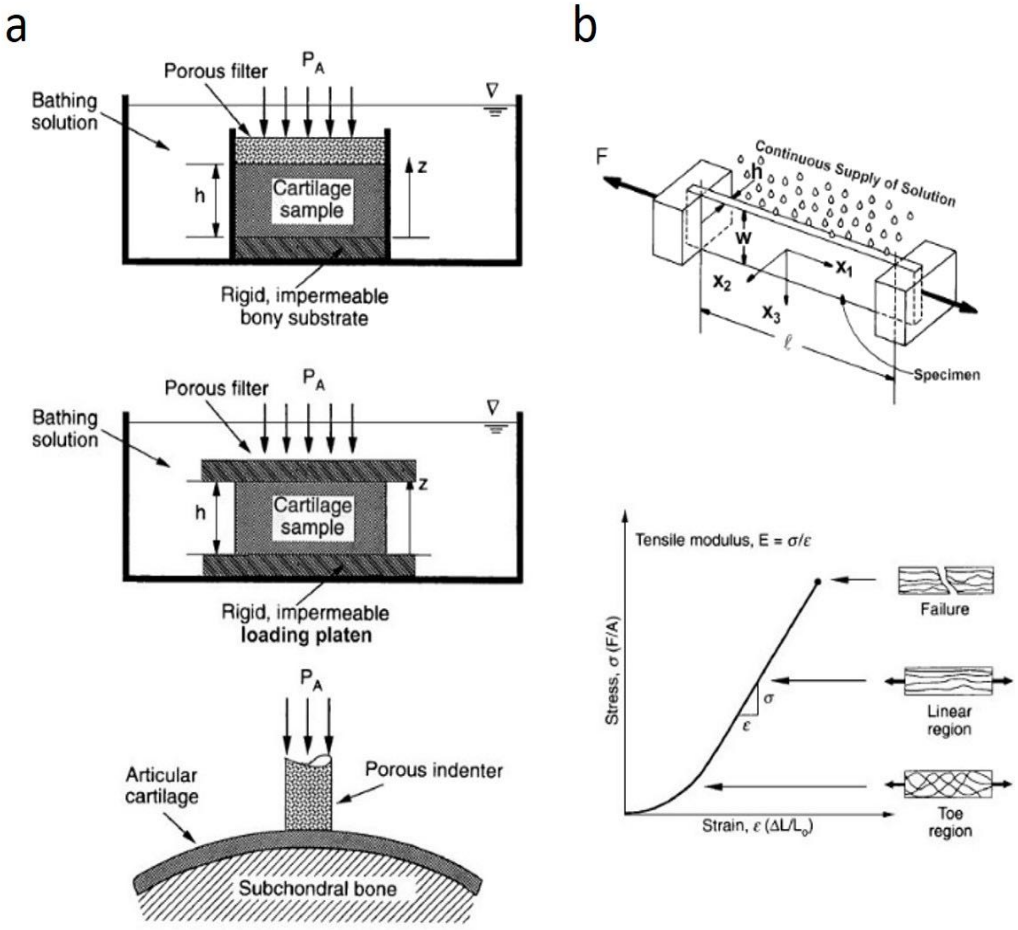

Figure 2-6 (a) Diagrams of the most used testing configurations to evaluate the compressive properties of articular cartilage: (top) confined compression, (middle) unconfined compression and (bottom) indentation. (b) Diagram of the tensile testing set-up (top) and typical tensile stress-strain graph (bottom) where each phase of the curved is associated to a schematic showing how collagen fibres re-arrange under tensile loading. (Mow et al., 2002).

2.2.2.2 Tensile properties

The tensile properties of articular cartilage are mainly attributed to the organization and structural properties of the collagen network present in the solid matrix of the tissue. When cartilage is subjected to tensile loading, the collagen fibres and the entrapped proteoglycans align and stretch in the loading direction. A non-linear toe region is

observed when the specimen is subjected to small deformations, due to re-alignment of the collagen fibrils as they pull through the proteoglycans (Figure 2.6 b). Following re-alignment, the tensile stress in the sample is high due to the intrinsic stiffness of the collagen network and the collagen fibres are stretched (Figure 2.6 b) (Akizuki et al., 1986; Kempson et al., 1973; Woo et al., 1976). The equilibrium tensile Young's modulus can be measured as the proportionality constant of the linear region of the tensile stress-strain curve and gives information about flow-independent stiffness of the collagen and proteoglycan solid matrix. The tensile modulus of articular cartilage ranges from 5 – 40 MPa, varying throughout the depth of the tissue as well as with the location of the joint surface (Mow et al., 2002). Generally, superficial zone cartilage samples are stiffer than specimens isolated from the middle and deep zones, as a result of the zonal collagen distribution. Moreover, samples oriented parallel to the split-line direction (indicating the collagen fibre direction) at the articular surface are stiffer in tension (Akizuki et al., 1986; Kempson et al., 1973; Mow et al., 2002). Overall, this demonstrates that articular cartilage possesses inhomogeneous and anisotropic tensile properties.

2.2.2.3 Tension-compression non-linearity

Comparison of articular cartilage compressive and tensile properties demonstrate that the equilibrium stiffness is typically 5 – 20 times higher in tension than in compression (Akizuki et al., 1986). This dramatic difference in cartilage tensile and compressive mechanical properties has an impact on the deformation mechanisms of the tissue in the presence of an external load (Mow et al., 1992). Under unconfined compression, cartilage specimens experience tension in the radial and transverse directions, and compression in the axial direction. In this case, the tension-compression non-linearity of articular cartilage lead to enhanced interstitial fluid load support (Jurvelin et al., 1997). Differences

between tensile and compressive properties were observed by Huang and co-workers (Huang et al., 2001; Huang et al., 2003) when performing confined compression tests on superficial zone cartilage samples as well as uniaxial tensile tests on cartilage specimens placed perpendicular and parallel to the local collagen fibres directions. The equilibrium compressive modulus was measured to be approximately 0.5 MPa. At small strains, the equilibrium tensile modulus reached 6.5 and 4.5 MPa parallel or perpendicular to the collagen fibres direction, respectively. At high strains, the tensile modulus was found to be 45 MPa along the split-line direction and 25 MPa perpendicular to this direction.

2.2.2.4 Fracture toughness

The fracture behaviour of articular cartilage is dependent on its unique structure. Crack formation and propagation is a key factor in the degeneration process of articular cartilage (Stok et al., 2007; Xiao et al., 2013). It has been reported that the osteoarthritic process in articular cartilage could be initiated by micro-mechanical damage to the cartilage surface due to overloading and damage, resulting in impaired joint function (Frost et al., 1999; McCormack et al., 1997). Fracture toughness is the parameter used to quantify the resistance of a loaded tissue matrix to the growth. A typical test for measuring apparent fracture toughness is characterized by the propagation of a crack through the specimen in order to measure the energy required to create a certain amount of new crack area (Taylor et al., 2012; Xiao et al., 2013). Traditional fracture mechanics uses three primary fracture loading modes to measure the apparent fracture toughness of materials, which is defined as the ability of a material to resist the propagation of cracks (Ahsan et al., 1999). Mode I loading opens a crack upon the application of tensile stresses normal to the crack plane. Mode II loading propagates a crack between two surfaces upon the application of in-plane shear forces. Mode III loading generates a crack by transverse

shearing. Mode I is the most used for cartilage, as tensile stresses are the primary forces responsible for crack opening (Ahsan et al., 1999), although fracture mechanics methods were originally developed to evaluate linear elastic materials. As articular cartilage is viscoelastic and anisotropic, crack propagation can vary in magnitude and mode, making it tricky to quantify the apparent fracture toughness of the tissue. Using Mode I loading such as single edge notch (SEN) tests, cartilage values of fracture toughness (J) have been reported to range from 0.14-1.2 kJ/m^2 (Adams et al., 2003; Chin-Purcell et al., 1996; Xiao et al., 2013). Because of the collagen fibres being arranged parallel to the articular surface, the superficial layer of articular cartilage is generally known to be more resistant to wear and shear forces compared to the middle and deep layers (Clarke et al., 1971).

2.2.2.5 Coefficient of friction

During joint articulation, articular cartilage must be able to provide a frictionless surface in order to prevent tissue degeneration and wear. The coefficient of friction (μ) of cartilage gliding on cartilage is used as a measure of cartilage lubricity, which is considered an indicator of tissue function. μ can be quantified by compressing the two opposing surfaces against each other, and then sliding (Gleghorn et al., 2008; Katta et al., 2008; Krishnan et al., 2010; Mow et al., 1984) or rotating (Lakin et al., 2013; Schmidt et al., 2007a; Wang et al., 1997) them against each other. Therefore, μ is calculated as the ratio between the normal and shear forces. μ of articular cartilage has been reported to be as low as 0.002, which means that a contact force of 1 kN across the joint generates a frictional shear force of only 2 N at the cartilage surface (Guilak et al., 2005). A number of factors such as magnitude of applied compressive force (Wang et al., 1997), sliding and rotating speed (Gleghorn et al., 2008; Schmidt et al., 2007b), number of oscillations or rotations (Lakin et al., 2017), and cartilage source can affect μ. In addition, μ is also

affected by cartilage matrix and synovial fluid components that include lubricin, hyaluronic acid and surface-active phospholipids (Schmidt et al., 2007a).

2.2.3 Bone composition and structure

Bone is a dynamic tissue that provides support to and protects organs in the body. It can be described as a composite material consisting of an inorganic and organic matrix. The inorganic phase, or mineral component, is responsible for bone strength and stiffness. It makes-up 55% of the tissue and is composed primarily of hydroxyapatite crystals and amorphous calcium phosphate (Sommerfeldt et al., 2001). The organic phase makes-up 20-30% of the wet weight of the tissue that consists mainly of type I collagen, small amounts of collagen type V and VII, non-collagenous glycoproteins and bone-specific proteoglycans (Sommerfeldt et al., 2001). There are three types of bone resident cells: osteocytes, osteoblasts and osteoclasts. In mature bone, osteocytes make-up 90% of the bone cells and are responsible for maintaining the bone matrix. On the other hand, osteoblasts and osteoclasts' main function is bone remodelling and resorption, respectively (Raggatt et al., 2010). Furthermore, bone-lining cells are present in the mature tissue, which attract osteoclasts and undifferentiated mesenchymal stem cells (MSCs). Such undifferentiated MSCs are stimulated to undergo osteoblasts differentiation in the case of a critical event, such as bone fracture (Raggatt et al., 2010).

From a morphology standpoint, bone can be divided into a denser and stiffer tissue called cortical (or compact) bone that compose the outer layers, and the inner more porous trabecular (or cancellous) bone with a central marrow cavity (Sommerfeldt et al., 2001; Wolfram et al., 2016). The subchondral bone is the area underlying the articular cartilage

immediately below the cartilage tidemark. It can be separated between subchondral plate (or cortical end plate) and subarticular spongiosa (or cancellous bone). The subchondral bone provides the cartilage with nutrients from the marrow as it is highly vascularized, with some vessels and nerves reaching to the calcified region of the cartilage (Imhof et al., 1999; Madry et al., 2010). Moreover, it serves as a supporting framework for the articular cartilage, playing a key role in absorbing stresses generated during everyday activity.

Bone development occurs *via* two mechanisms, intramembranous and endochondral ossification. During intramembranous ossification, MSCs undergo condensation followed by differentiation into osteoblasts and ultimately osteocytes. In the endochondral ossification process (Figure 2.7), a pre-existing cartilage template is systematically replaced by bone. The MSCs that have differentiated into chondrocytes increase approximately 2-fold in volume, resulting in the formation of hypertrophic chondrocytes that begin to secrete collagen type X and a number of angiogenic factors (Kronenberg et al., 2003; Mackie et al., 2008). As the matrix calcifies, nutrients will no longer be able to reach the hypertrophic chondrocytes that either trans-differentiate into osteoblasts or undergo apoptosis followed by disintegration of the surrounding cartilaginous tissue. This allows for invasion of blood vessels carrying osteogenic cells, many of which will become osteoblasts and form a periosteal collar of compact bone around the cartilage of the diaphysis, where the primary ossification centre will be created. A second ossification centre is formed in the epiphyseal regions, at the ends of the bone, where chondrocytes and cartilage continue to grow by increasing the bone

length as the cartilage in the diaphysis is replaced by bone tissue (Kronenberg et al., 2003).

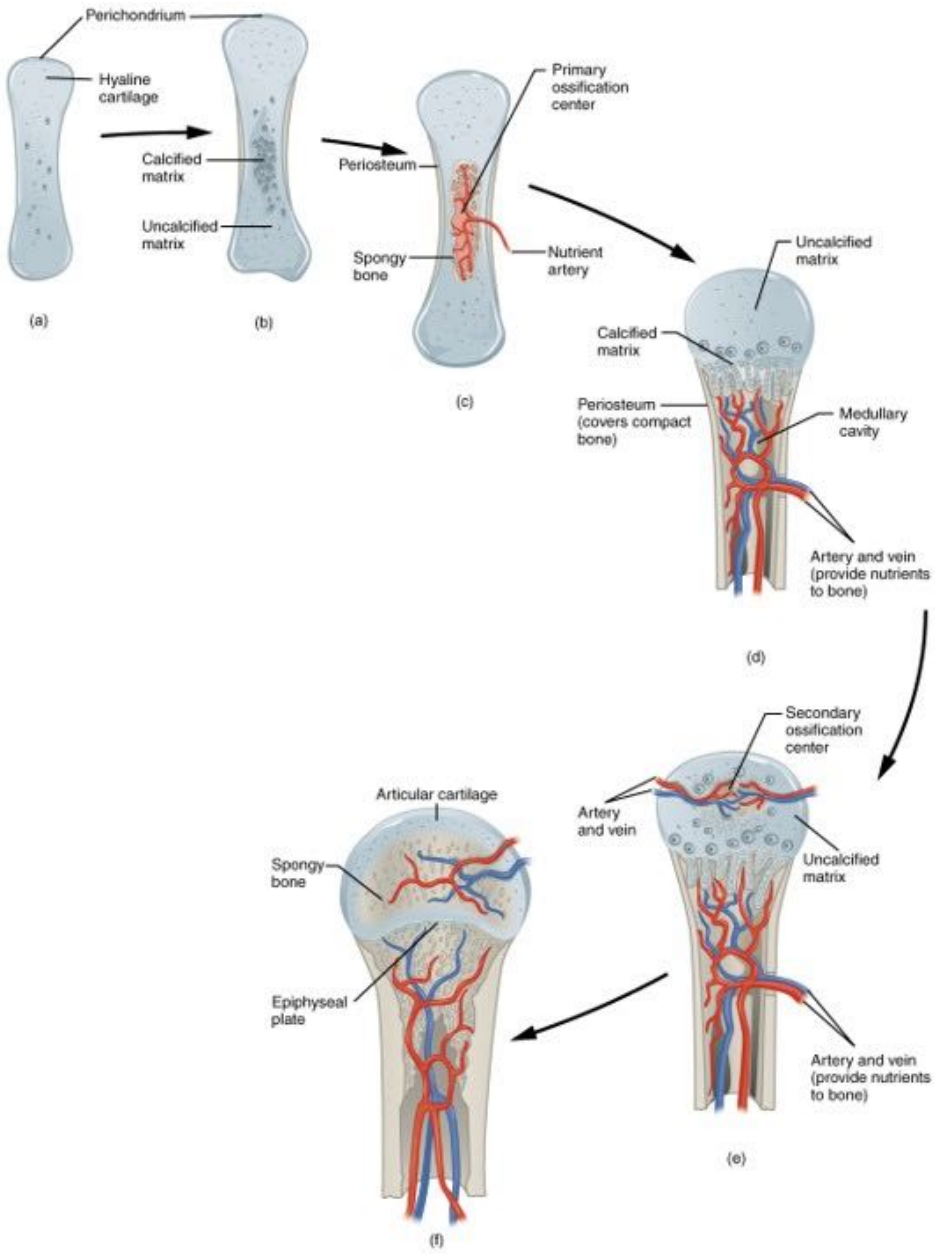

Figure 2-7 Schematic of the endochondral ossification process. (a) Condensed MSCs differentiating into chondrocytes forming a cartilage template. (b) The cartilage in the centre becomes calcified and the perichondrium forms. (c) Blood vessels invade the tissue while osteoblasts form and give rise to the periosteal collar. (d) Chondrocytes continue to proliferate at the ends of the bone increasing the bone length. (e) The secondary ossification centre is formed. (f) Articular cartilage tissue remains at the joint surface and at the epiphyseal plate.

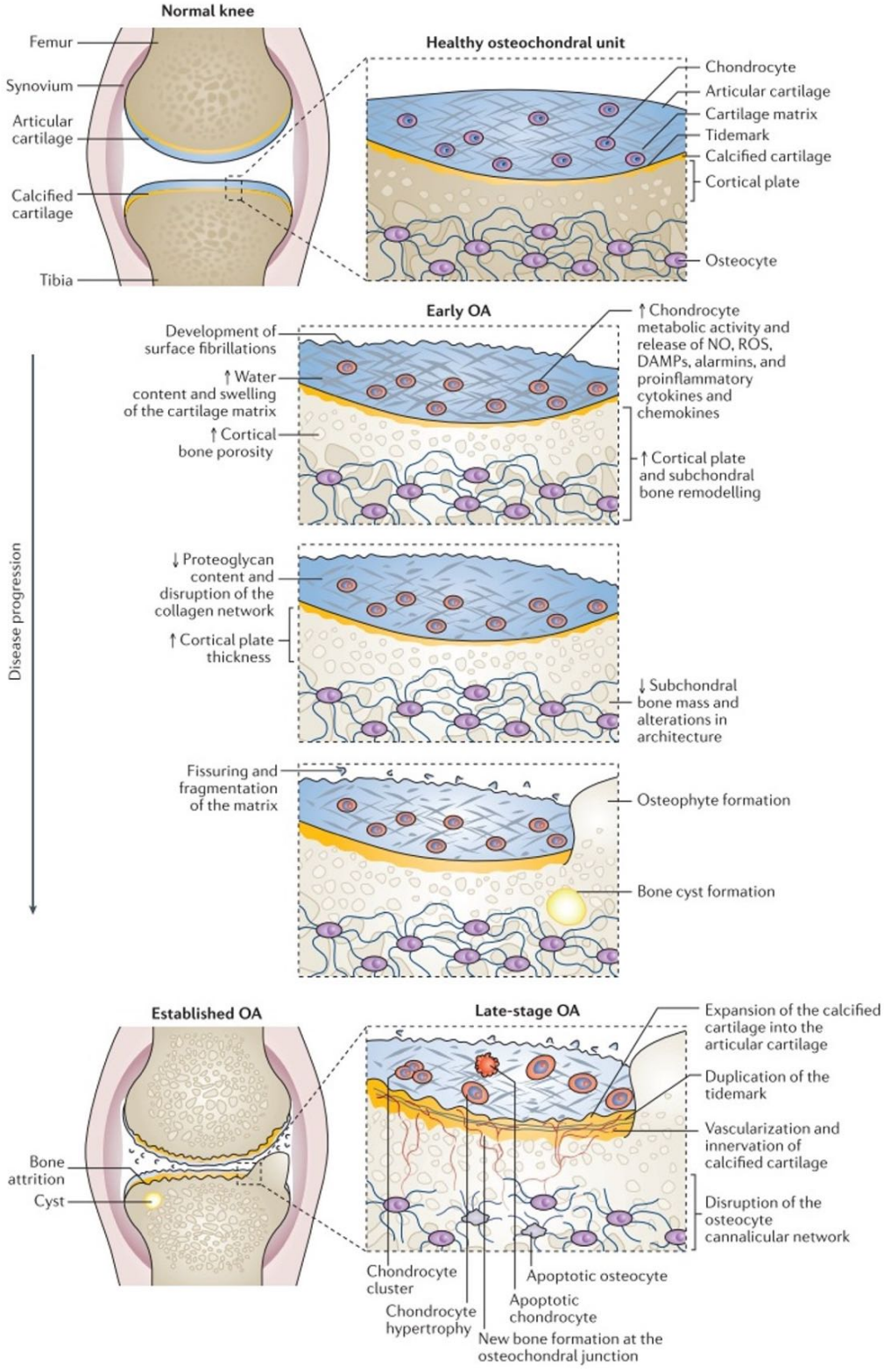

Figure 2-8 Schematic diagram demonstrating the sequential changes in the osteochondral tissue during the progression of osteoarthritis. (Goldring et al., 2016).

2.2.4 Changes in the osteochondral unit during osteoarthritis

Damage to either the articular cartilage or subchondral bone lesions can cause disruption of joint integrity, impaired movement, inflammation and significant pain. Lesions to the articular cartilage can also lead to narrowing of the joint space. If unable to heal, such lesions can degenerate into osteoarthritis (OA) (Figure 2.8), a major healthcare problem affecting millions of people worldwide (Johnson et al., 2014). Moreover, it was previously mentioned that the articular surface plays a key role in transferring the load across the joint and it has been demonstrated that increased load transfer as well as altered patterns of load distribution can accelerate the progression of OA (Roos et al., 2005). OA typically includes progressive loss of cartilage, osteophyte formation, remodelling and sclerosis of subchondral bone, inflammation of tendons and synovium tissue, and muscle weakness (Buckwalter et al., 2006; Madry et al., 2016). Osteochondral defects form in adults as a consequence of trauma to the cartilage and underlying subchondral bone or in association with ligament/meniscal tears. In young active individuals, osteochondral defects can occur as a result of osteochondritis dissecans, a condition characterized by bone sclerosis followed by cartilage fragmentation (Edmonds et al., 2013). In general, focal damage to the osteochondral complex gives rise to a series of repair and remodelling events that often have detrimental effects on the joint functionality leading to OA. In articular cartilage, one of the important changes caused by OA is the breakdown of the collagen network resulting in swelling of the matrix and subsequent increased water content which results in increased permeability, lower frictional forces and decreased matrix stiffness (Cooke et al., 2018; Goldring et al., 2016). Therefore, the articulating surface undergoes higher deformation and there is increased fluid flow, which reduce the load bearing properties. Alterations in

the collagen network composing the superficial zone also occur, affecting the tensile and shear resistant properties of the tissue and leading to further degradation (Goldring et al., 2016). These changes in the cartilage ECM are associated macroscopically with the presence of fibrillations characterized by microscopic cracks in the superficial zone. As the disease progresses, the fissures extend into the deeper regions of articular cartilage until they ultimately expose the subchondral bone (Lepage et al., 2019; Pritzker et al., 2006; Zhou et al., 2016). The structural and compositional changes in the cartilage also influence chondrocytes activity, as the excessive mechanical loading leads to phenotypic changes or to cell death. As tissue degradation increases, chondrocytes tend to form clusters and become hypertrophic (Goldring et al., 2016). Following delamination of the articular cartilage layers, calcified cartilage and underlying bone are exposed. The calcified cartilage is invaded by blood vessels from the subchondral bone, altering the cartilage homeostasis (Walsh et al., 2007). The subchondral bone experiences structural changes including thickening of the cortical plate, alterations in the mass, shape and orientation of the trabeculae, development of bone cysts and osteophytes at the joint margins (Madry et al., 2010). Furthermore, the state of mineralization of the tissue is altered, affecting the ability of the bone to deform under load (Burr et al., 2012; Day et al., 2001).

2.3 Advances in osteochondral tissue engineering

The osteochondral tissue is difficult to regenerate when damaged. The repair process relies on the migration of bone marrow stem cells (BMSCs) or progenitor cells into the defect site to regenerate the tissue (Seo et al., 2014). While an injury in the subchondral

bone, being a highly vascularized area, can be spontaneously repaired, any repair of the overlying articular cartilage layer is typically fibrocartilaginous in nature and tends to degenerate over time. Surgical therapies are commonly employed to treat cartilage and osteochondral defects. These procedures include arthroscopic debridement, microfracture, autologous chondrocyte implantation (ACI) and osteochondral autograft/allograft transplantation (Izadifar et al., 2012).

Arthroscopic debridement is characterized by removal of debris from damaged joints and is associated to pain alleviation (Laupattarakasem et al., 2008).

Microfracture involves the penetration of the subchondral bone to cause bleeding which facilitates the migration of progenitor cells from the bone marrow cavity into the defect. Although microfracture is still considered the gold standard by the FDA, it often results in inferior fibrocartilage poor mechanical properties, and limited sGAG and collagen type II levels compared to articular hyaline cartilage (Kalson et al., 2010; Mithoefer et al., 2009). This makes microfracture a temporary repair solution and more suited to smaller defect (Mithoefer et al., 2009; Vanlauwe et al., 2011).

ACI consists of a two-step procedure, where chondrocytes are first harvested from a low weight bearing area of the joint and expanded in monolayer *in vitro* until a sufficient number of cells is obtained. During a second surgery, expanded cells are injected into the lesion beneath a periosteal flap to secrete new cartilage matrix (Brittberg et al., 1994). The advantage of this technique is that using autologous cells prevents undesired immune reactions. However, chondrocytes when expanded in monolayer culture tend to de-differentiate, resulting in the production of inferior fibrocartilage or a mixture of hyaline and fibrocartilage (Diaz-Romero et al., 2008; Marlovits et al., 2004; Schnabel et al.,

2002). Another drawback of this technique is that two surgeries are required which increases the chance of infection. Matrix-induced autologous chondrocyte implantation (MACI) is a 'next generation' ACI, that involves similar steps except that cells are seeded onto, or encapsulated into a biomaterial (Kalson et al., 2010).

Larger sized defects that affect both articular cartilage and subchondral bone require different treatment approaches such as mosaicplasty or osteochondral autograft transplantation system (OATS). These involve the transplantation of one or more osteochondral plugs in the defect area, where the plug is harvested from an undamaged, low weight bearing area. Drawbacks include harvest site morbidity and potential degeneration of the implanted plugs as they originate in a low weight bearing area and might not be able to withstand much higher and more frequent loads (Hunziker et al., 2002). To overcome these limitations, allogenic cadaver plugs can be used, although immunogenic issues can arise and cryopreservation of the graft can lead to cell death and tissue deterioration (Hunziker et al., 2002). Clinical successes with the autograft/allograft methods have been reported, although many of them were for a younger population with no obvious signs of degeneration (Gudas et al., 2005).

In general, the repaired tissue generated using these techniques is primarily fibrocartilage which is biomechanically inferior compared to articular cartilage and contains more collagen type I (Rodrigues et al., 2011). Moreover, a total joint replacement is necessary when the damage to the osteochondral tissue is severe. The prosthesis consists of metal tibial and femoral components with plastic inserts between the two. This implant has a limited lifespan meaning that the probability of a second surgery is high. In addition, there are limitations in terms of implant loosening, stress shielding, wear and integration with the underlying bone.

Therefore, tissue engineering approaches have emerged as a promising advance for osteochondral tissue repair with the aim of promoting the regeneration of damaged tissues or the development of adequate tissue replacements. A number of key aspects determine the success of osteochondral tissue engineering. The primary requirements for scaffold biomaterials include biocompatibility and biodegradability to provide the cells with a biologically functional environment. The structural as well as the mechanical properties of a scaffold are important to provide adequate porosity and pore interconnectivity for nutrients diffusion and cell penetration, as well as mechanical functionality. Moreover, the type of scaffold and/or the employed scaffold manufacturing techniques determine how cells and signalling factors are utilized. The following sections will present the key aspects for the successful development of cartilage and bone tissue engineered scaffolds.

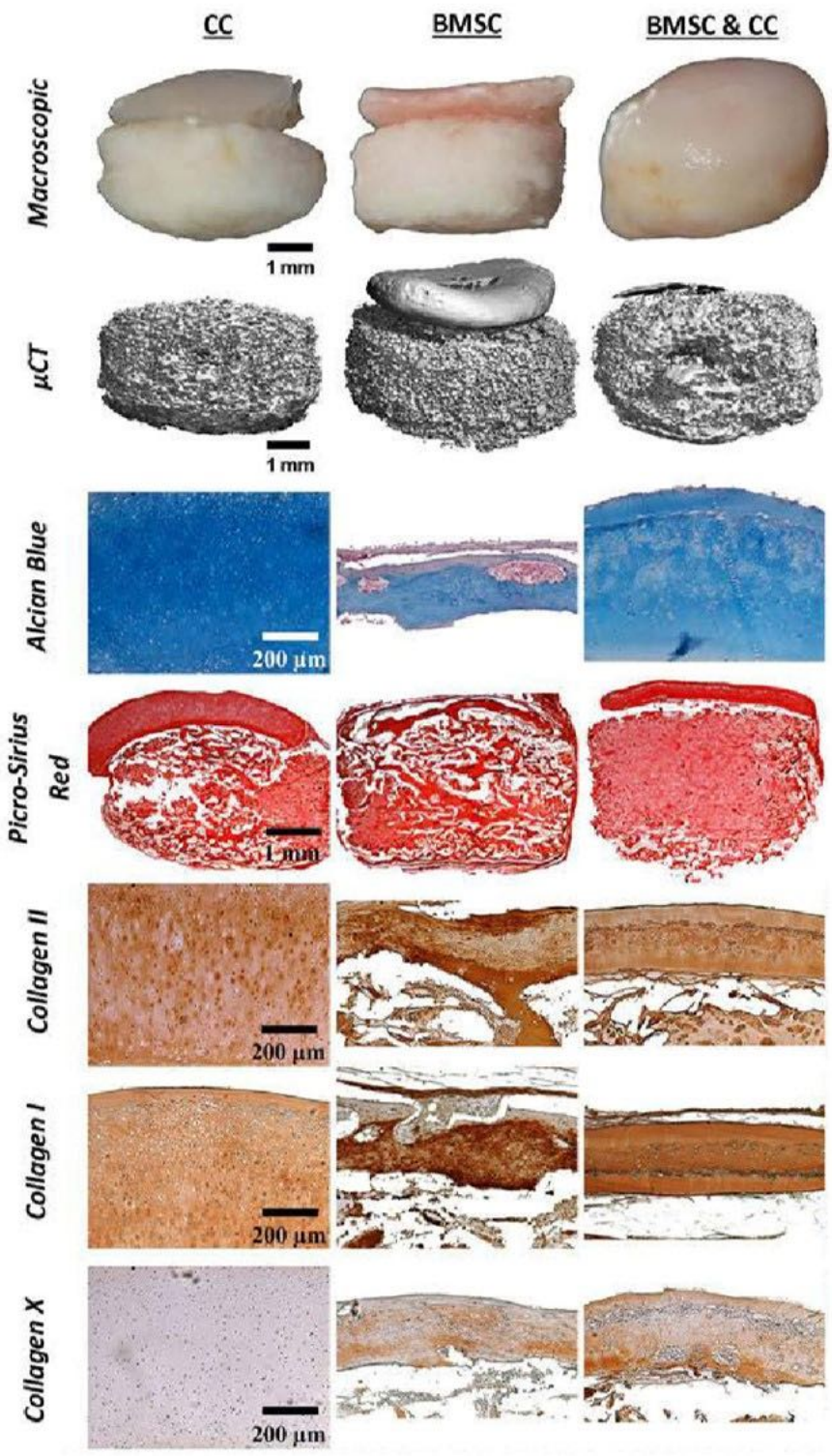

Figure 2-9 Analysis of bilayered constructs where the bone phase was characterized by a MSC-laden alginate hydrogel, while the chondral phase was derived from self-assembly of chondrocytes, BMSCs, or CCs and BMSCs. The top row shows macroscopic images of the scaffolds post-implantation, followed by micro CT scans, histological and immunohistochemical results. Adapted from (Mesallati et al. 2015).

2.3.1 Cell sources for osteochondral tissue engineering

For tissue engineering strategies that utilize exogenous cells as part of the regenerative strategy, the selection of a suitable cell source is essential to success. The first cell choice would be chondrocytes and osteoblasts as they are the native cells of cartilage and bone tissues, respectively. Chondrocytes are particularly attractive as they are used in clinical treatments and have been shown to form cartilage-like tissue both *in vitro* and *in vivo* (An et al., 2001; Brittberg et al., 1994; Mesallati et al., 2015). There is a number of limitations associated with the use of tissue-specific cells that include taking tissue biopsies which can cause donor site morbidity and further lesions (Matricali et al., 2010), and in the case of chondrocytes, limited number of available cells as well as cells gradually losing their phenotype when passaged *in vitro* (Benya et al., 1978; Darling et al., 2005).

BMSCs represent a promising alternative to tissue-specific cells as they have the capacity to proliferate extensively and differentiate along a number of lineages. Several studies have demonstrated that BMSCs can be primed to differentiate into chondrocyte-like cells in the presence of transforming growth factor-beta 3 (TGF-ß3) and hypoxic conditions (Almeida et al., 2017; Daly et al., 2016a; Johnstone et al., 1998; Vinardell et al., 2012). Nevertheless, chondrogenically primed BMSCs have the tendency to undergo endochondral ossification and form bone, making this approach more suitable for bone tissue engineering (Vinardell et al., 2012). A number of strategies have been explored to inhibit hypertrophy of MSCs and hence maintain a stable chondrocytic phenotype, once MSCs have differentiated into chondrocytes. For instance, co-culture of a small number of chondrocytes and a larger number of BMSCs has been successfully used to enhance the chondrogenic potential of BMSCs (Critchley et al., 2018b; Giovannini et al., 2010; Hendriks et al., 2009). It has been reported that osteochondral constructs can be

successfully engineered utilizing a MSC-laden alginate hydrogel for the bone region and a self-assembled co-culture of chondrocytes and MSCs in the cartilage region (Figure 2.9) (Mesallati et al., 2015). Following *in vivo* implantation, it was observed that a stable layer of articular cartilage was formed with no evidence of mineralization or vascularization, whereas the MSCs in the alginate hydrogel became hypertrophic undergoing endochondral ossification.

2.3.2 Functional design of cartilage and bone constructs

2.3.2.1 Biomaterials choice

The choice of biomaterials for osteochondral tissue engineering should meet a number of criteria. The selected material determines biological and physical properties of the tissue engineered scaffold facilitating cells adhesion, migration, proliferation and differentiation into tissue-specific cells. The ideal scaffold material is one which is biocompatible as it must not cause immune responses or foreign body reactions (O'Brien et al., 2011), has adjustable degradation rate possibly occurring simultaneously to tissue growth *in vivo*, provides appropriate mechanical support and a microenvironment capable of facilitating adequate ECM deposition. Materials for osteochondral tissue engineering include natural and synthetic polymers, decellularized ECMs, inorganic materials and their composites.

Hydrogels are hydrophilic polymeric networks characterized by high water content and swelling properties. Such properties have made them appealing materials for osteochondral tissue engineering because they mimic the 3D gel-like native ECMs. Generally, they can be divided into two categories: natural and synthetic hydrogels. Natural hydrogels (i.e. alginate, gelatin, collagen, agarose, fibrin) are often characterized

by structural similarities to native ECMs and in some cases possess inherent cell binding sites that can promote cell attachment, proliferation and growth; however, they usually have limited mechanical properties. Synthetic hydrogels (i.e. polyethylene glycol (PEG), polyvinyl alcohol (PVA), polyethylene oxide (PEO)) do not usually possess cell binding sites, but they are more versatile as they can be functionalized and their mechanical properties can be tailored to the specific application. Alginate and gelatin hydrogels will be discussed in more detail as they will be exploited in later chapters of this thesis.

Alginate is a negatively charged linear polysaccharide consisting of 1,4-linked α-l-guluronic acid (G) and ß-d-mannuronic acid (M) residues, which is isolated from brown algae (Drury et al., 2004; Drury et al., 2003). Alginate has been extensively used in tissue engineering due to its biocompatibility, non-immunogenicity and its capacity to undergo relatively fast gelation which allows for rapid cells encapsulation. In addition, alginate has the ability to absorb water and other molecules through capillary action (Axpe et al., 2016). Alginate forms a gel through ionic crosslinking with calcium ions such as calcium chloride, calcium sulphate, calcium carbonate or calcium phosphate (Lee et al., 2012). One drawback is that alginate is non-degradable by mammals, therefore it degrades by random dissolution *in vivo* (Boontheekul et al., 2005; Loibl et al., 2014). However, the degradation rate can be controlled by altering the degree of oxidation (Gomez et al., 2007) or by reducing the molecular weight of the polymer through gamma irradiation (Alsberg et al., 2003; Kong et al., 2002; Lee et al., 2003). Despite such methods increase the degradation rate of alginate, they also affect negatively their mechanical properties. Nevertheless, alginate has been shown to support chondrogenesis of stem cells and chondrocytes both *in vitro* and *in vivo* (Awad et al., 2004; Daly et al., 2016a; Igarashi et al., 2010; Mo et al., 2009; Sukegawa et al., 2012).

Gelatin is derived from denaturation of the triple-helix structure of collagen into single strand molecules through hydrolysis. Therefore, it retains some of the bioactive cues such as Arg-Gly-Asp (RGD) motifs from collagen, promoting cellular attachment, while cellular remodelling is facilitated by the presence of matrix metalloproteinase degradation sites (Klotz et al., 2018). Gelatin is a thermosensitive hydrogel, that dissolves at 37°C and gels at temperatures below 25°C in a concentration dependent manner. The most common use of gelatin in tissue engineering comes in its methacrylated form, gelatin methacryloyl (GelMA), which can be covalently crosslinked by UV light exposure overcoming the limitation of reversible thermal crosslinking. GelMA has been widely used for cartilage tissue engineering applications due to its high cell compatibility and the possibility to be easily combined with ECM-derived materials to stimulate tissue-specific ECM matrix production (Li et al., 2016; Schuurman et al., 2013; Visser et al., 2015).

Biodegradable synthetic polymers, including aliphatic polyesters (i.e. poly (glycolic acid) (PGA), poly (lactic acid) (PLA), polycaprolactone (PCL)), have been widely used as tissue engineered scaffolds. As they generally possess poor surface activity and cell affinity, a number of chemistries or processes to obtain functionalized blend or co-polymers have been applied to improve their intrinsic properties (Seo et al., 2014). For example, PCL was combined with PVA to produce electrospun scaffolds for cartilage tissue engineering. Incorporation of PVA resulted in improved hydrophilicity as well as the tensile properties of the PVA/PCL scaffolds, which supported proliferation and chondrogenic differentiation of MSCs *in vitro* (Shafiee et al., 2011).

Ceramics such as hydroxyapatite or calcium phosphates have been primarily used in bone tissue engineering. Such materials have excellent osteoinductivity and

osteoconductivity, and are known for promoting biomineralization (Nooeaid et al., 2012). Although ceramic-based scaffolds exhibit high stiffness, they are brittle and have low structural integrity making them unsuitable for load bearing applications.

As discussed in the previous paragraph, bone tissue engineering strategies that look to recapitulate the endochondral ossification process offer a promising route to bone regeneration (Sheehy et al., 2019). Several studies have shown that it is possible to repair critically-sized bone defects using endochondral strategies (Bernhard et al., 2017; Cunniffe et al., 2015; Harada et al., 2014). For example, cartilage templates have been formed by culturing BMSCs on a hyaluronic/gelatin sponge, and their capacity to regenerate carpal bone in a lapine model was investigated. After 12 weeks *in vivo*, the implanted constructs were filled with bony tissue and neo-vessels (Huang et al., 2006).

2.3.2.2 Scaffold mechanical properties

Hydrogels have been shown to support MSCs viability, differentiation and tissue-specific matrix formation especially in the presence of exogenous biochemical or biophysical cues. The mechanical properties (e.g. stiffness, viscoelasticity) of hydrogels play a key role in determining the phenotype of encapsulated cells (Engler et al., 2006; Park et al., 2011; Pek et al., 2010; Tse et al., 2011; Yeung et al., 2005). It has been shown this is determined in part by the stiffness of the hydrogels themselves. In general, cells are more adherent on rigid substrates than soft ones, and this stiffness-dependent cell adhesion regulates migration, morphology, gene expression and ultimately cell function (Engler et al., 2006; Guilak et al., 2009; Yeung et al., 2005). Engler et al. (Engler et al., 2006) demonstrated that MSCs differentiation could be modulated by the stiffness of the local substrate (Figure 2.10). When culturing human MSCs on type I collagen-coated polyacrylamide gels with variable compliance, it was observed that the stiffest substrates

(25-50 kPa) enhanced the expression of osteogenic markers and cells exhibited the typical cuboidal osteoblast morphology. The softest substrates (0.1-1 kPa) upregulated

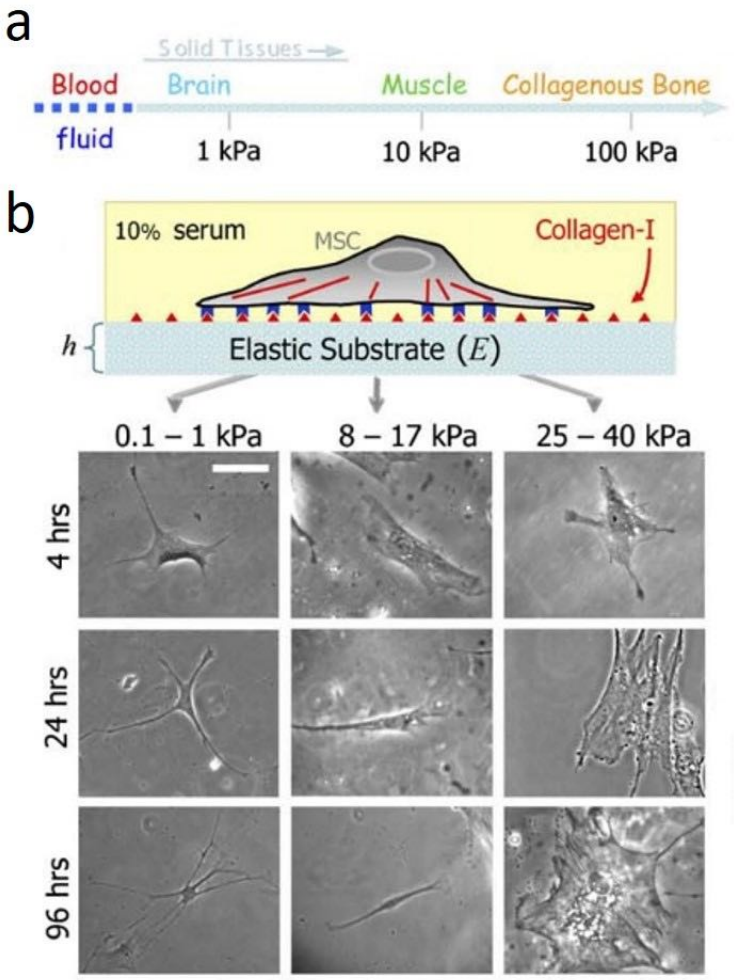

Figure 2-10 (a) Range of stiffness exhibited by solid tissues. (b) Human MSCSs cultured on polyacrylamide substrates change their morphology as the matrix stiffness varies (scale bar = 20 μm). Adapted from (Engler et al., 2006).

neurological markers and cells showed a dendritic morphology, while gels mimicking the stiffness of smooth muscle tissue (8-17 kPa) favoured myogenesis and adopted a spread cell morphology. Similar stiffness-dependent changes in MSC differentiation have been reported in 3D hydrogels (Pek et al., 2010).

A limitation of hydrogels for load-bearing applications is their poor mechanical properties. Several strategies have been explored to improve the mechanical properties of hydrogel scaffolds for tissue engineering applications. For example, the stiffness of alginate hydrogels has been shown to strongly depend on the efficiency of ionic crosslinking (Li et al., 2018). Four alginate-gelatin hydrogels were prepared with increasing phosphate buffered saline (PBS) concentrations. It was observed that high PBS ionic strength limited macromolecule interactions, thereby preventing the crosslinking of the alginate. This limited the availability of sites for embryonic stem cells to spread within the tissue engineered scaffolds, which instead formed isolated clusters. On the other hand, lower cell proliferation and aggregation was observed in the stiffest constructs (low ionic strength).

Other measures to enhance the mechanical performance of hydrogels include increasing crosslinker density, introduction of covalent crosslinks, modulation of material molecular weight and preculture to promote matrix deposition before the implantation of a tissue engineered graft (Anseth et al., 1996). The mechanical strength of hydrogels can usually be tuned by using lower or higher molecular weight hydrogels or by increasing or decreasing the number of crosslinking sites. Freeman et al. (Freeman et al., 2017) demonstrated that by using the same alginate bioink and calcium sulphate as a crosslinker, it was possible to spatially control the stiffness from the core to the periphery of MSC-laden bioprinted constructs by varying the material to crosslinker ratio. Dual Oil Red O and Alkaline Phosphatase staining showed that MSCs in the stiffer region (periphery) differentiated preferentially towards the osteogenic lineage, whereas in the soft core cells underwent adipogenesis. Although the introduction of high polymer concentration or chemical crosslinking can enhance hydrogels mechanical stability, this

does not necessarily represent an optimum solution. High polymer concentration can limit nutrients diffusion, and crosslinking agents are often toxic to cells. Moreover, despite the above mentioned modifications, the mechanical properties of the gels remain generally inadequate for high load bearing applications such as in osteochondral tissue engineering.

As cells in native tissues are responsive to different types of mechanical stimuli, it is hypothesized that the performance of hydrogel scaffolds is superior when they possess tissue specific-like mechanical properties. Commonly used hydrogels for tissue engineering comprise of only a single polymer, but recently intense effort has been dedicated to the development of more complex hydrogel systems by combining multiple polymer networks (Brigham et al., 2009; Chimene et al., 2016b; Jeon et al., 2017b; Liao et al., 2013a; Srikumar et al., 2017). The latter often exhibit superior mechanical properties compared to the single polymer networks and are known as Interpenetrating Network (IPN) hydrogels. IPNs are composed by separate polymer networks, physically entangled with each other where different chemistries are used to encourage the individual networks to crosslink only with themselves (Chimene et al., 2016b). The two networks cannot be separated unless chemical bonds are broken. Partial inter-network binding can occur depending on the type of crosslinking reaction and polymer used. For example, Jeon et al. (Jeon et al., 2017b) engineered highly elastic and tough IPNs based on alginate and gelatin. Mechanical stimulation of encapsulated human MSCs in the IPN hydrogel resulted in enhanced proliferation and osteogenic differentiation.

2.3.2.3 Composite scaffolds

More recently, the combination of biomimetic strategies to create both mechanically and biologically functional constructs has been explored. Hydrogels have mainly been

combined with solid polymer backbone materials, where the solid polymer provides a reinforcing skeleton for mechanical strength and the hydrogel offers a cell-supportive matrix within the scaffold (Izadifar et al., 2012; Moutos et al., 2010; Moutos et al., 2008). Advantages of using such hydrogel-solid composites include retention and homogeneous distribution of cells within the 3D solid scaffolds, hydrated cell-friendly environment within the hydrogel, possibility of delivering growth factors within the scaffold to better instruct cells, and better control over the shape of the scaffold (Izadifar et al., 2012). Cell-encapsulating hydrogels or acellular hydrogels have been incorporated into solid scaffolds *via* different methods that include casting, vacuum-assisted infusion and 3D bioprinting. Jung et al. (Jung et al., 2010) combined poly (L-lactide-co-Ɛ-caprolactone) scaffolds with chondrocyte-laden fibrin and hyaluronan hydrogels. After 8 weeks *in vivo*, a homogenously distributed layer of cartilage was formed with compressive properties comparable to native articular cartilage. Moutos et al. (Moutos et al., 2007a), infused 3D woven PGA structures with either agarose or fibrin gels which showed anisotropic, viscoelastic and tension-compression non-linearity properties similar to native articular cartilage (Figure 2.11). The hydrogel components seemed to be responsible for the viscoelastic behaviour, whereas the presence of the fibre network resulted in tension-compression non-linear properties which are believed to play a key role in the load bearing capacity under compression.

2.3.2.4 Multiphasic scaffolds

To replicate the biological and/or mechanical functionality of the native osteochondral tissue, a number of studies have explored the development of multiphasic scaffolds that could provide an optimal environment able to transfer adequate physical or chemical events from the cartilage to the bone layer. Recently, some effort has been made to design constructs that mimic the zonal structure and composition of articular cartilage. Self-assembling fabrication techniques have been used to engineer cartilage tissue by layering zone-specific chondrocytes to replicate the zonal organization of the cells in the native tissue (Elder et al., 2009b; Hu et al., 2006; Ofek et al., 2008). A limitation is that the initial mechanical properties of the cellular structures are low, although strategies such as 3D printing can be used to improve the mechanical functionality of self-assembled constructs.

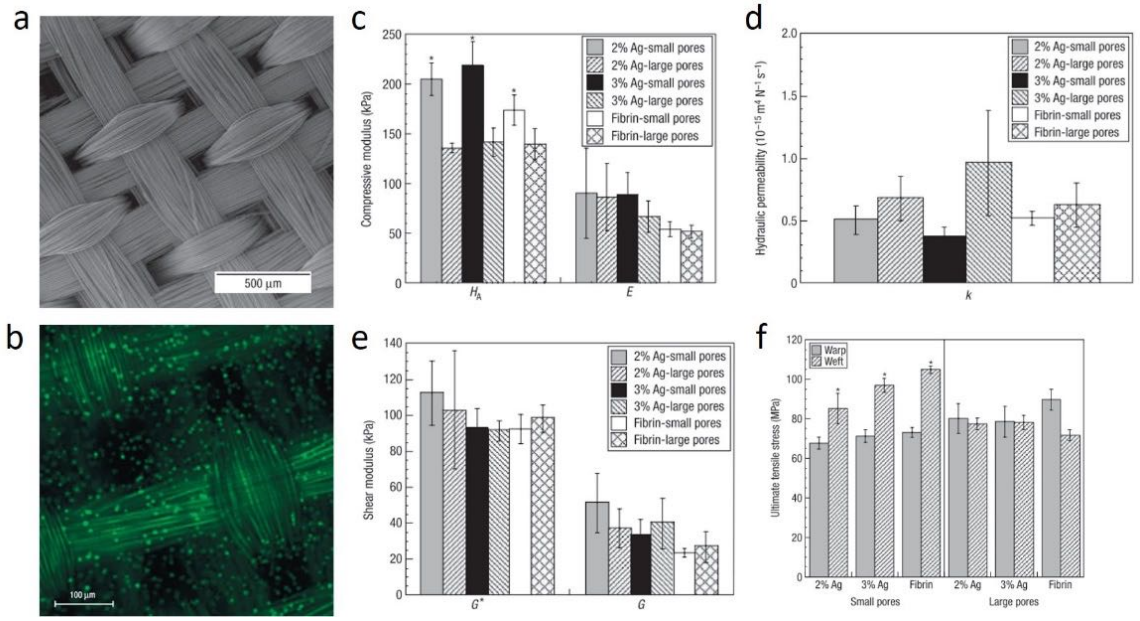

Figure 2-11 (a) Scanning electron microscope image of a 3D woven structure and (b) live-dead staining of porcine articular chondrocytes in a fibre-reinforced agarose composite. (c) Compressive modulus, (d) hydraulic permeability, (e) shear modulus and (f) ultimate tensile stress of fibre-reinforced gels. Adapted from (Moutos et al., 2007).

Another approach is to tailor the structural and/or biochemical design of solid or hydrogel scaffolds. For example, the orientation of fibre-based scaffolds can be modulated to determine mechanical and cell alignment properties of the native tissue (Wise et al., 2009; Woodfield et al., 2005). Articular cartilage- and growth plate-derived ECM biomaterials were used to create bi-layered scaffolds via freeze-drying. It was demonstrated that such multiphasic constructs were able to drive tissue-specific stem cell differentiation both in *vitro* and *in vivo* (Figure 2.12) (Cunniffe et al., 2019). In some studies cartilage and bone scaffolds have been engineered separately and joined later by suturing, glue or press fitting. For example, fibrin/PCL and PCL/PCL-tricalcium phosphate (TCP) scaffolds were fabricated individually to replace the cartilage and bone regions, respectively. Such constructs were seeded with cells and cultured in chondrogenic and osteogenic media before being combined into a single scaffold using fibrin glue (Swieszkowski et al., 2007). However, these methods are limited because of the poor integration between cartilage and bone phases, resulting in delamination. To overcome this issue, Grayson et al. (Grayson et al., 2010) proposed agarose-decellularized bone constructs, where the two materials were overlaid allowing the agarose to penetrate into the bone layer by 500 μm. Others have focused on developing trilayer constructs aiming to reproduce the interface zone of the osteochondral unit, which, in the native tissue, is important to provide a smooth compositional transition between the mineralized/vascular bone and the unmineralized/avascular articular cartilage. Qu et al. (Qu et al., 2011) developed trilayer osteochondral scaffolds where the cartilage phase was made of porous PVA, the bone phase comprised of nanohydroxyapatite-polyamide6 composites, and the interface was composed of non-porous PVA. After being seeded with adipose stem cells, such scaffolds showed the

potential to differentially support cartilage and bone tissue formation. In another study, Da et al. (Da et al., 2013) fabricated a multiphasic construct where the chondral phase was a sponge-like structure made of bovine cartilage ECM, whereas the bone phase was an interconnected tubular structure made of a poly (lactic-co-glycolic acid) (PLGA)/TCP core, embedded in collagen type I. Chondral and bone phases were separated by a PLGA/ß-TCP compact layer. The addition of the compact layer provided chondrogenic- and osteogenic-induced BMSCs with separate environments for optimal proliferation and differentiation. Triphasic constructs containing chemical and morphological gradients have also been produced (Filardo et al., 2013a; Kon et al., 2010; Tampieri et al., 2011).

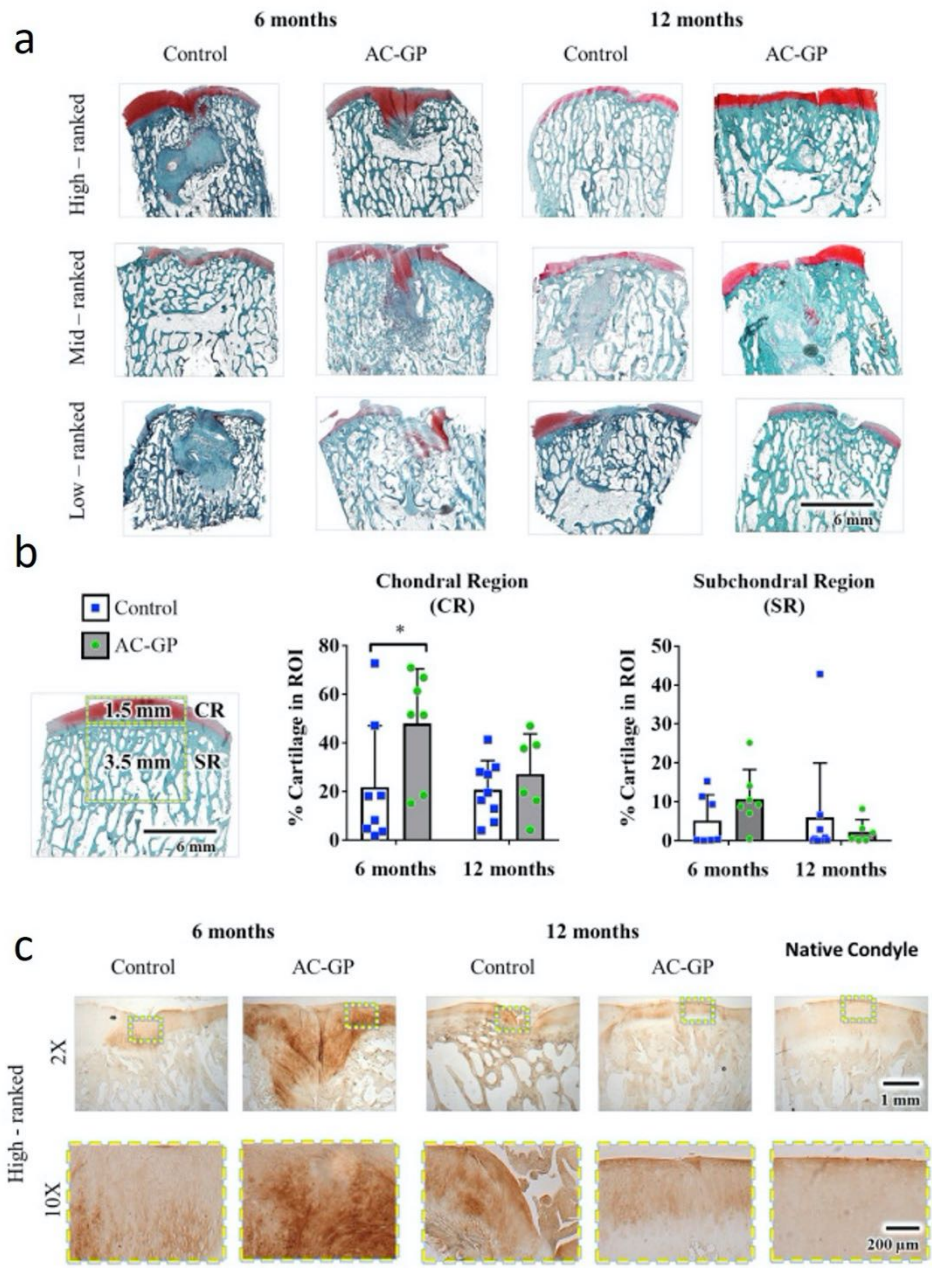

Figure 2-12 Evaluation of articular cartilage and subchondral bone repair post-implantation. (a) Safranin-O staining for cartilage matrix at 6 and 12 months, followed by (b) quantification of cartilage matrix present in chondral and subchondral bone region of the bi-layered scaffolds. (c) Immunohistochemical analysis of collagen type II for control and bi-layered samples compared to a native condyle control. (Cunniffe et al., 2019).

2.3.3 Growth factors delivery

Tissue regeneration is also possible by controlling the release of growth factors or other biomolecules over time from a biomaterial. In osteochondral tissue regeneration,

many growth factors work synergistically as molecular cues that stimulate cell maturation and differentiation towards a specific phenotype. The main families of growth factors involved in both cartilage and bone regeneration include fibroblast growth factors (FGFs), insulin-like growth factors (IGFs), transforming growth factors ß (TGFs-ß) and bone morphogenetic proteins (BMPs). Another important factor for bone is the vascular endothelial growth factor (VEGF).

In general, TGF-ß is able to induce MSCs differentiation into chondrocytes, promote their proliferation, increase ECM production and inhibit endochondral ossification (Giovannini et al., 2010). TGF-ß1, TGF-ß2 and TGF-ß3 have been widely used in cartilage tissue engineering, showing their capability in promoting chondrogenesis of BMSCs pellets and subsequently maintaining the chondrocytic phenotype (Giovannini et al., 2010). TGF-ß3 has also been incorporated into scaffolds and released in a controlled manner, resulting in chondrogenesis of human derived fat pad stem cells (Almeida et al., 2014).

BMPs are primarily responsible for triggering osteogenic differentiation of bone progenitor cells and MSCs present at the injury site (Bessa et al., 2010; Bose et al., 2013). In particular, BMP-2 has been shown to play a key role in expressing osteogenic markers. For example, osteocalcin and alkaline phosphatase expression is increased in the presence of BMP-2 (Sivashankari et al., 2016). For cartilage applications, BMP-7 is able to support MSCs chondrogenesis when combined with a member of the TGF family (Iwakura et al., 2013).

VEGF is a key regulator of angiogenesis during bone formation. It is responsible for stimulating the proliferation and migration of endothelial cells to form neo-vessels

(Hankenson et al., 2015; Nyberg et al., 2016). VEGF and BMP-2 have been sequentially released in a rat subcutaneous model, demonstrating improved bone and vessel formation when compared to release of BMP-2 only (Kempen et al., 2009).

2.4 3D bioprinting

3D bioprinting has become an attractive tool for tissue engineering, as it allows accurate and controlled spatial deposition of biomaterials, cells and exogenous biological cues. Moreover, current technologies enable the fabrication of complex, anatomically accurate geometries potentially mimicking the structure, composition and ultimately function of the target tissues/organs. Bioprinting aims at overcoming the limitations present in the traditional tissue engineering approaches. Seeding efficiency is improved due to simultaneous fabrication of the cellular and structural components, resulting in homogeneous/desired cell distribution within the bioprinted construct. Furthermore, the achievable spatial resolution allows for a multi-scale fabrication approach including the development of customized cellular microenvironments through the structuring of multiple biomaterials.

One of the main bioprinting techniques is microextrusion, where biomaterial filaments are extruded through a needle onto a solid substrate, from a pressurized syringe. The pressure can be applied mechanically or pneumatically by a screw or a piston (Murphy et al., 2014a). Moreover, the printer heads can be surrounded by cooling or heating sleeves to allow the printing of thermosensitive biomaterials. Many materials including polymers or polymer-ceramic composites have been used to create 3D structures *via* microextrusion. Hydrogels are the most commonly used because of their

capacity of encapsulating viable cells and growth factors. In the context of bioprinting, hydrogels incorporating cells or biomolecules are termed bioinks. Aside from supporting cell viability and tissue growth post-printing, a bioink must have adequate rheological properties that will determine printability of the bioink itself. The most important rheological properties to consider are viscosity, yield stress and shear thinning characteristics (Malda et al., 2013). Shear thinning is the non-Newtonian behaviour of fluids defined as the inverse relationship between the material viscosity and the shear force generated by the pressure applied during microextrusion (Guvendiren et al., 2012). This shear force decreases the viscosity of the bioink initiating flow through the needle; once the shear force is removed, the material viscosity increases resulting eventually in the material to hold its given shape (Chimene et al., 2016b; Murphy et al., 2014a). The viscosity of a bioink can be altered by varying the bioink concentration (Chang et al., 2010), printing temperature (Blaeser et al., 2016; Ouyang et al., 2016), by pre-crosslinking the bioink or combining it with sacrificial thickening materials that can be washed away post-printing.

Fused deposition modelling (FDM) is considered a type of microextrusion. The technique involves the extrusion of a molten thermopolymer (i.e. PCL, PLGA) through a temperature controlled needle using pressure. FDM does not allow the encapsulation of cells within the extruded material, but it permits high resolution control over the scaffold architecture, both internally and externally. In addition, polymeric structures fabricated *via* FDM are often used to reinforce softer cell-laden bioinks to provide structural and mechanical support. The polymer of interest in this thesis is PCL. PCL is a semi-crystalline aliphatic polyester characterized by melting temperature ranging from 59 and 64ºC, which enables it to be co-printed with bioinks with little or no negative effect on

cell viability (Woodruff et al., 2010). PCL is biodegradable as well as bioresorbable, presenting a total degradation rate of 2-4 years depending on the initial molecular weight of the construct (Gunatillake et al., 2003). It is an attractive material thanks to a number of advantages such as ease of shaping and manufacture which permit control over scaffold porosity to promote tissue ingrowth, delivery of biomolecules in a controlled manner, tailorable degradation kinetics and mechanical properties. The mechanical properties of 3D printed PCL scaffolds can be tailored by varying the polymer molecular weight or the scaffold structural features such as filament diameter, spacing and pattern (Olubamiji et al., 2016).

2.4.1 3D bioprinting of cartilage and bone-like tissues

Early cartilage and bone bioprinting studies used traditional hydrogels to evaluate the effect of 3D printing on cell viability and how printing and rheology parameters influenced cell function.

These studies demonstrated that 3D bioprinting could be used to create constructs with a viable homogeneous distribution of cells. For example, porous grid scaffolds were created through microextrusion of chondrocytes-laden GelMA hydrogels for cartilage tissue production (Schuurman et al., 2013). GAG and collagen type II were deposited after 4 weeks *in vitro*. Other approaches have shown that GelMA could be combined with more viscous components such as gellan gum, hyaluronic acid or fibrin to obtain more stable bioinks (Melchels et al., 2014; Schuurman et al., 2013; Zhou et al., 2017). Alternatively, GelMA fibres have been UV crosslinked immediately after being extruded during printing, to form stable structures (Ouyang et al., 2016).

For bone tissue engineering, alginate-based bioinks were mostly used in early studies. Poldervaart et al. 3D printed constructs made of alginate bioinks containing BMP-2-loaded gelatin microspheres to stimulate bone formation *in vivo* (Poldervaart et al., 2014). In another study, a bioink blend of alginate and gelatin promoted bone matrix production in the presence of human adipose derived stem cells, after 8 weeks *in vivo* (Wang et al., 2016). Bioprinting of growth factors has been used to accelerate vascularization during bone regeneration. For example, bioprinting has been used to engineer composite constructs containing dental pulp stem cells and spatial patterns of VEGF (centre) and BMP-2 (periphery) (Park et al., 2015). Vascularization was increased when VEGF was localized in the centre, compared to homogenous growth factor deposition.

Later studies have investigated the advantage of 3D printing tissue-derived ECM scaffolds. ECM has either been printed on its own or incorporated into existing bioinks, in order to provide encapsulated cells with biological cues that drive cell differentiation (Kim et al., 2017; Pati et al., 2014). Pati et al. demonstrated that printable bioinks can be developed by decellularizing and solubilizing cartilage ECM (Figure 2.13) (Pati et al., 2014). The ECM-derived bioink provided cartilage-specific factors that directed the differentiation of embedded MSCs into chondrocytes. In another study, Lee at al. (Lee et al., 2015) developed collagen/ECM/alginate-based bioinks from the matrix synthesised by pre-osteoblast cells cultured on gelled collagen. The addition of the alginate component increased the bioink printability. This bioink provided the embedded pre-osteoblasts with a more suitable microenvironment compared to pure alginate, which led to improved osteoblastic differentiation and higher levels of mineralization. Recent approaches have used bioprinting to engineer tissues with zonal differences. Cartilage constructs were 3D bioprinted creating a density gradient of bioink stiffness (Rhee et al.,

2016) or chondrocytes (Ren et al., 2016) throughout, resulting in a graded distribution of ECM components. 3D bioprintining has also been explored for the fabrication of

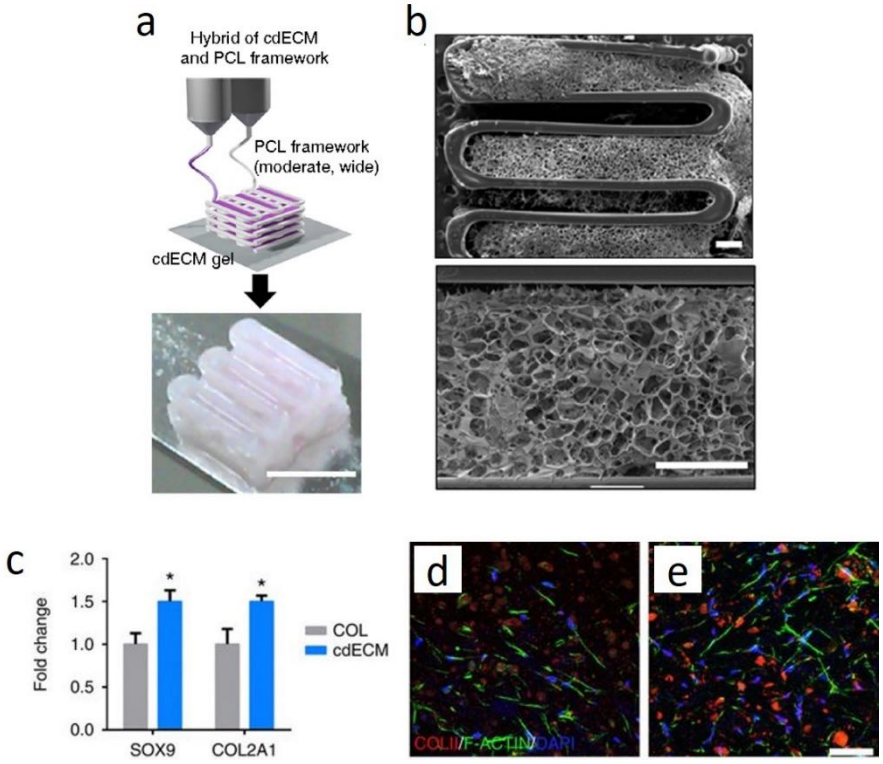

Figure 2-13 (a) Printing of cartilage ECM bioink with a PCL frame. (b) Representative microscopic images of cartilage ECM constructs (scale bar = 400 μm). (c) Quantification of SOX9 and COL2A1 genes in collagen (COL) and cartilage ECM-based (cdECM) gels. (d) Immunofluorescence images showing collagen type II (COLII), cell nuclei (DAPI) and F-actin in (d) COL and (e) cdECM constructs (scale bar = 200 μm). Adapted from (Pati et al., 2014).

multiphasic scaffolds. Bilayer cartilage constructs were fabricated by combining an articular chondroprogenitor cell-laden bioink and an MSC-laden bioink to mimic the superficial and deep zone of native articular cartilage, respectively (Levato et al., 2017). After 8 weeks *in vitro*, the constructs presented region-specific cellular and ECM composition with higher content of lubricin found in the superficial region.

2.4.2 3D bioprinting of fibre-reinforced hydrogels

As previously mentioned, one of the advantages of 3D printing is the ability to reinforce hydrogels with a stiffer polymer network with a defined architecture. Moreover, this network can be designed to mimic key structural and/or mechanical aspects of a specific tissue. The architecture of many native tissues is, in fact, characterized by the presence of a fibrous framework which not only provides structural integrity, but also anisotropy and depth-dependent mechanical properties (Aspden et al., 1994; Visser et al., 2015). Hydrogels have been reinforced with thermoplastic polymer fibres obtained *via* melt electrospinning writing (Bas et al., 2015; Bas et al., 2017c; Visser et al., 2015), solution electrospun (Eslami et al., 2014), woven (Boere et al., 2014; Liao et al., 2013a; Moutos et al., 2007a; Schuurman et al., 2011) and non-woven scaffolds (Marijnissen et al., 2002). This multiple-tool biofabrication strategy allows the hydrogels to be processed at low polymer concentrations, while the thermoplastic polymer network features can be tailored in order to obtain stable structures and secure the strength of the overall construct (Malda et al., 2013). Visser et al. (Visser et al., 2015) mechanically reinforced soft GelMA hydrogels with organized, highly porous, 3D printed PCL microfibre networks (Figure 2.14). Compared to the hydrogel or fibre scaffolds alone, the composite constructs showed a synergistic increase in stiffness up to 54-fold and approached that of native articular cartilage. When subjected to physiological compressive loading of 20% strain at 1Hz, chondrocytes incorporated in the composite scaffolds significantly upregulated the expression of ACAN and COL1A1 compared to non-reinforced gels. Bas et al. (Bas et al., 2017c) functionalized four-armed maleimide terminated PEG with Heparin (sPEG/Hep) to create a bioink that emulates the negatively charged proteoglycan matrix of articular cartilage. The soft sPEG/Hep bioink was then reinforced with melt

electrospun fibrous networks to mimic the biomechanical behaviour of articular cartilage. Above all, the high negative charge density and strong water retention capacity of the bioink led to a charge-driven osmosis similar to native articular cartilage that resulted into enhanced biological performance, as demonstrated by high chondrocyte viability and differentiation under physiological mechanical stimulation. Boere et al. (Boere *et al.*, 2014) fabricated reinforced scaffolds using a blend of PCL and poly(hydroxymethylglycolide-co-ε-caprolactone) functionalized with methacrylate groups. The blend-based constructs were then covalently linked to a chondrocyte-laden GelMA hydrogel to improve the integration between the materials. This resulted in an enhanced resistance to repeated axial and rotational loads. Furthermore, the embedded chondrocytes showed significant increase in cartilage-like matrix production both *in vitro* and *in vivo*.

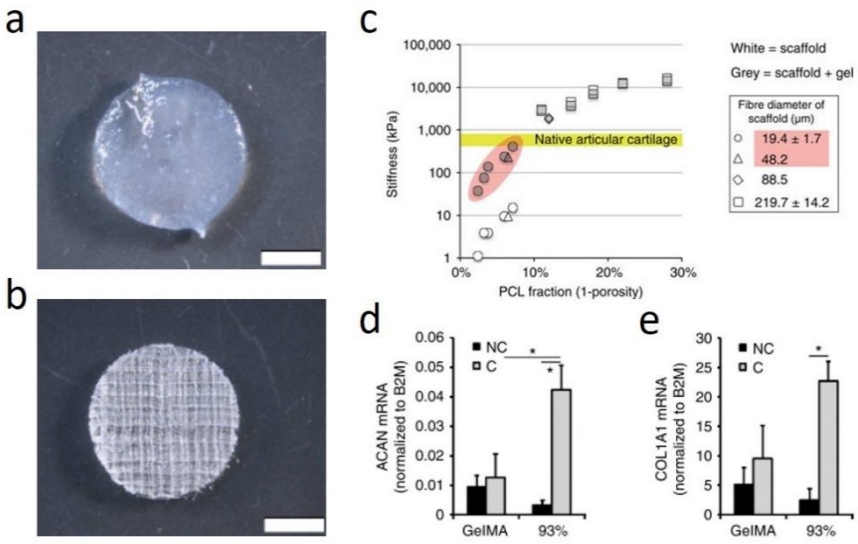

Figure 2-14 Macroscopic images of (a) GelMA-hyaluronic acid (HA) and (b) PCL-reinforced GelMA-HA constructs (scale bar = 2 mm). (c) Comparison of Young's moduli between PCL microfiber scaffolds alone, PCL-reinforced gels and native articular cartilage. (d, e) Gene expression analysis for (d) ACAN and (e) COL1A1. Adapted from (Visser et al., 2015).

3D printed PCL-based constructs have been used not only in an attempt to mimic the mechanical properties of native tissues, but also to provide mechanically stable implants that would allow a better integration with the surrounding environment *in vivo*. Osteochondral defects in a rabbit model were treated by 3D printing PCL networks supporting hyaluronic acid and collagen-based bioinks containing human MSCs in the cartilage and bone region of the construct, respectively (Shim et al., 2016). After 8 weeks, regeneration of thick neocartilage tissue was observed which integrated well with the adjacent tissue. Another emerging application of 3D bioprinted mechanically reinforced constructs is the fabrication of developmentally inspired templates for tissue or organ regeneration (Daly et al., 2016b; Jukes et al., 2008; Scotti et al., 2010). In the case of bone tissue regeneration, vertebrae-shaped hypertrophic cartilage templates were engineered *in vitro* by co-printing MSC-laden RGD-y irradiated alginate bioink and a

network of PCL microfibres (Figure 2.15) (Daly et al., 2016b). When implanted *in vivo*, the bioprinted construct matured into a vascularized bone organ.

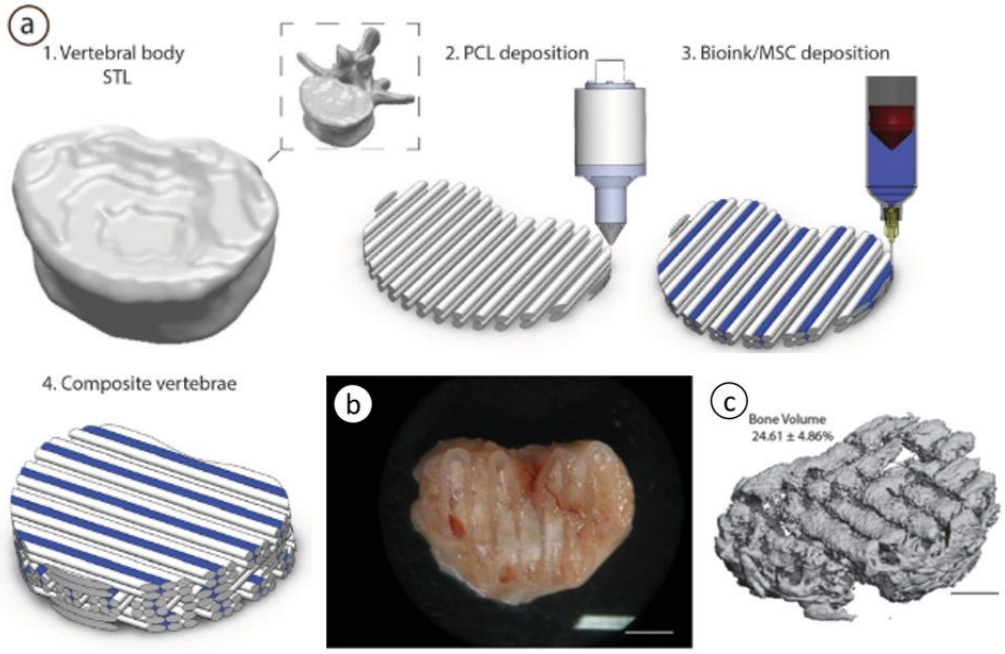

Figure 2-15 (a) Schematic of the multi-material bioprinting approach used to develop 3D bioprinted reinforced composite constructs in the shape of a vertebral body. After 12 weeks *in vivo*, vascularized bone-like tissue was formed as demonstrated by (b) macroscopic and (c) micro CT images (scale bar = 2 mm). Adapted from (Daly et al., 2016).

2.4.3 3D bioprinting of whole joints

Biological resurfacing of whole articulating joints represents an important but challenging strategy for tissue engineering. To date, tissue engineering has primarily focused on treating small cartilage or osteochondral defects, but diseases such as OA affect the entire joint surface. 3D bioprinting technology offers the potential to engineer functional tissue-specific scaffolds able to resurface an entire osteoarthritic joint.

For meniscus regeneration, Lee et al. (Lee et al., 2014) developed a 3D printed PCL meniscus-shaped implant loaded with PLGA microspheres to control the release of both

connective tissue growth factor (CTGF) and TGF-ß3. The spatial controlled release of CTGF and TGF-ß3 induced cells to form region-specific collagen type I and II matrices, similar to the native tissue. When grafted in place of a resected meniscus in an ovine model, the growth factor-releasing construct was found to facilitate the regeneration of the tissue with zone-specific matrix: collagen type I in the outer region and collagen type II in the inner region. Mechanical functionality was restored 3 months after implantation. In another study, 3D printing techniques were used to develop poly(ethylene glycol)-terephthalate/poly-(butylene terephthalate) implants for congruent articulating restoration in a rabbit knee model (Woodfield et al., 2009). After performing tibial and femoral osteotomies, the chondrogenically primed implants were fixed within the joints. It was observed that the implant was stable, and the formed articulating layer was functional. However, histological analysis of operated joints showed that the repaired tissue was more fibrous-like. For synovial joint regeneration, Lee et al. (Lee et al., 2010) 3D printed a PCL-hydroxyapatite scaffold mimicking the geometry of a rabbit proximal humeral joint (Figure 2.16). The fabricated constructs were infused with TGF-ß3 to promote host cells infiltration. After 4 months of implantation, bone growth and some cartilage repair were observed, while the animals showed no impaired movement.

All in all, these studies demonstrated the potential of 3D bioprinting strategies for whole joint regeneration. More recent advances, including high control over the spatial deposition of cells, biological cues, and biomaterials, open up the possibility to use multi-tool biofabrication approaches for engineering of more functional joint tissue implants.

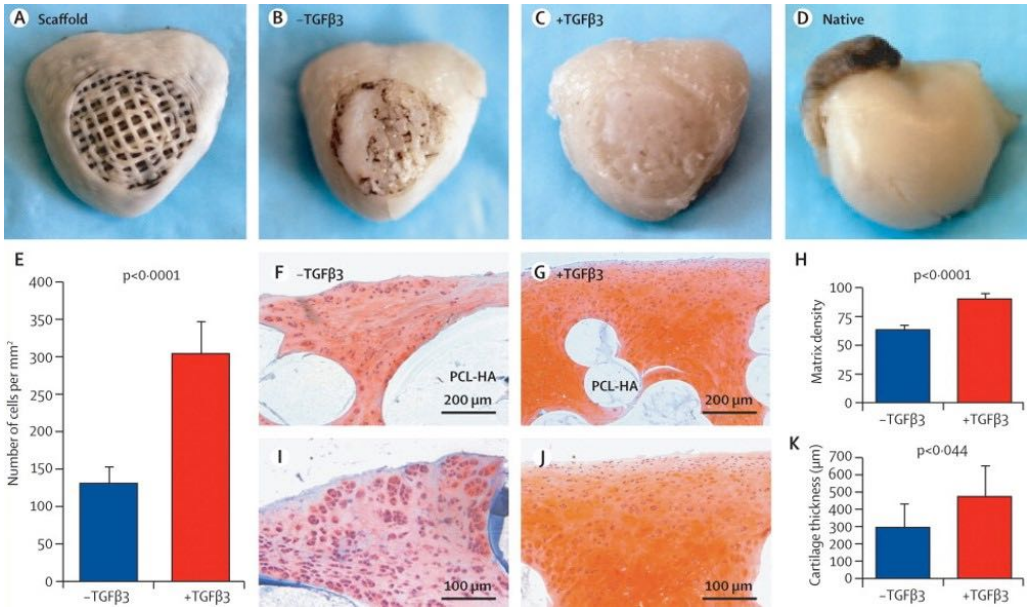

Figure 2-16 Development of humeral head shaped implants fabricated *via* FDM for synovial joint replacement in a lapine model. (a-d) Macroscopic images of the implant with or without TGF-ß3 in comparison to unimplanted construct and native tissue. (e) Number of cells per mm^2, (f, j) Safranin-O staining of the cartilage layer, (h) matrix density and (k) cartilage thickness present in constructs with and without TGF-ß3. (Lee et al., 2010).

2.5 Computational methods for aiding on the design of tissue engineered scaffolds

Computational modelling has been extensively explored to aid on the design of implants for tissue engineering. Traditionally, scaffolds are fabricated according to *in vitro* and *in vivo* experimental results by adopting a "trial-and-error" approach, which is expensive, time-consuming and has poor control over the scaffold properties. Design of a scaffold before fabrication using computational methods such as computer-aided design (CAD), finite element analysis (FEA) and computational fluid dynamics (CFD) is advantageous for a number of reasons. It can reduce the iteration of experiments, it becomes a predictive tool for scaffold properties prior to fabrication and testing, it permits the evaluation of some scaffold properties that are challenging to investigate

experimentally (i.e. stress and strain distribution), and it provides researchers with a broad range of choices for the design and/or optimization of scaffolds (Zhang et al., 2019). As previously discussed, geometrical and mechanical properties are believed to play a critical role in the successful development of implants for osteochondral tissue engineering. Geometrically, the construct needs to have adequate porosity and full interconnectivity (internal architecture) as well as functional external architecture to fit the defect dimensions. Mechanically, it needs to provide structural support to the surrounding tissue and distribute appropriate stresses and strains to the cells to influence subsequent tissue formation (Lohfeld et al., 2015). Finite element modelling (FEM) tools have been used to simulate how changes in the internal architecture and applied external forces can affect the scaffold performance (Eshraghi et al., 2012; Giannitelli et al., 2014).

Melchels et al. (Melchels et al., 2010) developed CAD models of 3D scaffolds with different architectures (cube, diamond and gyroid). The designed structures were fabricated by stereolithography and made either of poly(D,L-lactide) or poly(D,L-lactide-co-Ɛ-caprolactone). Bulk properties of the solid materials were used to implement finite element (FE) models to predict the deformation characteristics of the porous scaffolds. The gyroid structures were found to provide more evenly distributed mechanical stimuli within the construct, which would be beneficial for cell proliferation and differentiation. Lipowiecki et al. (Lipowiecki et al., 2010) studied how scaffold pore shape, pore size and loading regime influenced the scaffold stress distribution in the context of bone remodelling. Other studies investigated how the fabrication technique influenced scaffold architecture properties. Cahill et al. (Cahill et al., 2009) developed FE models of polyamide (PA) and PCL scaffolds fabricated using selective laser sintering, in order to predict the effective moduli of the constructs. Assuming isotropic material properties, it

was found that the effective modulus under compression was overpredicted by 67% for PCL scaffolds, whereas it was overestimated by 81, 125 and 147% in the x, y and z directions respectively for PA scaffolds. They suggested that microfeatures of the structure, such as roughness and microporosity, influenced the predicted scaffold mechanical properties. Entezari at al. (Entezari et al., 2016) optimized scaffold geometrical features such as filament size, pore size and amount of overlapping between filaments to design structures with high compressive strength while maintaining high porosity.

Among the number of factors that could affect cell fate, the local mechanical stimulation determined by fluid flow is very important and could be affected by the scaffold structure. Scaffold fluidic properties can be investigated and optimized using CFD. Almeida et al. (Almeida et al., 2013) explored the effect of varying pore size on the fluidic behaviour of scaffolds. It was predicted that scaffolds with smaller pores experienced variable wall shear stress and shear strain rate in different regions of the scaffold. Olivares et al. (Olivares et al., 2009) have investigated the scaffold behaviour under fluid flow and axial compression, observing that cell differentiation is more sensitive to fluid flow.

Combining FEM with mechanobiological models could potentially help evaluating the effect of specific biophysical factors on tissue *in vitro* and *in vivo*, and ultimately improving the scaffold design (Checa et al., 2009). O'Reilly et al. (O'Reilly et al., 2016) developed a model that simulated osteochondral defect repair following the implantation of different variations of a construct developed by Da et al. (Da et al., 2013) (Figure 2.17). It was predicted that the presence of a compact layer, separating the cartilage from the bone region of the scaffold, improved tissue formation as angiogenesis was confined to

the subchondral region of the defect. Moroni et al. (Moroni et al., 2007) performed a numerical investigation on the mechanical behaviour of poly(ethylene oxide-terephthalate)-co-poly(butylene terephthalate) anatomical 3D scaffolds as menisci

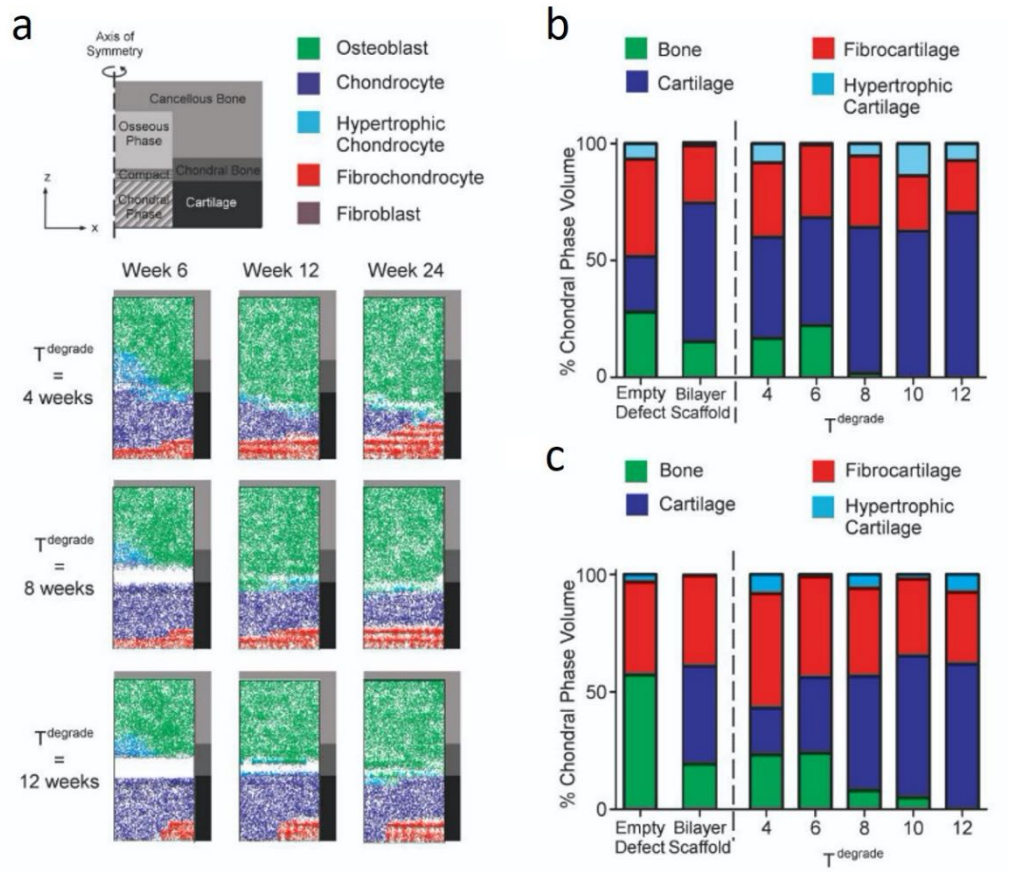

Figure 2-17 Simulating treatment of an osteochondral defect with a trilayer engineered scaffold. (a) Predictions of cell differentiation over 24 weeks. (b, c) Quantification of the different type of tissue forming within the chondral region of an empty defect, bilayer and trilayer scaffolds at 12 and 24 weeks. (O'Reilly et al., 2016).

replacements. A comparison between FE models of both the proposed scaffold and meniscectomy, suggested that the designed constructs would determine a more physiologic stress and strain distribution on the articular cartilage surface.

2.6 Bioreactor systems

Mechanical stimulation can directly influence the structure and function of musculoskeletal tissues at different stages of life. Chondrocytes have been shown to respond to a wide range of mechanical stimuli (i.e. hydrostatic pressure, osmotic pressure, fluid flow, shear, deformation) during development and growth (O'Conor et al., 2013). Growing interest has been paid in understanding the mechanobiology of MSCs and how to leverage mechanical and biophysical cues to drive MSCs differentiation, leading to appropriate tissue regeneration. Bioreactor systems have been explored to identify the specific mechanical environment to enhance tissue-specific matrix production within cell-encapsulated tissue engineered constructs.

A number of *in vitro* studies have demonstrated that the type of applied mechanical stimulus, duration and frequency, influence the cell response (Mauck et al., 2007). It has been shown that unconfined dynamic compression significantly improved the functional properties of chondrocyte-seeded scaffolds (Mauck et al., 2003; Mauck et al., 2000). Similar results were observed in MSC-seeded constructs. Aggrecan and collagen type II expression increased when human or rabbit MSC-based constructs were subjected to dynamic compressive loading (Huang et al., 2004). The presence of exogenous growth factors such as TGF-ß, can also determine the MSCs response to compressive loading. In the absence of TGF-ß, it was found that compressive loading alone resulted in chondrogenic differentiation that was comparable to stimulation with TGF-ß alone or TGF-ß plus loading (Kisiday et al., 2009). The architecture of cell-seeded constructs or the stiffness of the scaffold material were also found to affect how loading is transferred to the cells during mechanical stimulation. Bartnikowski et al. demonstrated how the internal architecture of 3D printed PCL scaffolds influenced the cellular response of

osteoblasts in perfusion bioreactor cultures. (Bartnikowski et al., 2014). Aziz et al. (Aziz et al., 2019) studied the effect of hydrostatic pressure on cell fate within a bi-layered hydrogel with soft and stiff layers. It was found that, high hydrostatic pressure inhibited late-stage osteogenesis of human MSCs in the stiffer layer; when hydrostatic pressure was reduced, mineralization was recovered.

2.7 Summary

Engineering both a mechanically functional and cell-instructive environment within tissue engineered constructs is critical to their likelihood of success. Engineering biomimetic scaffolds for the regeneration of the osteochondral unit will likely require a multi-disciplinary approach, involving the combined use of 3D bioprinting, computational modelling and bioreactor systems, which has not been identified yet . The integration of such advanced technologies could provide a framework for tissue engineering anatomically accurate regenerative implants for biological joint resurfacing. The literature review has discussed the potential of using co-cultures to produce cartilage-like tissue, and the advantage of forming hypertrophic cartilage templates, that can undergo endochondral ossification *in vivo*, to generate bone-like tissue. In general, studies have focused on engineering implants for treating focal defects, with only few papers on developing whole joint prosthesis. The literature review also showed that the mechanical environment and the structural organization of the native tissue components are key to the development of functional tissues, but difficult to recapitulate when engineering tissue replacements. Transitioning from repairing focal defects to resurface an entire joint will require providing a spatially defined, biomimetic environment with

both biological and mechanical functionality of the tissue engineered construct. The literature review highlights that a number of strategies including tailoring of constructs architecture, controlling spatial distribution of biomaterials, cells and biological cues within the construct, and providing suitable mechanical cues to the engineered construct could potentially result in the development of adequate tissue replacements. The most promising study by (Lee et al., 2010), showed the potential of using 3D printed polymer constructs loaded with a growth factor to recruit host cells, for repairing the shoulder joint of a rabbit. Despite this study has laid the groundwork for tissue engineering total joint prosthesis, additional steps of elucidating the optimal combination of cells, biomaterials and bioactive cues for both cartilage and bone tissue are required to engineer a functional biological joint.

The next chapter of this thesis (Chapter 3) will use FEM to aid in the design of 3D printed polymeric structures with desired mechanical properties. Recognizing that hydrogels alone do not possess suitable mechanical properties for load-bearing applications, Chapter 4 will use 3D bioprinting to produce fibre-reinforced IPN hydrogels with mechanical properties mimicking those of articular cartilage and capable of providing a pro-chondrogenic environment *in vitro* to encapsulated MSCs. FEM and experimental mechanical tests will be used to characterize the mechanical behaviour of the resulting composites. Chapter 5 will explore the ability to engineer both phenotypically stable articular cartilage and hypertrophic cartilage in 3D bioprinted bi-layered constructs *in vitro*. Specifically, the influence of co-cultures and mechanical stimulation as strategies to develop stable articular cartilage will be evaluated. With a view to develop 'off-the-shelf' implants for total joint resurfacing, Chapter 6 will investigate the capability of 3D bioprinted bi-layered constructs containing bioinks

functionalized with specific growth factors to regenerate 1) large osteochondral defects in the knee condyle of goats or 2) to replace the whole glenohumeral joint in rabbits.

Chapter 3
Integrating finite element modelling and 3D printing to engineer biomimetic polymeric scaffolds for tissue engineering

3.1 Introduction

Tissue engineering applications often require the use of porous and biocompatible three-dimensional (3D) scaffolds that serve as temporary templates for cell attachment and proliferation, ultimately promoting tissue specific extracellular-matrix secretion and functional regeneration (Hollister et al., 2016; O'Brien et al., 2011). For the engineering of many tissues, the geometry and mechanical properties of the scaffold are key factors that must be carefully tuned to appropriately direct regeneration. Geometrically, the scaffold needs both a suitable external architecture to properly fit the defect, and an internal architecture with sufficient porosity to facilitate cell migration and cell-cell interactions. Mechanically, it should have sufficient strength to resist physiological loading while appropriately distributing such stresses to the surrounding tissue during the regeneration process (Lohfeld et al., 2015).

3D printing technology in tissue engineering allows the fabrication of patient-specific scaffolds with high cell ingrowth capability, appropriate pore interconnectivity, highly controlled internal geometry and more recently the incorporation of bioinks containing cells (Giannitelli et al., 2014; Murphy et al., 2014a; Park et al., 2011). Among the number of 3D printing techniques available, Fused Deposition Modelling (FDM) has shown great potential in advancing the development of functional tissue replacements, as it enables

the fabrication of scaffolds with precisely defined compositions and architecture (Sachlos et al., 2003; Zein et al., 2002). Highly interconnected pore geometries with a wide range of pores size can be obtained by varying printing parameters such as needle diameter, extrusion pressure and speed (Olubamiji et al., 2016; Sachlos et al., 2003; Zein et al., 2002). Moreover, mechanically robust scaffolds can be produced with mechanical behavior mimicking that of several biological tissues (Olubamiji et al., 2016; Roohani-Esfahani et al., 2016; Woodfield et al., 2004).

From a mechanical point of view, there is still a lack of knowledge on the behavior of 3D printed structures under compressive load and how such implants might respond to physiological loading conditions. The absence of a simple and efficient framework to explain the micromechanical behavior of 3D scaffold structures can limit or slow down the development of appropriate tissue engineered scaffold designs. Previous studies attempting to develop functional scaffold designs have typically adopted a "trial-and-error" approach, where modifications to an existing design are assessed using experimental work. Computational methods that simulate the mechanical behavior of 3D constructs can also provide valuable insights into the structure-function relations of such implants (Giannitelli et al., 2014; Lacroix et al., 2009). A number of studies have used Finite Element Analysis (FEA) to optimize and/or evaluate scaffold designs in terms of oxygen diffusion (O'Reilly et al., 2016; Woo Jung et al., 2013), mechanical properties (Almeida et al., 2013; Eshraghi et al., 2012) and cell response to external stimuli (O'Reilly et al., 2016; Sun et al., 2004; Yan et al., 2010). The accuracy of such FE models strongly depends on how precisely the architecture of the printed structure is represented. Discrepancies between the originally designed structure and the actual printed geometry will always occur during the FDM process. For example, filaments from one layer of a

printed scaffold fuse to differing degrees into the previous layer, altering the geometry of the scaffold. The importance of considering these geometrical differences when developing FE models of 3D printed structures has only recently been appreciated (Gleadall et al., 2018; Naghieh et al., 2018). Therefore, FE analysis aided design of 3D printed scaffolds must consider the actual printed geometry of the construct, ideally without resorting to use of computationally expensive techniques that would limit the widespread use of such approaches.

The overall goal of this study was to develop a computationally efficient and accessible FE modelling strategy that could be used to design 3D printed polycaprolactone (PCL) scaffolds with user-defined mechanical properties. To this end, we first printed a range of PCL scaffolds with altered fibre spacing and fibre diameters, and then created Computer Aided Design (CAD)-based FE models of both the idealized scaffold designs (pre-fabrication) and the actual printed scaffolds (post-fabrication). The advantage of modelling actual printed geometries and the ability of such models to predict the mechanical behavior of complex 3D structures is demonstrated by comparing computational predictions to experimental measurements. The utility of this integrated approach is demonstrated by designing and 3D printing scaffolds with defined stiffness and elasticity, with a particular focus on articular cartilage tissue engineering. Computational efficiency will be ensured by using CAD-based scaffold representations, that only account for key geometrical features of the actual printed geometry parameters (e.g. fibre diameter, fibre spacing, layer fusion), to predict the mechanical behavior of 3D printed scaffolds. Using CAD-based FEA in this way is advantageous as there is no need to develop sample-specific models that require expensive and time-consuming imaging

techniques (i.e. micro-computed tomography (micro CT)) to determine the geometry of the scaffolds.

3.2 Materials and methods

3.2.1 Scaffold design and fabrication

All scaffold geometries were designed to obtain cube shaped constructs with dimensions 9 mm x 9 mm x 4 mm. To investigate how geometry features can influence scaffold mechanical properties and porosity, five different architectures were obtained by varying fibre spacing (s) (1 or 1.5 mm), fibre diameter (d) using two different needle sizes (25 or 30 Gauge) and internal fibre pattern (*Aligned*, *Single Offset* or *Double Offset*). Scaffold geometrical features are described in Figure 3.1a-d. The *Aligned* architectures (Figure 3.1b) were characterized by a fibrous network comprising of aligned filaments stacked in horizontal layers that followed a 0°0° - 90°90° pattern, whereby layer X was plotted orthogonally to layer X-2 (resulting in a 90° angle) and was plotted in the same relative position of layer X-1. By systematically varying fibre spacing and fibre diameter, three different *Aligned* designs were obtained. *Aligned 1* and *Aligned 2* structures had a filament diameter of 0.26 mm (25 gauge needle) and two different spacings, 1 and 1.5 mm respectively. This resulted in filament inter-spacings of 0.74 mm for *Aligned 1* and 1.24 mm for *Aligned 2*. To study the effect of filament diameter, *Aligned 3* architecture had a fibre diameter of 0.16 mm (30 gauge needle), while the fibre spacing was the same as the *Aligned 2* design (1.5 mm), resulting in a fibre inter-spacing of 1.34 mm. The *Single Offset* (Figure 3.1c) and *Double Offset* (Figure 3.1d) patterns are also orthogonal architectures characterized by layer X being printed with an offset distance, which is half

the fibre spacing, relatively to the position of layer X-4. Offset layers are present only in the xz-plane for *Single Offset* structures (showed in red in Figure 3.1c), whereas they are present in both xz- and yz- planes for *Double Offset* geometries (showed in red in Figure 3.1d). Fibres orientation was modified after the deposition of two consecutive layers in all geometries to provide the scaffolds with high side porosity.

All constructs were manufactured using the 3D Discovery bioplotter purchased from RegenHU (Switzerland) with spatial resolution of ± 5 µm. PCL pellets with an average molecular weight (Mn) of approximately 50,000 Da (CAPA 6500D, Perstorp, Sweden)

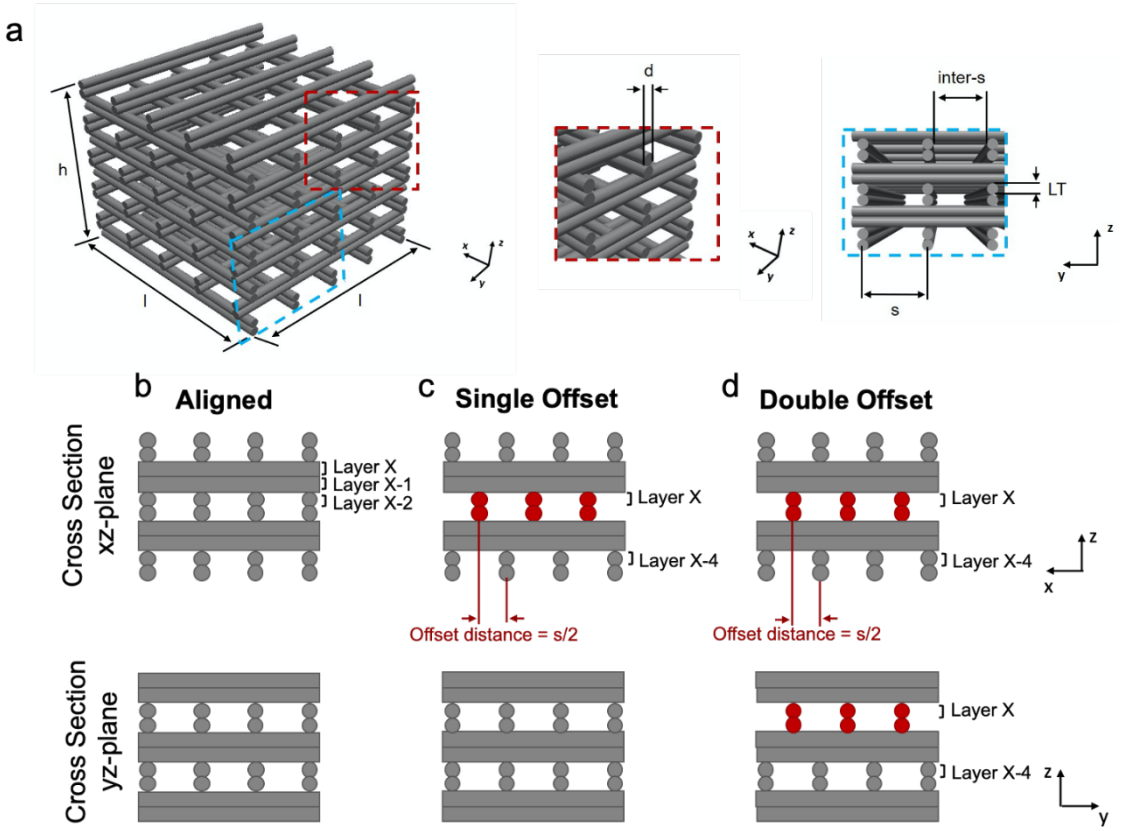

Figure 3-1 (a) Scaffold geometrical features: d, fibre diameter; s, fibre spacing; inter-s, fibre inter-spacing; LT, layer thickness; l, length of the scaffold; h, height of the scaffold. (b-d) Schematic describing the different filament patterns of the designed scaffolds consisting of a regular orthogonal architecture in the case of (b) the Aligned pattern, whereas offset layers are present only in one plane for (c) the *Single Offset* pattern or in both planes for (d) the *Double Offset* pattern. Offset layers are indicated in red.

were used as received. Porous PCL frames were fabricated via FDM using the parameters reported in Table 3.1.

Table 3-1 Summary of FDM printing parameters.

Printing Parameters	*Aligned 1* (*d*=0.3mm; *s*=1.0mm) *Aligned 2* (*d*=0.3mm; *s*=1.5mm)	*Aligned 3* (*d*=0.12mm; *s*=1.5mm) *Single Offset* (*d*=0.12mm; *s*=1.5mm) *Double Offset* (*d*=0.12mm; *s*=1.5mm)
Needle (Gauge)	25	30
Layer Thickness (mm)	0.22	0.1
Pressure (MPa)	0.5	0.1
Printing Speed (mm/s)	4	6
Extrusion Speed (revs/m)	14	10
Tank Temperature (°C)	70	86
Needle Temperature (°C)	70	78

3.2.2 Scaffold characterization

3.2.2.1 Geometry analysis

The geometry of the PCL scaffolds post-printing was characterized using micro-CT. Scans were performed using a Scanco Medical 40 µCT system (Scanco Medical, Switzerland) with a 70 kV and 114 µA x-ray source with a voxel size of 16 µm.

Simpleware™ ScanIP (Synopsys,Inc., USA) was used for processing, segmentation, 3D model reconstruction and analysis of the previously obtained CT images. Scaffolds fibre diameter and inter-spacing (inter-s) were measured from the top cross-sectional view of the reconstructed model, while the length of two consecutive fused layers was determined from the front cross-sectional view. Layer Fusion was calculated as follows:

$$Layer\ Fusion\ (mm) = (2 * designed\ LT) - FL \quad (1)$$

where LT refers to the ideally designed Layer Thickness (Figure 3.1) and FL indicates the length of two consecutive Fused Layers in the fabricated constructs.

3.2.2.2 Porosity

The theoretical porosity (P_t) of the designed scaffolds was estimated by volumes as follows:

$$P_t\ (\%) = 1 - \frac{V_{scaffold}}{V_{solid}} * 100 \quad (2)$$

where $V_{scaffold}$ is the theoretical volume of the porous cubic scaffold and V_{solid} is the volume of a non-porous cube with the same scaffold dimensions.

The porosity of the 3D printed structures was evaluated experimentally using the gravimetric method according to the following equation:

$$P_e\ (\%) = 1 - \frac{\rho_{scaffold}}{\rho_{PCL}} * 100 \quad (3)$$

where P_e is experimental porosity, $\rho_{scaffold}$ is the apparent density of the scaffold, whereas ρ_{PCL} is the PCL density which is 1.145 g/mL. $\rho_{scaffold}$ was obtained as:

$$\rho_{scaffold}(g/mL) = \frac{m_{scaffold}}{V_{scaffold}} \quad (4)$$

where $m_{scaffold}$ and $V_{scaffold}$ are the weight and the volume of the scaffold respectively. The weight of the 3D printed constructs was quantified using an analytical balance (Mettler Toledo Excellence XS205 DualRange with sensitivity of 0.01 mg).

3.2.3 Mechanical characterization

Mechanical tests were carried out in unconfined compression in air at room temperature (~25°C) using a twin column Zwick universal testing machine (Zwick, Roell, Germany). All samples (n = 4 per group) were subjected to a compressive-strain cycle load up to 5 cycles with nominal strain amplitude of 10, 20, 30, 40 and 50 % in sequence. The specimens were compressed at a cross-head speed of 1mm/min between two impermeable metal platens after applying an initial preload of 1 N. A 2,500 N load cell was used for testing samples produced with a 25 Gauge needle, whereas a 100 N load cell was used for those fabricated with a 30 Gauge needle. The load versus displacement data were recorded throughout. The engineering stress and strain were calculated by dividing the load value with the initial apparent cross-sectional area of each sample and the displacement value with the initial sample height, respectively. The elastic modulus was taken as the slope of the initial linear region of the plotted stress-strain curve obtained from the first compressive cycle.

The scaffold permanent deformation (PD), defined as apparent uniaxial plastic strain in the material, was calculated at the end of the tests as follows:

$$PD\ (\%) = \frac{Test\ Speed * \Delta t_5}{h_0} * 100 \quad (5)$$

where Δt_5 (s) is the interval of time at the start of the 5th cycle in which no force is applied, assuming the sample underwent permanent deformation, while h_0 (mm) is the height of the sample prior to test.

3.2.4 Finite element analysis

To predict the compressive properties of the 3D printed scaffolds, CAD-based FE models were developed using ABAQUS v6.14 (DS Simulia, USA). For *Aligned 1* (*d*=0.3mm; *s*=1.0mm) and *Aligned 2* (*d*=0.3mm; *s*=1.5mm) structures, ramp compression tests until 10 % strain were simulated for both an idealized and an actual printed scaffold representation. In the idealized models, pre-fabrication scaffold geometry features were reproduced. On the other hand, actual printed scaffold models were characterized by geometry parameters measured post-fabrication including layer fusion. For *Aligned 3* (*d*=0.12mm; *s*=1.5mm), *Single Offset* (*d*=0.12mm; *s*=1.5mm) and *Double Offset* (*d*=0.12mm; *s*=1.5mm) structures, only actual printed models were developed simulating the same mechanical loading conditions as for *Aligned 1* and *Aligned 2*. Both idealized and actual printed models consisted of a symmetric structure of approximately cubic scaffolds (4.5 mm x 4.5 mm x 4 mm). For all groups, the nodes at the top face of the scaffolds were given a displacement of approximately 0.4 mm corresponding to 10 % compressive strain. The nodes at the bottom ends of the constructs were constrained only in the direction of loading, allowing for scaffold expansion in the remaining two directions due to the Poisson's effect. Symmetry boundary conditions were also applied as the model was reduced to a quarter section cut along the xz and yz planes of symmetry. Therefore, x and y DOFs perpendicular to the symmetry planes were constrained.

The effective compressive modulus of the constructs was determined from the stress and strain values of the linear region of the curve calculated from the displacement and resultant reaction force data computed from the simulations. To compare the predictions to the experiments, the resultant reaction force was multiplied by four to evaluate the models' outputs for the entire constructs. Isotropic elastic behaviour was initially

assumed for *Aligned 1* and *Aligned 2* models. Quadratic ten-node tetrahedral elements (C3D10) were used. Table 3.2 summarizes the material properties of PCL which were obtained from literature (Lohfeld et al., 2015; Ragaert et al., 2009; Rosa et al., 2004).

3.2.4.1 Elastoplastic material model

As PCL will deform plastically once the stress in the material exceeds its yield stress, an elastoplastic material model is preferable to an elastic material model when the stress in the material is expected to exceed the yield stress during loading (Entezari et al., 2016; Ribeiro et al., 2017). To predict more accurately the PCL scaffolds' stress-strain behaviour under compression, uniaxial elastoplastic models were implemented (only for the actual printed geometries for all scaffold groups). The same model configuration and boundary conditions as in the purely elastic material models were applied. The plasticity model used was the von Mises yield criterion with isotropic hardening. To define the stress-strain curve, the yield and failure points of the material were considered as found in literature (Rosa et al., 2004). The implemented material parameters are summarized in Table 3.2. In Abaqus the plastic input parameters required were true stress and true plastic strain. Assuming no volume change in the specimen, the true stress (σ_{true}) was calculated as follows:

$$\sigma_{true} = \sigma_{eng} * (1 + \varepsilon_{eng}) \quad (6)$$

where σ_{eng} and ε_{eng} are engineering stress and strain.

The true total strain (ε_{true}) was calculated as:

$$\varepsilon_{true} = ln(1 + \varepsilon_{eng}) \quad (7)$$

from which the true plastic strain (ε_{pl}) was obtained as:

$$\varepsilon_{pl} = \varepsilon_{true} - \varepsilon_{el} = \varepsilon_{true} - \left(\frac{\sigma_{true}^{y}}{E}\right) \quad (8)$$

where ε_{el} is the elastic strain, σ_{true}^{y} is the true yield stress and E is the Young's modulus.

3.2.4.2 Determination of permanently deformed element volume fraction

To determine theoretically which scaffold architecture was more likely to undergo higher permanent deformation, the element volume fraction experiencing stress greater than 17 MPa, which is approximately the yield stress of PCL (Ragaert et al., 2009; Rosa et al., 2004), was quantified as follows:

$$Element\ Volume\ Fraction\ (\%) = \frac{(element\ volume_{\sigma>17MPa})}{(total\ element\ volume)} * 100 \quad (9)$$

where element $volume_{\sigma>17MPa}$ represents the volume of the elements in the FE model showing stress greater than 17 MPa, whereas total element volume represents the volume of all the elements composing the scaffold model.

Table 3-2 Elastic and plastic material parameters used for the numerical analysis of PCL scaffolds where E is the Young's modulus; ν is the Poisson's ration; $\boldsymbol{\sigma_{true}^{y}}$ is the true yield stress; $\boldsymbol{\varepsilon_{pl}^{y}}$ is the true plastic yield strain; $\boldsymbol{\sigma_{true}^{f}}$ is the true stress at failure; $\boldsymbol{\varepsilon_{pl}^{f}}$ is the true plastic strain at failure.

Material	Material Model	Material Properties
PCL	Isotropic elastic	E = 430 MPa
		ν = 0.3
	Isotropic plastic	$\sigma_{true}^{y} = 17.745\ MPa$
		$\varepsilon_{pl}^{y} = 0$
		$\sigma_{true}^{f} = 113.39\ MPa$
		$\varepsilon_{pl}^{f} = 1.3316$

3.2.5 Statistical analysis

Statistical analysis was performed using GraphPad (GraphPad Software, La Jolla California USA). Compressive modulus, porosity and permanent deformation analysis for varying filament spacing (*Aligned 1* vs. *Aligned 2*) and filament diameter (*Aligned 2* vs. *Aligned 3*) were examined using a student's t-test where means were compared. One-way analysis of variance (ANOVA) with the addition of Tukey's correction was used for multiple comparisons testing (*Aligned 3* vs. *Single Offset* vs. *Double Offset*). Results are expressed as mean ± standard deviation. For all comparisons, the level of significance was $p \leq 0.05$.

3.3 Results

3.3.1 The effect of filament diameter and spacing on the porosity and mechanical properties of 3D printed PCL scaffolds

3.3.1.1 Scaffold design and fabrication

To evaluate the effect of filament diameter and spacing on both the porosity and mechanical properties of 3D printed PCL scaffolds, three different idealized architectures were designed as shown in Figure 3.1b.

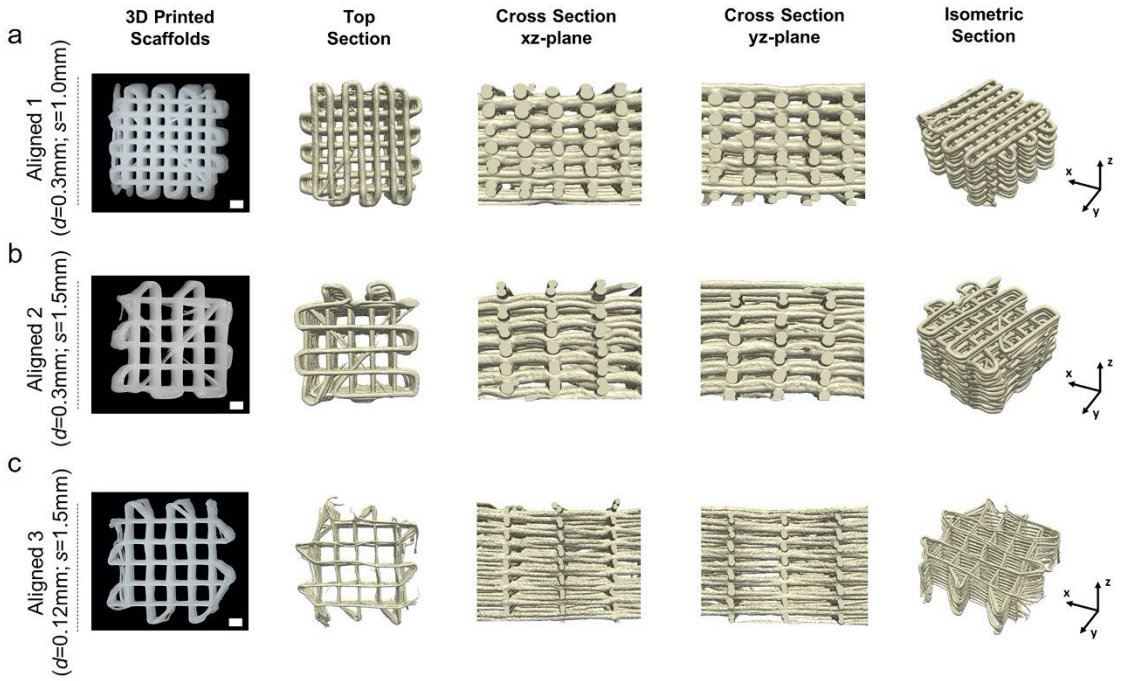

Figure 3-2 Microscopy and micro-CT images of (a) *Aligned 1* (*d*=0.3mm; *s*=1.0mm), (b) *Aligned 2* (*d*=0.3mm; *s*=1.5mm) and (c) *Aligned 3* (*d*=0.12mm; *s*=1.5mm) scaffolds fabricated via 3D printing. Scale bar: 1 mm.

The actual printed structures of the different scaffold designs are shown in Figure 3.2. 3D printing allowed for accurate and controlled deposition of PCL filaments, although micro-CT reconstructions demonstrate that some fibre diameter inhomogeneities exist in all three structures (Figure 3.2a-c). From the CT scans, the average fibre diameter was found to be approximately 0.3 mm in both the *Aligned 1* and *Aligned 2* architectures, whereas the filament diameter was about 0.12 mm for *Aligned 3*. Therefore, the inter-spacing between consecutive struts was smaller in *Aligned 1* (0.660 ± 0.017 mm) and *Aligned 2* (1.168 ± 0.089 mm) compared to the ideal designs, while it was bigger in *Aligned 3* (1.373 ± 0.025 mm). This had an effect on the resultant porosity of the actual printed scaffolds (Table 3.3). Compared to the idealized structures, *Aligned 1* and *Aligned 2* structures were less porous, whereas *Aligned 3* scaffolds had greater porosity. From

the cross-sections of the CT scan images (Figure 3.2), it was observed that the printed filaments in all architectures did not have a regular rounded shape as ideally designed. This is because some degree of fusion between consecutively deposited layers occurred. Layer Fusion, which is considered 0 in the ideal designs, was quantified according to equation (1). It was found to be approximately 0.08 mm in *Aligned 1* and *Aligned 2*, whereas it was approximately 0.02 mm in *Aligned 3* (Table 3.3).

3.3.1.2 Constructs porosity, permanent deformation and mechanical properties

The compressive modulus and the extent of permanent deformation following the application of cyclic strain was calculated for each scaffold design (Figure 3.3a). Representative stress-strain plots of the first loading cycle for the three architectures are shown in Figure 3.3b, while representative stress-strain graphs of the five applied compressive cycles are shown in Supplementary Figure 1a, b. As expected, increasing the filament fibre spacing from 1 mm (*Aligned 1*) to 1.5 mm (*Aligned 2*) increased the porosity and reduced the compressive modulus of the resulting scaffold (Table 3.3; Figure 3.3c). Both *Aligned 1* and *Aligned 2* geometries experienced permanent deformation after the application of the first compressive cycle (10 % applied strain) as it is shown in Supplementary Figure 2a, b for *Aligned 1* and *Aligned 2* scaffolds, respectively. Overall, the higher porosity scaffolds (*Aligned 2*) underwent higher permanent deformation (~25 %) compared to the less porous constructs (*Aligned 1*; ~22 %) (Figure 3.3e). Reducing the filament diameter (*Aligned 3*) also increased the porosity and reduced the compressive modulus of the scaffold (Table 3.3; Figure 3.3d). Moreover, lower permanent deformation was observed (Figure 3.3f).

Table 3-3 Idealized geometrical parameters defined for scaffold fabrication versus actual printed geometrical parameters measured after fabrication.

	Fibre Diameter (mm)		Fibre Spacing (mm)		Fibre Inter-spacing (mm)		Layer Fusion (mm)		Porosity (%)	
	Idealized Geometry	Actual Printed Geometry	Idealized Geometry	Actual Printed Geometry	Idealized Geometry	Actual Printed Geometry	Idealized Geometry	Actual Printed Geometry	Idealized Geometry	Actual Printed Geometry
Aligned 1 (d = 0.3mm; s = 1.0mm)	0.26	0.307 ± 0.014	1	1.064 ± 0.106	0.74	0.660 ± 0.017	0	0.084 ± 0.011	80.4	67.48 ± 0.931
Aligned 2 (d = 0.3mm; s = 1.5mm)	0.26	0.296 ± 0.021	1.5	1.465 ± 0.114	1.24	1.168 ± 0.089	0	0.076 ± 0.012	86.2	75.05 ± 1.267
Aligned 3 (d = 0.12mm; s = 1.5mm)	0.16	0.121 ± 0.015	1.5	1.540 ± 0.061	1.34	1.373 ± 0.025	0	0.018 ± 0.009	91.9	92.50 ± 3.840
Single Offset (d = 0.12mm; s = 1.5mm)	0.16	0.127 ± 0.030	1.5	1.526 ± 0.035	1.34	1.392 ± 0.041	0	0.022 ± 0.012	92.1	93.10 ± 5.081
Double Offset (d = 0.12mm; s = 1.5mm)	0.16	0.130 ± 0.023	1.5	1.530 ± 0.092	1.34	1.379 ± 0.103	0	0.025 ± 0.003	92.8	95.13 ± 3.290

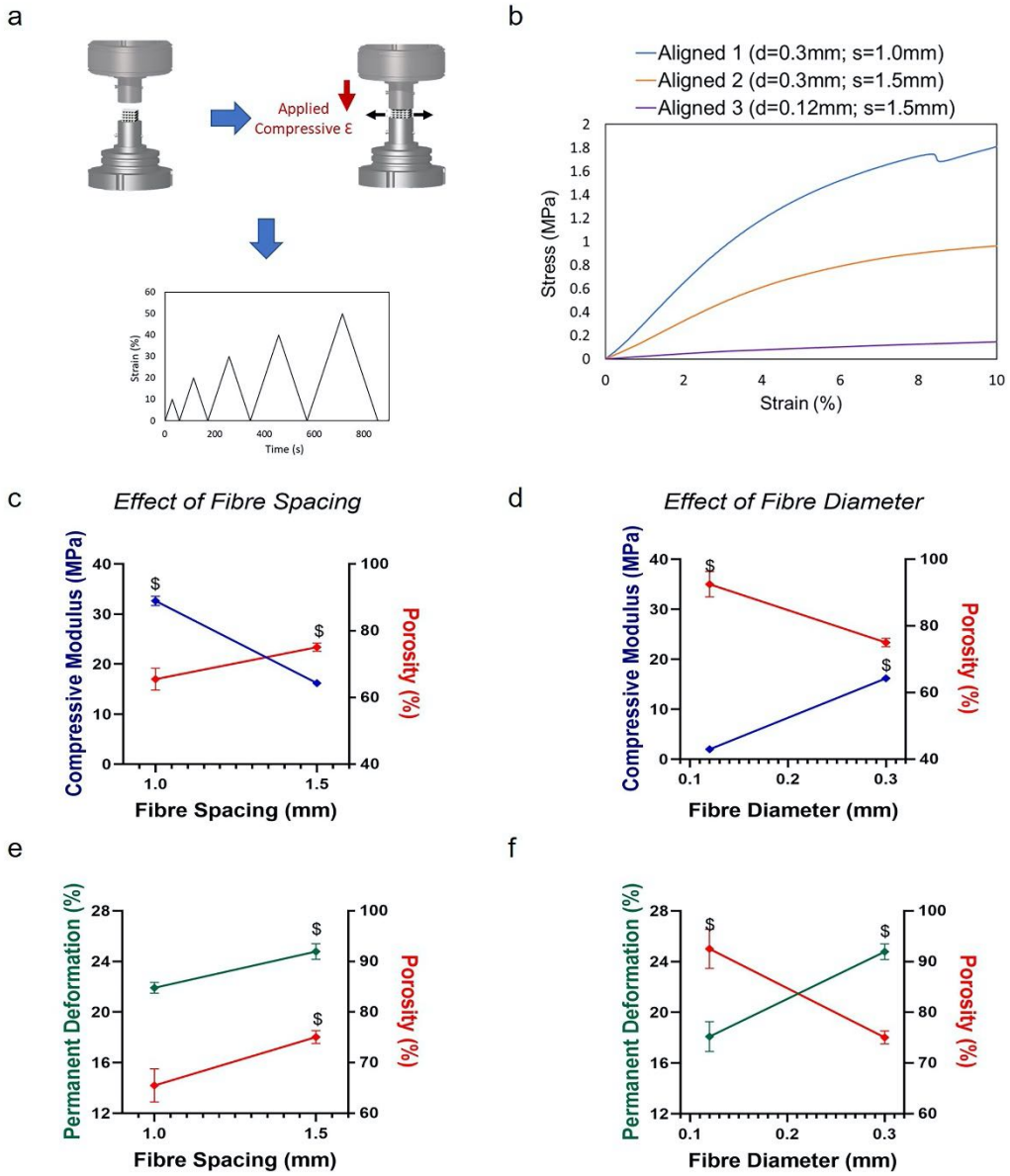

Figure 3-3 (a) Schematic illustration of the mechanical testing set-up and protocol used to perform unconfined cyclic compression tests. (b) Representative stress-strain curves for *Aligned 1* (*d*=0.3mm; *s*=1.0mm), *Aligned 2* (*d*=0.3mm; *s*=1.5mm) and *Aligned 3* (*d*=0.12mm; *s*=1.5mm) architectures. Effect of modifying (c, e) fibre spacing and (d, f) fibre diameter on porosity, compressive modulus and permanent deformation of 3D-printed PCL constructs. $^{\$}p<0.01$, n = 4 per group.

3.3.2 FE models incorporating actual printed geometries can accurately predict the mechanical behaviour of 3D printed scaffolds

FE simulations of unconfined ramp compression tests were first performed using both idealized and actual printed geometries for the *Aligned 1* (Figure 3.4a, c) and *Aligned 2* (Figure 3.4b, d) structures using an elastic material model. In idealized *in silico* models, the ideally designed geometry parameters generated by CAD models were used to represent the constructs. In actual printed models, scaffolds were reproduced using the structural features measured post-fabrication where the actual fibre diameter and the amount of fusion between layers were included as model parameters. The Von Mises stress was predicted to be higher at the crossover areas between consecutive printed layers for both idealized (Figure 3.4a, b) and actual printed (Figure 3.4c, d) models for the *Aligned 1* (Figure 3.4a, c) and *Aligned 2* (Figure 3.4b, d) scaffolds. Comparing the predicted stress-strain behaviour with the experimental results (Figure 3.5a, c), it can be observed that using the idealized representation of both *Aligned 1* (Figure 3.5a) and *Aligned 2* (Figure 3.5c) scaffolds resulted into a significant underestimation of the bulk compressive modulus (Figure 3.5b, d). On the other hand, the actual printed models, which reproduced key scaffold geometrical features (including layer fusion) as they were measured after fabrication, showed good agreement with the experimental measurement of compressive modulus for the *Aligned 1* (Figure 3.5b) and *Aligned 2* (Figure 3.5d) scaffolds. Nevertheless, actual printed models that considered only elastic material properties failed to accurately predict the stress-strain response, specifically the apparent transition from the linear elastic to the plastic region under compression (Figure 3.5a, c).

Due to the architecture of these scaffolds it is expected that some local permanent deformation will occur within the body of the scaffold once the localized stress exceeded

the material yield stress (the yield stress of PCL is estimated to be ~17 MPa (Ragaert et al., 2009; Rosa et al., 2004)). Therefore, an elastoplastic material model for PCL was introduced and simulations of ramp compression tests were performed only for the actual

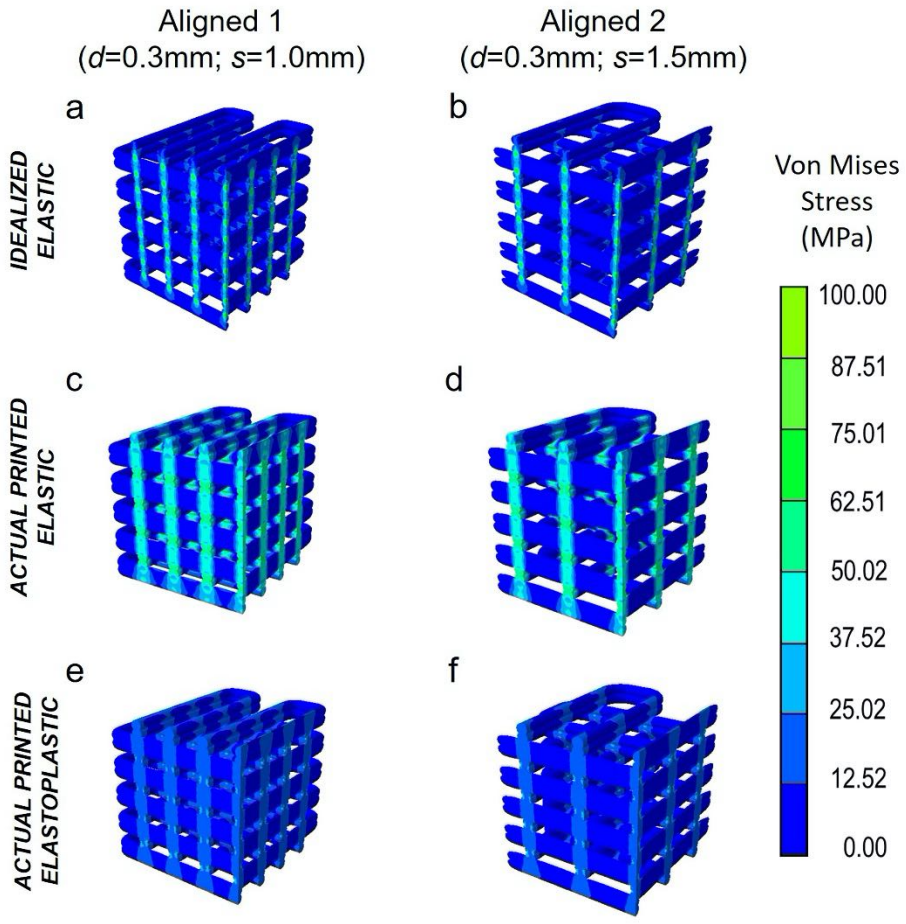

Figure 3-4 Comparison of von Mises stress distribution in (a, b) idealized elastic, (c, d) actual printed elastic and (e, f) actual printed elastoplastic models for (a, c, e) *Aligned 1* (*d*=0.3mm; *s*=1.0mm) and (b, d, f) *Aligned 2* (*d*=0.3mm; *s*=1.5mm) designs.

printed configurations of both *Aligned 1* (Figure 3.4e) and *Aligned 2* (Figure 3.4f). The predicted peak values of von Mises stress were lower using the elastoplastic material model (Figure 3.5a, c). Furthermore, the predicted stress-strain behaviour was more representative of experimental observations.

To evaluate the effect of varying filament diameter on scaffold mechanical properties using FEA, *in silico* models of the *Aligned 3* constructs were also developed using an elastoplastic material model and the actual printed geometry (Figure 3.6d-f). When comparing *Aligned 2* and *Aligned 3* models, it can be observed once again that the compressive forces are mainly supported at the filament junctions of adjacent layers, although the stresses generated within the *Aligned 3* structure were lower compared to *Aligned 2* (Figure 3.6a,d). The actual printed elastoplastic models were again capable of accurately predicting the stress-strain behaviour (Figure 3.6e) and compressive modulus (Figure 3.6f) of the scaffolds.

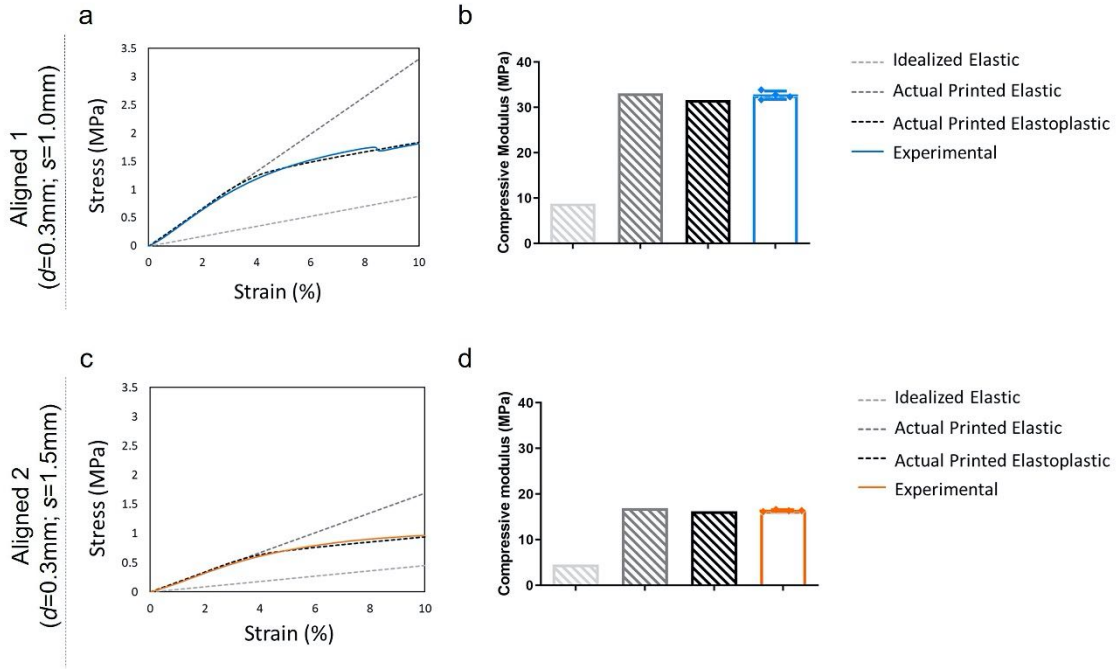

Figure 3-5 (a-d) Predicted (idealized elastic, actual printed elastic and actual printed elastoplastic) and experimental compression properties for *Aligned 1* (*d*=0.3mm; *s*=1.0mm) and *Aligned 2* (*d*=0.3mm; *s*=1.5mm) designs. Compression stress-strain diagrams (a, c) and compressive modulus values (b, d) for (a, b) *Aligned 1* (*d*=0.3mm; *s*=1.0mm) and (c, d) *Aligned 2* (*d*=0.3mm; *s*=1.5mm) structures.

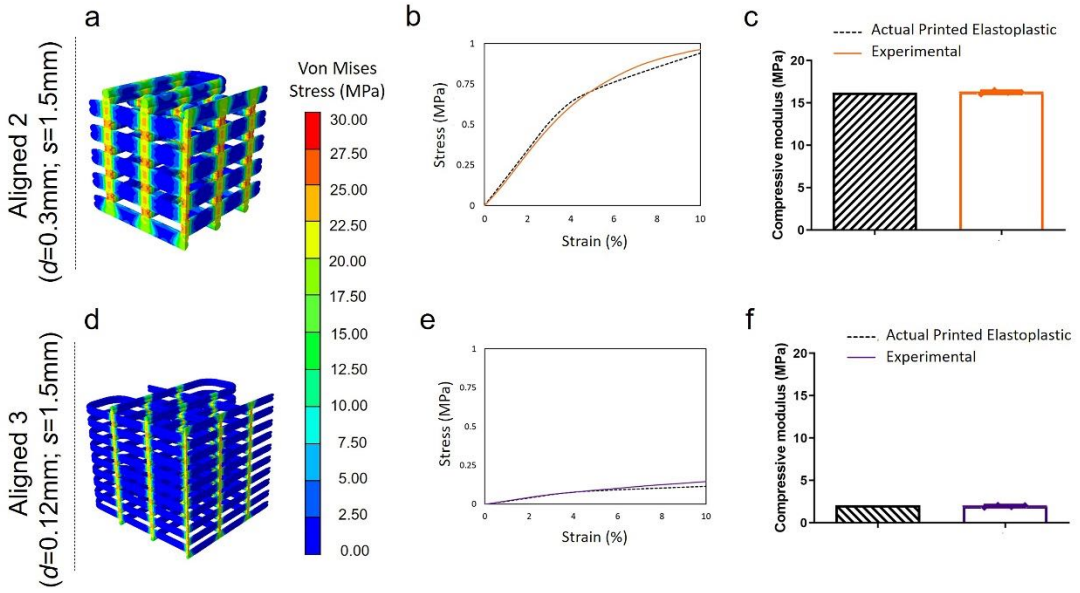

Figure 3-6 Comparison of von Mises stress distribution in actual printed elastoplastic models for (a) *Aligned 2* (*d*=0.3mm; *s*=1.5mm) and (d) *Aligned 3* (*d*=0.12mm; *s*=1.5mm) designs. Predicted and experimental (b, e) compression stress-strain diagrams and (c, f) compressive moduli for (b, c) *Aligned 2* (*d*=0.3mm; *s*=1.5mm) and (e,f) *Aligned 3* (*d*=0.12mm; *s*=1.5mm) structures.

3.3.3 FE modelling to inform on the design of 3D printed scaffolds with user defined mechanical properties

Having developed a computational framework that was able to accurately predict the uniaxial compression behaviour of 3D printed scaffolds, we next sought to leverage this approach to design scaffolds with biomimetic mechanical properties. Articular cartilage has a region specific-compressive modulus that varies from approximately 0.25 MPa to 1.8 MPa (Athanasiou et al., 1994; Boschetti et al., 2004). Ideally scaffolds designed to regenerate this tissue should have mechanical properties falling in the aforementioned range to provide a physiological-like mechanical environment.

The effect of varying filament pattern of fibrous constructs was evaluated. Figure 3.1c, d shows the strategies adopted to modify the scaffold fibre arrangement starting

from the *Aligned 3* structure. The new designed architectures had the same filament diameter and spacing as *Aligned 3*, but different filament pattern. The *Single Offset* architecture (Figure 3.1c) was characterized by offset layers present only in the xz-plane, whereas it showed a regular orthogonal arrangement in the yz-plane. The *Double Offset* scaffold (Figure 3.1d) differed from the previous one because it had offset layers in both xz- and yz- planes. The offset was set to 0.75 mm (half the fibre spacing) in both cases. *Single Offset* and *Double Offset* mechanical properties were predicted simulating compression tests as done previously. Von Mises stress plots for the *Single Offset* architecture (Figure 3.7a) were similar to the previously analysed structures if looking at the yz-plane where filaments are arranged orthogonally with no offset. Here higher levels of stress were experienced at the points where filaments crossed over. On the xz-plane, the stress was not particularly concentrated in certain areas, but it was more homogeneously distributed through the fibres.

In the *Double Offset* architecture model (Figure 3.7b), the same homogeneous stress contour, which was present only in the xz-plane for the *Single Offset* model, was observed throughout. This resulted in overall lower levels of stress experienced by the *Double Offset* architecture. Predicted compressive stress-strain curves (Figure 3.7c) showed that varying the filament pattern of the porous scaffolds from *Aligned 3* to *Single Offset* and *Double Offset* decreased the stiffness of the constructs. This was confirmed when calculating the compressive modulus (Figure 3.7d) which was 1.88, 0.56 and 0.22 MPa for *Aligned 3*, *Single Offset* and *Double Offset* respectively.

To predict which architecture is more likely to undergo higher permanent deformation, the element volume fraction of each model which experienced stress greater than 17 MPa (PCL yield stress) was calculated according to equation (9). Figure 3.7e

shows the quantified element volume fraction for the three analyed models. It was predicted that the *Aligned 3* configuration had the highest volume fraction (9.56 %) indicating this was the structure that would experience more permanent deformation when subjected to 10 % compression. The *Single Offset* model had a volume fraction of 4.44 % and the *Double Offset* model had 0.2%, thereby the latter having the lowest plastic deformation.

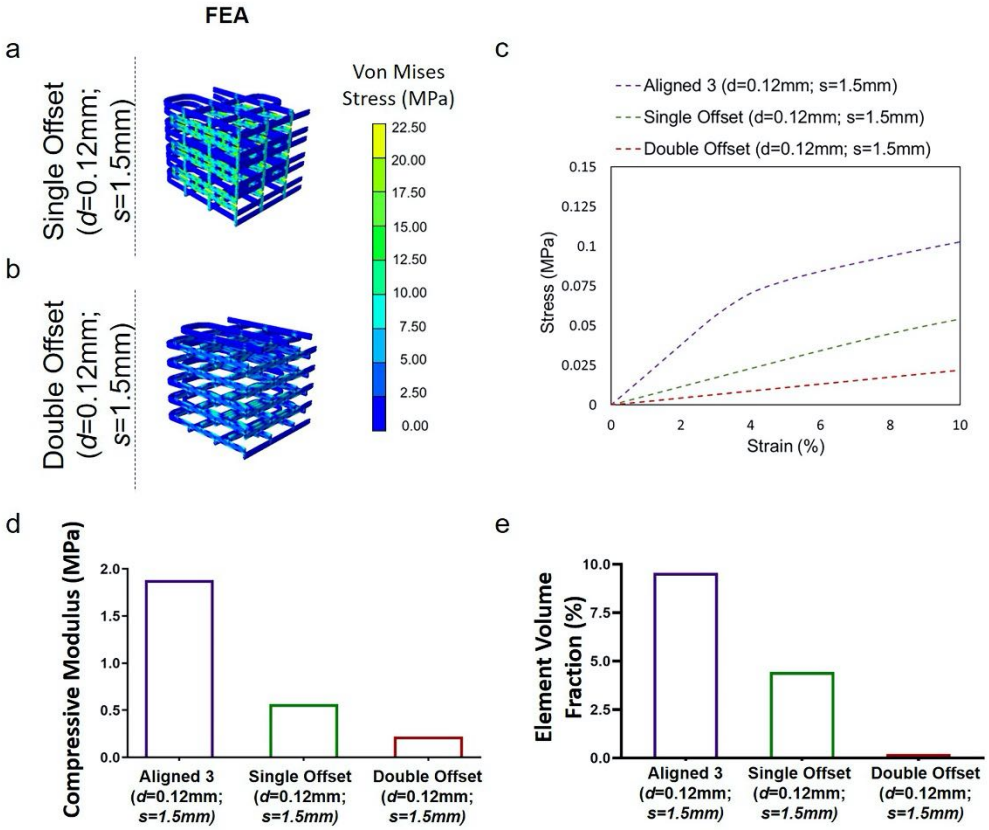

Figure 3-7 Von Mises stress contour plots for (a) *Single Offset* (*d*=0.12mm; *s*=1.5mm) and (b) *Double Offset* (*d*=0.12mm; *s*=1.5mm) structures. Computational (c) compression stress-strain graph, (d) compressive moduli and (e) element volume fraction experiencing stresses greater than 17 MPa (PCL yield stress) comparing *Aligned 3* (*d*=0.12mm; *s*=1.5mm), *Single Offset* (*d*=0.12mm; *s*=1.5mm) and *Double Offset* (*d*=0.12mm; *s*=1.5mm) geometries.

3.3.3.1 Models validation

Single Offset and *Double Offset* PCL constructs were 3D printed according to the fabrication parameters used for the *Aligned 3* architecture as reported in Table 3.1. Figure 8a shows microscope images of the obtained scaffolds. Constructs were mechanically tested following the same cyclic compression test protocol applied for the previous experiments. Representative stress-strain curves of the first loading cycle are shown in Figure 3.8b, in which *Aligned 3*, *Single Offset* and *Double Offset* mechanical properties are compared. Stress-strain graphs of the five applied compressive cycles are shown in Supplementary Figure 1c-e. As it was predicted, *Double Offset* constructs are the softest whereas *Aligned 3* structures are the stiffest among the three groups. This was evidenced by the differences in slope of the stress-strain curves. Moreover, the trend of the experimental curves matched the predicted ones. The fabricated scaffolds where characterized by high porosity which was about 90 % regardless of the filament pattern chosen (Figure 8c, d). In good agreement with the computational results, the *Single Offset* and *Double Offset* constructs had a compressive modulus of 0.817 ± 0.02 MPa and 0.320 ± 0.03 MPa respectively (Figure 3.8c). Furthermore, varying the arrangement of the scaffold filaments reduced the permanent deformation the constructs underwent after being subjected to cyclic compressive loadings. All scaffold geometries underwent plastic deformation after being subjected to 10 % compressive strain (Supplementary Figure 2c-e). Permanent deformation at the end of the test was measured to decrease from about 18 % in *Aligned 3* structures to approximately 16 and 14 % in *Single Offset* and *Double Offset* constructs respectively (Figure 3.8d). Once again, CAD-FE models based on actual printed scaffold geometry proved to be an efficient approach to design constructs with desired structural and mechanical properties.

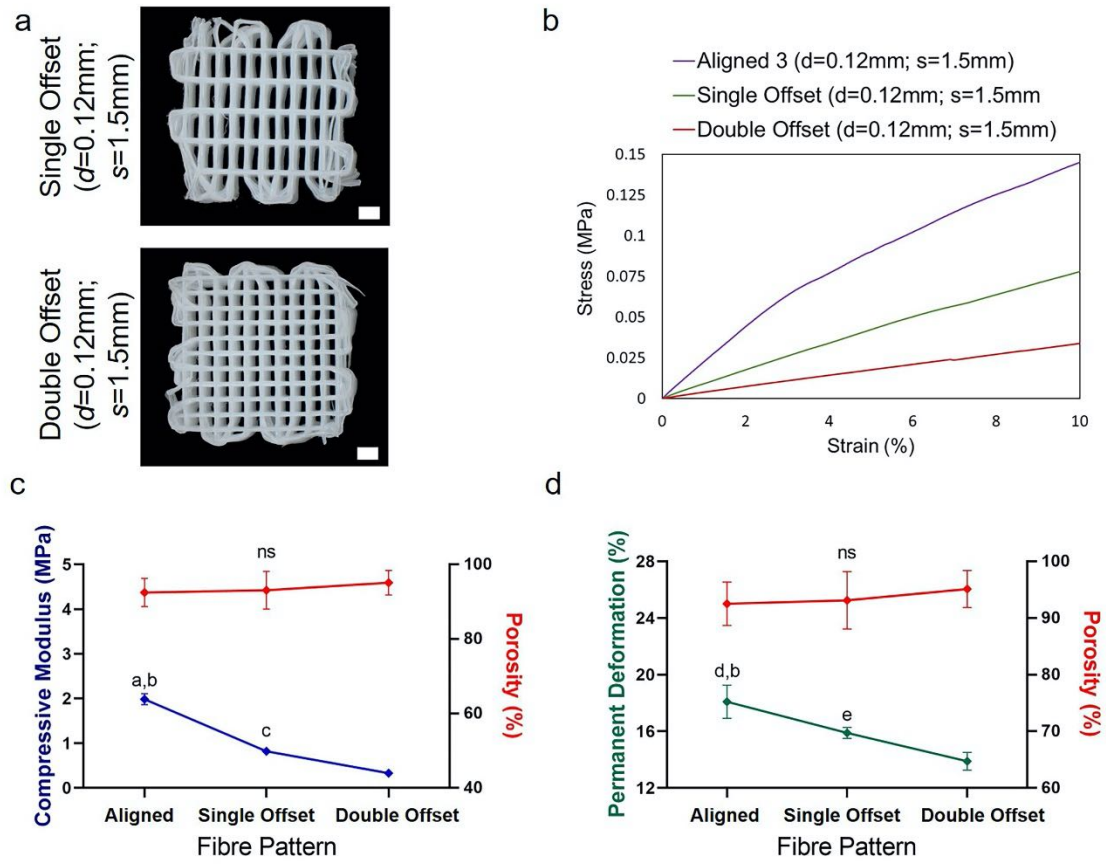

Figure 3-8 (a) Microscopy images of *Single Offset* (*d*=0.12mm; *s*=1.5mm) (top) and *Double Offset* (*d*=0.12mm; *s*=1.5mm) (bottom) 3D-printed PCL scaffolds; scale bar: 1mm. Representative experimental stress-strain curves for *Aligned 3* (*d*=0.12mm; *s*=1.5mm), *Single Offset* (*d*=0.12mm; *s*=1.5mm) and *Double Offset* (*d*=0.12mm; *s*=1.5mm) architectures. (c,d) Effect of modifying fibre pattern on porosity, compressive modulus and permanent deformation of 3D-printed PCL constructs. [a]p<0.0001 *Aligned 3* (*d*=0.12mm; *s*=1.5mm) vs. *Single Offset* (*d*=0.12mm; *s*=1.5mm), [b]p<0.0001 *Aligned 3* (*d*=0.12mm; *s*=1.5mm) vs. *Double Offset* (*d*=0.12mm; *s*=1.5mm), [c]p<0.0001 *Single Offset* (*d*=0.12mm; *s*=1.5mm) vs. *Double Offset* (*d*=0.12mm; *s*=1.5mm) when evaluating the compressive moduli, n = 4 per group. [d]p<0.01 *Aligned 3* (*d*=0.12mm; *s*=1.5mm) vs. *Single Offset* (*d*=0.12mm; *s*=1.5mm), [b]p<0.0001 *Aligned 3* (*d*=0.12mm; *s*=1.5mm) vs. *Double Offset* (*d*=0.12mm; *s*=1.5mm), [e]p<0.01 *Single Offset* (*d*=0.12mm; *s*=1.5mm) vs. *Double Offset* (*d*=0.12mm; *s*=1.5mm) when evaluating the permanent deformation, n = 4 per group.

3.4 Discussion

The fabrication of scaffolds with a controlled shape and interconnected pore network, as well as appropriate mechanical properties, is fundamental when developing tissue engineered constructs (Bracaglia et al., 2017; Hollister et al., 2005; O'Brien et al., 2011; Salerno et al., 2009; Woodfield et al., 2004). 3D printing allows such control and permits the creation of constructs that serve as temporary templates while the extracellular matrix is produced, and can provide a mechanical environment conductive to tissue formation, especially when combined with soft hydrogel materials (Bas et al., 2017c; Castilho et al., 2018; Critchley et al., 2017; Daly et al., 2016b; Liao et al., 2013a). Computational modelling has been increasingly applied to tissue engineering in order to aid in the design of such 3D scaffolds (Bas et al., 2017a; Hendrikson et al., 2017; Milan et al., 2009; Moroni et al., 2007). However, it can be challenging to develop FE models capable of accurately predicting scaffolds mechanical properties, at least in part due to unintended geometrical differences between the idealized and actual fabricated scaffolds (Cahill et al., 2009; Doyle et al., 2014; Lohfeld et al., 2015). Herein we described a strategy for designing 3D printed scaffolds with different structural and mechanical properties that is informed by a FE model that accounts for differences between the idealized scaffold geometry and what is eventually printed. Models of different scaffold architectures provided an insight into the structure-function relation of such scaffolds, and how modifying specific structural features can tailor the mechanical properties to those of a wide range of native tissues.

Using FDM, we produced a number of scaffolds made of PCL, which is a synthetic polymer widely used in 3D printing due to its biocompatibility, low melting temperature and mechanical stability (Critchley et al., 2017; Daly et al., 2017a; Olubamiji et al., 2016;

Woodruff et al., 2010). The optimal sets of fabrication parameters for two different needle sizes (25 and 30 Gauge) were chosen to obtain defined porous structures with a good resolution and to avoid delamination between consecutively printed layers. Varying PCL scaffold geometrical features such as filament spacing and diameter had an effect on scaffold porosity, mechanical properties and plastic deformation. Increasing the fibre spacing from 1 mm (*Aligned 1*) to 1.5 mm (*Aligned 2*), but maintaining the same fibre diameter, resulted in structures with a higher porosity and therefore a lower compressive modulus. The more porous scaffolds also experienced higher permanent deformation. This may be due to sagging of the filaments when spanning from one fibre to the next, resulting in densification (impacting of the fibres against one another) of the scaffold occurring earlier when compression forces are applied. Scaffold stiffness further decreased whereas porosity increased when reducing fibre diameter (*Aligned 3*), although lower permeant deformation was observed. This is likely due to the lower stresses (and hence material yielding) that are predicted to be generated within the scaffolds with lower fibre diameters as they are compressed.

Using micro CT, we revealed geometric discrepancies between idealized and actual printed structures which are dependent on the fabrication process. Depending on the set of fabrication parameters used, the PCL filament diameter was either larger (for the 25 Gauge needle) or smaller (for the 30 Gauge needle) than originally designed. Moreover, the shape of the individual fibres was hard to distinguish as consecutively printed layers fused together post-extrusion. Such discrepancies impact both scaffold geometry and mechanical properties (Domingos et al., 2012; Tellis et al., 2008; Zein et al., 2002), but to date there are only few modelling techniques that have simulated these geometrical variations which have mainly focused on scaffolds for the regeneration of hard tissues

(Campoli et al., 2013; Gleadall et al., 2018; Karamooz Ravari et al., 2014; Melancon et al., 2017; Naghieh et al., 2016; Naghieh et al., 2018). For example, Campoli et al. (Campoli et al., 2013) utilized FE models that implemented variations in the cross-section area of the struts in porous metallic biomaterials, showing good predictions when comparing computational and experimental results. Melancon et al. (Melancon et al., 2017) developed a morphological map that would capture structural differences post-fabrication of porous biomaterials, which was then used to create statistical based numerical models that incorporated such geometrical irregularities. These models produced more reliable predictions of experimentally measured mechanical properties. Ravari et al. (Karamooz Ravari et al., 2014) developed a strategy to take account of variations in filament diameter into their FE models of 3D printed structures, which also improved the predictive capacity of the computational models. Naghieh et al. (Naghieh et al., 2016; Naghieh et al., 2018) investigated the effect of fusion between the different layers in 3D printed scaffolds, and again demonstrated the importance of considering this when developing accurate FE models. In the current study, a FE modelling framework was used to design scaffolds with mechanical properties suitable for soft tissue applications. CAD-based FE models of the idealized and actual printed scaffold architectures were developed to study the impact of such geometrical differences when predicting the scaffold mechanical properties. Our models demonstrated that including layer fusion is essential to accurately modelling 3D printed scaffolds. Indeed, when comparing idealized to actual printed models (Figure 3.4 and 3.5), we have shown that the idealized model, in which layer fusion was not accounted for, was not able to provide accurate predictions because the geometry of the scaffold itself (e.g. scaffold height) was inaccurate. The actual printed models described filament diameter and amount of layer

fusion as measured post-fabrication. For both *Aligned 1* and *Aligned 2* designs, modelling the idealized structures lead to a significant underestimation of the mechanical properties compared to the experimental results. On the other hand, the predicted compressive stiffness of the actual printed designs showed good agreement with the experiments, especially when the plasticity of PCL was also considered. Implementing an elastoplastic material model not only accurately predicted the compressive elastic modulus of the 3D printed constructs but also captured the mechanical behaviour past the yield point. This was observed for *Aligned 1*, *Aligned 2* and *Aligned 3* scaffold models.

To demonstrate how the proposed computational approach could be used to help inform the design of a scaffold prior to printing, the laydown filament pattern of the actual printed *Aligned 3* structure was theoretically modified to obtain *Single Offset* and *Double Offset* architectures. Introducing offset layers in one plane only (*Single Offset*) or in two planes (*Double Offset*) reduced the compressive stiffness by almost one order of magnitude (compressive modulus was decreased from 1.88 to 0.56 and ultimately to 0.22 MPa for *Aligned 3*, *Single Offset* and *Double Offset* designs, respectively), despite the scaffold porosity being maintained constant. Varying the filament pattern also reduced the permanent deformation within the scaffolds following the application of a defined level of compressive strain. In the stiffer *Aligned* scaffolds, deformation of the entire scaffold primary occurs due to the filaments undergoing compressive strain. The scaffold is better designed to resist compressive deformation as columns of material are generated where filament layers overlap, and large strains and stresses are generated locally in the scaffold material at these points of overlap (Figure 3.4 and 3.6a, d). These large local stresses cause the material to locally undergo plastic deformation. In the softer *Offset* scaffolds, deformation of the scaffold occurs due to bending of the filaments. As the

scaffold deforms in this way, it offers less resistance to compressive loading and smaller stresses and strains are generated locally within the scaffold material (Figure 3.7a, b); such smaller local stresses result in lower levels of permanent deformation. Experimental compression tests confirmed the ability of the FE modelling framework to produce scaffolds with specific mechanical attributes prior to their fabrication. Experimentally, the porosity of the analysed structures was the same and the compressive moduli matched the predicted values. In summary, we have developed a computationally efficient modelling approach using CAD-based scaffold representations that account for key geometrical features of the actual printed construct to predict the mechanical behaviour of 3D printed scaffolds. Employing such CAD-based FE models by using the average values of the scaffold geometrical parameters measured experimentally is advantageous as there is no need to develop computationally expensive sample-specific models that require complex and time-consuming imaging techniques (i.e. micro CT) to accurately determine the geometry of the scaffolds. This approach is particularly beneficial in the initial scaffold design phase, although considering sample-specific geometries (which we have not undertaken in this study) will be important if trying to understand the variability in scaffold mechanical properties from print to print.

3.5 Conclusion

This study demonstrates the benefits of combining computational and experimental strategies for engineering spatially complex scaffolds. Specifically, a simple and relatively accessible FE strategy was developed, which was shown capable of successfully predicting the mechanical properties of 3D printed scaffolds prior to their

fabrication. The geometric discrepancies between scaffold designs pre- and post-fabrication was found to be critical in developing FE models capable of accurately predicting the mechanical behaviour of 3D printed scaffolds. A number of strategies to modulate the structural and mechanical properties of 3D printed PCL scaffolds was explored, allowing constructs to be obtained with compressive properties spanning from the kPa to the MPa range. Thus, the proposed FEA method combined with 3D printing represents a powerful approach to producing biomaterial scaffolds mimicking the mechanical properties of a broad range of biological tissues.

Chapter 4
Reinforcing interpenetrating network hydrogels with 3D printed polymer networks to engineer cartilage-mimetic composites

4.1 Introduction

Articular cartilage is a thin layer of connective tissue that lines the ends of bones within synovial joints. Under normal physiological conditions, cartilage provides a smooth, lubricated surface for articulation that facilitates load support and distribution across the joint. Biomechanically it functions as a multiphasic, fibre-reinforced material that has anisotropic, nonlinear and viscoelastic properties (Gannon et al., 2012; Moutos et al., 2007b; Mow et al., 1980). The complex load bearing properties of articular cartilage strongly depend on the anisotropic nature of the tissue, consisting primarily of collagen and proteoglycans, and the associated tension-compression nonlinearity (Guilak et al., 2001; Moutos et al., 2007b; Mow et al., 1980; Soltz et al., 2000). The negatively charged proteoglycans within articular cartilage generate an osmotic swelling pressure, which is balanced by a pre-stress that is developed in the collagen network (Gannon et al., 2012; Horkay et al., 2012). The compressive properties of cartilage typically increase as the proteoglycans content increases, and the loss of proteoglycans has been shown to make the tissue more prone to microdamage during mechanical loading (Buckwalter et al., 1994b; Kempson et al., 1970; Mow et al., 1980; Pastrama et al., 2019; Schmidt et al., 1990). The architecture and organization of the collagen fibres determine the intrinsic tensile stiffness and strength of cartilage (Bae et al., 2008; Lu et al., 2008; Schmidt et al.,

1990). The tensile modulus of articular cartilage is significantly higher than the compressive modulus (Kempson et al., 1968; Williamson et al., 2003). When cartilage is tested in unconfined compression, this tension-compression nonlinearity enhances fluid pressurization and elevates the dynamic modulus of the tissue (Park et al., 2004; Park et al., 2003), as the collagen network restricts lateral expansion of the tissue during compressive loading. The relative importance of the different matrix components on the overall mechanical properties of articular cartilage has been studied by depleting cartilage samples of collagen and/or proteoglycans (Federico et al., 2008; Moutos et al., 2007b; Pastrama et al., 2019; Schmidt et al., 1990). For example, the compressive modulus of the proteoglycan-depleted cartilage matrix may be as low as 3 kPa, representing less than 2% of the normal tissue modulus (Canal Guterl et al., 2010). Therefore, the collagen in articular cartilage can be considered as a fibrillar matrix that primarily sustains tension. Biomaterial strategies that aim to mimic articular cartilage should consider such complexities in their design.

As articular cartilage has poor regenerative capacity, damage to this tissue impairs its mechanical function and can lead to an abnormal loading within the joint. If left untreated, the damage can progress to osteoarthritis of the joint, causing significant pain and disability. This motivates the need for new regenerative approaches capable of restoring the normal biomechanics of the joint.

A number of tissue engineered strategies to engineer cartilage replacements have been developed (Almeida et al., 2015; Bas et al., 2017b; Bhattacharjee et al., 2015; Cunniffe et al., 2019; Izadifar et al., 2012; Johnstone et al., 2013; Kwon et al., 2019; Thorpe et al., 2013b; Yang et al., 2017). A typical approach is to design biomaterial environments capable of supporting chondrogenesis; this commonly involves combining

cells and/or bioactive molecules with hydrogels as a scaffolding material due to their high water content and attractive transport properties (Filardo et al., 2013b; Liao et al., 2013b; Neumann et al., 2016; Yang et al., 2018). Other than presenting pro-chondrogenic biological cues to the encapsulated cells, such biomaterial scaffolds must also provide a suitable mechanical environment capable of instructing cell fate as well as withstanding the challenging physiological loading conditions experienced *in vivo* upon implantation into the body (Johnstone et al., 2013). Commonly used single network hydrogels (e.g. alginate, gelatin methacryloyl (GelMA), agarose, polyethylene glycol, etc.) have been extensively studied and have been shown to provide an environment that is conducive to chondrogenesis. However, they are typically mechanically weak and unable to withstand the challenging environment of the joint (Hung et al., 2004; Neumann et al., 2016). Recently, more complex hydrogel systems such as interpenetrating network (IPN) hydrogels, characterized by the combination of multiple polymer networks have been investigated. Within such IPN hydrogels individual polymer networks are physically entangled with each other and crosslinked only with themselves using specific chemistries (Brigham et al., 2009; Chimene et al., 2016a; Jeon et al., 2017a; Xu et al., 2019). In general, such IPN hydrogels have displayed synergistic increases in mechanical properties, including increased toughness and elasticity when compared to the single hydrogel components. However, they do not mimic many of the features of load bearing tissues like articular cartilage, such as anisotropy and tension-compression nonlinearity. Furthermore, engineering IPN hydrogels with bulk mechanical properties approaching those of articular cartilage typically requires very high hydrogel polymer concentrations, resulting in biomaterial environments that are not compatible with robust extracellular

matrix (ECM) deposition by encapsulated cells (Bian et al., 2013; Malda et al., 2013; Sun et al., 2017).

To address these concerns, hydrogels can be reinforced with networks of fibres to produce composites with improved mechanical properties (Liao et al., 2013a; Liao et al., 2013b; Moffat et al., 2018; Moutos et al., 2007b; Visser et al., 2015). However, these techniques typically involve the use of complex biofabrication strategies (e.g. weaving, melt electrowriting) that are challenging to scale and personalize to specific patient anatomies. In contrast, Fused Deposition Modelling (FDM) can be used to 3D print fibre networks that are relatively simple to scale, with internal and external architectures that are easily defined based on medical imaging (Daly et al., 2017b; Murphy et al., 2014b).

In this study, alginate – GelMA IPNs were reinforced with polycaprolactone (PCL) networks printed using FDM to develop biomechanically competent composite constructs for cartilage tissue engineering. Alginate, GelMA and alginate – GelMA IPN hydrogel scaffolds were first mechanically characterized to investigate the benefit of combining the two single hydrogel components. These hydrogel bioinks were then reinforced with 3D printed PCL networks with architectures and mechanical properties inspired by the collagen network of articular cartilage. The reinforcement mechanism resulting from the combination of PCL networks with IPN hydrogels was examined using Finite Element Analysis (FEA). Finally, the ability of 3D bioprinted cell-laden PCL reinforced IPN constructs to support chondrogenesis was assessed *in vitro* over 6 weeks of culture.

4.2 Materials and methods

4.2.1 Materials preparation

Alginate was prepared by dissolving Alginate (PRONOVA UP LVG) in DMEM to make up a final concentration of 3.5% w/v. Cylindrical constructs were obtained by pouring the alginate solution into 2 mm high-6 mm diameter agarose-$CaCl_2$ moulds (DMEM, 3% w/v agarose, 45 mM $CaCl_2$) and allowed to crosslink for 20 min at room temperature. GelMA synthesis was previously described (Van Den Bulcke et al., 2000a). Briefly, GelMA was synthesized by reaction of porcine type A gelatin (Sigma- Aldrich, average molecular weight 40-50 kDa) with methacrylic anhydride (Sigma Aldrich) at 50 °C for 4 h. To achieve a high degree of functionalization, 10 mL of methacrylic anhydride was added to a 10% w/v gelatin solution in phosphate-buffered saline (PBS) under stirring for 1 h. The functionalized polymer was dialyzed against distilled water for 7 days at 40 °C to remove unreacted methacrylic anhydride, freeze-dried and stored at -20 °C protected from light until further use. GelMA constructs were formed by dissolving GelMA in DMEM (including 0.05 % v/v Irgacure (Sigma Aldrich) as photoinitiator) obtaining final concentrations of 5, 10 and 15% w/v. The GelMA solution was poured into polydimethylsiloxane (PDMS) moulds (same dimensions as for the agarose-$CaCl_2$ moulds) and exposed to UV light for 15 min (365 nm, 5 mW/cm^2) to perform the crosslinking. Alginate - GelMA IPN hydrogels were prepared by combining alginate solution (DMEM, 7% w/v) with GelMA solution of various concentrations (DMEM, 10, 20 and 30% w/v) containing 0.05% w/v Irgacure in 1:1 ratio. The final mixture was poured into the same agarose-$CaCl_2$ moulds used for alginate constructs and cured with 45 mM $CaCl_2$ and under UV light exposure for 20 and 15 min respectively.

4.2.2 Isolation and expansion of MSCs and CCs

Bone marrow was removed from the femoral shaft of a porcine donor and washed in high-glucose Dulbecco's Modified Eagle Medium (hgDMEM) (Biosciences) supplemented with 10% foetal bovine serum (FBS), 1% penicillin (100 U/mL) – streptomycin (100 µg/mL) (all Bioscience) and amphotericin B (2.5 µg/mL) (Sigma-Aldrich). A homogenous cell suspension was achieved by triturating with a 18G needle. The solution was centrifuged twice at 650g for 5 min, with removal of the supernatant. The resultant cell pellet was triturated, and the cell suspension was filtered through a 40 µm cell sieve (Sarstedt). Cell counting was performed with trypan blue and acetic acid before plating at a density of 5 x 10^3 cells/cm^2 and maintained in a humidified chamber. Following colony formation, cells were trypsinized, counted and re-plated for a further passage at a density of 5 x 10^3 cells/cm^2. FGF-2 (Prospec-Tany TechnoGene Ltd) was added to the media which was changed twice weekly.

Cartilage tissue from another porcine donor was rinsed with PBS, weighed and finely diced. Chondrocytes were isolated by digestion in hgDMEM containing 1% penicillin (100 U/mL) – streptomycin (100 µg/mL) and 8 mL/g of collagenase type II (350 U/mL) for 12-14 h under constant rotation at 37 °C. The resulting cell suspension was filtered through a 40 µm cell sieve, centrifuged and rinsed with PBS twice. Cell number and viability were determined using a haemocytometer and 0.4% trypan blue staining.

All expansion was conducted in hypoxic conditions and media was changed twice weekly.

4.2.3 3D bioprinting process

All 3D printed constructs were fabricated using the 3D Discovery bioplotter purchased from RegenHU with spatial resolution of ± 5 µm. Porous PCL (CAPA 6500D, Perstorp, Mn 50 kDa) scaffolds with two different geometries named *Aligned* and *Double Offset* were printed using a FDM printhead. All printing parameters are described in Table 4.1.

For the *in vitro* evaluation, previously printed PCL scaffolds were sterilized with ethylene oxide (EtO) and soaked overnight in a solution of 45 mM $CaCl_2$ to facilitate the crosslinking process of the hydrogels during printing. Prior to hydrogels printing, the PCL constructs were placed in each well of a 6-well plate by means of 3D printed poly lactic acid inserts containing PDMS moulds that kept the scaffolds in place in the centre of the well. This allowed for z-direction printing of the hydrogel bioinks through microextrusion bioprinting.

Table 4-1 Summary of FDM and microextrusion printing parameters for PCL and hydrogels.

Printing Parameters	**FDM printing**	**Microextrusion printing**		
Material	PCL	3.5% alginate	5% gelMA	IPN
Needle (Gauge)	30	23	23	23
Pressure (bar)	1	0.5	0.3	1.3
Screw Speed (revs/m)	10	-	-	-
Temperature (°C)	86 (tank), 78 (needle)	-	13	13
Layer Thickness (mm)	0.1	-	-	-
Extrusion Speed (mm/s)	6	4	2	4

To form the single hydrogel component bioinks, alginate and GelMA were dissolved at a concentration of 7 and 10 % w/v respectively. To produce the IPN bioink, alginate and GelMA were firstly dissolved to 14 and 20% w/v respectively and then mixed

together in 1:1 ratio using a luer lock system (7 and 10% w/v alginate and GelMA final respectively). As co-cultures of bone marrow-derived stromal cells (BMSCs) and chondrocytes (CCs) have been shown to support stable cartilage tissue formation resistant to hypertrophy and endochondral ossification *in vivo* (Mesallati et al., 2015), using the above mentioned luer lock system, the obtained bioinks were then combined with a mixture of BMSCs and CCs (3:1 ratio) in 1:1 ratio (3.5% w/v alginate final, 5% w/v GelMA final, 3.5% w/v alginate – 5% w/v GelMA IPN final, 20 x 10^6 cells/mL). Next the cell-laden bioinks were loaded into a pressure driven system to be bioprinted in the open pores of the PCL constructs. See Table 4.1 for printing parameters. Following the fabrication process, the constructs were fully crosslinked as follows: PCL + alginate scaffolds were immersed in a bath of 45 mM $CaCl_2$ for 20 mins; PCL + GelMA constructs underwent UV light exposure for 15 mins; PCL + IPN constructs were subjected to both $CaCl_2$ (45 mM) and UV light crosslinking for 15 and 20 min respectively.

4.2.4 *In vitro* culture conditions

3D bioprinted scaffolds were cultured for 6 weeks in chondrogenically defined media consisting of hgDMEM supplemented with 1% penicillin (100 U/mL) – streptomycin (100 µg/mL), sodium pyruvate (100 µg/mL), L-proline (40 µg/mL), L-ascorbic acid 2-phosphate (50 µg/mL), linoleic acid (4.7 µg/mL), bovine serum albumin (1.5 mg/mL), 1x insulin-transferrin-selenium, dexamethasone (100 nM) (all Sigma-Aldrich) and human TGF-ß3 (10 ng/mL) (Prospec-Tany TechnoGene Ltd). Media change was performed twice weekly. The oxygen tension was kept to 5% pO_2 for the first 3 weeks of culture, and then switched to 20% pO_2 for the final 3 weeks.

4.2.5 Live/Dead confocal microscopy

Cell viability was evaluated 24 h post-printing using a Live/Dead assay kit (Bioscience). Bioprinted cell-laden scaffolds were rinsed with phenol free medium and incubated in a solution containing 4 μM ethidium homodimer-1 and 2 μM calcein for 1 h. Following incubation, the scaffolds were rinsed again and imaged with Olympus FV-1000 Point-Scanning Confocal Microscope t 488 and 543 nm channels. Cell viability was quantified using Image-J software.

4.2.6 Biochemical analysis

The biochemical content of all constructs was quantified. Samples were digested with papain (125 μg/mL) in 0.1 M sodium acetate, 5 mM L-cysteine-HCl, 0.05 M ethylene-diamine-tetracetic acid (EDTA) (all Sigma-Aldrich) and pH 6 under constant rotation at 60 °C for 18 h. DNA content was assessed using the Hoechst Bisbenzimide 33258 dye assay. The amount of sulphated glycosaminoglycans (sGAG) was measured using the dimethyl methylene blue-binding assay (DMMB) (Blyscan, Bicolor Ltd.). Total collagen content was determined by quantifying the hydroxyproline content using the (dimethylamino)benzaldehyde and chloramine T assay and a hydroxyproline to collagen ratio of 1:7.69.

4.2.7 Histological and immunohistochemical analysis

Scaffolds were fixed with 4% paraformaldehyde solution, dehydrated in graded series of ethanol, embedded in paraffin wax, sectioned at 8 μm and affixed to microscope slides. The sections were stained with Alcian Blue/Aldehyde Fuchsin, Picrosirius Red and Alizarin Red to assess for sGAG, collagen and calcium content.

Immunohistochemical technique was used to evaluate collagen types II and X. Sections were rehydrated and treated with chondroitinase ABC (Sigma-Aldrich) in a humidified environment at 37 °C to enhance permeability of the extracellular matrix. This was followed by incubation in goat serum to block non-specific sites and the relevant collagen type II (sc52658, 1:400) (mouse monoclonal; Santa Cruz Biotechnology) or collagen type X (ab49945, 1:200) primary antibodies (mouse monoclonal; Abcam) were applied overnight at 4 °C. Treatment with peroxidase preceded the application of the secondary antibody (collagen type II, B7151, 1:300; collagen type X, ab49760, 1:200) at room temperature for 1 h. Thereafter, all sections were incubated with ABC reagent (Vectastain PK-400; Vector Labs) for 45 min. Finally, sections were developed with DAB peroxidase (Vector Labs) for 5 min. Positive and negative controls were included in the immunohistochemical staining protocols.

4.2.8 Mechanical characterization

All mechanical experiments were performed at room temperature (~25 °C) using a twin column Zwick universal testing machine (Zwick, Roell). Unconfined compression tests were carried out in a PBS bath using a 100 N load cell. To ensure contact between the surface of the scaffolds (n = 4 per group) and the top compression platen, a preload of 0.05 N was used for hydrogels alone constructs, whereas 0.5 N preload was applied to PCL alone as well as composite constructs. A combined stress-relaxation and dynamic compression protocol (Figure 4.1a) was implemented, where a series of compressive strains were applied in increasing steps of 10% to a maximum of 30%. Peak strain was reached within 500 s and the equilibrium stress was obtained after a relaxation time of 45 min. After the relaxation phase, five compressive cycles at 1% strain at a frequency of 1 Hz were superimposed. Ramp (or compressive), equilibrium and dynamic moduli were

quantified at each strain increment. The ramp modulus was calculated as the slope of the initial linear region of the obtained stress-strain curves. The equilibrium modulus was determined as the equilibrium force divided by the sample's cross-sectional area divided by the applied strain. The dynamic modulus was measured as the average force amplitude over the five cycles divided by the sample's cross-sectional area divided by the applied strain amplitude.

Cell-laden 3D bioprinted constructs underwent a shorter version of the stress-relaxation and dynamic compression protocol, to prevent cell death as there was no temperature and/or oxygen control during testing. Samples (n = 3) were subjected to 20% compressive strain followed by 45 min relaxation time and five dynamic compressive cycles at 1% strain and 1 Hz frequency. Ramp, equilibrium and dynamic moduli were quantified as explained in the previous paragraph.

Uniaxial tensile tests on 3D printed dog bone-shaped PCL samples were performed. Each sample (n = 4 per group) was mounted on a sandpaper frame with Araldite glue (Huntsman). The sandpaper frame, along with the PCL scaffold attached to it, was then fixed between two grips. Every test started after cutting through the frame to allow for stretching of the sample. Tensile specimens were tested using a 2500 N load cell at a displacement rate of 1 mm/min and loaded to 50% strain. The tensile modulus was taken as the slope of the stress-strain plots between 2 and 7% strain.

4.2.9 Finite Element Analysis

IPN only, PCL only and composite constructs (4.5 mm x 4.5 mm x 4 mm) were modelled using axisymmetric FE models developed in Abaqus 6.14 (DS Simulia, USA) to evaluate von Mises stress, maximum principal stress, hydrostatic pressure and scaffold

lateral expansion upon loading application. PCL structures were modelled according to a previously described approach (Schipani et al., 2019). PCL reinforced IPN constructs were simulated by placing an IPN hydrogel matrix inside the pores of the PCL scaffold. A tie interaction between the PCL and IPN meshes was applied in order to constrain the translation degrees of freedom of the common nodes of the IPN to those of the PCL scaffold. The models simulated ramp compression tests in unconfined configuration, until 10% strain was applied. For all groups, the nodes at the bottom ends of the scaffolds were constrained only in the loading direction, allowing for scaffold lateral expansion in the other two directions. A displacement of approximately 0.4 mm was prescribed through a platen that was considered a rigid body and in full contact with the nodes at the top surface of the scaffolds. Symmetric boundary conditions were applied to the constructs' inner faces. The engineering compressive modulus of the constructs was obtained from the stress and strain values of the linear region of the curve, calculated from the displacement and resultant reaction force data computed from the simulations. Quadratic ten-node tetrahedral elements (C3D10) were used. Material properties were determined from experimental mechanical testing. Isotropic elastic behaviour was assumed for the IPN hydrogel with a Poisson's ratio of 0.49, representing an almost incompressible material (Castilho et al., 2018). Based on our previous work (Schipani et al., 2019), isotropic

elastic and plastic material properties were assigned to the PCL. Material properties of both PCL and IPN are summarized in Table 4.2.

Table 4-2 Material parameters for the PCL and IPN hydrogel used for the numerical analysis.

Material	*Material Model*	*Material Properties*
PCL	Isotropic elastic	E = 430 MPa; ν = 0.3
	Isotropic plastic	σ^{y}_{true} = 17.745 MPa; ε^{y}_{true} = 0; σ^{f}_{true} = 113.39 MPa; ε^{f}_{true} = 1.3316
IPN	Isotropic elastic	E = 0.036 MPa; ν = 0.49

4.2.10 Statistical analysis

Results are presented as mean ± standard deviation. Statistical analysis was performed with GraphPad (GraphPad Software, La Jolla California, USA). Experimental groups were analysed for significant differences using either a t-test or a general linear model for analysis of variance (ANOVA) and performing Tukey's post-test. For all comparisons, significance was accepted for $p \leq 0.05$.

4.3 Results

4.3.1 Alginate – GelMA IPNs possessed superior mechanical properties to their single hydrogel components

The mechanical properties of alginate – GelMA IPN hydrogels were first compared to that of the individual hydrogel components. This was achieved using a series of stress-relaxation tests combined with dynamic tests in an unconfined compression configuration

(Figure 4.1a). The ramp phase of the unconfined compression test clearly showed that the IPN hydrogel was significantly stiffer than either the alginate or GelMA hydrogel alone (Figure 4.1b). From the ramp phase of each compression test (to either 10%, 20% or 30% strain), it was possible to quantify the ramp modulus of the hydrogels (Figure 4.2a; Table 4.3). The ramp modulus of IPN hydrogel was significantly higher than the alginate and GelMA only hydrogels, and significantly higher than the sum of the individual hydrogel components (shown by the red dashed line) at 20% and 30% strain, demonstrating a synergistic increase in stiffness. Strain stiffening was observed for all three hydrogels, with the ramp modulus increasing with the applied strain amplitude. Stress-relaxation tests were next used to determine the equilibrium modulus of the hydrogels in the absence of fluid flow. Stress-time curves (Figure 4.1b) revealed the distinct stress-relaxation behaviour of each hydrogel. Alginate gels exhibited a complete relaxation of the stress after only 900 s, presumably due to the unbinding of the ionic crosslinker followed by polymer matrix flow (Chaudhuri et al., 2016; Gu et al., 2017; Metzger et al., 2015; Zhao et al., 2010). In contrast, GelMA hydrogels displayed relatively little stress relaxation. The IPN hydrogel stress-relaxation response fell in between that of the alginate and GelMA alone, where the equilibrium state was reached after about 1500 s.

Both the equilibrium and dynamic modulus of IPN hydrogels were higher than the sum of the individual alginate and GelMA hydrogels, significantly so at 20% and 30% strain (Figure 4.2b, c; Table 4.3).

4.3.2 3D printing of PCL networks with tension-compression nonlinearity

3D printing parameters (Table 4.1) were varied in order to obtain two distinct 3D PCL geometries named *Aligned* and *Double Offset* (Figure 4.3a, b). The *Aligned* geometry (Figure 4.3a) was characterized by a regular orthogonal architecture in a lay-down pattern of 0°0°/90°90° forming square pores. The *Double Offset* geometry (Figure 4.3a)

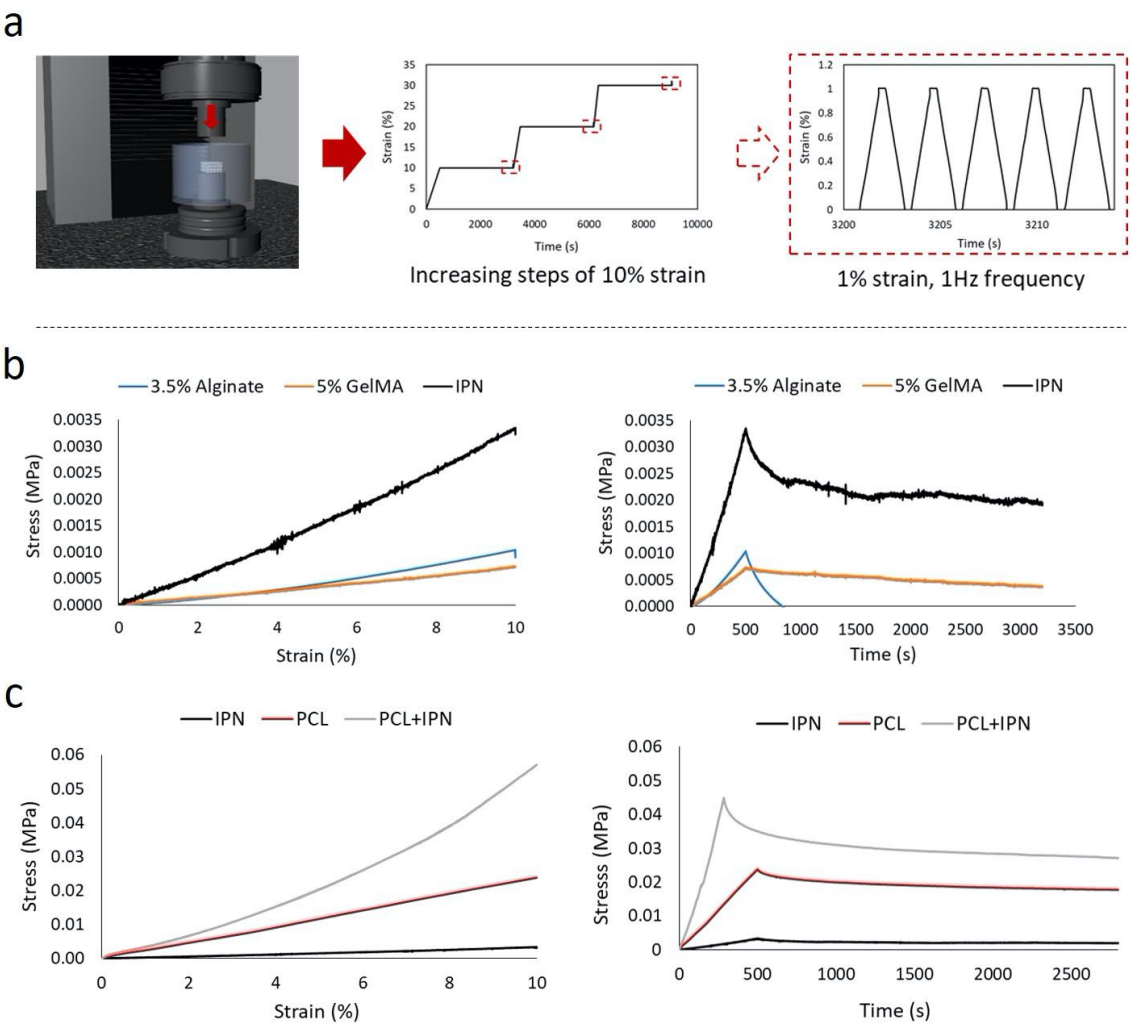

Figure 4-1 (a) Schematic representation of the unconfined compression testing configuration where the loading protocol consisted in a series of applied strain levels (10, 20 and 30% strain) followed by relaxation. After reaching equilibrium, cyclic loading at 1% amplitude and 1Hz frequency was applied at each strain level. (b, c) Representative stress-strain and stress-time curves when comparing (b) 3.5% alginate, 5% GelMA and IPN constructs and (c) IPN, PCL and PCL + IPN scaffolds.

consisted of an orthogonal architecture with the same lay-down pattern. This differed from the *Aligned* pattern because of the presence of offset layers every other four layers that were deposited at an offset distance equal to half the fibre spacing. The obtained 3D network/scaffold architectures were tested in uniaxial tension and compression configurations to evaluate the effect of network geometry on the degree of tension-compression nonlinearity. *Aligned* constructs were stiffer in both tension and compression compared to *Double Offset* networks (Figure 4.3c, d), with more dramatic differences observed in the compressive properties of the PCL networks. The tensile stiffness was 14.795 ± 0.278 MPa for the *Aligned* geometry and 8.358 ± 0.990 MPa for the *Double Offset* one (Figure 4.3c), whereas the compressive modulus was 1.341 ± 0.095 and 0.218 ± 0.014 MPa for *Aligned* and *Double Offset* samples respectively (Figure 4.3d). When quantifying the ratio between tensile and compressive moduli, higher tension-

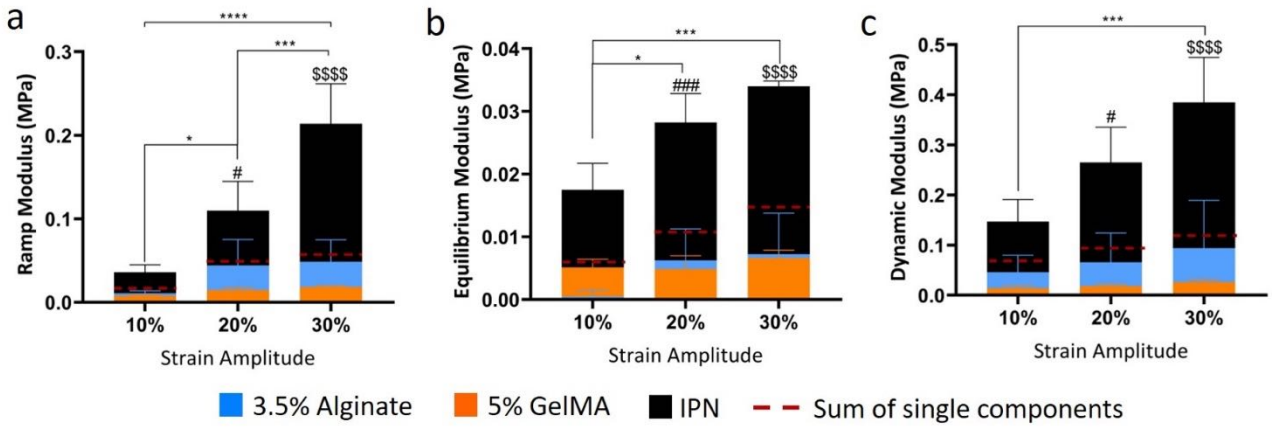

Figure 4-2 (a) Ramp modulus, (b) equilibrium modulus and (c) dynamic modulus in unconfined compression of 3.5% alginate (blue bars), 5% GelMA (orange bars) and IPN (black bars) hydrogels when applying increasing levels of strain amplitude: 10, 20 and 30%. The sum of the modulus of the single component hydrogels for each applied strain is indicated by the dashed red line. #p<0.01and ###p<0.001 IPN vs. 3.5% alginate and 5% GelMA at 20% applied strain; $^{\$\$\$\$}$p<0.0001 IPN vs. 3.5% alginate and 5% GelMA at 30% strain amplitude; *p<0.01, ***p<0.001 and ****p<0.0001 vs. IPN; n = 4 per group.

compression nonlinearity was observed in the *Double Offset* networks in comparison to *Aligned* samples (Figure 4.3e).

Table 4-3 Summary of constructs mechanical properties under unconfined compression.

	Ramp Modulus (MPa)			**Equilibrium Modulus (MPa)**			**Dynamic Modulus (MPa)**		
	10% strain	20% strain	30% strain	10% strain	20% strain	30% strain	10% strain	20% strain	30% strain
3.5% Alginate	0.011 ± 0.003	0.044 ± 0.031	0.049 ± 0.026	0.001 ± 0.001	0.006 ± 0.005	0.007 ± 0.007	0.046 ± 0.034	0.066 ± 0.058	0.094 ± 0.095
5% GelMA	0.008 ± 0.001	0.015 ± 0.003	0.018 ± 0.002	0.005 ± 0.002	0.005 ± 0.003	0.007 ± 0.002	0.015 ± 0.006	0.018 ± 0.005	0.027 ± 0.005
IPN	0.036 ± 0.009	0.110 ± 0.035	0.214 ± 0.048	0.013 ± 0.011	0.028 ± 0.005	0.034 ± 0.001	0.147 ± 0.044	0.265 ± 0.070	0.385 ± 0.090
Double Offset PCL	0.221 ± 0.060	0.304 ± 0.041	0.623 ± 0.092	0.246 ± 0.041	0.261 ± 0.043	0.395 ± 0.036	0.515 ± 0.127	0.777 ± 0.117	1.603 ± 0.205
Double Offset PCL + IPN	0.775 ± 0.081	1.034 ± 0.378	1.445 ± 0.256	0.203 ± 0.215	0.652 ± 0.284	0.957 ± 0.527	0.757 ± 0.195	1.415 ± 0.285	2.293 ± 0.352

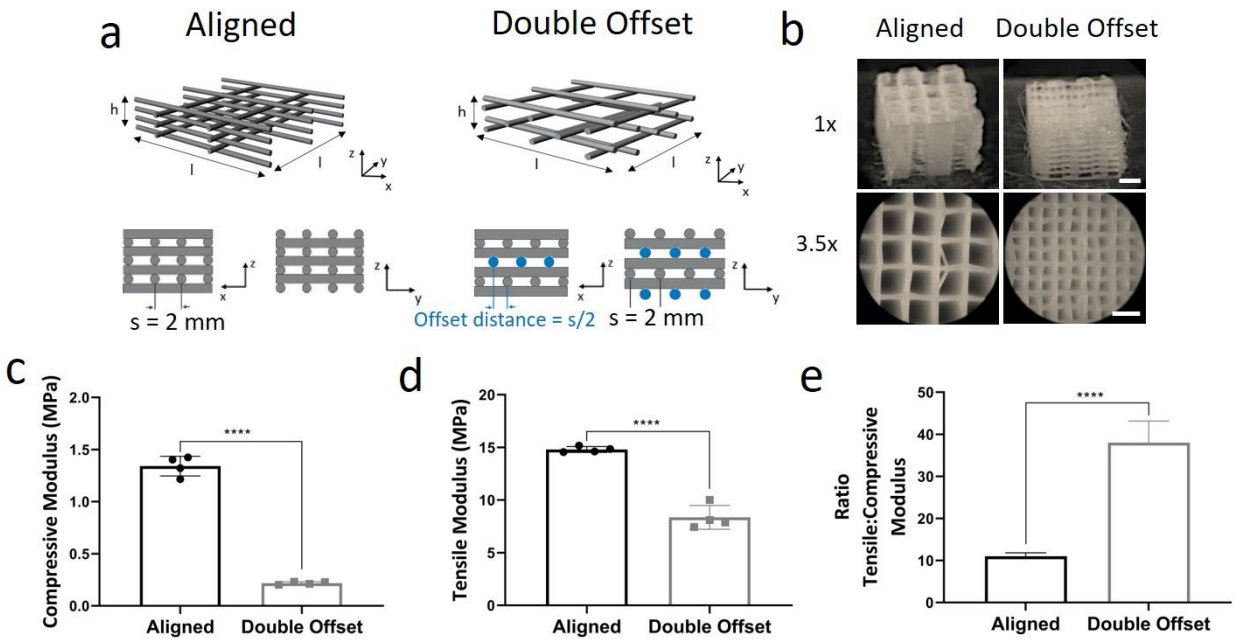

Figure 4-3(a) Schematic of the PCL scaffolds depicting the *Aligned* geometry characterized by a regular orthogonal architecture and the *Double Offset* geometry comprising of offset layers present in both xz and yz planes. Offset layers are shown in blue. Scaffold architecture features are also indicated: h, height of the scaffold; l, length of the scaffold; s, fibre spacing. (b) Microscopy images of *Aligned* (left column) and *Double Offset* (right column) constructs. Scale bar: 2 mm. (c) Tensile modulus, (d) compressive modulus and (e) ratio between tensile and compressive modulus of *Aligned* (black bars) and *Double Offset* (grey bars) 3D printed PCL scaffolds. ****$p<0.0001$; n = 4 per group.

4.3.3 Combining IPN hydrogels with reinforcing PCL networks to produce biomimetic composites with mechanical properties comparable to native cartilage

Alginate – GelMA IPNs were next reinforced with 3D printed PCL networks with two distinct architectures (*Aligned* and *Double Offset*). The PCL scaffolds were infused with different alginate - GelMA IPN hydrogel formulations where the alginate concentration (3.5% w/v) was maintained constant, whereas the GelMA content was increased (5, 10 and 15% w/v). The resulting composite constructs were subjected to compression tests to determine their ramp modulus in comparison to PCL scaffolds alone,

IPNs alone and the sum of the moduli of the individual components (Figure 4.4a-c). After infusing the *Double Offset* PCL scaffolds with the IPN hydrogels (Figure 4.4b), a synergistic increase in stiffness was observed for all IPN formulations. Specifically, the ramp modulus of the composite samples (grey bars) was higher than the sum of the moduli of the single components (blue dashed lines) as well as to the individual components, i.e. the PCL scaffolds (red bars) and IPN gels (black bars). The ramp modulus of the composite increased as the GelMA content in the IPN increased (0.554 ± 0.090, 0.665 ± 0.140 and 0.713 ± 0.153 MPa at 5, 10 and 15% w/v GelMA concentration, respectively). Moreover, *Double Offset* PCL + IPN constructs were significantly stiffer than the *Double Offset* PCL alone samples (0.218 ± 0.014 MPa), showing approximately 2.5-, 3- and 3.3-fold increases in stiffness at 5, 10 and 15% w/v GelMA concentrations, respectively. Combining the *Aligned* PCL constructs with the IPN hydrogels (Figure 4.4c) did not result in the same synergistic increase in stiffness. The ramp moduli of the composite constructs did not increase as the GelMA content in the IPN gels increased (1.147 ± 0.149, 1.183 ± 0.164 and 1.206 ± 0.195 MPa at 5, 10 and 15% w/v GelMA concentration, respectively). Furthermore, there was no statistical difference in ramp modulus compared to the *Aligned* PCL alone scaffolds (1.261 ± 0.051 MPa), indicating that the PCL component was dominating the mechanical behaviour of the composite.

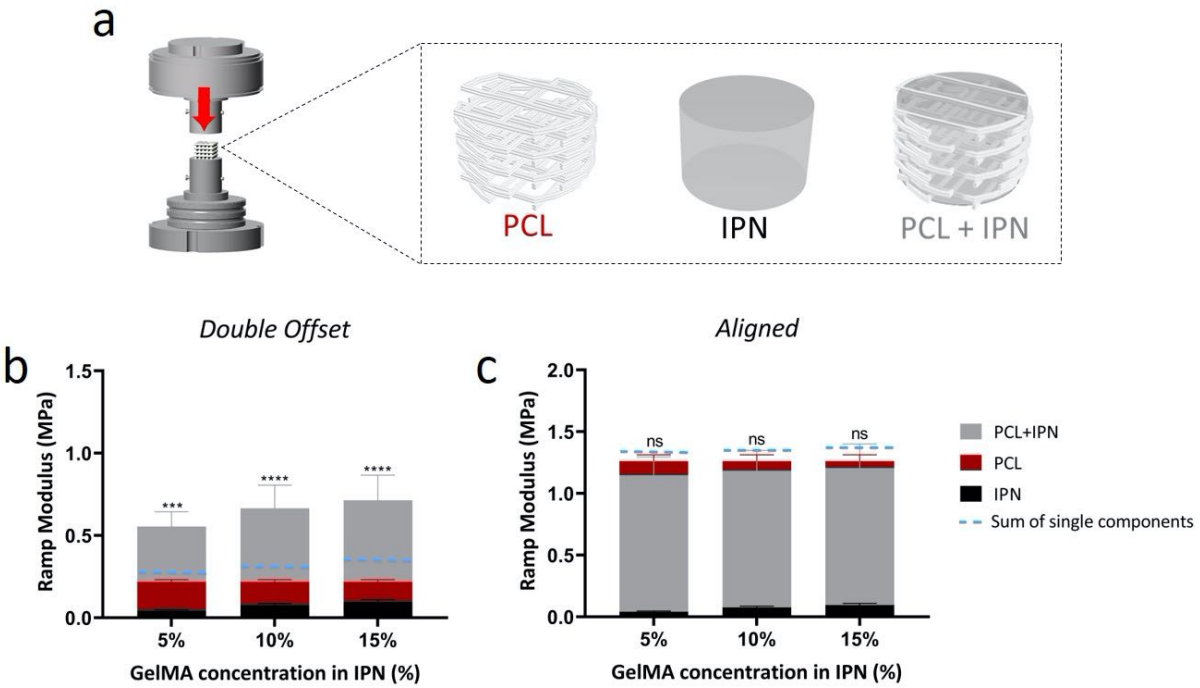

Figure 4-4 (a) Schematic illustration of the mechanical testing set-up and scaffold groups (PCL, IPN and PCL + IPN) that underwent compression tests. (b, c) Ramp moduli of PCL frames (red bars), IPN hydrogels (black bars) and PCL + IPN scaffolds (grey bars) when varying GelMA concentration in the IPN from 5 to 15% (w/v). Results are shown for groups containing either the (b) *Double Offset* or (c) *Aligned* PCL geometry. The sum of the compressive modulus of the individual components for each GelMA concentration is indicated by the dashed blue line. ***p<0.001 and ****p<0.0001; n = 4 per group.

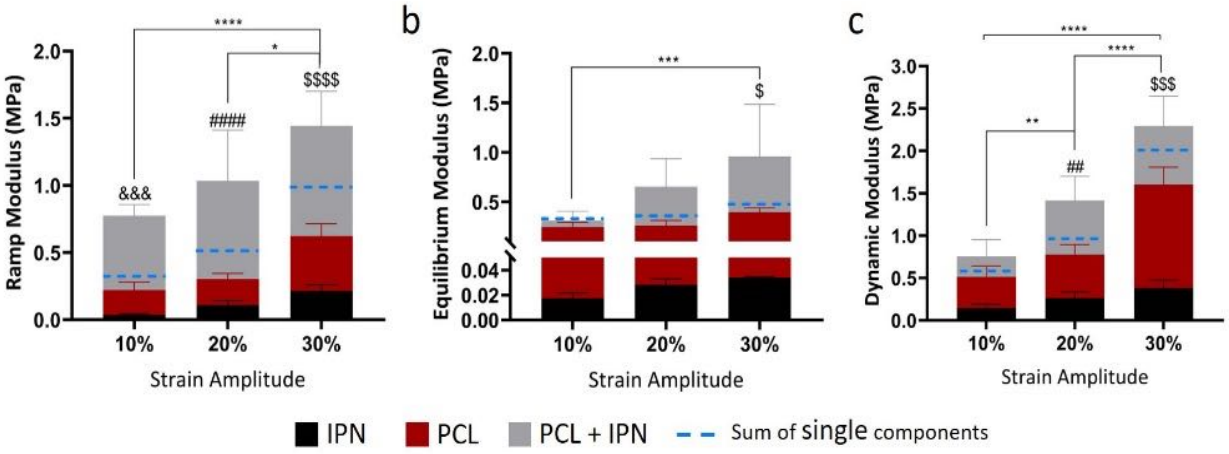

Figure 4-5 (a) Ramp modulus, (b) equilibrium modulus and (c) dynamic modulus in unconfined compression of IPN hydrogel (black bars), *Double Offset* PCL (red bars) and PCL + IPN (grey bars) scaffolds when applying increasing levels of strain amplitude: 10, 20 and 30%. The sum of the moduli of the individual components for each applied strain is indicated by the dashed blue line. $^{\&\&\&}$p<0.001 PCL + IPN vs. PCL at 10% applied strain; $^{\#\#}$p<0.01 and $^{\#\#\#\#}$p<0.0001 PCL + IPN vs. PCL at 20% applied strain; $^{\$}$p<0.05 and $^{\$\$\$}$p<0.001 PCL + IPN vs. PCL at 30% applied strain; *p<0.05, **p<0.01, ***p<0.001 and ****p<0.0001 vs. PCL + IPN; n = 4 per group.

The ramp, equilibrium and dynamic moduli of the composites were also assessed after the application of 10, 20 and 30% strain for the *Double Offset* PCL design (Figure 4.5a-c; Table 4.3). Stiffness was found to increase with increases in the applied strain amplitude. For all strain levels, the ramp moduli was significantly higher for the composite constructs (grey bars; 0.775 ± 0.081, 1.034 ± 0.378 and 1.445 ± 0.256 MPa when applying 10, 20 and 30% strains respectively) compared to the PCL alone (red bars; 0.221 ± 0.060, 0.304 ± 0.041 and 0.623 ± 0.092 MPa at 10, 20 and 30% applied strain amplitudes respectively), the IPN alone (black bars) as well as the sum of the individual components (blue dashed line) at all applied strain amplitudes (Figure 4.5a; Table 4.3). The equilibrium modulus of the PCL + IPN composites was only higher than the PCL scaffolds alone at higher strain levels.

The dynamic modulus for composite constructs was measured to be 0.757 ± 0.195, 1.415 ± 0.285 and 2.293 ± 0.352 MPa at 10, 20 and 30% applied strain amplitudes respectively, whereas it increased from 0.515 ± 0.127 to 1.603 ± 0.205 MPa and 0.147 ± 0.044 to 0.385 ± 0.090 MPa for PCL and IPN alone, respectively.

4.3.4 FE modelling to better understand the mechanism by which 3D printed fibre networks mechanically reinforce IPN hydrogels

FEA was next utilized to better understand the mechanism by which the PCL networks were mechanically reinforcing the IPN hydrogels. FE simulations were performed of uniaxial compression tests on the IPN alone, PCL alone and composite constructs for both *Double Offset* and *Aligned* PCL-based structures (Figure 4.6). The predicted stress-strain behaviour (Figure 4.6a, b) and compressive modulus (Figure 4.6c, d) of all groups were in good agreement with the experimental results. Having demonstrated that this computational approach was able to accurately predict the

compressive mechanical behaviour of 3D printed scaffolds, we next sought to investigate how the *Double Offset* PCL network was reinforcing the IPN hydrogels. When comparing the expansion in both x- and y-direction of IPN in *Double Offset* PCL + IPN, *Aligned* PCL + IPN and IPN alone models, it was observed that reinforcing the IPN with either of the PCL networks reduced lateral expansion of the composite, with the lowest expansion observed in the *Double Offset* PCL composite (Figure 4.6e). Next, the average hydrostatic pressure produced in the IPN when applying 10% compressive strain was predicted. In general, higher pressure was generated within the IPN in the presence of both *Aligned* and *Double Offset* PCL, with the highest values predicted in *Double Offset* PCL + IPN structures. Compared to IPN alone, there was approximately a 24- and 7.5-fold increase in hydrostatic pressure in *Double Offset* PCL + IPN and *Aligned* PCL + IPN constructs, respectively (Figure 4.6f). The FE model also predicted higher stresses in the PCL filaments within the *Double Offset* PCL network in composites compared to *Double Offset* PCL only structures (Figure 4.6g). On the other side, little difference in von Mises

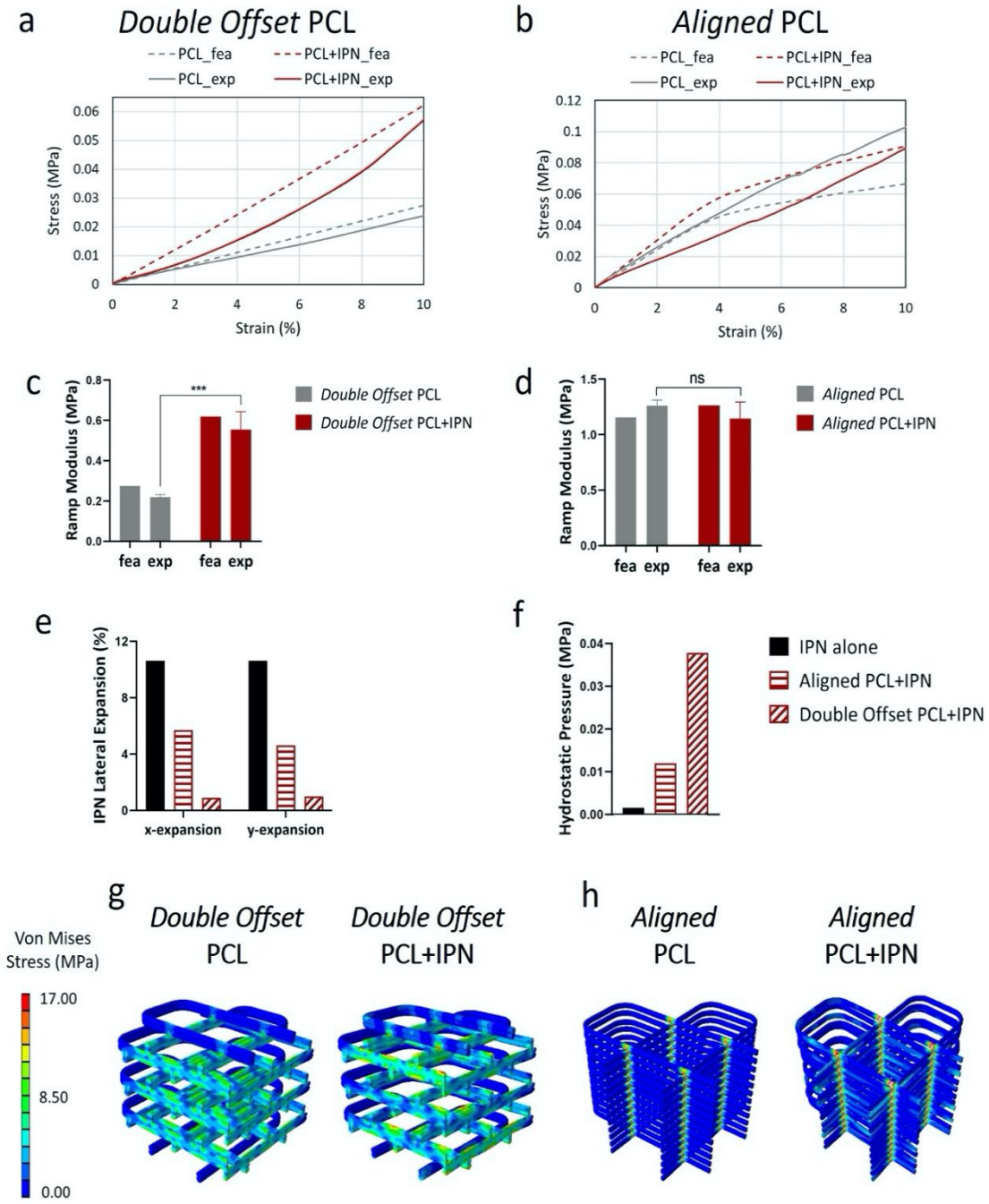

Figure 4-6 Computational and experimental (a, b) compressive stress-strain curves and (c, d) ramp modulus for (a, c) *Double Offset* and (b, d) *Aligned* PCL-based structures; ***p<0.001; n = 4 per group. Comparison of predicted IPN (e) lateral expansion and (f) hydrostatic pressure in IPN alone, *Aligned* PCL+IPN and *Double Offset* PCL+IPN structures. Von Mises stress contour plots for (g) *Double Offset* and (h) *Aligned* PCL-based constructs.

stress distribution was predicted in the PCL network of the *Aligned* PCL + IPN composites compared to *Aligned* PCL only scaffolds (Figure 4.6h). Together, the FE

models suggest two related mechanisms by which the *Double Offset* PCL network reinforces the IPN hydrogel. Firstly, the presence of the IPN in the PCL network increases the tensile stresses generated in the PCL filaments (see also Supplementary Figure 3), allowing them to play a greater role in supporting the applied load. Secondly, the PCL network is predicted to limit lateral expansion of the composite and lead to higher magnitudes of hydrostatic pressure being generated within the IPN. Such reinforcement mechanisms are enhanced by PCL networks with greater tension-compression nonlinearity. The FE simulations further demonstrate that the combination of the *Double Offset* PCL network with the IPN produce a cartilage biomimetic construct.

4.3.5 PCL reinforced cell-laden IPNs fabricated using 3D bioprinting support chondrogenesis with minimal hypertrophy

Having successfully obtained composite constructs with mechanical properties comparable to those of native cartilage, we proceeded to assess the capacity of these composites to provide a pro-chondrogenic environment *in vitro*. With a view to bioprinting cell-laden implants, we established a multiple-tool biofabrication process that first involved the bioprinting of the porous reinforcing *Double Offset* PCL networks in the shape of a cylinder (6 mm x 6 mm). In a second bioprinting step, the obtained PCL networks were placed in a moulding system that kept them in the centre of the well of a 6-well plate, which facilitated the z-direction bioprinting of the bioinks (alginate, GelMA and alginate - GelMA IPNs containing a co-culture of BMSCs and CCs) into the PCL networks (Figure 4.7a). Z-direction bioprinting consists of depositing the cell encapsulating-bioinks within the empty pores of the previously printed PCL networks by moving the needle in the z-direction. The bioprinted constructs were then transferred to chondrogenic media and cultured in static conditions at 5% O_2 for the first 3 weeks and

then at 21% O_2 for further 3 weeks. To verify that cell viability was not affected by the 3D printing process or the post-fabrication crosslinking of the bioinks, all constructs were analysed using live-dead staining after 24 h of culture (Figure 4.7b-c). All bioinks supported high levels of cell viability (~80%; Figure 4.7c), showing that the fabrication process was not overly harmful to the cells.

Over 6 weeks of *in vitro* culture, the ramp modulus of the PCL reinforced GelMA and IPN-based composites progressively increased (Figure 4.7d-f). The PCL reinforced-IPN constructs possessed the highest ramp modulus at all time points reaching values of 1.469 ± 0.326 MPa compared to 0.830 ± 0.114 and 0.927 ± 0.082 MPa for alginate-based and GelMA-based composites respectively at day 42 (Figure 4.7d). No major differences in the equilibrium modulus were observed between the different groups, which was approximately 0.350 MPa after 42 days of culture (Figure 4.7e). Significant increases in dynamic modulus with time in culture were only observed in the GelMA-based composites (Figure 4.7f). All three PCL reinforced bioinks supported the development of a hyaline cartilage-like tissue that stained positive for sGAG and collagen type II deposition (Figure 4.8a-c). sGAG and collagen deposition appeared quite pericellular within the IPN-based composites at day 21 (Figure 4.8b) but become more diffuse with further time in culture (Figure 4.8c). What was presumed to be non-specific type X collagen staining, was observed in the GelMA-based composites at day 1, making it difficult to assess type X collagen deposition in this group. There was no positive staining for collagen type X in the other groups at any time point, suggesting that the engineered tissues were not becoming hypertrophic with time in culture. Alginate and GelMA-based scaffolds showed some positive staining for Alizarin Red at day 42, demonstrating the presence of calcium deposits. In contrast, no evidence of calcium deposition was

observed in IPN-based composites, suggesting then the development of phenotypically stable articular cartilage-like tissue within the IPNs. Histological observations were confirmed by biochemical analysis, which demonstrated that sGAG and collagen content

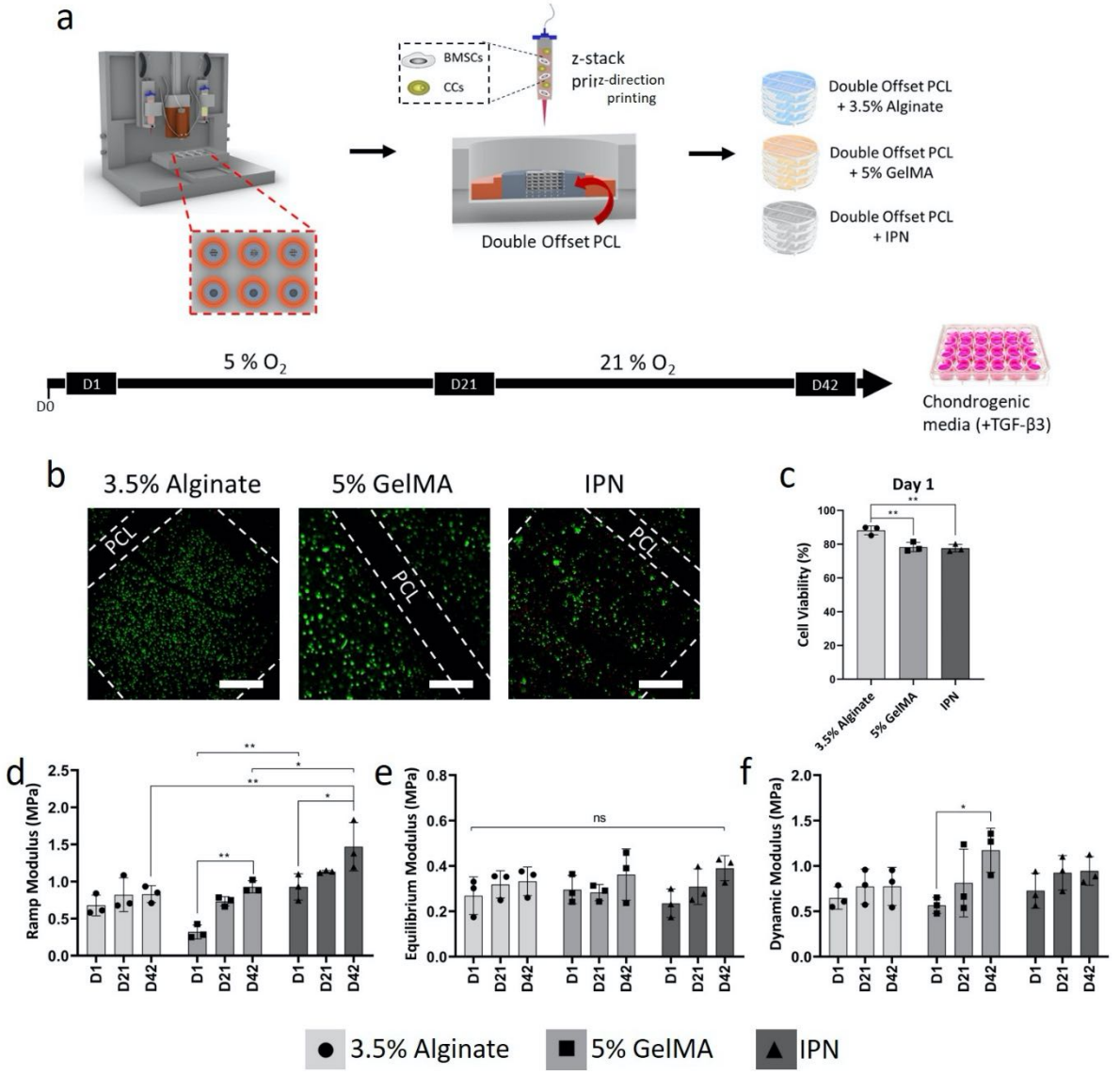

Figure 4-7 (a) Schematic of the experimental set-up: *Double Offset* PCL frames were 3D printed *via* FDM and then placed in a moulding system that kept the PCL scaffolds in the centre of each well of a 6-well plate to facilitate microextrusion (z-direction printing) of the cell-laden bioinks. Obtained composite constructs were cultured in chondrogenic media for the first 3 weeks in hypoxia and the following 3 weeks in normoxia. (b) Representative images of Live/Dead staining used to determine the cell viability of 3.5% alginate, 5% GelMA and IPN bioinks. Scale bar: 200 µm. (c) Quantitative analysis of the cell viability for all of the bioinks. (d) Ramp modulus, (e) equilibrium modulus and (f) dynamic modulus for all composite groups after day 1, 21 and 42 of culture. *p<0.05, **p<0.01, ***p<0.001 and ****p<0.0001; n = 3 per group.

significantly increased over the culture period, with no drama tic differences observed between the three hydrogel groups (Figure 4.8e-f).

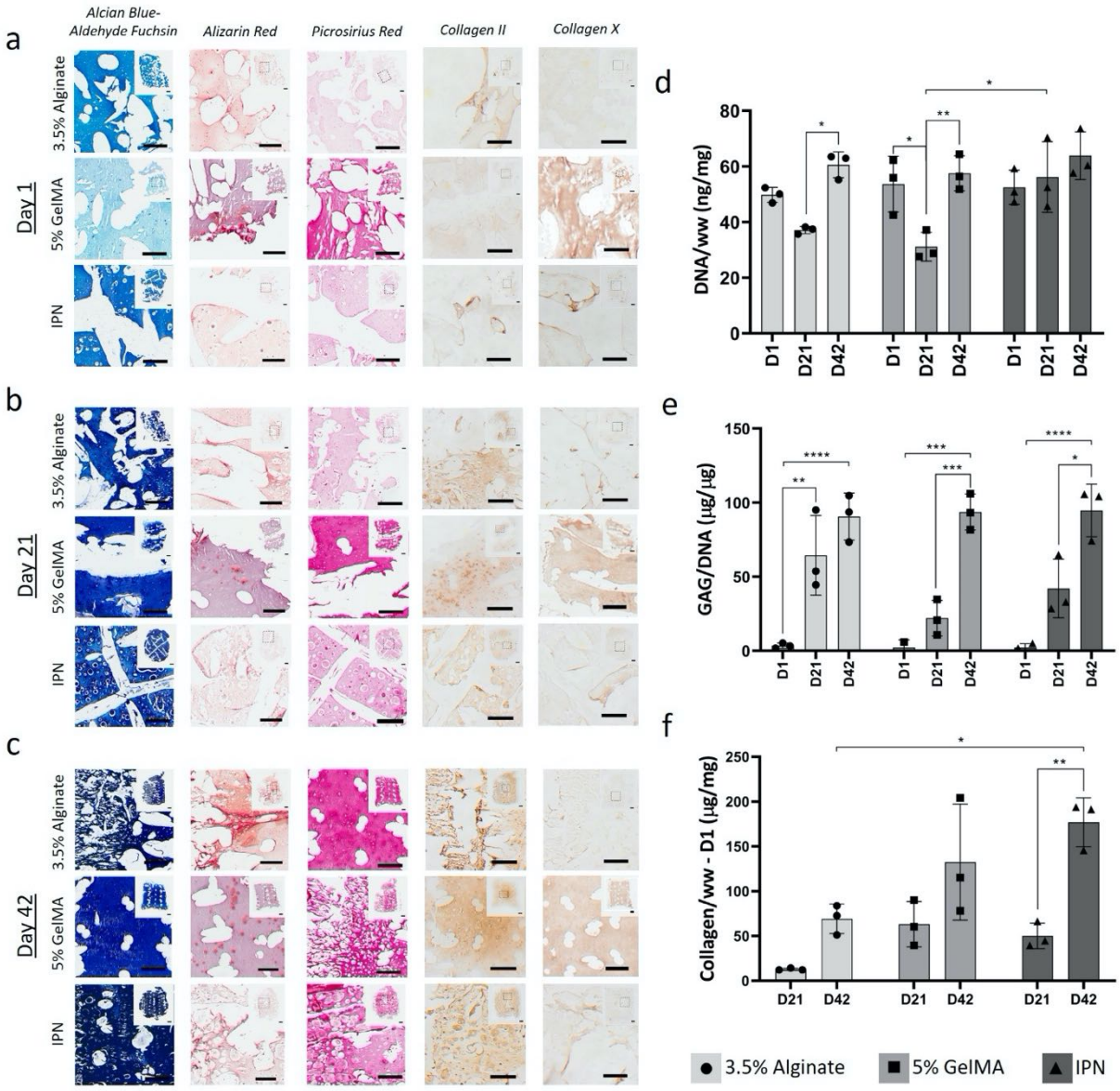

Figure 4-8 (a-c) Histological and immunohistochemical staining of all 3D bioprinted constructs groups after (a) 1, (b) 21 and (c) 42 days of *in vitro* culture. Scale bar: 500 µm. (d-f) Biochemical analysis of all composites, including (d) DNA content normalized to wet weight (ng/mg), (e) GAG/DNA and (f) collagen/DNA after day 1, 21 and 42 of *in vitro* culture. *p<0.05, **p<0.01, ***p<0.001 and ****p<0.0001; n = 3 per group.

4.4 Discussion

Engineering constructs that mimic the complex structure, composition and biomechanics of the articular cartilage represents a promising route to joint regeneration. Such tissue engineering strategies require the development of biomaterials that mimic the mechanical properties of articular cartilage whilst simultaneously providing an environment supportive of chondrogenesis. Particularly, equilibrium and dynamic properties are important functional parameters to measure when assessing articular cartilage and biomaterials designed to regenerate this tissue (Gannon et al., 2012; Guilak et al., 2001; Mow et al., 2002; Mow et al., 1980). The dynamic properties of a biomaterial reflect its capacity to generate fluid load support, which in the case of articular cartilage is associated with the low permeability of the solid matrix (Gannon et al., 2012; Soltz et al., 2000).

The goal of this study was to use 3D bioprinting to engineer PCL-reinforced alginate-GelMA IPNs that were both pro-chondrogenic and biomimetic of the mechanical properties of articular cartilage. The benefit of combining alginate and GelMA single hydrogel components to form IPNs was demonstrated, as synergistic increases in mechanical properties were observed. In spite of the improvements associated with the IPN hydrogel, its equilibrium and dynamic mechanical properties still remained at least one order of magnitude lower than that of native articular cartilage (Beck et al., 2016b; Jurvelin et al., 1997; Little et al., 2011; Park et al., 2004). Therefore, recognizing that hydrogels alone (Critchley et al., 2019; Critchley et al., 2017; Daly et al., 2016a; Daly et al., 2017b; Erickson et al., 2009; Hofmann et al., 2006), even IPN hydrogels, fail to recapitulate the complex mechanical properties of articular cartilage, this chapter next investigated whether it was possible to design more biomimetic materials with nonlinear

mechanical properties by reinforcing IPN hydrogels with 3D printed PCL networks with distinct tension-compression nonlinearity. As tension-compression nonlinearity is believed to play a critical role in the load-bearing capacity of articular cartilage by enhancing fluid pressurization under compression, we hypothesized that reinforcing IPN hydrogels with PCL network designs that were relatively soft in compression and stiff in tension (*Double Offset* PCL) would result in the development of constructs that more closely mimicked the mechanical behaviour of the native tissue. The obtained ramp modulus values for the *Double Offset* PCL + IPN constructs fell in the range of native tissue properties (Beck et al., 2016b; Little et al., 2011; Shepherd et al., 1997). In unconfined compression, the equilibrium modulus of articular cartilage ranges from approximately 0.2 to 2 MPa (Athanasiou et al., 1994; Gannon et al., 2015b; Gao et al., 2014; Jurvelin et al., 1997; Little et al., 2011; Mow et al., 2002), whereas the dynamic modulus in response to cyclic loading ranges from approximately 10 to 60 MPa, depending on the loading frequency (Bian et al., 2008; Kinnunen et al., 2011; Liao et al., 2013b; Little et al., 2011; Park et al., 2004). The composite 3D printed PCL reinforced IPN constructs possessed equilibrium moduli that fell in the range of native cartilage equilibrium properties (Figure 4.5b; Table 4.3). Although the dynamic modulus of PCL + IPN composites did not match the values of the native tissue, it showed a marked improvement compared to PCL and IPN alone (Figure 4.5c; Table 4.3), reaching the same order of magnitude as articular cartilage. The fact that the dynamic properties of the composite did not reach native values is likely related to the fact its permeability is significantly higher than that of articular cartilage. While a lower permeability (and hence a superior capacity to generate fluid load support) could be achieved by increasing the density of the IPN, this could negatively impact nutrient transport and waste removal

once the biomaterial is seeded with cells for tissue engineering applications. Hence, the properties achieved can be viewed as a balance between providing initial mechanical function (mimicking native equilibrium and ramp modulus values) and an environment supportive of chondrogenesis (that was assessed *in vitro*).

FE models were used to better understand the interactions between the different components of fibre-reinforced composites, revealing that reinforcement of IPN hydrogels with the *Double Offset* PCL network limited the radial expansion of the composite and increased the hydrostatic pressure generated within the IPN upon the application of compressive loading. This is similar to when articular cartilage is subjected to compressive loading, as the collagen network resists lateral expansion and fluid pressurization supports a significant component of the applied load. Other studies have reported similar reinforcement mechanisms, mainly when reinforcing hydrogels with electrospun fibres. For example, Castilho et al. (Castilho et al., 2018) demonstrated that the reinforcement effect of microfibre reinforced GelMA composites derived either from fibres being pulled in tension by the expansion of the hydrogel, or from the support provided by the hydrogel in preventing buckling of the fibres under compression.

Finally, multiple-tool biofabrication techniques were used to 3D bioprint PCL-reinforced IPN hydrogels laden with a co-culture of BMSCs and CCs. The bioprinted biomimetic composites were found to support robust chondrogenesis, with encapsulated cells producing hyaline-like cartilage that stained strongly for sGAG and type II collagen deposition, and negatively for type X collagen and calcium deposition. Together these results demonstrated that alginate – GelMA IPNs were able to support robust chondrogenesis, with levels of ECM deposition comparable to that observed in the individual hydrogels. Importantly, it was shown that the increased mechanical properties

achieved with the IPN did not negatively affect its biological functionality. Usually, hydrogels presenting cell binding motifs such as GelMA can facilitate cell-cell and cell-matrix interactions leading more to fibrocartilage-like tissue formation (Awad et al., 2004; Daly et al., 2016a; Levett et al., 2014a; Levett et al., 2014b; Schuurman et al., 2013). In contrast, alginate is known to be an inert material and should facilitate BMSCs to develop a round shape, which is known to support a chondrogenic phenotype (Benya et al., 1982; Daly et al., 2016a; Rowley et al., 1999). Given that a co-culture of CCs and BMSCs is known to support the generation of phenotypically stable articular cartilage (Bian et al., 2011; Cooke et al., 2011; Fischer et al., 2010; Kang et al., 2012; Mesallati et al., 2015), we did not expect to see dramatic difference in hypertrophy and progression along an endochondral pathway in the three different hydrogel bioink groups. Importantly, the stiffer IPN based composites supported the development of cartilage resistant to calcification after 6 weeks of culture, despite the fact that stiffer hydrogel environments can be more supportive of chondrocyte hypertrophy (Bian et al., 2013; Engler et al., 2006; Nguyen et al., 2012; Zhu et al., 2018).

Together, the findings demonstrate that the PCL + IPN composites possess equilibrium and ramp compressive properties comparable to articular cartilage immediately post-biofabrication. Furthermore, the composites support robust chondrogenesis, ensuring that the mechanical properties of cell-laden constructs continue to improve with time in culture as the encapsulated cells secrete a cartilage-like ECM.

4.5 Conclusion

This work represents a significant step towards developing biomechanically functional biomaterials for cartilage tissue engineering. The combination of alginate – GelMA IPN hydrogels with appropriately designed 3D printed PCL networks enables the engineering of composites with mechanical properties that are mimetic of normal articular cartilage. Importantly, such composite constructs provide encapsulated cells with an environment conducive to chondrogenesis, resulting in robust production of articular cartilage-like matrix.

Chapter 5
3D bioprinting of layered constructs with spatially distinct mechanics and cellular phenotype for osteochondral tissue engineering

5.1 Introduction

Effective treatment of cartilage and osteochondral defects remains a significant challenge. The goal of tissue engineering is to produce functional constructs *in vitro* that can effectively regenerate damaged or diseased tissues *in vivo*. To engineer functional tissue replacements for cartilage and osteochondral defect repair, various combinations of cells, scaffolds, growth factors and bioreactor systems have been explored (Almeida et al., 2014; Bian et al., 2013; Erickson et al., 2009; Huang et al., 2010; Mesallati et al., 2017; Thorpe et al., 2008). The earliest example of this is autologous chondrocyte implantation (ACI), which is now a well-established treatment for regenerating articular cartilage lesions using culture expanded autologous chondrocytes (CCs) originally harvested from non-load bearing locations (Brittberg et al., 1994). However, this technique does not consistently result in hyaline cartilage regeneration, which can be related to the fact that chondrocyte expansion to obtain a sufficient number of cells causes fibroblastic de-differentiation, with decreased synthesis of proteoglycans and expression of collagen type II and increased expression of collagen type I (Bian et al., 2010; Darling et al., 2005; Fischer et al., 2010). A possible solution to overcome these limitations is the use of co-cultures of CCs and mesenchymal stromal cells (MSCs), as a small number of CCs that have undergone less *in vitro* expansion can be combined with a larger number

of MSCs to produce stable cartilage. The use of such co-cultures is advantageous because MSCs can be easily obtained and can be induced to differentiate into cartilage even after expansion, limiting the need for high numbers of CCs (Boeuf et al., 2010; Hendriks et al., 2009). Moreover, it has been demonstrated that CCs can stimulate chondrogenesis of MSCs (Liu et al., 2010), suppress hypertrophy (Bian et al., 2010) and increase extracellular matrix (ECM) synthesis (Acharya et al., 2012; Bian et al., 2010; Giovannini et al., 2010). This approach can ultimately facilitate the scaling-up of tissue engineering strategies by increasing the number of therapeutic cells available for engineering larger constructs.

Besides the choice of cell source and associated expansion conditions, the mechanical environment is also known to be a potent regulator of cell phenotype. A crucial role is played by the mechanical properties of the tissue engineered construct, which ideally will match those of the native tissue to provide cells with a mechanical physiological environment *in vivo* (Little et al., 2011). Receiving appropriate mechanical cues has been shown to enhance matrix synthesis by cells encapsulated within scaffolds (Li et al., 2008; Schulz et al., 2007; Valonen et al., 2010). To engineer functional cartilage, 3D woven polycaprolactone (PCL) scaffolds containing human MSCs were able to produce higher collagen content and a more homogeneous matrix when cultured in an oscillating bioreactor system compared to static controls (Valonen et al., 2010). In another study, a bioreactor system able to simultaneously apply compression and shear forces was used in order to guide MSCs chondrogenesis in polyurethane/methylcellulose composites (Cochis et al., 2017). Mechanical stimulation resulted in higher expression of chondrogenic genes and increase in glycosaminoglycan (GAG) production. Compressive deformational loading, specifically cyclic unconfined compression, is the most utilized

system of mechanical stimulation in cartilage tissue engineering (Bian et al., 2012; Cao et al., 2019; Mauck et al., 2002; O'Conor et al., 2013). Depending on the loading regime, dynamic compression of MSC-encapsulated scaffolds has been reported to produce a pro-chondrogenic response that is beneficial for the repair of cartilage tissue (Huang et al., 2010; Kisiday et al., 2009; Kock et al., 2012; Mauck et al., 2007; Thorpe et al., 2010). However, there have also been studies demonstrating that mechanical stimulation can suppress chondrogenesis of MSCs (Thorpe et al., 2010; Thorpe et al., 2008), or is more effective if delayed or applied in the presence of growth factors (Mouw et al., 2007; O'Conor et al., 2013; Thorpe et al., 2010). In addition, different mechanical cues have been shown to either enhance (Bernhard et al., 2018; Carroll et al., 2014) or suppress (Elder et al., 2009a; Nazempour et al., 2017) hypertrophy and progression along an endochondral pathway when applied to chondrogenically primed MSCs.

In this chapter, 3D printing was first used to fabricate bi-layered PCL networks with depth dependent mechanical properties for osteochondral tissue engineering. An alginate-gelatin methacryloyl (GelMA) interpenetrating network (IPN) hydrogel was then spatially deposited into the chondral layer of the construct, while an RGD-γ irradiated alginate hydrogel bioink was deposited into the osseous layer. The objective of this study was to engineer phenotypically stable articular cartilage in the chondral region of the construct, and hypertrophic cartilage destined to form endochondral bone in the osseous region. To generate hypertrophic cartilage in the osseous region, bone marrow-derived stromal cells (BMSCs) were loaded into the RGD-γ irradiated alginate hydrogel bioink, while two distinct approaches were explored to engineer phenotypically stable articular cartilage in the chondral region of the construct. In the first, a co-culture of BMSCs and CCs were deposited within the chondral layer of the construct. In the second, dynamic

compression was applied to bioprinted constructs containing only BMSCs in both the chondral and osseous layers, to explore if the application of physiologically relevant mechanical cues is sufficient to support the development of phenotypically stable articular cartilage. These bioprinted constructs were cultured for 42 days *in vitro* in the presence of transforming growth factor-ß3 (TGF-ß3) before being assessed biochemically and histologically to determine the tissue phenotypes generated within the two layers of bioprinted construct.

5.2 Materials and methods

5.2.1 Cell-laden bioinks preparation

For the chondral layer of the 3D printed bi-layered PCL networks, an alginate – GelMA IPN bioink was used. GelMA was produced according to a previously reported protocol (Van Den Bulcke et al., 2000b). GelMA was synthesized by reaction of porcine type A gelatin (Sigma Aldrich) with methacrylic anhydride (Sigma Aldrich) at 50 °C for four hours. Methacrylic anhydride was added to a 10% solution of gelatin in PBS under constant stirring. To achieve a high degree of functionalization, 0.6 g of methacrylic anhydride was added per gram of gelatin. The functionalized polymer was dialyzed against distilled water for 7 days at 40 °C to remove methacrylic acid and anhydride, freeze-dried and stored at −20 °C until use. To prepare the IPN bioink, alginate (PRONOVA IP LVG) and GelMA (including the photoinitiator Irgacure (Sigma-Aldrich) at a final concentration of 0.05% v/v) were firstly dissolved in DMEM at a concentration of 14 and 20% w/v respectively and then mixed together at a 1:1 ratio using a dual syringe approach. Prior to bioprinting, the obtained IPN bioink was then combined

either with a mixture of BMSCs and CCs (3:1 ratio) or BMSCs only at a 1:1 ratio, resulting into IPN final concentration of 3.5% w/v alginate - 5% w/v GelMA and cell density of 20 x 10^6 cells/mL.

For the osseous layer of the 3D printed bi-layered PCL networks, an RGD-*γ* irradiated alginate bioink was used. Low-molecular-weight sodium alginate (58,000 g/mol) was prepared by irradiating sodium alginate (Pronatal LF20/40, 196,000 g/mol; Pronova Biopolymers, Oslo. Norway) at a gamma dose of 5 Mrad as previously described (Jeon et al., 2010). RGD-modified (arginine-glycine aspartic acid) alginate was prepared by coupling the GGGGRGDSP to the alginate by carbodiimide reaction chemistry. To prepare the RGD-*γ* irradiated alginate bioink, RGD-*γ* irradiated alginate was dissolved in DMEM at a concentration of 7% w/v. To make the bioink printable, the bioink viscosity was increased by adding sterile methylcellulose (Sigma-Aldrich) to a 7% solution of RGD-*γ* irradiated alginate at a ratio of 1:2 w/w (methylcellulose:alginate). Prior to bioprinting, the RGD-*γ* irradiated alginate-methylcellulose hydrogel was combined with BMSCs using the above mentioned dual syringe approach, obtaining an RGD-*γ* irradiated alginate bioink final concentration of 3.5% w/v and cell density of 20 x 10^6 cells/mL. The cell-laden osseous layer bioink was then pre-crosslinked with 45 mM $CaCl_2$ (7:3, v/v bioink:$CaSO_4$) for 40 mins at 37°C.

5.2.2 Design and fabrication of 3D bi-layered constructs

Bi-layered PCL (CAPA 6500D, Perstorp, Mn 50 kDa) networks (6 mm in diameter, 6 mm in height) were 3D printed *via* fused deposition modelling (FDM) using the 3D Discovery bioplotter purchased from RegenHU with spatial resolution of ± 5 μm. The filament pattern of the PCL network was varied in order to obtain two distinct geometries resulting in a denser region (named *Aligned*) for the osseous layer (6 mm in diameter, 3

mm in height), and a softer region (named *Double Offset*) for the chondral layer (6 mm in diameter, 3 mm in height). The *Aligned* design consisted of a regular orthogonal architecture, following a 0°0°/90°90° pattern with a filament spacing of 0.75 mm. The *Double Offset* design was characterized by a 0°0°/90°90° orthogonal pattern with the presence of offset layers every other four layers. In this case the filament spacing was 2 mm, whereas the offset layers were deposited at an offset distance of 1 mm. Previously printed PCL constructs were sterilized with EtO and soaked overnight in a solution of 45 mM $CaCl_2$ to facilitate the crosslinking process of the hydrogels during printing. Prior to hydrogels printing, the PCL constructs were placed in each well of a 6-well plate by means of 3D printed poly lactic acid (PLA) inserts containing polydimethylsiloxane (PDMS) moulds that kept the scaffolds in place in the centre of the well.

The cell-laden bioinks were loaded into a pressure driven system to be microextruded in the open pores of the bi-layered PCL networks, using a z-direction printing approach as described in Chapter 4. Z-direction printing permitted the controlled spatial deposition of the layer-specific bioinks. 3D printing parameters for both PCL, chondral and osseous layers bioinks are summarized in Table 5.1. Post-bioprinting, bi-layered constructs were

Table 5-1 Summary of PCL and hydrogel bioinks printing parameters.

Printing Parameters	***FDM printing***	***Microextrusion printing***	
Material	PCL	alginate-gelMA IPN	RGD-γ irradiated alginate
Needle (Gauge)	30	23	25
Pressure (MPa)	0.1	0.13	0.03
Screw Speed (revs/m)	10	-	-
Temperature (°C)	86 (tank), 78 (needle)	13	-
Layer Thickness (mm)	0.1	-	-
Extrusion Speed (mm/s)	6	4	4

fully crosslinked with 45 mM $CaCl_2$ and UV light exposure for 15 and 20 mins respectively.

5.2.3 Isolation and expansion of MSCs and CCs

Bone marrow was removed from the femoral shaft of a porcine donor and washed in high-glucose Dulbecco's Modified Eagle Medium (hgDMEM) (Biosciences) supplemented with 10% foetal bovine serum (FBS), 1% penicillin (100 U/mL) – streptomycin (100 µg/mL) (all Bioscience) and amphotericin B (2.5 µg/mL) (Sigma-Aldrich). A homogenous cell suspension was achieved by triturating with a 18G needle. The solution was centrifuged twice at 650g for 5 min, with removal of the supernatant. The resultant cell pellet was triturated, and the cell suspension was filtered through a 40 µm cell sieve (Sarstedt). Cell counting was performed with trypan blue and acetic acid before plating at a density of 5 x 10^3 cells/cm^2 and maintained in a humidified chamber. Following colony formation, cells were trypsinized, counted and re-plated for a further passage at a density of 5 x 10^3 cells/cm^2. FGF-2 (Prospec-Tany TechnoGene Ltd) was added to the media which was changed twice weekly. Tripotentiality was confirmed prior to use as previously described (Vinardell et al., 2009).

Cartilage tissue from another porcine donor was rinsed with PBS, weighed and finely diced. Chondrocytes were isolated by digestion in hgDMEM containing 1% penicillin (100 U/mL) – streptomycin (100 µg/mL) and 8 mL/g of collagenase type II (350 U/mL) for 12-14 h under constant rotation at 37 °C. The resulting cell suspension was filtered through a 40 µm cell sieve, centrifuged and rinsed with PBS twice. Cell number and

viability were determined using a haemocytometer and 0.4% trypan blue staining. All expansion was conducted in hypoxic conditions and media was changed twice weekly.

5.2.4 *In vitro* culture conditions

3D bioprinted scaffolds were cultured for 6 weeks in chondrogenically defined media consisting of hgDMEM supplemented with 1% penicillin (100 U/mL) – streptomycin (100 µg/mL), sodium pyruvate (100 µg/mL), L-proline (40 µg/mL), L-ascorbic acid 2-phosphate (50 µg/mL), linoleic acid (4.7 µg/mL), bovine serum albumin (1.5 mg/mL), 1x insulin-transferrin-selenium, dexamethasone (100 nM) (all Sigma-Aldrich) and human TGF-ß3 (10 ng/mL) (Prospec-Tany TechnoGene Ltd). Media change was performed twice weekly. The oxygen tension was kept to 5% pO_2 for the first 3 weeks of culture, and then switched to 20% pO_2 for the final 3 weeks.

Two separate *in vitro* evaluations were carried out to study the effect of 1) using a co-culture of BMSCs and CCs in the chondral layer and BMSCs only in the osseous layer and 2) mechanical stimulation when BMSCs only were encapsulated within both the chondral and osseous layers of the constructs on matrix deposition. Constructs that received mechanical stimulation underwent unconfined dynamic compression immediately after printing, using a custom-built bioreactor system. A linear actuator was used to control the displacement of a porous flat-ended compression platen. BMSCs-laden constructs were placed onto a non-porous platen sitting in a glass dish and presenting small pins that served to anchor the constructs in place and prevent floating of the samples. The bioreactor unit was placed in a cell culture incubator where oxygen conditions could be controlled. Constructs underwent dynamic loading for 2 h/day (5 days/week) by applying a compressive strain of 10% at 1 Hz frequency. After each

loading session, the constructs were kept in the bioreactor dishes in culture medium under standard conditions.

5.2.5 Biochemical analysis

The biochemical content of all constructs was quantified. Samples were digested with papain (125 μg/mL) in 0.1 M sodium acetate, 5 mM L-cysteine-HCl, 0.05 M ethylene-diamine-tetracetic acid (EDTA) (all Sigma-Aldrich) and pH 6 under constant rotation at 60 °C for 18 h. DNA content was assessed using the Hoechst Bisbenzimide 33258 dye assay. The amount of sulphated glycosaminoglycans (sGAG) was measured using the dimethyl methylene blue-binding assay (DMMB) (Blyscan, Bicolor Ltd.). Total collagen content was determined by quantifying the hydroxyproline content using the (dimethylamino)benzaldehyde and chloramine T assay and a hydroxyproline to collagen ratio of 1:7.69.

5.2.6 Histological and immunohistochemical analysis

Scaffolds were fixed with 4% paraformaldehyde solution, dehydrated in graded series of ethanol, embedded in paraffin wax, sectioned at 8 μm and affixed to microscope slides. The sections were stained with Alcian Blue/Aldehyde Fuchsin, Picrosirius Red and Alizarin Red to assess for sGAG, collagen and calcium content.

Immunohistochemical technique was used to evaluate collagen types II and X. Sections were rehydrated and treated with chondroitinase ABC (Sigma-Aldrich) in a humidified environment at 37 °C to enhance permeability of the extracellular matrix. This was followed by incubation in goat serum to block non-specific sites and the relevant collagen type II (sc52658, 1:400) (mouse monoclonal; Santa Cruz Biotechnology) or collagen type X (ab49945, 1:200) primary antibodies (mouse monoclonal; Abcam) were

applied overnight at 4 °C. Treatment with peroxidase preceded the application of the secondary antibody (collagen type II, B7151, 1:300; collagen type X, ab49760, 1:200) at room temperature for 1 h. Thereafter, all sections were incubated with ABC reagent (Vectastain PK-400; Vector Labs) for 45 min. Finally, sections were developed with DAB peroxidase (Vector Labs) for 5 min. Positive and negative controls were included in the immunohistochemical staining protocols.

5.2.7 Live/dead confocal microscopy

Cell viability was evaluated 24 h post-printing using a Live/Dead assay kit (Bioscience). Bioprinted cell-laden scaffolds were rinsed with phenol free medium and incubated in a solution containing 4 µM ethidium homodimer-1 and 2 µM calcein for 1 h. Following incubation, the scaffolds were rinsed again and imaged with Olympus FV-1000 Point-Scanning Confocal Microscope t 488 and 543 nm channels. Cell viability was quantified using Image-J software.

5.2.8 Mechanical testing

Mechanical experiments were performed on the PCL chondral and osseous layers printed separately. Uniaxial unconfined compression tests were carried out in a PBS bath at room temperature (~25 °C) using a twin column Zwick universal testing machine (Zwick, Roell) equipped with a 200 N load cell. To ensure contact between the surface of the scaffolds (n = 4 per group) and the top compression platen, a preload of 0.5 N preload was applied to the PCL constructs. Samples were subjected to ramp compression with a speed of 1 mm/min until 10% strain. The ramp modulus was taken as the slope of the stress-strain curve between 2-8% strain.

5.2.9 Statistical analysis

Results are presented as mean ± standard deviation. Statistical analysis was performed with GraphPad (GraphPad Software, La Jolla California, USA). Experimental groups were analysed for significant differences using either a t-test or a general linear model for analysis of variance (ANOVA) and performing Tukey's post-test. For all comparisons, significance was accepted for $p \leq 0.05$.

5.3 Results

5.3.1 3D printing of fibre-reinforced hydrogels for osteochondral tissue engineering

Bi-layered PCL networks were generated using FDM by varying the geometry parameters within the construct to obtain a relatively soft chondral layer and a relatively stiff osseous layer (Figure 5.1a i, ii). Scanning Electron Microscopy (SEM) image shows a cross-section of the bi-layered PCL network where the interface between the chondral and osseous regions can be observed (Figure 5.1b). By altering fibre pattern and spacing, it was possible to generate two PCL structures differing significantly in compressive properties, as demonstrated by the difference in slope of the stress-strain curves (Figure 5.1c). As expected, the chondral layer of the PCL structure was softer with a ramp modulus of 0.192 ± 0.02 MPa (blue bar; Figure 5.1d) which is mimetic of the compressive properties of articular cartilage (Beck et al., 2016a; Little et al., 2011; Shepherd et al., 1997). The osseous layer was noticeably stiffer with a ramp modulus of 13.79 ± 2.48 MPa (grey bar; Figure 5.1d) which is in the range of compressive properties for hypertrophic cartilage (Mente et al., 1994).

Microextrusion printing was used to deposit layer-specific cell-laden bioinks. A microscopic image of the resulting biphasic composite construct is shown in Figure 5.1e. The chondral region (top 3 mm) of the bi-layered PCL scaffold was filled with an alginate-GelMA IPN hydrogel (optimized in Chapter 4) seeded either with a co-culture of BMSCs and CCs (Study 1; Figure 5.1f i) or with BMSCs only (Study 2; Figure 5.1g i), while the osseous region (bottom 3 mm) of all constructs was filled with an RGD-γ irradiated alginate hydrogel seeded with BMSCs only (Study 1; Figure 5.1f ii, and Study 2; Figure 5.1g ii).

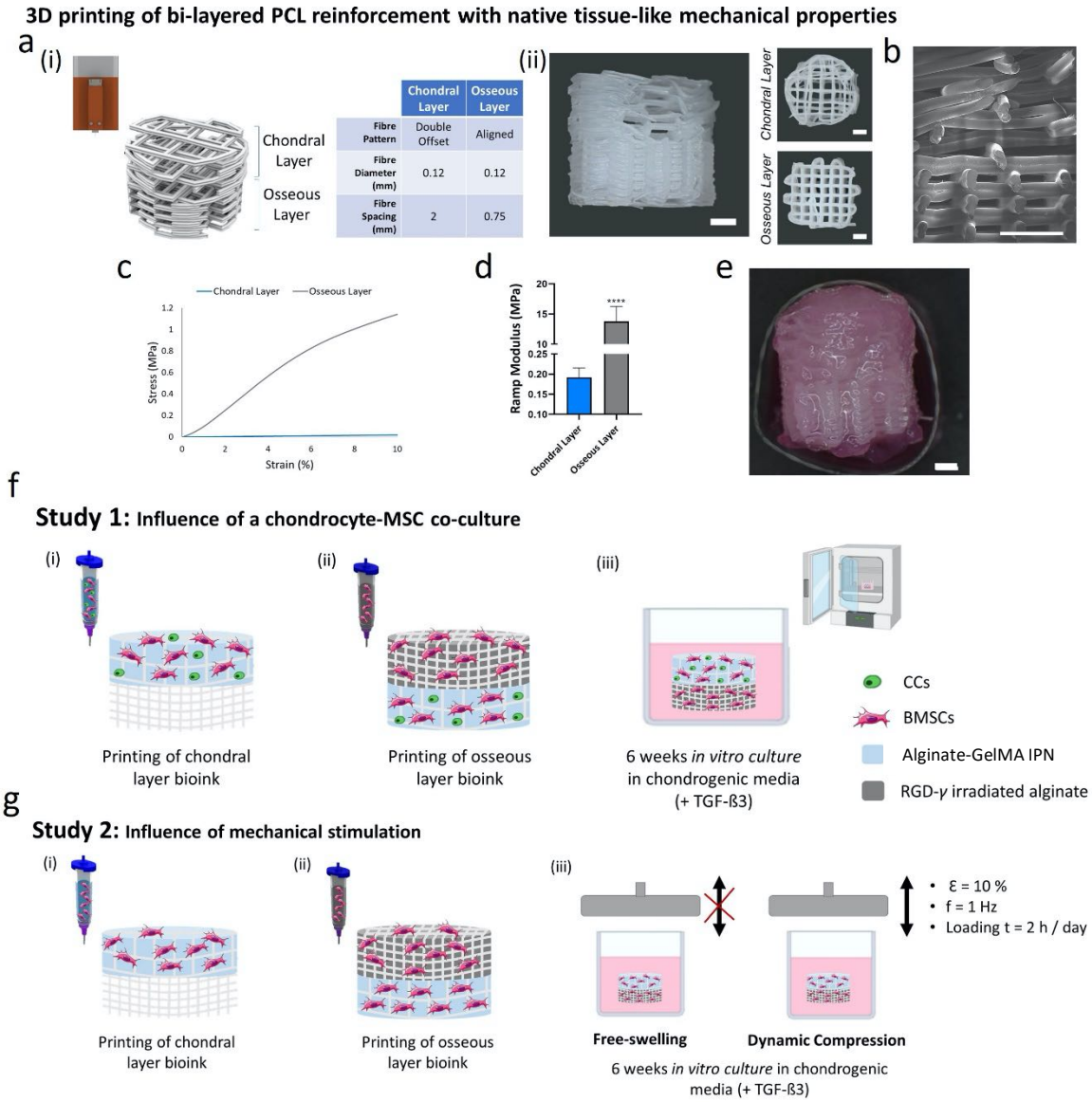

Figure 5-1 Summary of the experimental plan and mechanical characterization of the PCL reinforcement networks. (a) (i) Schematic of the bi-layered 3D PCL network and description of the geometry parameters characterizing the chondral and osseous layers of the PCL scaffold. (ii) Macroscopic images of frontal, top (chondral layer) and bottom (osseous layer) views of the biphasic PCL reinforcement. (b) SEM image showing the PCL bi-layered scaffold in cross-section. (c) Representative compressive stress-strain curves and (d) ramp modulus for the chondral (blue bar) and osseous (grey bar) PCL structures. (e) Macroscopic image of a bi-layered construct after incorporating layer-specific bioinks. (f) Schematic of the steps to assess the influence of a chondrocyte-MSC co-culture (Study 1). To form the composite constructs, (i) an alginate-GelMA IPN bioink (blue) encapsulating a co-culture of BMSCs and CCs was deposited within the chondral layer and (ii) an RGD- γ irradiated alginate bioink (grey) containing BMSCs only was printed within the osseous layer; (iii) composite constructs were cultured *in vitro* for 6 weeks for the first 21 days at 5% O_2 and the following 21 days at 20% O_2. (g) Schematic of the steps to assess the influence of mechanical stimulation (Study 2). To form the composite constructs, BMSCs only were encapsulated in both (i) an alginate-GelMA IPN bioink (blue) for the chondral layer and (ii) an RGD- γ irradiated alginate bioink (grey) for the osseous layer; (iii) composite constructs were cultured *in vitro* for 6 weeks either in static or dynamic conditions for the first 21 days at 5% O_2 and the following 21 days at 20% O_2. Scale bars: 1 mm.

5.3.2 Study 1: 3D bioprinting of layered constructs with spatially distinct cell populations

This thesis next sought to determine whether printing a co-culture of BMSCs and CCs into the top chondral layer could support the engineering of phenotypically stable articular cartilage. Cell viability was assessed 1 day after bioprinting, with live/dead staining (Figure 5.2a) demonstrating approximately 90% cell viability in both the chondral and osseous layers (Figure 5.2b). To determine the effect of depositing distinct cell populations in the two layers of the construct on matrix deposition, the bioprinted constructs were next cultured *in vitro* for 6 weeks (Figure 5.1f).

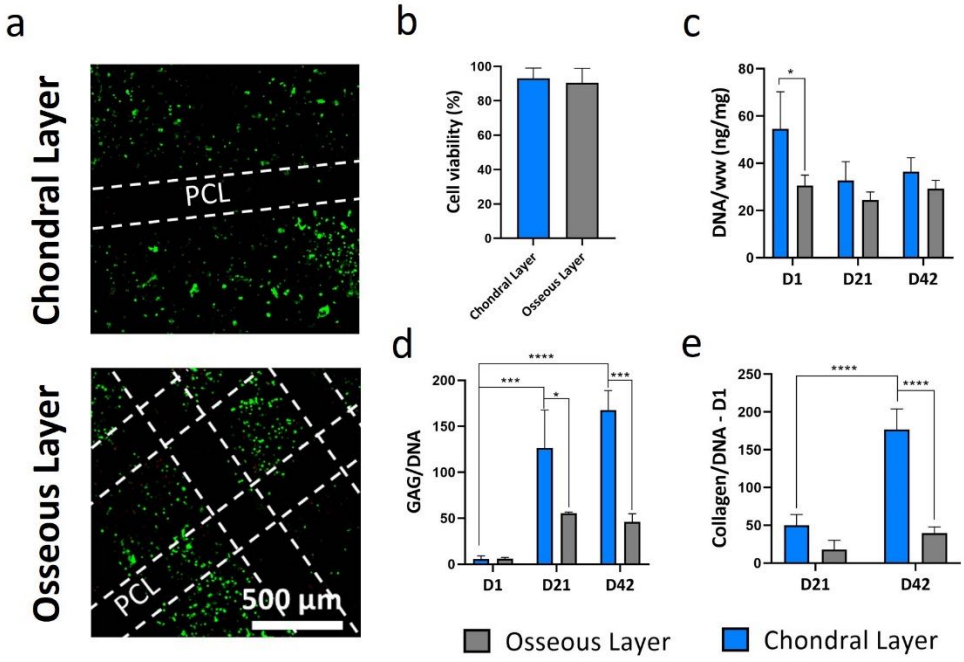

Figure 5-2 (a) Live/dead images of the BMSCs and CCs-laden chondral layer bioink (top) and BMSCs-laden osseous layer bioink (bottom) (b) Quantitative analysis of the cell viability for the chondral (blue bar) and osseous (grey bar) layers. (c) DNA content normalized per wet weight, (d) GAG/DNA and (e) collagen/DNA after 1, 21 and 42 days *in vitro*. ****$p < 0.0001$, ***$p < 0.001$ and *$p < 0.05$.

The bi-layered, PCL-reinforced bioinks supported robust chondrogenesis, as evident by abundant cartilage matrix deposition throughout the constructs (Figure 5.2c-e). The co-culture in the chondral layer stimulated the production of higher levels of GAG (Figure 5.2d) and collagen (Figure 5.2e) deposition compared to the BMSCs in the osseous layer. The histological analysis confirmed these findings, with the chondral layer staining more intensely for Alcian Blue/Aldehyde Fuchsin compared to the osseous layer (Figure 5.3a). Some evidence of calcium deposits was observed in the osseous layer, whereas the chondral layer stained negative for Alizarin Red (Figure 5.3b). Picrosirius Red staining was homogeneous throughout the construct (Figure 5.3c), with both layers staining positive for collagen type II (Figure 5.3d). Only the osseous layer stained positively for the hypertrophic marker collagen type X (Figure 5.3e).

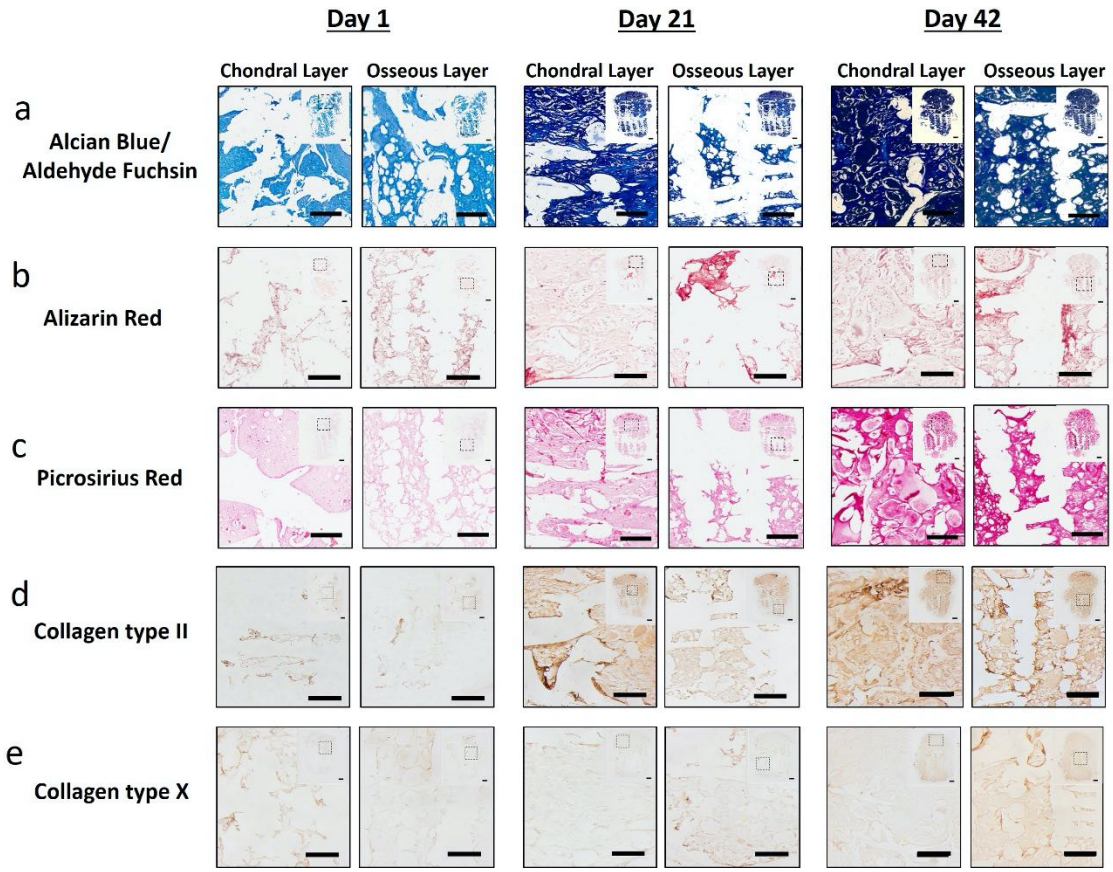

Figure 5-3 Histological and immunohistochemical analysis of chondral and osseous layers showing (a) Alcian Blue/Aldehyde Fuchsin, (b) Alizarin Red, (c) Picrosirius Red, (d) collagen type II and (e) collagen type X after day 1, 21 and 42 of *in vitro* culture. Scale bar: 500 µm.

5.3.3 Study 2: The influence of dynamic compression on matrix deposition within bi-layered PCL reinforced cell-laden hydrogels

This thesis next sought to determine whether the application of dynamic compression to bi-layered constructs containing only BMSCs would support the development of spatially distinct cellular phenotypes within the two regions of the construct. As the top chondral layer is over 50 times less stiff than the underlying osseous layer, BMSCs in this region will experience significantly larger deformation compared to cells in the osseous layer, which will be subjected to relatively little mechanical stimulation. The bioprinting process did not affect cell viability in either of the layers of the bi-layered

constructs (Figure 5.4a), with approximately 80% BMSCs viability in both the chondral and osseous layers at day 1 (Figure 5.4b). To determine the effect of mechanical stimulation on matrix deposition, the bioprinted constructs were cultured *in vitro* for 6 weeks in either free-swelling or dynamic culture conditions (Figure 5.1g).

There was a trend toward higher levels of collagen and GAG production in the chondral layer (Figure 5.4d, e) of dynamically stimulated (white bars) constructs after 42 days *in vitro*. The chondral layer of dynamically compressed constructs stained more intensely for Alcian Blue/Aldehyde Fuchsin compared to those maintained in static culture (Figure 5.5a). Conversely, the staining for cartilage matrix components in the osseous layer was comparable in both culture conditions (Figure 5.5a). There were no dramatic differences in Picrosirius Red staining for collagen deposition between the chondral layers of scaffolds subjected to either static or dynamic culture, whereas the osseous layer of samples cultured in static conditions stained more intensely for collagen deposition (Figure 5.5b). Positive staining for Alizarin Red was observed in the core region of both chondral and osseous layers of constructs cultured in static conditions (Figure 5.5c). In contrast, dynamic stimulation suppressed calcium deposition in both chondral and osseous layers of the samples (Figure 5.5c).

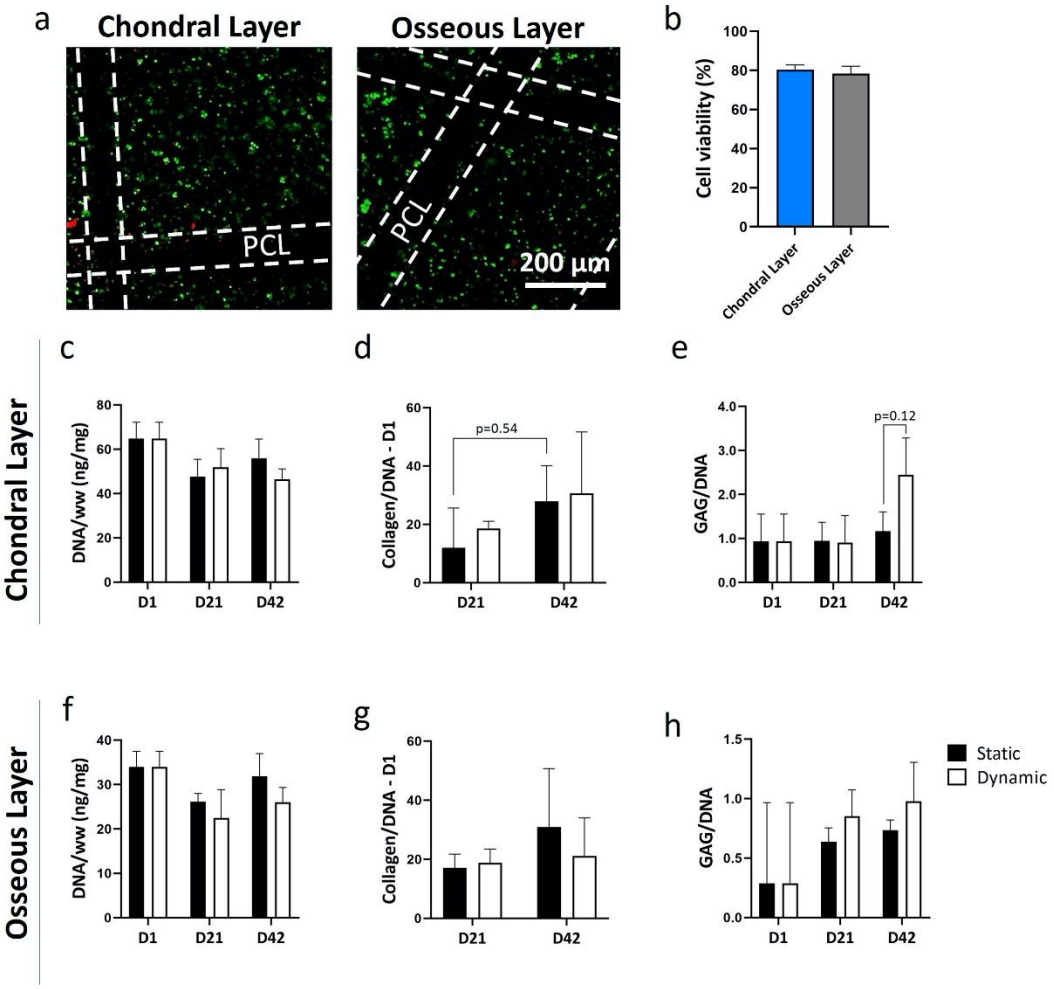

Figure 5-4 (a) Live/dead images of the BMSCs-laden chondral (top) and osseous (bottom) layers bioinks. (b) Quantitative analysis of the cell viability for the chondral (blue bar) and osseous (grey bar) layers. Biochemical analysis of the (c-e) chondral and (f-h) osseous layers in BMSCs only-laden biphasic composites comparing static and dynamic conditions after 1, 21 and 42 days *in vitro*. Quantification of (c, f) DNA content normalized per wet weight, (d, g) collagen/DNA and (e, h) GAG/DNA in the (c-e) chondral and (f-h) osseous layers of the bi-layered constructs.

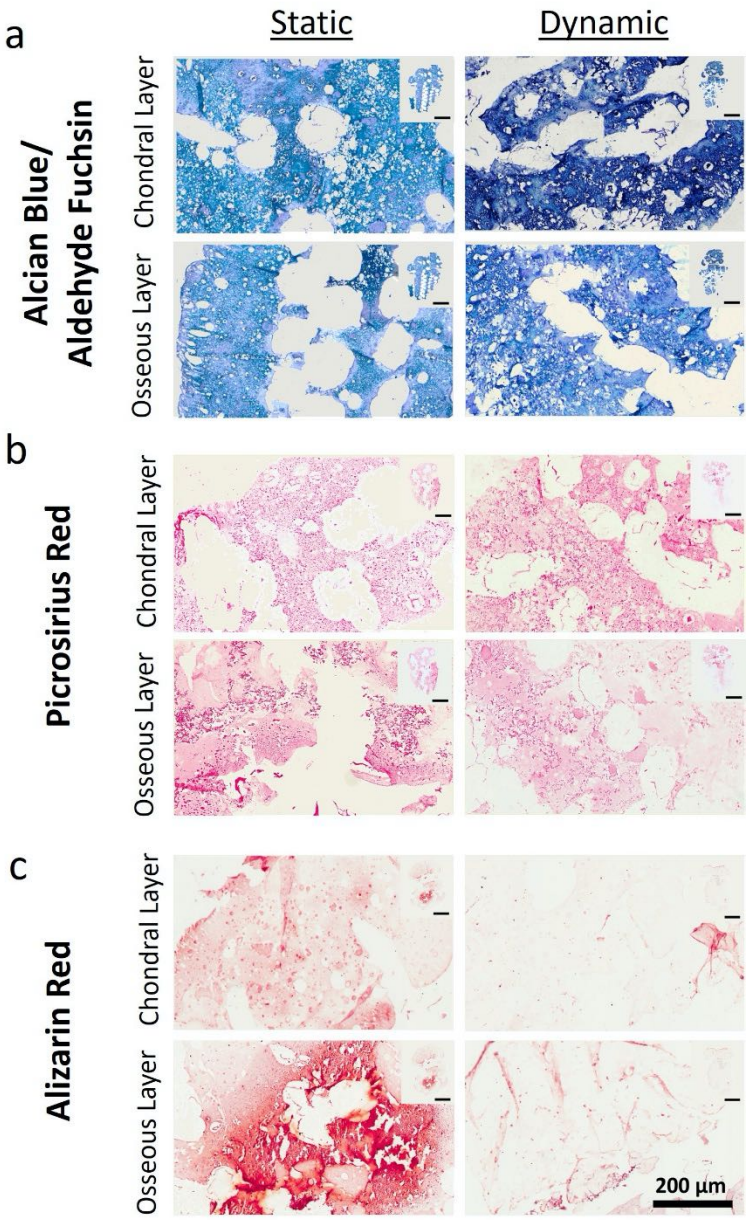

Figure 5-5 Histological analysis of chondral and osseous layers containing BMSCs only in static and dynamic culture conditions showing (a) Alcian Blue/Aldehyde Fuchsin, (b) Picrosirius Red and (c) Alizarin Red after 42 days of *in vitro* culture.

5.4 Discussion

Tissue engineering aims to regenerate damaged tissues by developing biological substitutes able to restore and maintain tissue function. Regardless of the tissue type, a

number of key considerations must be taken into account in order to engineer such functional biological substitutes. Cell population and mechanical factors are important parameters that have been shown to influence the structure and function of engineered tissues (O'Brien et al., 2011; Plunkett et al., 2011; Seo et al., 2014). In cartilage tissue engineering, the use of co-cultures has received increased interest for two main reasons: 1) the availability of chondrocytes is limited and 2) the observation that MSCs tend to form hypertrophic cartilage tissue with inferior biochemical and biomechanical properties. From a mechanical standpoint, scaffolds need to possess adequate biomechanical properties to function within a challenging load bearing environment, but must also transfer appropriate biophysical cues to seeded cells to ensure their tissue-specific differentiation. Cyclic unconfined compression has been one of the most investigated systems of mechanical stimulation to influence the fate of undifferentiated MSCs (Huang et al., 2004; Mauck et al., 2002; O'Conor et al., 2013; Terraciano et al., 2007).

The overall aim of this study was to determine the impact of either 1) cell population or 2) mechanical stimulation when developing functional constructs for osteochondral tissue engineering. To this end, a multi-tool biofabrication strategy was used to develop a bi-layered construct reinforced with a fibrous PCL network, where the internal architecture was tuned to obtain constructs with hyaline cartilage- and hypertrophic cartilage-like mechanical properties for the chondral and osseous layers of the constructs, respectively. Moreover, microextrusion printing parameters were tailored to precisely control the spatial deposition of layer-specific cell-encapsulated bioinks (i.e. alginate-GelMA IPN hydrogel for the chondral layer and RGD-γ irradiated alginate hydrogel for the osseous layer) into the osteochondral construct. Two strategies were used to engineer

osteochondral tissue *in vitro* for 6 weeks in the presence of chondrogenic media (containing TGF-ß3). 3D bioprinted bi-layered composites contained either 1) a co-culture of BMSCs and CCs in the chondral layer and BMSCs only in the osseous layer cultured in static conditions or 2) BMSCs only in both chondral and osseous layers cultured in either static or dynamic conditions. Overall, it was found that the co-culture of BMSCs and CCs within the chondral layer promoted the development of a hyaline cartilage-like matrix, that stained negative for hypertrophic markers. Dynamic compression provided an alternative mechanism to engineer phenotypically stable cartilage. BMSCs in both chondral and osseous layers produced a calcified matrix when cultured in static conditions, with the application of dynamic compression suppressing the formation of such calcium deposits throughout the construct.

Previous studies have demonstrated that the use of co-cultures of MSCs and CCs can increase the production of cartilage ECM both *in vitro* (Acharya et al., 2012; Bian et al., 2011; Critchley et al., 2018b; Meretoja et al., 2012; Mesallati et al., 2017; Mesallati et al., 2015; Wu et al., 2011) and *in vivo* (Dahlin et al., 2014; Liu et al., 2010; Mesallati et al., 2015; Sabatino et al., 2015). It has been reported that this is due to two related phenomena: MSCs secreting factors such as TGF-ß3, IGF-1, FGF-1 and FGF-2 that drive the proliferation of CCs, and CCs stimulating MSCs chondrogenesis (Acharya et al., 2012; Wu et al., 2013; Wu et al., 2011). Furthermore, co-culture of BMSCs and CCs seemed to play a role in suppressing hypertrophy by significantly reducing mineralization in cartilaginous constructs (Acharya et al., 2012; Bian et al., 2011; Fischer et al., 2010; Kang et al., 2012). This is in agreement with our work where the BMSCs and CCs co-culture in the chondral layer stimulated significantly more robust chondrogenesis compared to BMSCs only in the osseous layer. Moreover, the co-culture appeared to

inhibit hypertrophy and mineralization in the chondral layer as evidenced by the negative staining for collagen type X and Alizarin Red, which was not the case for scaffolds where the chondral layer was seeded with BMSCs only.

Dynamic loading was initiated immediately after printing of BMSC-laden bioinks in the bi-layered PCL network. While the application of dynamic compression had no statistically significant effect on sGAG or collagen deposition, there was a trend towards higher levels of sGAG in the chondral region of compressed constructs which was also observed histologically. This relatively moderate response to mechanical stimulation could possibly be explained by the fact that the external loading was applied shortly after BMSCs encapsulation, meaning that cells were still at an early stage in the differentiation process and perhaps not responding to biophysical stimulation as expected. Earlier studies have demonstrated that initiating the loading soon after cell seeding could have a detrimental effect on cartilage-specific matrix production, with BMSCs response to dynamic compression varying during the process of chondrogenesis (Huang et al., 2010; O'Conor et al., 2013; Thorpe et al., 2010; Thorpe et al., 2008). In contrast, dynamic loading was shown to significantly enhance MSCs chondrogenesis in the presence of growth factors if applied after a chondrogenic preculture period. Mouw et al. (Mouw et al., 2007) reported that when dynamic loading was introduced after preculturing agarose gels containing BMSCs in chondrogenic media for 16 days, there was an increase in aggrecan and Col2α1 gene expression and GAG synthesis. In another study, Thorpe et al. (Thorpe et al., 2010) observed that the application of dynamic compression after 21 days of chondrogenic differentiation did not inhibit chondrogenesis of MSCs showing a trend toward higher levels of GAG/DNA compared to constructs that were subjected to loading from day 0.

Dynamic compression was found to suppress calcium deposition throughout the bi-layered constructs. Other studies have also observed that dynamic compression can suppress hypertrophy and progression along an endochondral pathway (Bian et al., 2012; Thorpe et al., 2013a). Given that the osseous layer was dramatically stiffer than the chondral layer, and hence the levels of mechanical stimulation noticeably lower, it might have been expected that this suppression of hypertrophy would have been confined to the chondral layer of the implant. This suggests that MSCs are either sensitive to the relatively low levels of mechanical stimulation in the osseous layer, or that soluble factors secreted by MSCs in the chondral layer in response to the higher levels of mechanical stimulation were also influencing cells in the osseous region. Beside the duration of preculture and application of growth factors, the response of MSCs can potentially be modulated by varying loading parameters and the mechanical properties of the substrate in which cells are encapsulated. Further studies are required to investigate these hypotheses.

5.5 Conclusion

To conclude, 3D bioprinting was successfully used to engineer bi-layered PCL reinforced composites with layer-specific cell-laden bioinks for osteochondral tissue engineering. The effect of utilizing specific cell populations or mechanical stimulation, key factors for developing functional engineered tissues, has been investigated. While both approaches showed promise, further work is clearly required to identify the combination of scaffold spatial mechanical properties and extrinsic mechanical stimulation protocols to engineer bi-layered constructs with spatially distinct tissue phenotypes. In contrast, simply printing

a co-culture of BMSCs and CCs provides a robust approach to engineering phenotypically stable articular cartilage onto the surface of osteochondral implants.

Chapter 6
3D bioprinting of osteochondral implants for biological joint resurfacing

6.1 Introduction

Osteoarthritis (OA) is a chronic degenerative disease that involves the entire synovial joint, including the articular cartilage, subchondral bone and synovium (Escobar Ivirico et al., 2017; Glyn-Jones et al., 2015; Kuyinu et al., 2016). It affects about 3.8% of the population globally representing a substantial and increasing health burden worldwide (Hawker et al., 2019). OA is typically associated with aging of the population and obesity, although lately it is also frequently affecting younger and more active individuals (Buckwalter et al., 2006; Gioe et al., 2007). While focal cartilage and osteochondral defects can be repaired surgically to improve joint function (at least in the short-medium term), the only solution for end-stage OA is total knee arthroplasty (TKA) to replace the diseased joint with a permanent implant (Angele et al., 2016; Gomoll et al., 2012). Despite the fact that TKA is well established, complications such as loosening, wear and osteolysis that could necessitate a second more complex surgery are not uncommon (Keeney et al., 2011; Schiavone Panni et al., 2009). Therefore, there has been increased interest in exploring new regenerative approaches that could delay or ideally prevent the need for TKA.

Significant advances have been made in the field of tissue engineering with numerous studies demonstrating that cartilage- and bone-like tissues can be engineered using specific combinations of biomaterials, cells and bioactive factors. For engineering

complex biological interfaces such as the osteochondral unit, multiphasic scaffolds or hydrogels have shown promise for osteochondral tissue engineering (Cunniffe et al., 2019; Ding et al., 2013; Grayson et al., 2010; Lee et al., 2010; Mano et al., 2008; Melchels et al., 2011; Mesallati et al., 2015; Santo et al., 2013; Sheehy et al., 2013). Stratified biomaterial scaffolds can provide an adequate 3D environment for cellular distribution, proliferation and differentiation due to their biocompatibility and biomimetic features (Liu et al., 2013). However, the fabrication of multiphasic scaffolds that can provide mechanical stability while successfully controlling the production of native-like tissue remains a significant challenge, especially when the ultimate goal is to regenerate a whole articular joint. The ideal tissue engineered implant for the repair and regeneration of large osteochondral defects must fulfil specific criteria. The engineered scaffold must be able to stimulate the production of hyaline cartilage-like tissue and mineralized bony tissue simultaneously; provide mechanical functionality immediately after implantation; and fit the often anatomically complex shape and size of the defect to be treated (Jiang et al., 2010; Liu et al., 2013; O'Brien et al., 2011).

The aforementioned scaffold requirements could potentially be achieved by using multiple-tool bioprinting strategies to spatially pattern specific combinations of biomaterials, cells and growth factors in 3D space (Daly et al., 2017a; Mouser et al., 2016; Murphy et al., 2014a; Schon et al., 2016). In the context of entire joint regeneration, small number of studies have explored the use of Fused Deposition Modelling (FDM) to produce anatomically defined scaffolds. Biphasic scaffolds matching the geometry of the femoral head were fabricated by seeding chondrocytes into a chondral region fabricated from poly(lactic-co-glycolic acid) (PLGA) and bone marrow-derived stromal cells (BMSCs) into an osseous region fabricated from polycaprolactone (PCL)/hydroxyapatite

(HA) (Ding et al., 2013). Following subcutaneous implantation, histological analysis showed deposition of specific cartilage and bone extracellular matrix (ECM) as well as good integration at the osteochondral interface. In another study, micro computed tomography (CT) was used to create 3D printed anatomically accurate scaffolds using poly(ethylene glycol)-terephthalate/poly-(butylene terephthalate) (PEGT/PBT) to replace both the femoral head and the tibial plateau in a lapine model (Woodfield et al., 2009). Rabbit chondrocytes (CCs) were seeded onto the constructs and cultured for 5 weeks *in vitro* before implantation. Post-implantation, histological evaluation of the joint demonstrated that fibrous-like tissue had formed throughout with little evidence of a hyaline cartilage layer, highlighting the challenge of regenerating hyaline cartilage when resurfacing an entire joint surface. FDM has also been used to produce PCL/HA scaffolds for resurfacing the rabbit proximal humeral joint (Lee et al., 2010). The anatomically shaped porous constructs were infused with transforming growth factor- ß3 (TGF-ß3). 4 months post-implantation, hyaline-like cartilage was found covering the surface of the scaffolds while blood vessels were observed in the osseous region. This study demonstrated that the incorporation of bioactive factors in 3D printed constructs is a promising strategy for biological joint resurfacing.

In this chapter, PCL reinforced bioinks functionalized with different growth factors were used to 3D print: 1) a biphasic construct to treat large osteochondral defects in the knee condyle of goats and 2) a scaled up, anatomically shaped bi-layered prosthesis for whole joint resurfacing which was tested in a pilot study in the glenohumeral (shoulder) joint of rabbits. To promote the formation of articular cartilage, a sulfated alginate-gelatin methacryloyl (GelMA) interpenetrating network (IPN) bioink containing BMSCs and TGF-ß3 was deposited within the chondral layer of the implants. For the osseous region,

an acellular RGD- γ irradiated alginate-based bioink containing either vascular endothelial growth factor (VEGF) or bone morphogenetic protein-2 (BMP-2) was microextruded in the centre and periphery of the osseous layer, respectively. Given the challenging mechanical environment both implants will experience *in vivo*, the PCL reinforcement was designed with the goal of providing adequate local and global mechanical properties as well as an appropriate fixation to facilitate the implantation of the anatomically shaped prosthesis. For both animal models, constructs did not receive any *in vitro* priming and were implanted the day after fabrication. Finally, the efficacy of this tissue engineering approach was assessed 1) after 6 months in a caprine model of osteochondral defect regeneration in the femoral condyle and 2) after 3 months in a pilot-lapine model study of humeral head regeneration through micro CT, histological and immunohistochemical analysis.

6.2 Materials and methods

6.2.1 Isolation and expansion of BMSCs

BMSCs were isolated from the femoral shaft of either goats or rabbits, and expanded in high glucose Dulbecco's Modified Eagle's Medium (hgDMEM) GlutaMAX supplemented with either 10% v/v goat or rabbit serum, 10% v/v FBS, 100 U/mL penicillin, 100 µg/mL streptomycin, 2.5 µg/mL amphotericin B at 5% pO2 (all Gibco, Biosciences, Dublin, Ireland). Following colony formation, MSCs were trypsinized, counted, seeded at density of 5000 cells/cm^2 in 500 cm^2 triple flasks (Thermo Fisher Scientific), supplemented with hgDMEM, 10% v/v FBS, 100 U/mL penicillin, 100 µg/mL streptomycin, 2.5 µg ml/mL amphotericin B, and 5 ng/mL human fibroblastic

growth factor-2 (FGF-2; Prospec-Tany TechnoGene Ltd., Israel) and expanded to passage 2 at 5% pO2.

6.2.2 Materials preparation

Chondroinductive bioink

GelMA was produced according to a previously reported protocol (Van Den Bulcke et al., 2000b). GelMA was synthesized by reaction of porcine type A gelatin (Sigma Aldrich) with methacrylic anhydride (Sigma Aldrich) at 50 °C for four hours. Methacrylic anhydride was added to a 10% solution of gelatin in PBS under constant stirring. To achieve a high degree of functionalization, 0.6 g of methacrylic anhydride was added per gram of gelatin. The functionalized polymer was dialyzed against distilled water for 7 days at 40 °C to remove methacrylic acid and anhydride, freeze-dried and stored at −20 °C until use.

The sulfation of alginate was performed following a previously described protocol (Freeman et al., 2008). Briefly, 0.6 g of alginate (LVG, Pronova, MW = ~75 kDa) was dissolved at 0.2% w/v in deionized water at 4 °C. Then, 20 g of Dowex-X8 ion exchange resin (100-200 mesh, H+ form) (Sigma-Aldrich) was added to the alginate solution and stirred for 30 mins. After centrifugation of the obtained mixture, the supernatant was collected, and the pH adjusted to approximately 6.0 using tributylamine (TBA) (Sigma-Aldrich). The solution was then filtered and lyophilized to obtain TBA-alginate. Next, 0.6 g of TBA-alginate was resuspended in 200 mL of Dimethylformamide (DMF)/sulfuric acid (H_2SO_4) solution, followed by the addition of 12 g of N, N'-dicyclohexylcarbodiimide (DCC) (Sigma-Aldrich) and stirring for 2 h at room temperature. At the end of the reaction, the solution was filtered to separate the precipitate

from the filtrate. The filtrate was mixed with three equal volumes of dichloromethane (Sigma-Aldrich), from which a second precipitate was collected. These precipitates were further dissolved in 0.5 N sodium hydroxide (NaOH) (Sigma-Aldrich) for 30 mins. This time the precipitate was discarded, while the filtrate was dialyzed against deionized water for 3 days and lyophilized to obtain the sulfated alginate.

To produce the chondroinductive bionk GelMA, normal alginate and sulfated alginate were dissolved in sterile hgDMEM to obtain GelMA at a concentration of 30.8% w/v, and both normal alginate and sulfated alginate at a concentration of 3.08% w/v. Prior to bioprinting, these three components were mixed with Irgacure (photoinitiator), BMSCs and TGF-ß3 (Peprotech, UK) to obtain final concentrations of 10% w/v of GelMA, 1% w/v of normal alginate-sulfated alginate, 0.05% v/v of Irgacure, 5 µg/mL of TGF-ß3 and cell density of $20x10^6$ cells/mL.

Osteoinductive and vascular bioinks

Low-molecular-weight sodium alginate (58,000 g/mol) was prepared by irradiating sodium alginate (Protanal LF20/40, 196,000 g/mol; Pronova Biopolymers, Oslo, Norway) at a gamma dose of 5 Mrad as previously described (Jeon et al., 2010). RGD-modified (arginine-glycine aspartic acid) alginate was prepared by coupling the GGGGRGDSP to the alginate by carbodiimide reaction chemistry.

The base bioink to produce the osteoinductive and vascular bioinks was prepared by dissolving RGD-γ irradiated alginate in sterile hgDMEM to make up a concentration of 3.5% w/v. To increase the viscosity of the bioink to make it printable, sterile methylcellulose (Sigma-Aldrich) was added to a 3.5% alginate solution of RGD-γ irradiated alginate at a ratio of 1:2 w/w (methylcellulose:alginate). To create the

osteoinductive bioink, laponite (Laponite XLG, BYK Additives & Instruments, UK) was added to the alginate-methylcellulose hydrogel at a ratio of 6:1 w/w. Prior to bioprinting, 12 µg/mL of BMP-2 (Peprotech, UK) were added to the osteoinductive hydrogel using a dual syringe approach. The bioink was then pre-crosslinked with 60 mM $CaSO_4$ (7:3, v/v bioink:$CaSO_4$) for 15 mins at 37°C. To obtain the vascular bioink, nano-sized hydroxyapatite (nHA) particles were prepared according to a previously described protocol (Cunniffe et al., 2010). nHA particles were then added to the alginate-methylcellulose bioink at a ratio of 1:1 w/w to facilitate the adsorption and immobilization of VEGF within the hydrogel due to the strong electrostatic attraction between nHA (Chen et al., 2014b). Prior to bioprinting, 5 µg/mL of VEGF (Gibco Life Technologies, Gaithersburg, MD, USA) were added to the vascular hydrogel using a dual syringe approach. The bioink was then pre-crosslinked with 60 mM $CaSO_4$ (7:3, v/v bioink:$CaSO_4$) for 30 mins at 37°C.

6.2.3 Implants design and 3D bioprinting

Both implants were 3D bioprinted using the 3D Discovery bioplotter purchased from RegenHU with spatial resolution of ± 5 µm. Implants consisted of porous PCL (CAPA 6500D, Perstorp, Mn = 50 kDa) networks printed *via* FDM and characterized by two different architectures for the chondral layer (2 mm high for the osteochondral plug and 0.6 mm high for the shoulder prosthesis) and the osseous layer (4 mm high for the osteochondral plug and 5 mm high for the shoulder prosthesis). The bi-layered PCL geometry used for the osteochondral plug derived from the outcomes of Chapters 3, 4 and 5. As replacing an entire joint means subjecting the 3D printed implant to a more challenging mechanical environment, the PCL design for the humeral head-shaped scaffold was refined through a series of improvements. Compared to the osteochondral

plug design, the shoulder implant was further reinforced by reducing the overall scaffold porosity. Moreover, the implant comprised of a 3D printed intramedullary stem for surgical fixation. Previously printed PCL scaffolds underwent NaOH treatment to improve surface hydrophilicity of the scaffold (5 M NaOH, overnight at room temperature), washed with absolute alcohol and PBS, and sterilized with EtO. Prior to bioinks printing, the PCL frames were placed in a custom-made moulding system that kept the scaffolds in place in the centre of the printing stage. This allowed for accurate spatial deposition of the bioinks through microextrusion bioprinting in the z-direction.

Table 6-1 Summary of FDM printing parameters for osteochondral plug and shoulder joint prosthesis.

Printing Parameters	***FDM printing***	
Implant type	Osteochondral plug	Joint prosthesis
Material	PCL	PCL
Needle (Gauge)	30	27
Pressure (MPa)	0.1	0.15
Screw Speed (revs/m)	10	16.4
Temperature (°C)	86 (tank), 78 (needle)	75 (tank), 80 (needle), 45 (printer stage)
Layer Thickness (mm)	0.1	0.197
Extrusion Speed (mm/s)	6	4.8

Bioinks were loaded into a pressure driven system to be bioprinted in the open pores of the PCL frames. The vascular and osteoinductive bioinks were printed within the centre and periphery of the osseous layer, respectively. The BMSC-laden chondroinductive bioink was bioprinted homogeneously throughout the chondral layer of the implants. Printing parameters for PCL and all bioinks are summarized in Table 6.1 and 6.2,

respectively. Post-printing, the implants were fully crosslinked with 60 mM $CaCl_2$ and UV light exposure for 15 and 20 min, respectively.

Table 6-2 Summary of microextrusion bioprinting parameters for the tissue-specific bioinks.

Printing Parameters	***Microextrusion bioprinting***		
Material	Vascular bioink	Osteoinductive bioink	Chondroinductive bioink
Needle (Gauge)	25	25	23
Pressure (MPa)	0.05	0.03	0.13
Temperature (°C)	-	-	13
Extrusion Speed (mm/s)	2	4	4

6.2.4 Mechanical testing

Mechanical characterization of both osteochondral plugs and shoulder joint implants was performed prior to implantation using a twin column Zwick universal testing machine (Zwick, Roell). All tests were carried out at room temperature (~25 °C) in a PBS bath using a 200 N load cell. To mimic the site of implantation *in vivo*, osteochondral plugs (n = 4) were tested in confined compression and subjected to a compressive strain cycle load up to 1000 cycles, where the chondral layer of the implant was compressed by 10% strain at 1 Hz frequency. Humeral head-shaped implants (n = 4) were tested in unconfined compression by applying 1000 compressive cycles at 15% strain at a frequency of 1 Hz. The permanent deformation experienced by the scaffolds upon loading application was evaluated.

6.2.5 *In vitro* culture conditions

3D bioprinted constructs, both osteochondral plugs and anatomically shaped implants, were cultured in growth medium at hypoxic conditions for the first 3 weeks of culture, and then switched at normoxic conditions for the final 3 weeks. Media change was performed twice weekly.

6.2.6 Biochemical analysis

To quantify the constructs' biochemical content, samples were digested with papain (125 µg/mL) in 0.1 M sodium acetate, 5 mM L-cysteine-HCl, 0.05 M ethylene-diamine-tetracetic acid (EDTA) (all Sigma-Aldrich) and pH 6 under constant rotation at 60 °C for 18 h. DNA content was assessed using the Hoechst Bisbenzimide 33258 dye assay. The amount of sulphated glycosaminoglycans (sGAG) was measured using the dimethyl methylene blue-binding assay (DMMB) (Blyscan, Bicolor Ltd.). Total collagen content was determined by quantifying the hydroxyproline content using the (dimethylamino)benzaldehyde and chloramine T assay and a hydroxyproline to collagen ratio of 1:7.69.

6.2.7 Histological and immunohistochemical analysis

In vitro samples were fixed in 4% paraformaldehyde solution, dehydrated in graded series of ethanol, embedded in paraffin wax, sectioned at 8 µm and affixed to microscope slides. The sections were stained with Alcian Blue/Aldehyde Fuchsin, Picrosirius Red and Alizarin Red to assess for sGAG, collagen and calcium content, respectively.

In vivo samples were fixed in 10% formalin (Sigma, Ireland) for 3 days under agitation at room temperature. The samples were decalcified using Decalcifying Solution-Lite (Sigma-Aldrich) for approximately 5 weeks. Samples were frequently x-

rayed to determine if any mineral content remained. When no mineral was visible the sample was considered decalcified. Decalcified samples were cut along the plane, dehydrated and paraffin wax embedded. Histological sections were cut to a thickness of 10 μm and stained with Safranin-O and Picrosirius Red to evaluate cell and tissue structure, presence of cartilage tissue and collagen content, respectively.

Collagen types II and X were identified through immunohistochemistry. Paraffinized samples were rehydrated and antigen retrieval was performed using chondroitinase ABC, 0.25 U/ml, (Sigma) at 37°C for 1 h. This was followed by incubation in a blocking buffer (10% goat (for *in vitro* samples) or donkey (for *in vivo* samples) serum and 1% BSA in PBS) to prevent binding of non-specific sites. Rinses were performed in between each step in PBS. The relevant primary anti-bodies for collagen type II (sc52658, 1:400, mouse monoclonal; Santa Cruz Biotechnology) and collagen type X (ab49945, 1:200, mouse monoclonal; Abcam) were applied overnight at 4°C. Endogenous peroxidase activity was blocked by submersing the slides in 3% hydrogen peroxide solution for 20 minutes in the dark. Then, the secondary antibody, (collagen type II, B7151, 1:300; collagen type X, ab49760, 1:200) was added for 1h at room temperature. Colour was developed using the Vectastain ABC reagent (Vectastain ABC kit: Vector Laboratories) for 45 min and exposure to peroxidase DAB substrate kit (Vector laboratories) for 5 min. Slides were dehydrated and mounted with Vectamount medium (Vector Laboratories). Positive and negative controls were included in the immunohistochemical staining protocol.

6.2.8 Live/Dead confocal microscopy

Cell viability was evaluated 24 h post-printing using a Live/Dead assay kit (Bioscience). Bioprinted cell-laden scaffolds were rinsed with phenol free medium and incubated in a solution containing 4 μM ethidium homodimer-1 and 2 μM calcein for 1

h. Following incubation, the scaffolds were rinsed again and imaged with Olympus FV-1000 Point-Scanning Confocal Microscope t 488 and 543 nm channels. Cell viability was quantified using Image-J software.

6.2.9 Surgical procedure

Osteochondral defect in a caprine model

The surgical procedure in a caprine model was carried out as previously described (Cunniffe et al., 2019; Levingstone et al., 2016). Briefly, skeletally mature (at least 2 years old) goats (n = 8) were sedated using diazepam (0.3-0.4 mg/kg IV) and butorphanol (0.2 mg/kg IV). Epidural was administered using morphine (0.2 mg/kg). Following placement of an intravenous catheter, anesthesia was induced with propofol (maximum dose 4 mg/kg IV). Anesthesia was maintained using isoflurane with ventilation to maintain normal end tidal CO_2 between 4.6 and 6 kPa. Isotonic fluids were provided at 10 ml/kg/h. Following induction of anesthesia, the goats were placed in dorsal recumbency and an arthrotomy of each stifle joint was then performed using the lateral para-patellar approach. A critically sized defect, 6 mm in diameter x 6 mm in depth, was created in each medial femoral condyle using a hand drill, a flattened drill bit and a depth guide. The joint was flushed with sterile PBS and the stifle joints were assigned to one of the two treatment groups: 1) Empty control and 2) 3D printed (3DP) bi-layered scaffold. The 3DP scaffold was press-fit into the defect site before routine closure of the joint capsule, subcutaneous tissues and skin. Morphine (0.1-0.2 mg/kg IM) and non-steroidal anti-inflammatory drugs (Carprofen (1.5-2.5 mg/kg subcutaneously) (Rimadyl)) were administered at the end of anesthesia. Following surgery, goats were housed in small indoor pens to allow skin incisions to heal and were allowed full weight bearing immediately. During this period the animals were closely monitored to ensure adequate

analgesia. Carprofen and antibiotics (Amoxicillin (Noroclav)) were administered for 5 days post-surgery. Two weeks post-operatively, following removal of sutures, animals were let out to pasture for the remainder of the study period. Euthanasia was carried out with an overdose of sodium pentobarbital (Euthatal) administered by IV injection after 6 months post-implantation to permit harvesting of the treated joints. Ethical evaluation and approval were administered by University College Dublin and the Health Products Regulatory Authority (HPRA), Ireland.

Total joint replacement in a lapine model

The surgical procedure in a lapine model was carried out similarly to a previously reported procedure (Lee et al., 2010). New Zealand white rabbits (n = 3; 12 weeks of age) were anesthetized with xylazine and buprenorphine and maintained using isofluorane and oxygen. The surgical site was prepared by shaving and washing with chlorhexidine surgical scrub and alcohol. Surgical drapes were used to cover the non-incision area. The acromial head of the deltoid muscle will be tenotomised at its origin and retracted distally with a craniolateral approach. The infraspinatus muscle was tenotomised at its insertion and retracted caudally. The lateral joint capsule was incised from cranial to caudal to expose the humeral head by internal rotation and complete lateral luxation. The humeral head of the right shoulder was resected using a surgical saw. To accommodate the stem of the implant, the medullary cavity was enlarged using a surgical drill with a diameter of 2.2 mm. The cavity was cleaned with sterile PBS prior to implanting the shoulder joint prosthesis by press-fitting. The joint capsule, infraspinatus and deltoid tendons were reattached using Ethicon 2-0 vicryl sutures, whereas the skin was closed with Ethicon 4-0 vicryl sutures. Post-surgery, rabbits were kept into individual pens for the first 5 weeks to facilitate joint stabilization with post-operative analgesia buprenorphine, given for 7

days. After the first 5 weeks, the animals were permitted to move freely until the end of the study. Rabbits were sacrificed after 3 months using sodium pentobarbital (Euthatal). This protocol and study were reviewed and approved by the ethics committee of Trinity College Dublin, Ireland and Health Products Regulatory Authority (HPRA), Ireland.

6.2.10 Macroscopic evaluation

Macroscopic evaluation of the joints was performed immediately upon opening the joint (Table 6.3) (Levingstone et al., 2016). 1.5 cm^3 sections containing the defect site were harvested, samples were fixed in formalin solution and the level of mineralization within the repaired tissue (5mm diameter cylindrical region) was quantified using micro CT (Scanco Medical, Switzerland) at a threshold of 210, corresponding to a density of

Table 6-3 Macroscopic scoring system for cartilage repair. Maximum score possible is 8.

Characteristic	Grading	Score
Edge integration (new tissue relative to native cartilage)	Full	2
	Partial	1
	None	0
Smoothness of cartilage surface	Smooth	2
	Intermediate	1
	Rough	0
Degree of cartilage filling	Flush	2
	Slight depression	1
	Depressed/overgrown	0
Colour of cartilage	Opaque	2
	Translucent	1
	Transparent	0

399.5 mg hydroxyapatite/cm^3. Bone density (bone volume (BV)/total volume (TV)) was calculated for two regions of interest named subchondral bone plate (SBP) and subarticular spongiosa (SAS), defined as the upper 1 mm and the bottom 3 mm of the bony region of the defect, respectively.

6.2.11 Statistical analysis

All statistical analysis was performed using GraphPad Prism 8.2.0. All values are reported as means ± standard deviation. Experimental groups were analysed for significant differences using either a t-test or a general linear model for analysis of variance (ANOVA) and performing Tukey's post-test. Significance for all statistical analysis was defined as $p \leq 0.05$.

6.3 Results

6.3.1 3D bioprinting osteochondral plugs through controlled spatial deposition of tissue-specific bioinks

Porous bi-layered PCL networks were 3D printed using FDM. To produce a softer network for the chondral layer and a stiffer region for the osseous layer, unique network designs were defined for each layer (Figure 6.1a i). The osseous layer of the implant was produced by printing an orthogonal array of PCL microfibres (120 µm diameter) with a filament spacing of 1.2 mm, while the chondral layer consisted of a *Double Offset* fibre pattern (described in Chapters 3, 4 and 5) with filament spacing of 2 mm. Prior to bioprinting of the bioinks, these PCL networks were placed in a custom-made moulding system that kept the scaffolds in place in the centre of the printing stage. This allowed for accurate spatial deposition of the bioinks through microextrusion bioprinting in the z-

direction (Figure 6.1a ii-iv). A chondroinductive bioink containing BMSCs and TGF-ß3 was microextruded homogeneously throughout the chondral layer of the implants (shown in pink; Figure 6.1a ii). A vascular bioink containing VEGF was microextruded within the central pores of the osseous layer (shown in red; Figure 6.1a iii), whereas an osteoinductive bioink containing BMP-2 was extruded within the rest of the pores of the osseous region (shown in yellow; Figure 6.1a iv). The final construct at the end of the printing process can be observed in Figure 6.1b. To assess their mechanical stability,

bioprinted constructs were subjected to cyclic testing in confined compression to mimic the conditions at the site of implantation (Figure 6.1c). Constructs underwent low

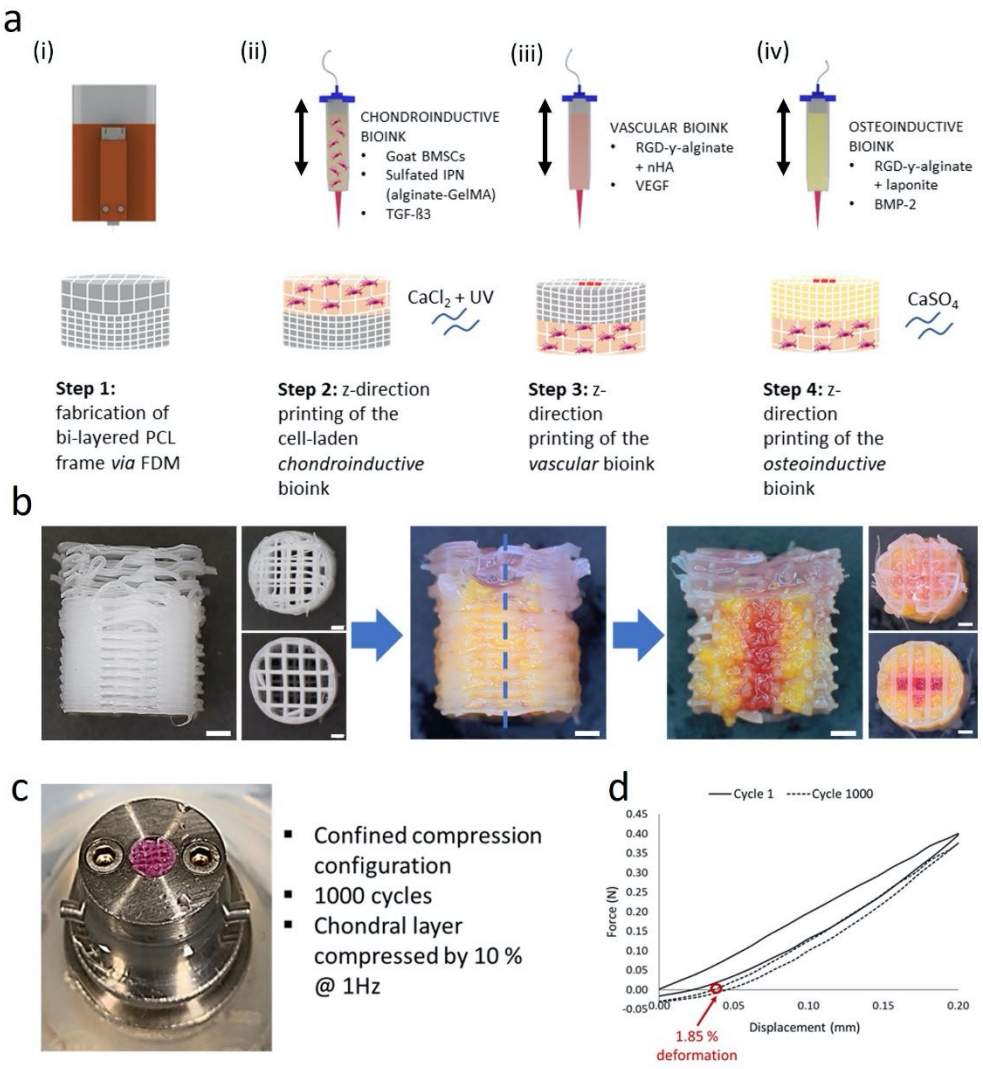

Figure 6-1 Summary of the printing approach and mechanical characterization of the obtained osteochondral plugs. (a) Schematic of the different steps to form 3DP bi-layered constructs: (i) the biphasic PCL network was produced *via* FDM; (ii) the BMSC-laden chondroinductive bioink (pink) was deposited within the chondral layer of the scaffold and crosslinked with $CaCl_2$ and UV light; finally the (iii) vascular (red) and (iv) osteoinductive (yellow) bioinks were microextruded in the centre and periphery of the osseous layer respectively, and crosslinked with $CaSO_4$. (b) Macroscopic images of the 3DP bi-layered PCL constructs before and after printing of the bioinks. Scale bar: 1 mm. (c) Macroscopic image of the mechanical testing set-up and protocol used to perform cyclic confined compression tests. (d) Representative force-displacement curves for the first (black solid line2) and last (black dashed line) applied cycles. The approximate permanent deformation experienced by the implant at the end of the test is also shown by the red circle.

permanent deformation of approximately 1.85% at the end of the tests, with low hysteresis observed during the unloading cycles (Figure 6.1d).

For *in vitro* evaluation, constructs were transferred to standard basal media and cultured for 42 days. Live/dead staining, immediately post-fabrication, indicated that BMSCs remained viable within the chondroinductive bioink (Figure 6.2a). Biochemical, histological and immunohistochemical evaluation after 3 and 6 weeks of *in vitro* culture demonstrated that the BMSCs had undergone chondrogenesis in the chondral layer of the scaffold (Figure 6.2b-e)). DNA (Figure 6.2b), sGAG (Figure 6.2c) and collagen (Figure 6.2d) content increased overtime. Histological staining for Aldehyde Fuchsin/Alcian

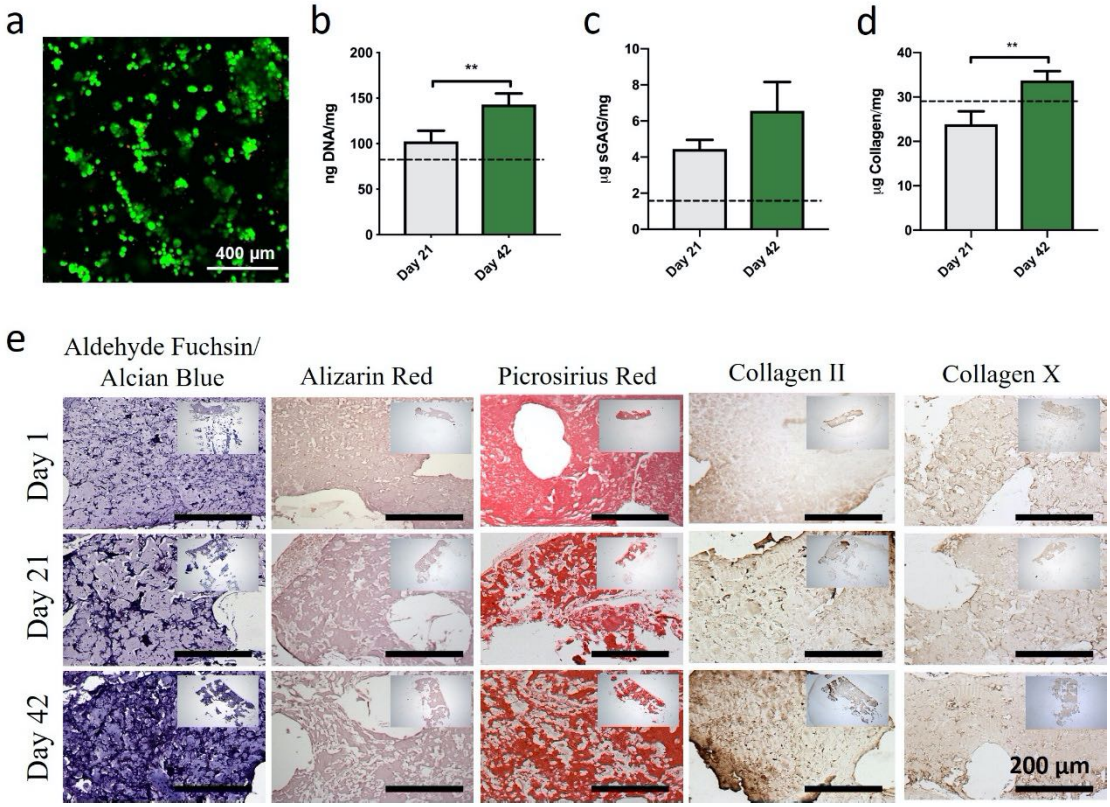

Figure 6-2 *In vitro* analysis. (a) Live/dead staining used to assess cell viability within the chondroinductive bioink post-printing. (b) DNA, (c) sGAG and (d) collagen content normalized to wet weight after 21 and 42 days. Values at day 1 are represented by the black dashed line. (e) Histological and immunohistochemical staining of the chondral layer after 1, 21 and 42 days of *in vitro* culture. **p<0.01.

Blue and Picrosirius Red along with immunohistochemical staining for collagen type II confirmed that cartilage-like matrix was deposited in the chondral layer (Figure 6.2e). No evidence of staining for Alizarin Red or collagen type X was observed in the chondral layer at any time point (Figure 6.2e).

For *in vivo* evaluation, constructs were produced the night before surgeries were performed in order to minimize growth factor release prior to implantation.

6.3.2 Macroscopic repair and micro CT assessment of bone regeneration in empty and treated osteochondral defects

To evaluate their regenerative capacity *in vivo*, the 3D bioprinted constructs were implanted into critically sized osteochondral defects (6 mm high x 6 mm diameter) created in the medial femoral condyles of goats (Figure 6.3a). 6 months after scaffold implantation, the quality of repair was compared to that of empty defects that received no implant. The macroscopic appearance of the defects left empty were compared to those treated with the 3DP bi-layered scaffolds (Figure 6.3b), with no significant difference in the macroscopic scoring observed between the two groups (empty = 4.22 ± 1.07, 3DP bi-layered scaffold = 2.82 ± 1.63) (Figure 6.3c). 3D reconstruction images obtained from micro CT scanning of the harvested osteochondral sections appeared to show better bone regeneration in the empty defects (Figure 6.3d), although gaps of varying size were observed in the repair bone of both groups. The BV quantified within both the SAS (bottom 3 mm of the bone region of the defect) and SBP (upper 1 mm of the bone region of the defect) regions of the defect was higher in empty controls compared to animals treated with the 3DP bi-layered scaffolds (Figure 6.3e).

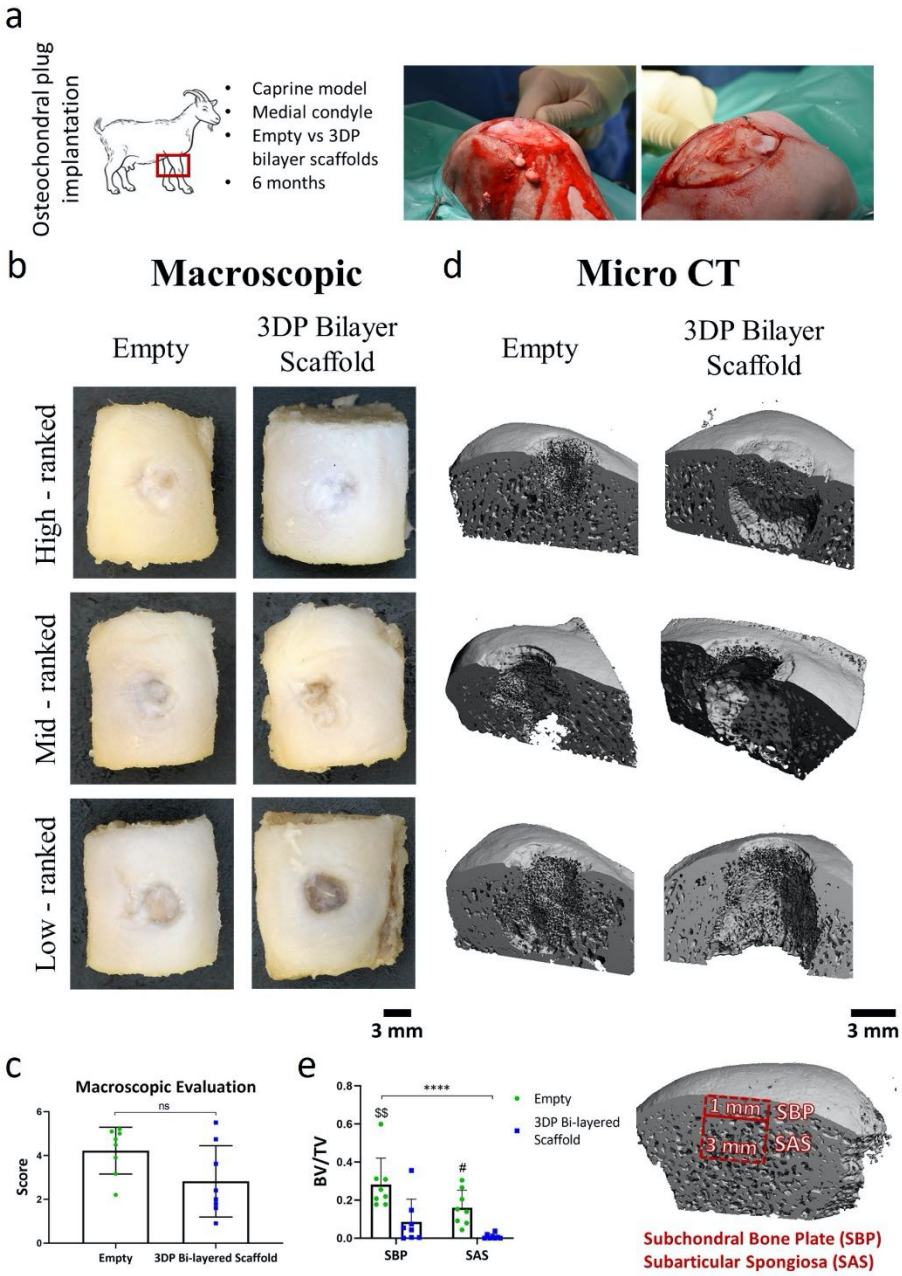

Figure 6-3 (a) Summary of the *in vivo* experiment in a caprine model in the medial condyle, comparing empty defects to defects treated with 3DP bi-layered constructs at a timepoint of 6 months. (b) Macroscopic representative images of healing achieved through spontaneous repair in defects left untreated or treated with 3DP bi-layered scaffolds. (c) Quantification of the macroscopic appearance of the defects. (d) Reconstructed micro CT images showing the distribution of mineralized tissue across the defect. (e) Quantification of the bone volume within the SBP and SAS regions of the defect. ****$p<0.0001$; $^{\$\$}p<0.01$ Empty vs. 3DP Bi-layered Scaffold in SBP; $^{\#}p<0.05$ Empty vs. 3DP Bi-layered Scaffold in SAS.

6.3.3 Production of cartilage-like tissue was comparable in empty and treated osteochondral defects

The level of cartilage repair was evaluated in more detail *via* histological and immunohistochemical staining (Figure 6.4). The percentage of repaired tissue staining positive for Safranin-O (Figure 6.4a), an indicator of cartilage tissue development, was comparable in the chondral region of both defects left empty and treated with 3DP bi-layered scaffolds (Figure 6.4b). In the subchondral region, a trend towards higher levels of cartilage tissue formation was found in the defects left empty, although this was not statistically significant (Figure 6.4b). In many animals, the chondral region of the defect area in both groups also stained positive for collagen type II (Figure 6.4c), the most abundant type of collagen present in hyaline cartilage. The percentage of collagen type II quantified in the chondral region of the defects showed a trend toward higher content of collagen type II in defects treated with 3DP bi-layered constructs (Figure 6.4d). Staining for collagen type X was not detected in any of the groups (Figure 6.4d). The structure of the newly formed collagen fibre network was evaluated using polarized light microscopy (PLM). Collagen fibre arrangement in both experimental groups (Figure a, b) was compared to that of the native tissue (Figure 6.5c) by quantifying the angle of orientation and the dispersion of fibre orientation in the superficial (Top) and deep (Bottom) region of cartilage (Figure 6.5 d, e). Overall, a parallel fibre orientation (approaching 0°) was observed in the superficial region of both groups, although the empty defect group showed a lower range of dispersion (Figure 6.5d). In contrast, the directionality of the collagen fibres in the deep region had a wide dispersion in both defects left empty and treated with 3DP bi-layered scaffolds (Figure 6.5e).

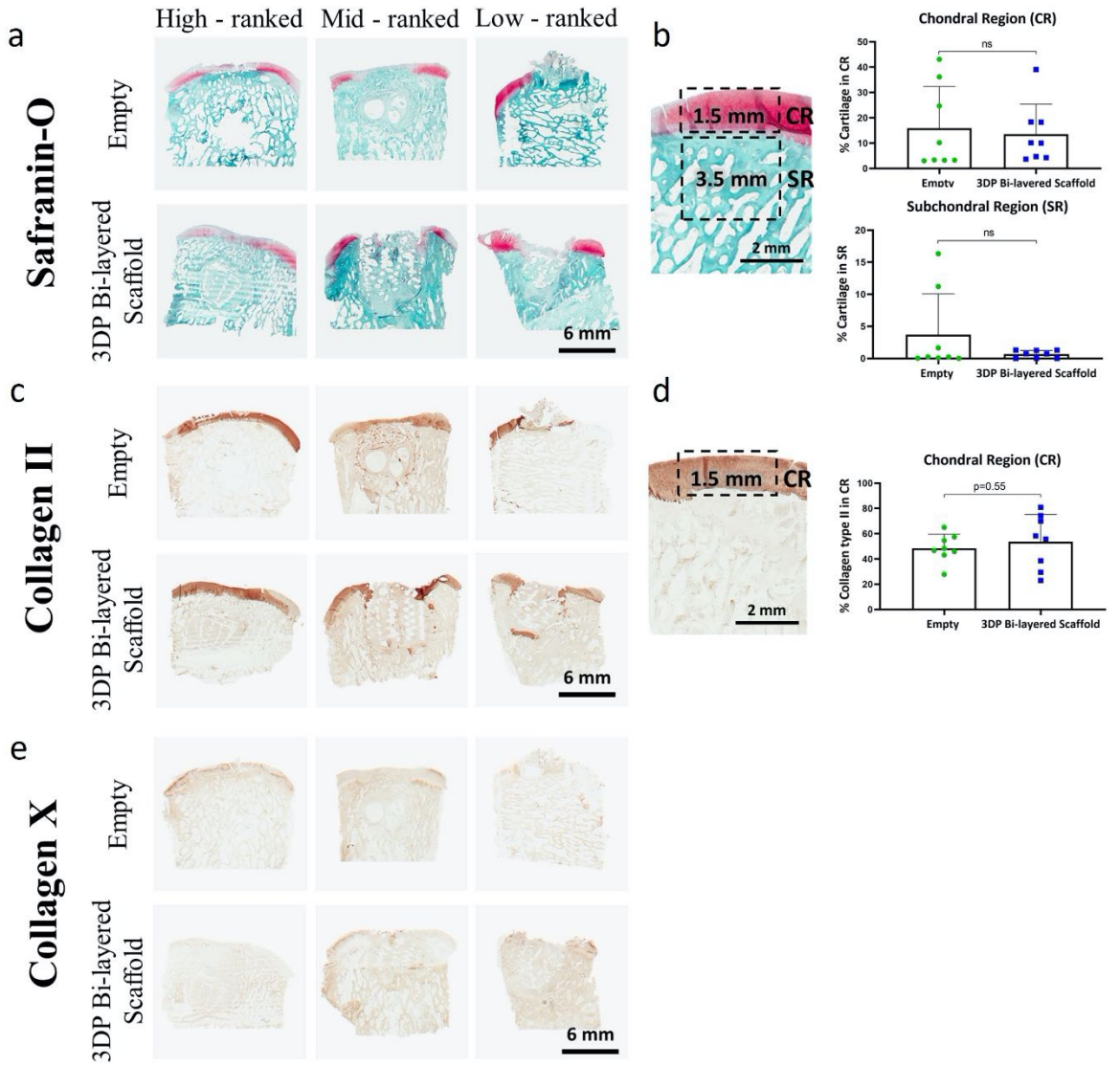

Figure 6-4 (a) Safranin-O staining (red) for cartilage matrix in the repaired tissue in defects left empty and treated with 3DP bi-layered scaffolds. (b) Quantification of the percentage of newly formed cartilage in the chondral and subchondral regions. (c) Staining and (d) quantification of collagen type II present in the repaired cartilage of the chondral region in empty controls and defects treated with 3DP bi-layered scaffolds. (e) Collagen type X stained samples for empty control and 3DP bi-layered scaffold treated groups.

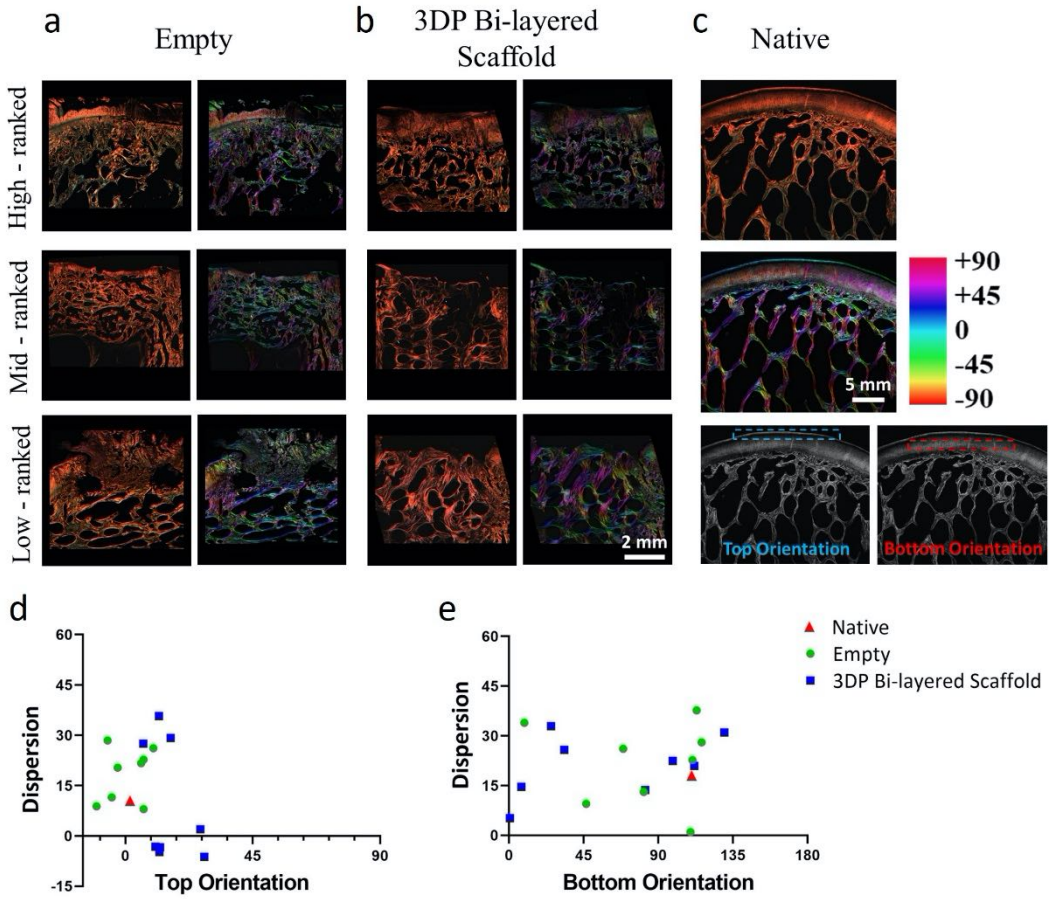

Figure 6-5 Analysis of collagen fibre arrangement within repaired cartilage. (a-c) PLM and colour map images indicating the orientation of collagen fibres within the repaired tissue of (a) empty controls and (b) 3DP bi-layered scaffold treated group in comparison to (c) native tissue. (d, e) Evaluation of the collagen fibre orientation in the (d) superficial region (Top) and (e) deep region (Bottom) of the repaired tissue relative to the native tissue.

6.3.4 Design and 3D bioprinting of anatomically shaped prosthesis to replace the glenohumeral joint in a lapine model

An anatomically accurate, bi-layered 3D bioprinted glenohumeral joint prosthesis was successfully engineered using multiple-tool biofabrication strategies. First, the right shoulder joint of a healthy rabbit was scanned using micro CT and the region of interest (humeral head) was isolated and 3D reconstructed (Figure 6.6a i, ii). The obtained 3D

reconstruction was converted to an STL file for the design of both the internal architecture of the implant and a stem for fixation *in vivo* (Figure 6.6a iii). Finally, the complete implant was 3D printed in an orthogonal fashion using PCL (Figure 6.6 iv).

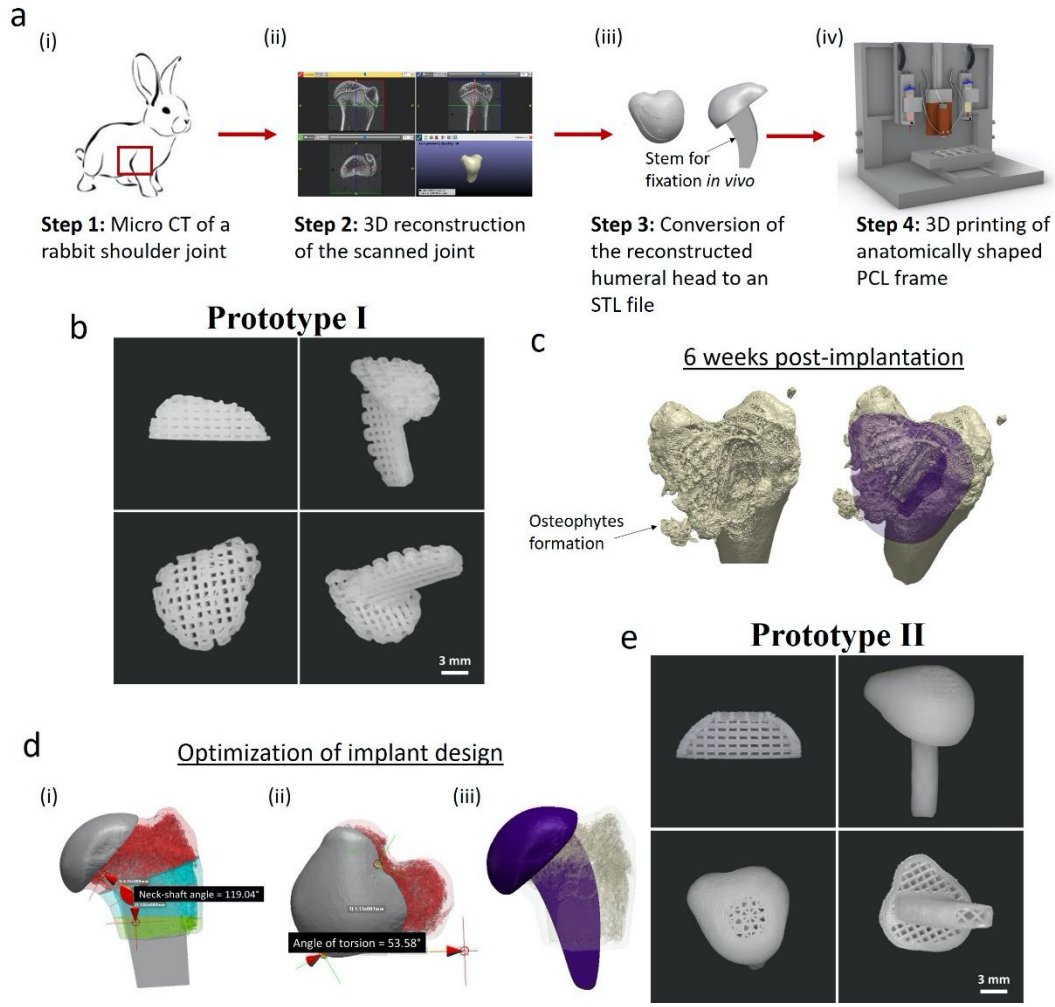

Figure 6-6 (a) Schematic of the steps used to fabricate anatomically shaped PCL prosthesis: (i) scan of native rabbit shoulder joint; (ii) 3D reconstruction of the humeral head that was converted to (iii) an STL file for design refinement and addition of a stem for fixation *in vivo*; (iv) 3D printing of the anatomically accurate PCL scaffold. (b) Macroscopic images of Prototype I of the whole joint prosthesis. (c) Micro CT images of the rabbit shoulder joint after a 6 weeks pilot showing failure of the Prototype I implant due to instable fixation that caused osteophytes formation. (d) Micro CT analysis of native joint to aid on the optimization of the implant design by evaluating the (i) neck-shaft angle and (ii) angle of torsion. (e) Macroscopic images of Prototype II of the whole joint prosthesis.

The first design of the 3D printed humeral head-shaped PCL scaffold (Prototype I) was highly porous, showing side porosity in both the head and stem of the implant (Figure 6.6b). In addition, the head and fixation were fabricated in two separate steps. The stem was then attached to the centre of the bone region of the prosthesis by heating the base for approximately 20 seconds at 60°C. To assess the suitability of the implant design as well as the mechanical stability, a 6 weeks pilot study was performed where PCL only scaffolds were implanted. Post-implantation, it was found that the humeral head of the implant detached from the stem causing inflammation in the joint and damage to the glenoid cavity, resulting in osteophytes formation (Figure 6.6c). Moreover, no tissue infiltration was observed in the stem despite this stayed in place.

This motivated the implementation of several changes to improve the design and mechanical performance of the prosthesis. Micro CT scans of healthy joints (n = 3) were accurately analysed to study the alignment of the humeral head with respect to the humerus as well as the shape and dimensions of the humerus medullary cavity. Two relevant parameters were calculated, namely the neck-shaft angle (119.04°) (Figure 6.6d i) and the angle of torsion (54.58°) (Figure 6.6d ii), with the goal of ensuring appropriate positioning of the stem on the head and accurate fitting of the prosthesis *in situ* (Figure 6.6d iii). To increase the strength of the PCL structure, the overall porosity of the implant was decreased by increasing the percentage of infill in both chondral and osseous layers. Moreover, a non-porous 3D printed shell was added in the outermost region of the implant. To ensure mechanical stability between the humeral head scaffold and fixation, the fabrication process was further optimized. This was done by directly 3D printing the stem onto the base of the humeral head by lowering the needle down in the head structure

by approximately 250 µm; this resulted in good fusion between the two parts. The obtained prosthesis (Prototype II) is shown in Figure 6.6e.

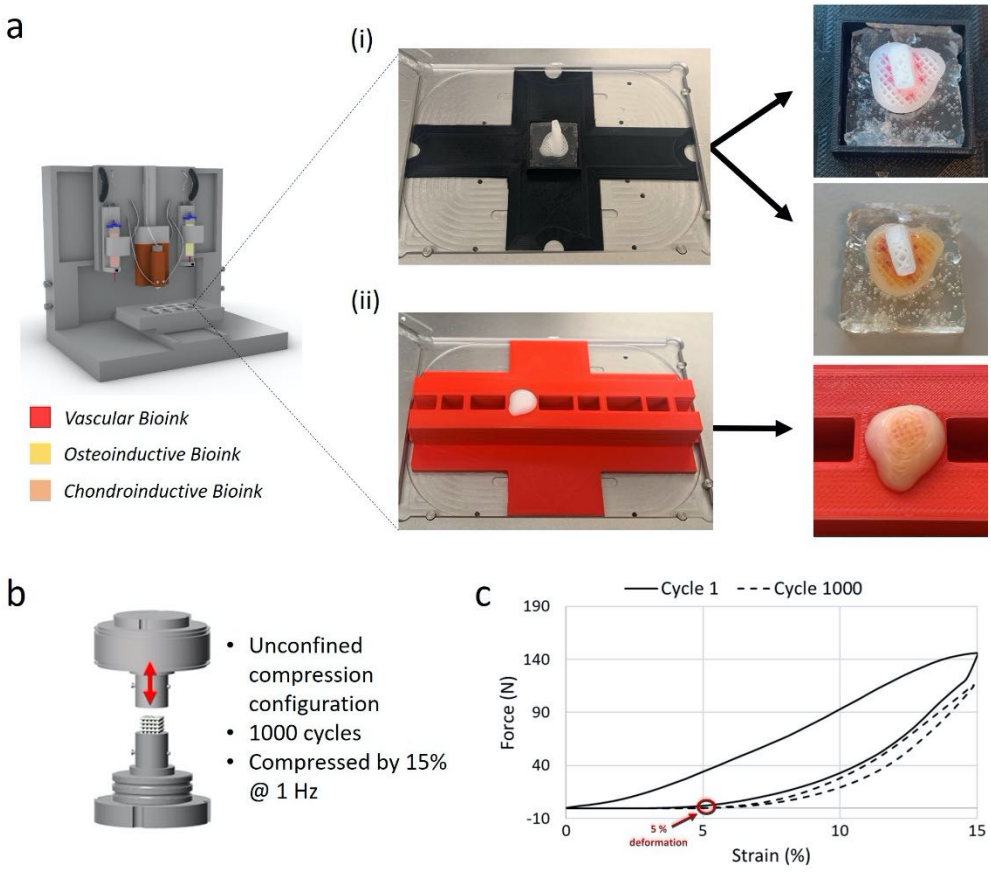

Figure 6-7 Summary of the bioinks bioprinting approach and mechanical characterization of the obtained joint prosthesis. (a) Previously printed PCL constructs were placed in two sets of custom-made moulds for the deposition of (i) vascular (red) and osteoinductive (yellow) bioinks and (ii) BMSC-laden chondronductive bioink. (b) Depiction of the mechanical testing set-up and protocol used to perform cyclic unconfined compression tests. (c) Representative force-strain curves for the first (black solid line) and last (black dashed line) applied cycles. The approximate permanent deformation experienced by the implant at the end of the test is also shown by the red circle.

Similarly to the osteochondral plug, region specific bioinks were precisely deposited within the open pores of the implant. Because of the irregular shape of the head structure and the presence of the stem, two sets of custom-made moulds were used for the microextrusion of the bioinks. First, the implant was placed with the osseous layer facing

upward to facilitate the deposition of the vascular and osteoinductive bioinks (Figure 6.7a). The vascular ink (red) was extruded in alternating pores surrounding the stem, whereas the osteoinductive ink (yellow) was deposited in the rest of the pores of the osseous layer (Figure 6.7a i). Then, the implant was flipped to allow the deposition of the BMSC-encapsulated chondroinductive bioink (pink) within the chondral layer (Figure 6.7a ii). Post-bioprinting, the mechanical strength of the humeral head structure was evaluated under cyclic unconfined compression (Figure 6.7b). Mechanical testing showed that the implant experienced a permanent deformation of approximately 5% after the application of 1000 cycles (Figure 6.7c). Moreover, significant hysteresis was observed during the first unloading cycle, which was markedly decreased in the last applied cycle.

6.3.5 Failure of the biological joint surfacing implant *in vivo*

The tissue engineered prosthesis was easy to handle and fit well into the defect site (Figure 6.8a). 10 days after implantation, all rabbits regained mobility and were weight bearing on the joint that had received surgery. Despite the prosthesis stayed in place throughout the 3-month time period, upon sacrifice of the animals it was observed that the humeral head structure had lost its integrity and no longer appeared whole due to mechanical failure of the implant (Figure 6.8b). However, tissue formation (indicated by the yellow arrows) was observed in 2/3 animals where the implant did not undergo total mechanical failure. Micro CT analysis post-implantation revealed that the remaining implant stimulated bone tissue formation especially around the stem area (indicated by the yellow dashed line), demonstrating that good osseointegration of the prosthesis with the host tissue occurred (Figure 6.8c).

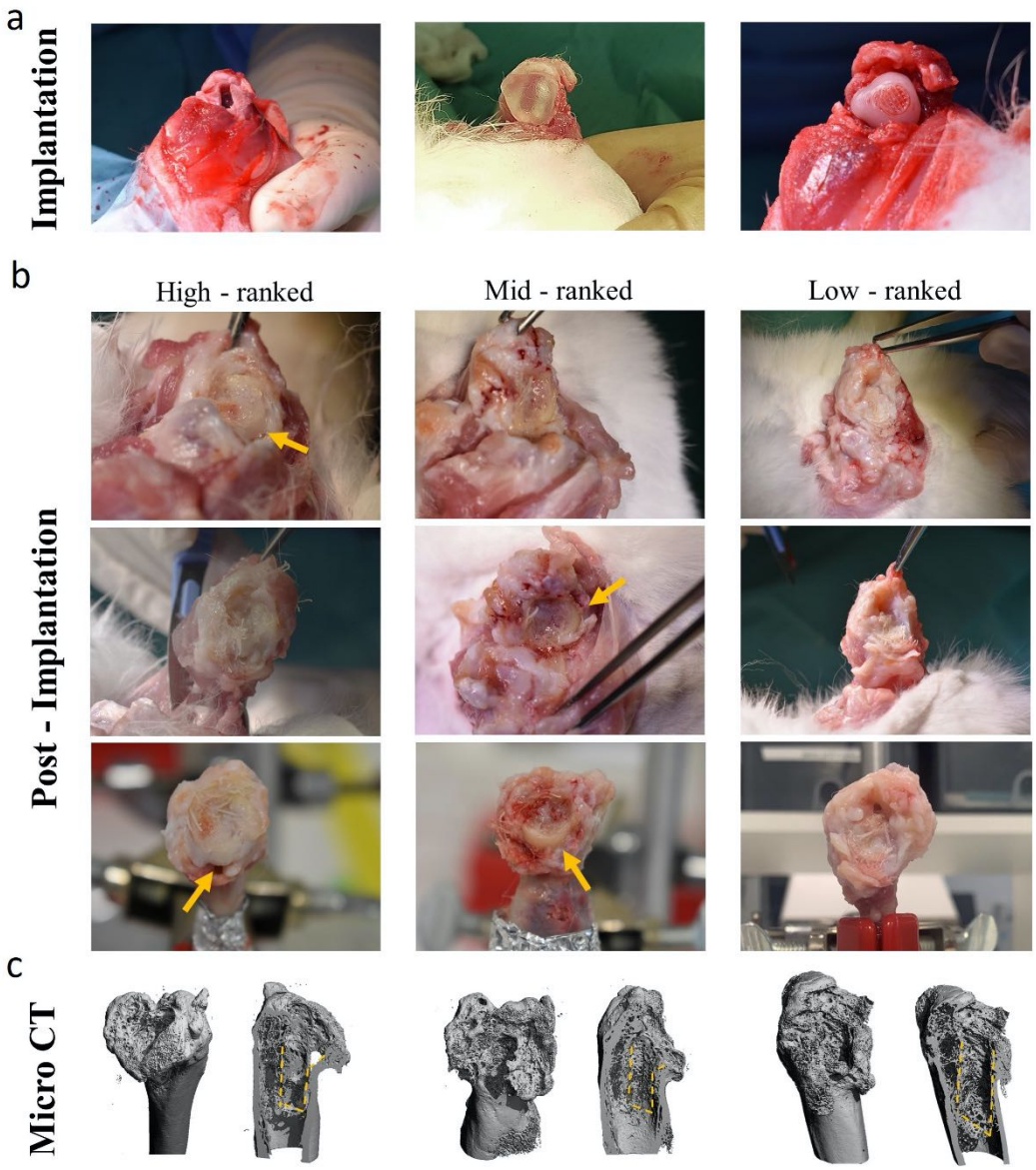

Figure 6-8 (a) Macroscopic images of the scaffold during implantation by press fitting into the medullary cavity. (b) Macroscopic evaluation of the operated joint post-implantation showing failure of the scaffold. The yellow arrows point to the repaired tissue. (c) Micro CT images showing mineralized tissue formed at the site of implantation, especially around the stem (yellow dashed line) of the scaffold.

6.4 Discussion

Engineering multiphasic tissues for load bearing applications requires the development of mechanically and biologically competent constructs. This study

describes a novel bioprinting approach for engineering 'off-the-shelf' implants to treat either large osteochondral defects or replace an entire articular joint. Using multiple-tool biofabrication in combination with micro CT it was possible to obtain scaled-up, anatomically accurate joint prosthesis. In addition, a process for bioprinting a number of growth factors-containing bioinks (i.e. chondroinductive, vascular and osteoinductive bioinks) into the PCL network was successfully established to control the accurate deposition of each bioink within specific areas of the implant. *In vitro*, we found that the BMSCs laden-chondroinductive bioink stimulated the production of hyaline cartilage-like ECM in the chondral region of the biphasic construct. In contrast, the acellular vascular and osteoinductive bioinks in the osseous region of the construct progressively degraded overtime, which is necessary to promote bone tissue formation and vessel infiltration once these constructs are implanted *in vivo*. In spite of these promising *in vitro* findings, the *in vivo* outcomes did not provide compelling evidence to support the continued use of the proposed bioprinting strategy in either of the investigated animal models.

The quality of repair in the osteochondral defects created in goats was assessed 6 months after implantation. Histological and immunohistochemical results demonstrated that the formation of hyaline cartilage-like tissue in the chondral layer was comparable in the two groups, whereas levels of bone repair was generally greater in the empty control defects. Overall, animal-to-animal variability in the quality of the repair was observed. In animals that demonstrated good hyaline cartilage regeneration following implantation of the 3DP bi-layered scaffold (i.e. Goat 4 and 8; Supplementary Figure 5), good regeneration of the subchondral bone was also observed, with residual scaffold material found lower down in the subchondral bone. This suggests one of two possible

outcomes. The first explanation is that the implant directly supported hyaline cartilage and subchondral bone regeneration, with incomplete conversion of the distal region of the implant into bone. The second explanation is that the implant dramatically subsided *in vivo*, leaving behind space for spontaneous regeneration of the overlaying cartilage and bone. This spontaneous regeneration may have been enhanced by a chronic, low-level inflammatory response to the implant material, which could result in the production of cytokines and growth factors by macrophages that are permissive to osteochondral defect regeneration. Therefore, a better understanding of the interactions between biomaterials and the biological environment they encounter is critical for the success of tissue engineering approaches. Such knowledge could inform on the design of immunomodulatory materials that could potentially influence the immune response toward desired functions. Further studies are required to explore these hypotheses.

In the remaining animals, the outcomes could be classified into one of two different categories. In some animals (i.e. Goat 2, 5 and 7; Supplementary Figure 5), little or no downward migration of the implant was observed. The absence of implant migration did not correlate with improved levels of articular cartilage regeneration, despite the presence of region specific bioinks and growth factors that were expected to support osteochondral-like tissue formation. In previous chapters of this thesis, alginate-GelMA IPN and RGD-γ irradiated alginate bioinks have been successfully used to produce stable cartilage- and hypertrophic cartilage-like matrix *in vitro*, respectively. In the current study, the alginate component of the IPN bioink was modified by chemical sulfation. This process has been shown to provide the alginate with an analogous molecular structure to sulfated GAGs found in native cartilage and to support robust chondrogenesis of BMSCs and CCs *in vitro* (Arlov et al., 2017; Li et al., 2019; Mhanna et al., 2014). In spite of this,

the BMSCs present in the chondral layer in these animals did not promote cartilage tissue formation. In the remaining animals (i.e. Goat 1, 3 and 6; Supplementary Figure 5), some subsidence of the implant is observed, with no evidence of subchondral bone regeneration. In these animals, a collagen rich tissue forms on the surface of the implant, which typically stains weakly for proteoglycans.

In most cases, the osseous region of the implant failed to promote robust regeneration of bone. RGD-γ irradiated alginate was the bioink used to engineer the osseous layer of the bi-layered constructs. Typically, alginate does not contain specific ligands for cell adhesion and it is generally slow to degrade, which can be a limitation for bone development. In this study, alginate was modified by introducing RGD peptides that have been shown to support cellular proliferation, an osteogenic phenotype (Alsberg et al., 2001) and stimulate endochondral bone formation (Daly et al., 2016b). In addition, the alginate hydrogel was modified using γ irradiation, which is a strategy known to accelerate its degradation and enhance the capacity of the material to support bone regeneration (Alsberg et al., 2001; Alsberg et al., 2003; Kong et al., 2004; Simmons et al., 2004). RGD-γ irradiated alginate bioinks have previously been shown to support endochondral bone formation *in vivo*, especially when combined with relevant growth factors (Critchley et al., 2018a; Priddy et al., 2014; Simmons et al., 2004). A number of growth factors, including VEGF and BMP-2, have been shown to promote bone regeneration in different models (Lieberman et al., 2002). The therapeutic benefit of VEGF is typically attributed to its ability to enhance angiogenesis, while BMP-2 has an osteoinductive function. It has been reported that VEGF does not play a role in driving MSC differentiation towards the osteogenic pathway and that alone, it is not able to heal critically sized bone defects (Peng et al., 2002). On the other side, a lack of VEGF has

been shown to disrupt the repair of large bone defects (Maes et al., 2002; Street et al., 2002). Therefore, multiple studies have explored therapies that combined the delivery of VEGF and BMP-2 to improve bone regeneration (Carano et al., 2003; Kanczler et al., 2010; Patel et al., 2008). For example, in a recent study carried out in the lab by Dr. Freeman, the spatial patterning of VEGF and BMP-2 within 3D bioprinted constructs has shown to enhance angiogenesis and bone regeneration of critically sized femoral bone defects in rats.

In this chapter, despite region specific bioinks have been combined with relevant growth factors to promote cartilage and bone tissue formation, it seemed that the resulting 3DP bi-layered construct did not undergo osseointegration with the surrounding host tissue, leading to subsidence of it, and bone or cartilage tissue forming around it. We hypothesized that because of the instability of the implant due to poor osseointegration, the BMSCs present in the chondral layer did not promote cartilage tissue formation. Moreover, we speculated that the lack of implant integration intensified the inflammatory response of the host and consequently affected the outcome of the healing process. It has been reported that, even if a biomaterial is considered biocompatible, the physicochemical properties of the tissue engineered construct can trigger an adverse immune reaction that can cause failure of the implant itself (Andorko et al., 2017; Longoni et al., 2018; Mariani et al., 2019).

The outcome of the pilot study exploring total shoulder regeneration in rabbits was analysed 3 months after implantation. The PCL reinforcement geometry was successfully optimized to ensure anatomical accuracy as well as a stable fixation *in situ* which facilitated osseointegration of the prosthesis. However, post-implantation it was observed that the scaled-up implants had failed mechanically affecting the repair process.

Generally, the mechanical strength of PCL implants can be improved by increasing the fibre diameter or infill pattern, similar to what other studies have used for whole joint resurfacing approaches (Moroni et al., 2006; Olubamiji et al., 2016). However, this would result in a highly dense PCL implant that could dramatically limit tissue infiltration and would be difficult to degrade overtime. Alternatively, blends of PCL with stiffer and/or osteoinductive materials such as HA and ß-tricalcium phosphate (ß-TCP) could be used to increase the implant mechanical stability and facilitate bone tissue formation (Gonçalves et al., 2016; Jiao et al., 2019; Lee et al., 2010; Park et al., 2018). Another option could be the development of metal-polymer composite implants, which could benefit from the stiffness of metals for the bone region as well as from the elasticity and biological cues of polymers for the chondral region (Díaz Lantada et al., 2016; Okulov et al., 2018). Finally, whilst the mechanical characterization of the joint prosthesis pre-implantation indicated that the 3D printed construct would be experiencing a relatively low permanent deformation in compression, clearly a more physiological-like testing regime is required to assess the mechanical performance of an implant.

6.5 Conclusion

Taken together, the present study showed the potential of multiple-tool 3D bioprinting techniques to develop scaled-up composite biological joint prosthesis by 1) accurately designing both the external and internal architecture of the reinforcement polymeric network of the implant and 2) controlling the simultaneous spatial deposition of tissue-specific bioinks. Whilst significant changes need to be made to improve the *in vivo*

outcomes of this strategy, the concept of engineering spatially complex patterns of growth factors within bioprinted implants has been demonstrated.

Chapter 7
Final Discussion & Conclusion

7.1 Summary

The objective of this thesis was to engineer functional osteochondral implants suitable for biological joint resurfacing that mimicked key mechanical properties of the native tissue and provided specific biological cues supportive of functional osteochondral tissue engineering. In Chapter 3, a novel approach that combined CAD-based FE models with 3D printing strategies was developed to design mechanically functional PCL networks for cartilage tissue engineering. FE models, that during the design step considered geometry discrepancies between the idealized and actual printed geometry, could be successfully used to predict the mechanical behaviour of 3D printed PCL scaffolds. With a view to developing biomimetic constructs for cartilage tissue engineering, Chapter 4 investigated the optimal combination of PCL network architecture and alginate-GelMA IPN hydrogel bioinks. The 3D bioprinted PCL-reinforced IPN hydrogels had mechanical properties mimicking those of the native tissue and, after the incorporation of a co-culture of BMSCs and CCs within the IPN hydrogel, were able to promote stable cartilage-like tissue formation *in vitro*. In Chapter 5, cell co-cultures and mechanical stimulation were explored as strategies to direct BMSCs fate in 3D bioprinted PCL-reinforced biphasic hydrogels that had depth-dependent compressive properties. It was demonstrated that the use of a co-culture of BMSCs and CCs in the chondral layer and BMSCs only in the osseous layer of the biphasic constructs was a promising approach to promote osteochondral-like tissue formation *in vitro*. Finally, in Chapter 6 a novel multiple-tool

biofabrication approach was used to engineer 'off-the-shelf' implants for biological joint resurfacing. The spatial deposition of chondroinductive, osteoinductive and vascular bioinks containing BMSCs and TGF-ß3, BMP-2, and VEGF respectively, was precisely patterned within 3D printed bi-layered PCL networks. Furthermore, in combination with micro CT, it was possible to bioprint a scaled-up, anatomically accurate prosthesis to resurface an entire synovial joint. Despite the promising *in vitro* outcomes, the *in vivo* results were not as expected in both treatment of large osteochondral defects in goats and resurfacing of the glenohumeral joint in rabbits. Whilst a significant revision of the undertaken strategies is needed to improve the *in vivo* results, a framework for engineering complex patterns of growth factors within whole joint implants has been provided.

The thesis began by establishing a strategy for designing 3D printed PCL scaffolds with tailored architecture and mechanical behaviour that is informed by CAD-based FE models that consider differences between an idealized scaffold geometry and what is actually fabricated (Chapter 3). Integrating FEM with tissue engineering strategies is being increasingly explored as a powerful tool to aid in optimizing the design of implants and/or understanding how implant design can influence the tissue regeneration process (Lacroix et al., 2009). To date, when designing tissue engineered scaffolds, only few modelling approaches have included geometrical variations that depend on the adopted fabrication technique (Campoli et al., 2013; Melancon et al., 2017; Naghieh et al., 2018). Such variations influence the scaffold geometry and mechanical properties, making the computational predictions less valuable. Herein, we developed a FEM framework that considered scaffold fibre diameter, fibre spacing and layer fusion as measured post-printing. This allowed us to use the proposed computational approach to accurately

understand the structure-mechanics relationship of 3D printed polymeric scaffolds and therefore, to theoretically modify geometrical features to obtain constructs with target compressive properties.

Chapter 4 focused on developing the chondral region of a scaled-up implant for osteochondral tissue regeneration. To this end, alginate-GelMA IPN bioinks were reinforced with 3D printed PCL networks with structures and mechanical properties inspired by the collagen network of articular cartilage. A synergistic increase in compressive properties was observed when the IPN bioink was reinforced with PCL networks characterized by the highest tension-compression nonlinearity. In addition, such composites showed equilibrium and dynamic mechanical properties that mimicked those of native cartilage. FE models used to study the reinforcement mechanism of these composites showed that PCL networks with a specific architecture reduced lateral expansion and enhanced the hydrostatic pressure generated within the IPN following application of compressive loading. Finally, IPNs containing a co-culture of BMSCs and CCs were bioprinted within biomimetic PCL networks and their capacity to support chondrogenesis was assessed. After 6 weeks *in vitro*, such bioprinted biomimetic composites were found to provide a pro-chondrogenic environment, where encapsulated cells produced hyaline-like cartilage matrix that stained positively for sGAG and type II collagen, and negatively for calcium deposition and type X collagen. Taken together, this chapter demonstrated how 3D bioprinting technology can be utilized to engineer constructs that are both conducive to chondrogenesis and biomimetic of the mechanical properties of articular cartilage.

In Chapter 5 the design and fabrication strategies adopted in Chapter 3 and 4 were utilized to 3D bioprint bi-layered cartilaginous composites with heterogeneous

mechanical properties for osteochondral tissue regeneration. The internal architecture of the PCL network was tailored to create chondral and endochondral/osseous layers with hyaline and hypertrophic cartilage-like compressive properties, respectively. With a view towards using such cartilage templates to regenerate osteochondral defects, different approaches were investigated where hyaline and hypertrophic cartilage layers were engineered using either 1) co-cultures of MSCs and CCs or 2) mechanical stimulation. Encouraged by a number of studies in the literature reporting that co-cultures of MSCs and CCs lead to more stable cartilage, while MSCs alone tend to produce hypertrophic cartilage tissue destined to form bone (Bian et al., 2011; Hendriks et al., 2009; Mesallati et al., 2015), this thesis used a co-culture of BMSCs and CCs to engineer stable articular cartilage within alginate-GelMA IPN bioink in the chondral layer, and BMSCs only in a RGD-γ irradiated alginate hydrogel bioink in the osseous layer of 3D printed bi-layered constructs. This thesis also explored the application of dynamic compression to BMSC-laden hydrogels to modulate chondrogenesis and hypertrophy of MSC, as such stimuli have previously been shown to promote a pro-chondrogenic response in MSC-laden scaffolds (Huang et al., 2010; Mauck et al., 2007). After 6 weeks *in vitro*, the use of the co-culture of BMSCs and CCs in the chondral layer of the 3D printed bi-layered constructs produced stable articular cartilage-like ECM with no evidence of collagen type X and calcium deposits, whereas the BMSCs in the osseous layer stained positive for calcium and collagen type X. Dynamic compression enhanced the production of sGAG in the chondral compared to the osseous layer of constructs containing only BMSCs, although such mechanical stimulation was found to suppress mineralization in both layers of the constructs. These results showed how different tissue engineering approaches can

be leveraged to regulate cell fate to produce implants with spatially defined tissue phenotypes.

The final chapter (Chapter 6) focused on using the outcomes of the previous chapters of this thesis to produce 'off-the-shelf' implants and assessing their ability to regenerate osteochondral tissue in two *in vivo* models. The first model considered treating large osteochondral defects in the knee condyle of goats. The second model was a pilot study where the engineered osteochondral implant was scaled-up and its design was refined to withstand the challenging mechanical environment *in vivo* in order to resurface the entire shoulder joint in rabbits. To create 'off-the-shelf' products, implants did not receive *in vitro* priming and cells were only present in the chondral layer. To stimulate the production of layer-specific tissues, a process for bioprinting a number of growth factors-containing bioinks (i.e. chondroinductive, vascular and osteoinductive bioinks) into the PCL network was successfully established to control the accurate deposition of each bioink within specific areas of the implant. Although animal-to-animal variability was observed, the quality of repair in the osteochondral defects created in goats was comparable between empty controls and defects treated with the 3D printed bi-layered constructs. Following implantation of the printed constructs, the outcomes could be classified into three categories: 1) implants that stayed in place and did not improve articular cartilage and bone regeneration despite the presence of region-specific growth factors-containing bioinks; 2) implants that were partially resorbed or showed some subsidence and did not promote subchondral bone regeneration, but formed tissue that stained strongly for collagen and weakly for proteoglycans on the surface; 3) implants that were partially resorbed or migrated lower down in the subchondral bone, which resulted in good hyaline cartilage and subchondral bone regeneration. In the latter case,

we hypothesized that the implant was either directly responsible for tissue formation, or left space for spontaneous regeneration of cartilage and bone due to a mild but chronic inflammatory response to the implant that produced cytokines and growth factors, resulting in enhanced osteochondral tissue formation. In the case where the osseous region of the implant did not succeed in promoting bone regeneration, we speculate that insufficient osseointegration likely had negative effect on the healing process. In rabbits, despite the design of the implant for total joint resurfacing was optimized ensuring anatomical accuracy and stability *in situ*, mechanical failure was observed affecting the healing process.

In summary, this thesis provides a novel tissue engineering framework to develop functional joint prosthesis. The adoption of multiple-tool biofabrication strategies allowed the development of biomimetic implants by spatially patterning mechanically reinforced constructs with cell-laden tissue-specific bioinks. It was also demonstrated how the integration of FEM aided in designing the internal architecture of such implants prior to bioprinting, allowing target specific mechanical properties to be achieved. FEM also provided a better understanding of the interactions between the different components of the implant and helped to explain the biomimetic nature of such composites.

7.2 Conclusions

- If geometrical differences between the idealized and actual printed materials are considered, CAD-based FEM can effectively be used to design *a priori* 3D printed polymeric networks with user-defined mechanical properties.

- 3D bioprinting can be used to engineer biomimetic fibre-reinforced IPN hydrogels for cartilage tissue engineering. The internal architecture of the fibrous networks can be tuned to produce composites that mimic key mechanical properties of native articular cartilage.
- Using CAD-based FEM it is possible to better understand the interactions between components of fibre-reinforced hydrogels and characterize their mechanical behaviour.
- PCL-reinforced IPN hydrogels, containing a co-culture of BMSCs and CCs, support the development of a hyaline cartilage-like tissue whose mechanical properties continue to improve with time in culture. Such engineered tissues can be deposited onto the surface of osteogenic implants to produce constructs for osteochondral tissue engineering.
- Dynamic compression stimulation of MSC laden scaffolds with spatially defined mechanical properties can be used to produce constructs with spatially defined tissue phenotypes.
- Using multiple-tool biofabrication technology it is possible to engineer 'off-the-shelf', anatomically accurate biological joint resurfacing implants containing spatially defined bioinks functionalized with specific growth factors.

Such bioprinting approaches could potentially be used as alternative therapeutic options for treating large joint defects and ultimately osteoarthritis. However, future work must address the limitations identified in this thesis, primarily to improve the mechanical stability and facilitate osseointegration of the 3D printed implant *in vivo*.

7.3 Future directions

Chapter 3 of this thesis identified a CAD-based FEM approach that used the average values of scaffold geometrical parameters to design the internal architecture of 3D printed PCL networks to produce scaffolds with defined mechanical properties. Although this approach was effectively employed in these studies, considering sample-specific geometries will be important if trying to understand the variability in scaffold mechanical properties from print to print. In addition, varying the needle gauge and printing parameters would result in a different printing resolution, meaning that a new characterization of the geometry parameters (fibre diameter, fibre spacing and layer fusion) of actual printed versus ideally designed structures must be performed.

In Chapter 4, 3D bioprinted biomimetic PCL reinforced-IPN hydrogel composites were developed, where the PCL network architecture was designed with relatively high tension-compression nonlinearity which is believed to play a critical role in the load-bearing capacity of normal articular cartilage. Importantly, while the addition of alginate-GelMA IPNs in the PCL network resulted in equilibrium properties matching those of articular cartilage, dynamic properties were still inferior. The mechanical functionality of articular cartilage derives from the depth dependant organization of the collagen network and its interaction with negatively charged sGAGs (Mow et al., 1992). The sGAG molecules function to generate a swelling pressure that is partially responsible for supporting the load within the tissue. To further improve the performance of our fibre-reinforced composites, more targeted design approaches and material selection to mimic the composition of cartilage could be explored. For example, Bas et al. (Bas et al., 2017c) utilized soft hydrogels that emulated the proteoglycan matrix of cartilage by using negatively charged star-shaped poly(ethylene glycol)/heparin hydrogels. These soft

biomimetic hydrogels combined with PCL electrospun fibre networks resulted in composites that showed cartilage-like mechanical nonlinearity, anisotropy and viscoelasticity, and promoted neocartilage formation *in vitro*. Castilho et al. (Castilho et al., 2019) produced PCL bi-layered micro-fibre networks that mimicked the arrangement of the collagen fibres in the superficial and middle/deep zone of native cartilage. They showed that including the superficial reinforcing layer greatly improved the load-bearing properties of micro-fibre reinforced GelMA hydrogels.

Chapter 5 explored the use of cell co-cultures and mechanical stimulation on matrix deposition in 3D bioprinted bi-layered composites for osteochondral tissue engineering. Dynamic compression stimulation enhanced sGAG production compared to constructs cultured in static conditions, while also suppressed mineralization in both the chondral and osseous layers of the constructs. One limitation of this study might be that the loading was applied from day 1, which has been reported to be detrimental for chondrogenesis (O'Conor et al., 2013). Delayed loading or other loading regimes could be investigated to identify the best conditions for promoting osteochondral-like tissue *via* mechanical stimulation. In addition, as in this chapter using a co-culture of BMSCs and CCs was shown to be the most powerful regulator of chondrogenesis, it would be interesting to study the simultaneous effect of mechanical stimulation and co-culture on chondrogenesis in the developed 3D bioprinted composites.

Chapter 6 investigated the *in vivo* performance of the 3D bioprinted 'off-the-shelf' osteochondral implants with region-specific growth factors-eluting bioinks. A limitation in the goat model study was the poor osseointegration of the 3D bioprinted implants which we hypothesized lead to an adverse immune reaction that affected the healing process by neglecting the presence of the incorporated growth factors. Therefore, some

changes in the implant design are needed to improve the stability of the constructs in the defect. This could be done for example by incorporating cells throughout and providing some *in vitro* priming before implantation, although this would go against the goal of developing 'off-the-shelf' products. Another option could be to investigate the design of immunomodulatory biomaterials that could potentially influence the immune response toward desired functions. In the rabbit model, further improvement of the mechanical properties of the anatomically shaped implant is required. The outcomes of this study showed that PCL alone is not the optimal reinforcing material for these applications. Increasing the amount of PCL is not a viable option as the implant would be too dense and could negatively impact tissue infiltration. Therefore, osteoinductive components could be incorporated to accelerate bone tissue formation and increase the mechanical stability of the prosthesis. Alternatively, metal-polymer hybrid constructs could be engineered to effectively withstand the challenging load-bearing environment *in vivo* when attempting to resurface an entire joint. Moreover, a wider range of mechanical tests that include tensile, shear and long-term cyclic loading should be carried out to verify the mechanical performance of an implant before implantation. These could be combined with FEM techniques to determine if design changes in the reinforcing network are needed prior to implantation.

References

Acharya, C., A. Adesida, P. Zajac, M. Mumme, J. Riesle, I. Martin, and A. Barbero (2012) Enhanced chondrocyte proliferation and mesenchymal stromal cells chondrogenesis in coculture pellets mediate improved cartilage formation *Journal of Cellular Physiology*, **227** 88-97.

Adams, D.J., K.M. Brosche, and J.L. Lewis (2003) Effect of specimen thickness on fracture toughness of bovine patellar cartilage. *Journal of biomechanical engineering*, **125** 927-929.

Ahadian, S., H. Savoji, and A. Khademhosseini (2018) Recent advances in hydrogels for tissue engineering *Chemical Engineering Progress*, **114** 59-75.

Ahsan, T. and R.L. Sah (1999) Biomechanics of integrative cartilage repair *Osteoarthritis and Cartilage*, **7** 29-40.

Akizuki, S., V.C. Mow, F. Müller, J.C. Pita, D.S. Howell, and D.H. Manicourt (1986) Tensile properties of human knee joint cartilage: I. Influence of ionic conditions, weight bearing, and fibrillation on the tensile modulus *Journal of Orthopaedic Research*, **4** 379-392.

Almeida, H.A. and P.J. Bártolo (2013) Numerical simulations of bioextruded polymer scaffolds for tissue engineering applications *Polymer International*, **62** 1544-1552.

Almeida, H.V., G.M. Cunniffe, T. Vinardell, C.T. Buckley, F.J. O'Brien, and D.J. Kelly (2015) Coupling Freshly Isolated CD44(+) Infrapatellar Fat Pad-Derived Stromal Cells with a TGF-beta3 Eluting Cartilage ECM-Derived Scaffold as a Single-Stage Strategy for Promoting Chondrogenesis *Adv Healthc Mater*, **4** 1043-53.

Almeida, H.V., Y. Liu, G.M. Cunniffe, K.J. Mulhall, A. Matsiko, C.T. Buckley, F.J. O'Brien, and D.J. Kelly (2014) Controlled release of transforming growth factor-β3 from cartilage-extra-cellular-matrix-derived scaffolds to promote chondrogenesis of human-joint-tissue-derived stem cells *Acta Biomaterialia*, **10** 4400-4409.

Almeida, H.V., K.J. Mulhall, F.J. O'Brien, and D.J. Kelly (2017) Stem cells display a donor dependent response to escalating levels of growth factor release from extracellular matrix-derived scaffolds *Journal of Tissue Engineering and Regenerative Medicine*, **11** 2979-2987.

Alsberg, E., K.W. Anderson, A. Albeiruti, R.T. Franceschi, and D.J. Mooney (2001) Cell-interactive alginate hydrogels for bone tissue engineering *Journal of Dental Research*, **80** 2025-2029.

Alsberg, E., H.J. Kong, Y. Hirano, M.K. Smith, A. Albeiruti, and D.J. Mooney (2003) Regulating bone formation via controlled scaffold degradation *Journal of Dental Research*, **82** 903-908.

An, Y.H., D. Webb, A. Gutowska, V.A. Mironov, and R.J. Friedman (2001) Regaining chondrocyte phenotype in thermosensitive gel culture *Anatomical Record*, **263** 336-341.

Andorko, J.I. and C.M. Jewell (2017) Designing biomaterials with immunomodulatory properties for tissue engineering and regenerative medicine *Bioengineering & Translational Medicine*, **2** 139-155.

Angele, P., P. Niemeyer, M. Steinwachs, G. Filardo, A.H. Gomoll, E. Kon, J. Zellner, and H. Madry (2016) Chondral and osteochondral operative treatment in early osteoarthritis. *Knee surgery, sports traumatology, arthroscopy : official journal of the ESSKA*, **24** 1743-52.

Anseth, K.S., C.N. Bowman, and L. Brannon-Peppas (1996) Mechanical properties of hydrogels and their experimental determination *Biomaterials*, **17** 1647-1657.

Archer, C.W., H. Morrison, and A.A. Pitsillides (1995) The cellular aspects of the development of synovial joints and articular cartilage *Ontogenez*, **26** 259-269.

Arlov, Ø. and G. Skjåk-Bræk (2017) Sulfated alginates as heparin analogues: A review of chemical and functional properties *Molecules*, **22** 1-16.

Armstrong, C.G., W.M. Lai, and V.C. Mow (1984) An analysis of the unconfined compression of articular cartilage *Journal of Biomechanical Engineering*, **106** 165-173.

Aspden, R.M. (1994) Fibre reinforcing by collagen in cartilage and soft connective tissues *Proceedings of the Royal Society B: Biological Sciences*, **258** 195-200.

Athanasiou, K.A., A. Agarwal, and F.J. Dzida (1994) Comparative study of the intrinsic mechanical properties of the human acetabular and femoral head cartilage *Journal of Orthopaedic Research*, **12** 340-349.

Athanasiou, K.A., M.P. Rosenwasser, J.A. Buckwalter, T.I. Malinin, and V.C. Mow (1991) Interspecies comparisons of in situ intrinsic mechanical properties of distal femoral cartilage *Journal of Orthopaedic Research*, **9** 330-340.

Awad, H.A., M.Q. Wickham, H.A. Leddy, J.M. Gimble, and F. Guilak (2004) Chondrogenic differentiation of adipose-derived adult stem cells in agarose, alginate, and gelatin scaffolds *Biomaterials*, **25** 3211-3222.

Axpe, E., M. Oyen, E. Axpe, and M.L. Oyen (2016) Applications of Alginate-Based Bioinks in 3D Bioprinting *International Journal of Molecular Sciences*, **17** 1976.

Aziz, A.H., K. Eckstein, V.L. Ferguson, and S.J. Bryant (2019) The effects of dynamic compressive loading on human mesenchymal stem cell osteogenesis in the stiff layer of a bilayer hydrogel *Journal of Tissue Engineering and Regenerative Medicine*.

Bae, W.C., V.W. Wong, J. Hwang, J.M. Antonacci, G.E. Nugent-Derfus, M.E. Blewis, M.M. Temple-Wong, and R.L. Sah (2008) Wear-lines and split-lines of human patellar cartilage: relation to tensile biomechanical properties. *Osteoarthritis and cartilage*, **16** 841-5.

Bartnikowski, M., T.J. Klein, F.P.W. Melchels, and M.A. Woodruff (2014) Effects of scaffold architecture on mechanical characteristics and osteoblast response to static and perfusion bioreactor cultures *Biotechnology and Bioengineering*, **111** 1440-1451.

Bas, O., D. D'Angella, J.G. Baldwin, N.J. Castro, F.M. Wunner, N.T. Saidy, S. Kollmannsberger, A. Reali, E. Rank, E.M. De-Juan-Pardo, and D.W. Hutmacher (2017a) An Integrated Design, Material, and Fabrication Platform for Engineering Biomechanically and Biologically Functional Soft Tissues *ACS Applied Materials and Interfaces*, **9** 29430-29437.

Bas, O., E.M. De-Juan-Pardo, M.P. Chhaya, F.M. Wunner, J.E. Jeon, T.J. Klein, and D.W. Hutmacher (2015) Enhancing structural integrity of hydrogels by using highly organised melt electrospun fibre constructs *European Polymer Journal*, **72** 451-463.

Bas, O., E.M. De-Juan-Pardo, C. Meinert, D. D'Angella, J.G. Baldwin, L.J. Bray, R.M. Wellard, S. Kollmannsberger, E. Rank, C. Werner, T.J. Klein, I. Catelas, and D.W. Hutmacher (2017b) Biofabricated soft network composites for cartilage tissue engineering *Biofabrication*, **9** 025014.

Bas, O., E.M. De-Juan-Pardo, C. Meinert, D. D'Angella, J.G. Baldwin, L.J. Bray, R.M. Wellard, S. Kollmannsberger, E. Rank, C. Werner, T.J. Klein, I. Catelas, and D.W. Hutmacher (2017c) Biofabricated soft network composites for cartilage tissue engineering *Biofabrication*, **9**.

Beck, E.C., M. Barragan, M.H. Tadros, S.H. Gehrke, and M.S. Detamore (2016a) Approaching the compressive modulus of articular cartilage with a decellularized cartilage-based hydrogel. *Acta biomaterialia*, **38** 94-105.

Beck, E.C., M. Barragan, M.H. Tadros, S.H. Gehrke, and M.S. Detamore (2016b) Approaching the compressive modulus of articular cartilage with a decellularized cartilage-based hydrogel *Acta Biomater*, **38** 94-105.

Benya, P.D., S.R. Padilla, and M.E. Nimni (1978) Independent regulation of collagen types by chondrocytes during the loss of differentiated function in culture *Cell*, **15** 1313-1321.

Benya, P.D. and J.D. Shaffer (1982) Dedifferentiated chondrocytes reexpress the differentiated collagen phenotype when cultured in agarose gels *Cell*, **30** 215-224.

Bernhard, J., J. Ferguson, B. Rieder, P. Heimel, T. Nau, S. Tangl, H. Redl, and G. Vunjak-Novakovic (2017) Tissue-engineered hypertrophic chondrocyte grafts enhanced long bone repair *Biomaterials*, **139** 202-212.

Bernhard, J.C., E. Hulphers, B. Rieder, J. Ferguson, D. Rünzler, T. Nau, H. Redl, and G. Vunjak-Novakovic (2018) Perfusion Enhances Hypertrophic Chondrocyte Matrix Deposition, but Not the Bone Formation *Tissue Engineering - Part A*, **24** 1022-1033.

Bessa, P.C., R. Machado, S. Nürnberger, D. Dopler, A. Banerjee, A.M. Cunha, J.C. Rodríguez-Cabello, H. Redl, M. van Griensven, R.L. Reis, and M. Casal (2010) Thermoresponsive self-assembled elastin-based nanoparticles for delivery of BMPs *Journal of Controlled Release*, **142** 312-318.

Bhattacharjee, M., J. Coburn, M. Centola, S. Murab, A. Barbero, D.L. Kaplan, I. Martin, and S. Ghosh (2015) Tissue engineering strategies to study cartilage development, degeneration and regeneration *Advanced Drug Delivery Reviews*, **84** 107-122.

Bian, L., J.V. Fong, E.G. Lima, A.M. Stoker, G.A. Ateshian, J.L. Cook, and C.T. Hung (2010) Dynamic mechanical loading enhances functional properties of tissue-engineered cartilage using mature canine chondrocytes *Tissue Engineering - Part A*, **16** 1781-1790.

Bian, L., C. Hou, E. Tous, R. Rai, R.L. Mauck, and J.A. Burdick (2013) The influence of hyaluronic acid hydrogel crosslinking density and macromolecular diffusivity on human MSC chondrogenesis and hypertrophy *Biomaterials*, **34** 413-421.

Bian, L., E.G. Lima, S.L. Angione, K.W. Ng, D.Y. Williams, D. Xu, A.M. Stoker, J.L. Cook, G.A. Ateshian, and C.T. Hung (2008) Mechanical and biochemical characterization of cartilage explants in serum-free culture. *Journal of biomechanics*, **41** 1153-9.

Bian, L., D.Y. Zhai, R.L. Mauck, and J.A. Burdick (2011) Coculture of human mesenchymal stem cells and articular chondrocytes reduces hypertrophy and enhances functional properties of engineered cartilage *Tissue Engineering - Part A*, **17** 1137-1145.

Bian, L., D.Y. Zhai, E.C. Zhang, R.L. Mauck, and J.A. Burdick (2012) Dynamic compressive loading enhances cartilage matrix synthesis and distribution and suppresses hypertrophy in hMSC-laden hyaluronic acid hydrogels *Tissue Engineering - Part A*, **18** 715-724.

Blaeser, A., D.F. Duarte Campos, U. Puster, W. Richtering, M.M. Stevens, and H. Fischer (2016) Controlling Shear Stress in 3D Bioprinting is a Key Factor to Balance Printing Resolution and Stem Cell Integrity *Advanced Healthcare Materials*, **5** 326-333.

Boccaccio, A., A.E. Uva, M. Fiorentino, G. Mori, and G. Monno (2016) Geometry design optimization of functionally graded scaffolds for bone tissue engineering: A mechanobiological approach *PLoS ONE*, **11**.

Boere, K.W.M., J. Visser, H. Seyednejad, S. Rahimian, D. Gawlitta, M.J. Van Steenbergen, W.J.A. Dhert, W.E. Hennink, T. Vermonden, and J. Malda (2014) Covalent attachment of a three-dimensionally printed thermoplast to a gelatin hydrogel for mechanically enhanced cartilage constructs *Acta Biomaterialia*, **10** 2602-2611.

Boeuf, S. and W. Richter (2010) Boeuf, S., & Richter, W. (2010). Chondrogenesis of mesenchymal stem cells: role of tissue source and inducing factors. Stem cell research & therapy, 1(4), 31. doi:10.1186/scrt31Chondrogenesis of mesenchymal stem cells: role of tissue source and inducing f *Stem cell research & therapy*, **1** 31.

Boontheekul, T., H.-J. Kong, and D.J. Mooney (2005) Controlling alginate gel degradation utilizing partial oxidation and bimodal molecular weight distribution *Biomaterials*, **26** 2455-2465.

Boschetti, F., G. Pennati, F. Gervaso, G.M. Peretti, and G. Dubini (2004) Biomechanical properties of human articular cartilage under compressive loads. *Biorheology*, **41** 159-166.

Bose, S., S. Vahabzadeh, and A. Bandyopadhyay (2013) Bone tissue engineering using 3D printing *Materials Today*, **16** 496-504.

Bracaglia, L.G., B.T. Smith, E. Watson, N. Arumugasaamy, A.G. Mikos, and J.P. Fisher (2017) 3D printing for the design and fabrication of polymer-based gradient scaffolds *Acta Biomaterialia*, **56** 3-13.

Brigham, M.D., M. Eng, A. Bick, E. Lo, A. Bendali, J.A. Burdick, D. Ph, and A. Khademhosseini (2009) Mechanically Robust and Bioadhesive Collagen Semi-Interpenetrating Networks *Tissue Engineering: Part A*, **15** 1645-1653.

Brittberg, M., A. Lindahl, A. Nilsson, C. Ohlsson, O. Isaksson, and L. Peterson (1994) Treatment of deep cartilage defects in the knee with autologous chondrocyte transplantation. *The New England journal of medicine*, **331** 889-95.

Buckley, C.T., T. Vinardell, and D.J. Kelly (2010) Oxygen tension differentially regulates the functional properties of cartilaginous tissues engineered from infrapatellar fat pad derived MSCs and articular chondrocytes *Osteoarthritis and Cartilage*, **18** 1345-1354.

Buckwalter, J.A. and H.J. Mankin (1998) Articular cartilage repair and transplantation *Arthritis and Rheumatism*, **41** 1331-1342.

Buckwalter, J.A. and J.A. Martin (2006) Osteoarthritis. *Advanced drug delivery reviews*, **58** 150-67.

Buckwalter, J.A., V.C. Mow, and A. Ratcliffe (1994a) Restoration of Injured or Degenerated Articular Cartilage *Journal of the American Academy of Orthopaedic Surgeons*, **2** 192-201.

Buckwalter, J.A., P.J. Roughley, and L.C. Rosenberg (1994b) Age-Related changes in cartilage proteoglycans: Quantitative electron microscopic studies *Microscopy Research and Technique*, **28** 398-408.

Burke, D.P. (2013) An investigation into the role of substrate stiffness and oxygen availability in the regulation of stem cell differentiation during tissue regeneration 140 - 160.

Burr, D.B. and M.A. Gallant (2012) Bone remodelling in osteoarthritis *Nature Reviews Rheumatology*, **8** 665-673.

Cahill, S., S. Lohfeld, and P.E. McHugh (2009) Finite element predictions compared to experimental results for the effective modulus of bone tissue engineering scaffolds fabricated by selective laser sintering *Journal of Materials Science: Materials in Medicine*, **20** 1255-1262.

Campoli, G., M.S. Borleffs, S. Amin Yavari, R. Wauthle, H. Weinans, and A.A. Zadpoor (2013) Mechanical properties of open-cell metallic biomaterials manufactured using additive manufacturing *Materials and Design*, **49** 957-965.

Canal Guterl, C., C.T. Hung, and G.A. Ateshian (2010) Electrostatic and non-electrostatic contributions of proteoglycans to the compressive equilibrium modulus of bovine articular cartilage *Journal of Biomechanics*, **43** 1343-1350.

Cao, W., W. Lin, H. Cai, Y. Chen, Y. Man, J. Liang, Q. Wang, Y. Sun, Y. Fan, and X. Zhang (2019) Dynamic mechanical loading facilitated chondrogenic differentiation of rabbit BMSCs in collagen scaffolds *Regenerative Biomaterials*, **6** 99-106.

Carano, R.A.D. and E.H. Filvaroff (2003) Angiogenesis and bone repair *Drug Discovery Today*, **8** 980-989.

Carroll, S.F., C.T. Buckley, and D.J. Kelly (2014) Cyclic hydrostatic pressure promotes a stable cartilage phenotype and enhances the functional development of cartilaginous grafts

engineered using multipotent stromal cells isolated from bone marrow and infrapatellar fat pad *Journal of Biomechanics*, **47** 2115-2121.

Castilho, M., G. Hochleitner, W. Wilson, B. van Rietbergen, P.D. Dalton, J. Groll, J. Malda, and K. Ito (2018) Mechanical behavior of a soft hydrogel reinforced with three-dimensional printed microfibre scaffolds *Scientific Reports*, **8** 1245.

Castilho, M., V. Mouser, M. Chen, J. Malda, and K. Ito (2019) Bi-layered micro-fibre reinforced hydrogels for articular cartilage regeneration *Acta Biomaterialia*, **95** 297-306.

Chang, R., K. Emami, H. Wu, and W. Sun (2010) Biofabrication of a three-dimensional liver micro-organ as an in vitro drug metabolism model *Biofabrication*, **2**.

Chaudhuri, O., L. Gu, D. Klumpers, M. Darnell, S.A. Bencherif, J.C. Weaver, N. Huebsch, H.P. Lee, E. Lippens, G.N. Duda, and D.J. Mooney (2016) Hydrogels with tunable stress relaxation regulate stem cell fate and activity *Nat Mater*, **15** 326-34.

Checa, S. and P.J. Prendergast (2009) A mechanobiological model for tissue differentiation that includes angiogenesis: A lattice-based modeling approach *Annals of Biomedical Engineering*, **37** 129-145.

Chen, H., F.Y. Ghori-Javed, H. Rashid, M.D. Adhami, R. Serra, S.E. Gutierrez, and A. Javed (2014a) Runx2 regulates endochondral ossification through control of chondrocyte proliferation and differentiation *Journal of bone and mineral research : the official journal of the American Society for Bone and Mineral Research*, **29** 2653-65.

Chen, Y., J. Wang, X. Zhu, Y. Fan, and X. Zhang (2014b) Adsorption and release behaviors of vascular endothelial growth factor on porous hydroxyapatite ceramic under competitive conditions *Journal of Biomaterials and Tissue Engineering*, **4** 155-161.

Chimene, D., K.K. Lennox, R.R. Kaunas, and A.K. Gaharwar (2016a) Advanced Bioinks for 3D Printing: A Materials Science Perspective *Ann Biomed Eng*, **44** 2090-102.

Chimene, D., K.K. Lennox, R.R. Kaunas, and A.K. Gaharwar (2016b) Advanced Bioinks for 3D Printing: A Materials Science Perspective *Annals of Biomedical Engineering*, **44** 2090-2102.

Chin-Purcell, M.V. and J.L. Lewis (1996) Fracture of articular cartilage. *Journal of biomechanical engineering*, **118** 545-556.

Clarke, I.C. (1971) Surface characteristics of human articular cartilage--a scanning electron microscope study. *Journal of Anatomy*, **108** 23-30.

Clarkin, C. and B.R. Olsen (2010) On bone-forming cells and blood vessels in bone development *Cell Metabolism*, **12** 314-316.

Cochis, A., S. Grad, M.J. Stoddart, S. Farè, L. Altomare, B. Azzimonti, M. Alini, and L. Rimondini (2017) Bioreactor mechanically guided 3D mesenchy mal stem cell chondrogenesis using a biocompatible novel thermo-reversible methylcellulose-based hydrogel *Scientific Reports*, **7** 1-12.

Cohen, N.P., R.J. Foster, and V.C. Mow (1998) Composition and Dynamics of Articular Cartilage : Structure , Function , and Maintaining H ealthy State *Journal of Orthopadic and sports physical therapy*, **28** 203-215.

Cooke, M.E., A.A. Allon, T. Cheng, A.C. Kuo, H.T. Kim, T.P. Vail, R.S. Marcucio, R.A. Schneider, J.C. Lotz, and T. Alliston (2011) Structured three-dimensional co-culture of mesenchymal stem cells with chondrocytes promotes chondrogenic differentiation without hypertrophy. *Osteoarthritis and cartilage*, **19** 1210-8.

Cooke, M.E., B.M. Lawless, S.W. Jones, and L.M. Grover (2018) Matrix degradation in osteoarthritis primes the superficial region of cartilage for mechanical damage *Acta Biomaterialia*, **78** 320-328.

Cooper, B.G., R.C. Stewart, D. Burstein, B.D. Snyder, and M.W. Grinstaff (2016) A Tissue-Penetrating Double Network Restores the Mechanical Properties of Degenerated Articular Cartilage *Angewandte Chemie - International Edition*, **55** 4226-4230.

Critchley, S., G. Cunniffe, A. O'Reilly, P. Diaz-Payno, R. Schipani, A. McAlinden, D. Withers, J. Shin, E. Alsberg, and D.J. Kelly (2019) Regeneration of Osteochondral Defects Using Developmentally Inspired Cartilaginous Templates *Tissue Eng Part A*, **25** 159-171.

Critchley, S., P. Diaz, R. Schipani, A. Mcalinden, D. Withers, J. Shin, E. Alsberg, D. Kelly, T. Centre, M. Engineering, A. Materials, V. Medicine, S.S. Clinic, B. Engineering, O. Surgery, N. Centre, R. Medicine, C.A. Prof, and T. Centre (2018a) Regeneration of osteochondral defects using developmentally inspired cartilaginous templates 1-36.

Critchley, S.E., R. Eswaramoorthy, and D.J. Kelly (2018b) Low-oxygen conditions promote synergistic increases in chondrogenesis during co-culture of human osteoarthritic stem cells and chondrocytes *Journal of Tissue Engineering and Regenerative Medicine*, **12** 1074-1084.

Critchley, S.E. and D.J. Kelly (2017) Bioinks for bioprinting functional meniscus and articular cartilage *Journal of 3D Printing in Medicine*, **1** 269-290.

Cunniffe, G.M., P.J. Díaz-Payno, E.J. Sheehy, S.E. Critchley, H.V. Almeida, P. Pitacco, S.F. Carroll, O.R. Mahon, A. Dunne, T.J. Levingstone, C.J. Moran, R.T. Brady, F.J. O'Brien, P.A.J. Brama, and D.J. Kelly (2019) Tissue-specific extracellular matrix scaffolds for the regeneration of spatially complex musculoskeletal tissues *Biomaterials*, **188** 63-73.

Cunniffe, G.M., F.J. O'Brien, S. Partap, T.J. Levingstone, K.T. Stanton, and G.R. Dickson (2010) The synthesis and characterization of nanophase hydroxyapatite using a novel dispersant-aided precipitation method *Journal of Biomedical Materials Research - Part A*, **95** 1142-1149.

Cunniffe, G.M., T. Vinardell, E.M. Thompson, A.C. Daly, A. Matsiko, F.J. O'Brien, and D.J. Kelly (2015) Chondrogenically primed mesenchymal stem cell-seeded alginate hydrogels promote early bone formation in critically-sized defects *European Polymer Journal*, **72** 464-472.

Da, H., S.-J. Jia, G.-L. Meng, J.-H. Cheng, W. Zhou, Z. Xiong, Y.-J. Mu, and J. Liu (2013) The impact of compact layer in biphasic scaffold on osteochondral tissue engineering. *PloS one*, **8** e54838.

Dahlin, R.L., L.A. Kinard, J. Lam, C.J. Needham, S. Lu, F.K. Kasper, and A.G. Mikos (2014) Articular chondrocytes and mesenchymal stem cells seeded on biodegradable scaffolds for the repair of cartilage in a rat osteochondral defect model. *Biomaterials*, **35** 7460-9.

Daly, A.C., S.E. Critchley, E.M. Rencsok, and D.J. Kelly (2016a) A comparison of different bioinks for 3D bioprinting of fi brocartilage and hyaline cartilage *Biofabrication*, **8** 1-10.

Daly, A.C., G.M. Cunniffe, B.N. Sathy, O. Jeon, E. Alsberg, and D.J. Kelly (2016b) 3D Bioprinting of Developmentally Inspired Templates for Whole Bone Organ Engineering. *Advanced healthcare materials*, **5** 2353-62.

Daly, A.C., F.E. Freeman, T. Gonzalez-Fernandez, S.E. Critchley, J. Nulty, and D.J. Kelly (2017a) 3D Bioprinting for Cartilage and Osteochondral Tissue Engineering *Advanced Healthcare Materials*, **1700298** 1700298.

Daly, A.C., F.E. Freeman, T. Gonzalez-Fernandez, S.E. Critchley, J. Nulty, and D.J. Kelly (2017b) 3D Bioprinting for Cartilage and Osteochondral Tissue Engineering *Adv Healthc Mater*, **6**.

Daly, A.C., B.N. Sathy, D.J. Kelly, D.J. Kelly, T. Centre, T. Biomedical, and T.C. Dublin (2018) Engineering large cartilage tissues using dynamic bioreactor culture at defined oxygen conditions Corresponding author : *Journal of Tissue Engineering*, **In press**.

Darling, E.M. and K.A. Athanasiou (2005) Rapid phenotypic changes in passaged articular chondrocyte subpopulations *Journal of Orthopaedic Research*, **23** 425-432.

Darling, E.M. and K.A. Athanasiou (2003) Biomechanical strategies for articular cartilage regeneration. *Annals of biomedical engineering*, **31** 1114-24.

Day, J.S., M. Ding, J.C. Van Der Linden, I. Hvid, D.R. Sumner, and H. Weinans (2001) A decreased subchondral trabecular bone tissue elastic modulus is associated with pre-arthritic cartilage damage *Journal of Orthopaedic Research*, **19** 914-918.

Diaz-Romero, J., D. Nesic, S.P. Grogan, P. Heini, and P. Mainil-Varlet (2008) Immunophenotypic changes of human articular chondrocytes during monolayer culture reflect bona fide dedifferentiation rather than amplification of progenitor cells. *Journal of cellular physiology*, **214** 75-83.

Díaz Lantada, A., H. Alarcón Iniesta, and J.P. García-Ruíz (2016) Composite scaffolds for osteochondral repair obtained by combination of additive manufacturing, leaching processes and hMSC-CM functionalization *Materials Science and Engineering C*, **59** 218-227.

Ding, C., Z. Qiao, W. Jiang, H. Li, J. Wei, G. Zhou, and K. Dai (2013) Regeneration of a goat femoral head using a tissue-specific, biphasic scaffold fabricated with CAD/CAM technology *Biomaterials*, **34** 6706-6716.

Domingos, M., F. Chiellini, A. Gloria, L. Ambrosio, P. Bartolo, and E. Chiellini (2012) Effect of process parameters on the morphological and mechanical properties of 3D Bioextruded poly(1-caprolactone) scaffolds *Rapid Prototyping Journal*, **18** 56-67.

Doyle, H., S. Lohfeld, P. McDonnell, and P. McHugh (2014) Evaluation of a Multiscale Modelling Methodology to Predict the Mechanical Properties of PCL/β-TCP Sintered Scaffold Materials. *Annals of biomedical engineering*, **43** 1989-1998.

Drury, J.L., R.G. Dennis, and D.J. Mooney (2004) The tensile properties of alginate hydrogels *Biomaterials*, **25** 3187-3199.

Drury, J.L. and D.J. Mooney (2003) Hydrogels for tissue engineering: Scaffold design variables and applications *Biomaterials*, **24** 4337-4351.

Edmonds, E.W. and J. Polousky (2013) A review of knowledge in osteochondritis dissecans: 123 years of minimal evolution from könig to the ROCK study group general *Clinical Orthopaedics and Related Research*, **471** 1118-1126.

Elder, B.D. and K.A. Athanasiou (2009a) Hydrostatic pressure in articular cartilage tissue engineering: from chondrocytes to tissue regeneration. *Tissue engineering. Part B, Reviews*, **15** 43-53.

Elder, S.H., A.J. Cooley, A. Borazjani, B.L. Sowell, H. To, and S.C. Tran (2009b) Production of hyaline-like cartilage by bone marrow mesenchymal stem cells in a self-assembly model *Tissue Engineering - Part A*, **15** 3025-3036.

Engler, A.J., S. Sen, H.L. Sweeney, and D.E. Discher (2006) Matrix Elasticity Directs Stem Cell Lineage Specification *Cell*, **126** 677-689.

Entezari, A., S.-I. Roohani-Esfahani, Z. Zhang, H. Zreiqat, C.R. Dunstan, Q. Li, V.M. Goldberg, P.V. Giannoudis, H. Dinopoulos, E. Tsiridis, E. Gentleman, R.O. Ritchie, J.S. Carson, M.P. Bostrom, T.L. Arinzeh, T. Tran, J. Mcalary, G. Daculsi, H. Li, J. Chang, S. Cai, J. Blaker, S. Nazhat, V. Maquet, A. Boccaccini, S. Roohani-Esfahani, Y.H. Chen, S.W. Zhou, Q. Li, Y.H. Chen, S.W. Zhou, Q. Li, P. Miranda, A. Pajares, F. Guiberteau, P. Miranda, A. Pajares, E. Saiz, A.P. Tomsia, F. Guiberteau, Y. Yan, S.-H. Park, D. Ngo, A. Scordelis, J.C. Simo, J. Oliver, F. Armero, M. Jirásek, J. Dolbow, T. Belytschko, T. Belytschko, T. Black, F. Amiri, C. Anitescu, M. Arroyo, S.P.A. Bordas, T. Rabczuk, Z. Zhang, Z. Zhang, S.I. Roohani-Esfahani, P. Newman, H. Zreiqat, N. Zhan, J.L. Chen, Q. Liu, S.-I. Roohani-Esfahani, Y. Chen, J. Shi, H. Zreiqat, K. Lin, C. Wu, J. Chang, Z. Zhang, C. Wu, J. Chang, W. Zhai, C.T. Wu, Y.X. Luo, G. Cuniberti, Y. Xiao, M. Gelinsky, E. Giner, N. Sukumar, J. Tarancon, F. Fuenmayor, J. Shi, D. Chopp, J. Lua, N. Sukumar, T. Belytschko, B. Karihaloo, Q. Xiao, Z. Zhang, M. Thompson, Z. Zhang, C. Field, Q. Li, and M. Swain (2016) Fracture behaviors of ceramic tissue scaffolds for load bearing applications *Scientific Reports*, **6** 28816.

Erickson, I.E., A.H. Huang, C. Chung, R.T. Li, J.A. Burdick, and R.L. Mauck (2009) Differential Maturation and Structure–Function Relationships in Mesenchymal Stem Cell- and Chondrocyte-Seeded Hydrogels *Tissue Engineering Part A*, **15** 1041-1052.

Escobar Ivirico, J.L., M. Bhattacharjee, E. Kuyinu, L.S. Nair, and C.T. Laurencin (2017) Regenerative Engineering for Knee Osteoarthritis Treatment: Biomaterials and Cell-Based Technologies *Engineering*, **3** 16-27.

Eshraghi, S. and S. Das (2012) Micromechanical finite-element modeling and experimental characterization of the compressive mechanical properties of polycaprolactone-hydroxyapatite composite scaffolds prepared by selective laser sintering for bone tissue engineering *Acta Biomaterialia*, **8** 3138-43.

Eslami, M., N.E. Vrana, P. Zorlutuna, S. Sant, S. Jung, N. Masoumi, R.A. Khavari-Nejad, G. Javadi, and A. Khademhosseini (2014) Fiber-reinforced hydrogel scaffolds for heart valve tissue engineering *Journal of Biomaterials Applications*, **29** 399-410.

Eyre, D. (2002) Collagen of articular cartilage *Arthritis Research*, **4** 30-35.

Federico, S. and W. Herzog (2008) On the anisotropy and inhomogeneity of permeability in articular cartilage *Biomechanics and Modeling in Mechanobiology*, **7** 367-378.

Filardo, G., E. Kon, A. Di Martino, M. Busacca, G. Altadonna, and M. Marcacci (2013a) Treatment of knee osteochondritis dissecans with a cell-free biomimetic osteochondral scaffold: Clinical and imaging evaluation at 2-year follow-up *American Journal of Sports Medicine*, **41** 1786-1793.

Filardo, G., E. Kon, A. Roffi, A. Di Martino, and M. Marcacci (2013b) Scaffold-based repair for cartilage healing: A systematic review and technical note *Arthroscopy - Journal of Arthroscopic and Related Surgery*, **29** 174-186.

Fischer, J., A. Dickhut, M. Rickert, and W. Richter (2010) Human articular chondrocytes secrete parathyroid hormone-related protein and inhibit hypertrophy of mesenchymal stem cells in coculture during chondrogenesis *Arthritis Rheum*, **62** 2696-2706.

Freeman, F.E. and D.J. Kelly (2017) Tuning alginate bioink stiffness and composition for controlled growth factor delivery and to spatially direct MSC Fate within bioprinted tissues *Scientific Reports*, **7** 1-12.

Freeman, I., A. Kedem, and S. Cohen (2008) The effect of sulfation of alginate hydrogels on the specific binding and controlled release of heparin-binding proteins *Biomaterials*, **29** 3260-3268.

Frost, H.M. (1999) Joint anatomy, design, and arthroses: Insights of the Utah paradigm *Anatomical Record*, **255** 162-174.

Gannon, A.R., T. Nagel, A.P. Bell, N.C. Avery, and D.J. Kelly (2015a) The changing role of the superficial region in determining the dynamic compressive properties of articular cartilage during postnatal development *Osteoarthritis Cartilage*, **23** 975-84.

Gannon, A.R., T. Nagel, A.P. Bell, N.C. Avery, and D.J. Kelly (2015b) Postnatal changes to the mechanical properties of articular cartilage are driven by the evolution of its Collagen network *European Cells and Materials*, **29** 105-123.

Gannon, A.R., T. Nagel, and D.J. Kelly (2012) The role of the superficial region in determining the dynamic properties of articular cartilage *Osteoarthritis Cartilage*, **20** 1417-25.

Gao, L.L., C.Q. Zhang, H. Gao, Z.D. Liu, and P.P. Xiao (2014) Depth and rate dependent mechanical behaviors for articular cartilage: Experiments and theoretical predictions *Materials Science and Engineering C*, **38** 244-251.

Giannitelli, S.M., D. Accoto, M. Trombetta, and A. Rainer (2014) Current trends in the design of scaffolds for computer-aided tissue engineering *Acta Biomaterialia*, **10** 580-594.

Gioe, T.J., C. Novak, P. Sinner, W. Ma, and S. Mehle (2007) Knee arthroplasty in the young patient: Survival in a community registry *Clinical Orthopaedics and Related Research* 83-87.

Giovannini, S., J. Diaz-Romero, T. Aigner, P. Heini, P. Mainil-Varlet, and D. Nesic (2010) Micromass co-culture of human articular chondrocytes and human bone marrow mesenchymal stem cells to investigate stable neocartilage tissue formation in vitro *European Cells and Materials*, **20** 245-259.

Gleadall, A., I. Ashcroft, and J. Segal (2018) VOLCO: A predictive model for 3D printed microarchitecture *Additive Manufacturing*, **21** 605-618.

Gleghorn, J.P. and L.J. Bonassar (2008) Lubrication mode analysis of articular cartilage using Stribeck surfaces *Journal of Biomechanics*, **41** 1910-1918.

Glyn-Jones, S., A.J.R. Palmer, R. Agricola, A.J. Price, T.L. Vincent, H. Weinans, and A.J. Carr (2015) Osteoarthritis *The Lancet*, **386** 376-387.

Goldring, S.R. and M.B. Goldring (2016) Changes in the osteochondral unit during osteoarthritis: Structure, function and cartilage bone crosstalk *Nature Reviews Rheumatology*, **12** 632-644.

Gomez, C.G., M. Rinaudo, and M.A. Villar (2007) Oxidation of sodium alginate and characterization of the oxidized derivatives *Carbohydrate Polymers*, **67** 296-304.

Gomoll, A.H., G. Filardo, L. de Girolamo, J. Espregueira-Mendes, J. Esprequeira-Mendes, M. Marcacci, W.G. Rodkey, J.R. Steadman, R.J. Steadman, S. Zaffagnini, and E. Kon (2012) Surgical treatment for early osteoarthritis. Part I: cartilage repair procedures. *Knee surgery, sports traumatology, arthroscopy : official journal of the ESSKA*, **20** 450-66.

Gonçalves, E.M., F.J. Oliveira, R.F. Silva, M.A. Neto, M.H. Fernandes, M. Amaral, M. Vallet-Regí, and M. Vila (2016) Three-dimensional printed PCL-hydroxyapatite scaffolds filled with CNTs for bone cell growth stimulation *Journal of Biomedical Materials Research - Part B Applied Biomaterials*, **104** 1210-1219.

Grayson, W.L., S. Bhumiratana, P.H. Grace Chao, C.T. Hung, and G. Vunjak-Novakovic (2010) Spatial regulation of human mesenchymal stem cell differentiation in engineered osteochondral constructs: effects of pre-differentiation, soluble factors and medium perfusion. *Osteoarthritis and cartilage*, **18** 714-23.

Gu, L., O. Chaudhuri, H.-p. Lee, D.J. Mooney, and M.E. Levenston (2017) Mechanical confinement regulates cartilage matrix formation by chondrocytes *Nature Materials*, **16** 1243-1251.

Gudas, R., R.J. Kalesinskas, V. Kimtys, E. Stankevičius, V. Toliušis, G. Bernotavičius, and A. Smailys (2005) A prospective randomized clinical study of mosaic osteochondral autologous transplantation versus microfracture for the treatment of osteochondral defects in the knee joint in young athletes *Arthroscopy - Journal of Arthroscopic and Related Surgery*, **21** 1066-1075.

Guilak, F. (2005) The slippery slope of arthritis *Arthritis and Rheumatism*, **52** 1632-1633.

Guilak, F., D.L. Butler, and S.A. Goldstein (2001) Functional tissue engineering: the role of biomechanics in articular cartilage repair. *Clinical orthopaedics and related research* S295-305.

Guilak, F., D.M. Cohen, B.T. Estes, J.M. Gimble, W. Liedtke, and C.S. Chen (2009) Control of stem cell fate by physical interactions with the extracellular matrix. *Cell stem cell*, **5** 17-26.

Gunatillake, P.A. and R. Adhikari (2003) Biodegradable synthetic polymers for tissue engineering. *European cells & materials*, **5** 1-16; discussion 16.

Guvendiren, M., H.D. Lu, and J.A. Burdick (2012) Shear-thinning hydrogels for biomedical applications *Soft Matter*, **8** 260-272.

Hankenson, K.D., K. Gagne, and M. Shaughnessy (2015) Extracellular signaling molecules to promote fracture healing and bone regeneration *Advanced Drug Delivery Reviews*, **94** 3-12.

Harada, N., Y. Watanabe, K. Sato, S. Abe, K. Yamanaka, Y. Sakai, T. Kaneko, and T. Matsushita (2014) Bone regeneration in a massive rat femur defect through endochondral ossification achieved with chondrogenically differentiated MSCs in a degradable scaffold *Biomaterials*, **35** 7800-7810.

Hardingham, T.E. and A.J. Fosang (1992) Proteoglycans: many forms and many functions. *FASEB journal : official publication of the Federation of American Societies for Experimental Biology*, **6** 861-70.

Hawker, G.A. (2019) Osteoarthritis is a serious disease *Clinical and experimental rheumatology*, **37** 3-6.

Henderson, I.J.P. and D.P. La Valette (2005) Subchondral bone overgrowth in the presence of full-thickness cartilage defects in the knee *Knee*, **12** 435-440.

Hendriks, J., J. Riesle, and C.A. van Blitterswijk (2009) Co-culture in cartilage tissue engineering. *Journal of tissue engineering and regenerative medicine*, **1** 170-8.

Hendrikson, W.J., A.J. Deegan, Y. Yang, C.A. van Blitterswijk, N. Verdonschot, L. Moroni, and J. Rouwkema (2017) Influence of Additive Manufactured Scaffold Architecture on the Distribution of Surface Strains and Fluid Flow Shear Stresses and Expected Osteochondral Cell Differentiation *Frontiers in Bioengineering and Biotechnology*, **5** 6.

Hoemann, C.D., C.-H. Lafantaisie-Favreau, V. Lascau-Coman, G. Chen, and J. Guzmán-Morales (2012a) The cartilage-bone interface. *The journal of knee surgery*, **25** 85-97.

Hoemann, C.D., C.-H. Lafantaisie-Favreau, V. Lascau-Coman, G. Chen, and J. Guzmán-Morales (2012b) The cartilage-bone interface *The journal of knee surgery*, **25** 85-97.

Hofmann, S., S. Knecht, R. Langer, D.L. Kaplan, G. Vunjak-Novakovic, H.P. Merkle, and L. Meinel (2006) Cartilage-like Tissue Engineering Using Silk Scaffolds and Mesenchymal Stem Cells *Tissue Engineering*, **0** 060915113954001.

Hollister, S.J. (2005) Porous scaffold design for tissue engineering. *Nature materials*, **4** 518-24.

Hollister, S.J., C.L. Flanagan, R.J. Morrison, J.J. Patel, M.B. Wheeler, S.P. Edwards, and G.E. Green (2016) Integrating Image-Based Design and 3D Biomaterial Printing to Create Patient Specific Devices within a Design Control Framework for Clinical Translation *ACS Biomaterials Science and Engineering*, **2** 1827-1836.

Horkay, F. (2012) Interactions of cartilage extracellular matrix macromolecules *Journal of Polymer Science, Part B: Polymer Physics*, **50** 1699-1705.

Hu, J.C. and K.A. Athanasiou (2006) A self-assembling process in articular cartilage tissue engineering *Tissue Engineering*, **12** 969-979.

Huang, A.H., M.J. Farrell, M. Kim, and R.L. Mauck (2010) Long-term dynamic loading improves the mechanical properties of chondrogenic mesenchymal stem cell-laden hydrogels *European Cells and Materials*, **19** 72-85.

Huang, C.-Y.C., K.L. Hagar, L.E. Frost, Y. Sun, and H.S. Cheung (2004) Effects of cyclic compressive loading on chondrogenesis of rabbit bone-marrow derived mesenchymal stem cells. *Stem cells (Dayton, Ohio)*, **22** 313-23.

Huang, C.Y., V.C. Mow, and G.A. Ateshian (2001) The role of flow-independent viscoelasticity in the biphasic tensile and compressive responses of articular cartilage *Journal of Biomechanical Engineering*, **123** 410-417.

Huang, C.Y., M.A. Soltz, M. Kopacz, V.C. Mow, and G.A. Ateshian (2003) Experimental verification of the roles of intrinsic matrix viscoelasticity and tension-compression nonlinearity in the biphasic response of cartilage *Journal of Biomechanical Engineering*, **125** 84-93.

Huang, J.I., M.M. Durbhakula, P. Angele, B. Johnstone, and J.U. Yoo (2006) Lunate arthroplasty with autologous mesenchymal stem cells in a rabbit model. *The Journal of bone and joint surgery. American volume*, **88** 744-52.

Hung, C.T., R.L. Mauck, C.C.B. Wang, E.G. Lima, and G.A. Ateshian (2004) A paradigm for functional tissue engineering of articular cartilage via applied physiologic deformational loading *Annals of Biomedical Engineering*, **32** 35-49.

Hunter, D.J. and S. Bierma-Zeinstra (2019) Osteoarthritis *The Lancet*, **393** 1745-1759.

Hunziker, E.B. (2002) Articular cartilage repair: Basic science and clinical progress. A review of the current status and prospects *Osteoarthritis and Cartilage*, **10** 432-463.

Igarashi, T., N. Iwasaki, Y. Kasahara, and A. Minami (2010) A cellular implantation system using an injectable ultra-purified alginate gel for repair of osteochondral defects in a rabbit model *Journal of Biomedical Materials Research - Part A*, **94** 844-855.

Imhof, H., M. Breitenseher, F. Kainberger, T. Rand, and S. Trattnig, *Importance of subchondral bone to articular cartilage in health and disease*, in *Topics in Magnetic Resonance Imaging*. 1999. p. 180-192.

Ito, M.M. and M.Y. Kida (2000) Morphological and biochemical re-evaluation of the process of cavitation in the rat knee joint: Cellular and cell strata alterations in the interzone *Journal of Anatomy*, **197** 659-679.

Iwakura, T., R. Sakata, and A.H. Reddi (2013) Induction of chondrogenesis and expression of superficial zone protein in synovial explants with TGF-β1 and BMP-7 *Tissue Engineering - Part A*, **19** 2638-2644.

Izadifar, Z., X. Chen, and W. Kulyk (2012) Strategic design and fabrication of engineered scaffolds for articular cartilage repair. *Journal of functional biomaterials*, **3** 799-838.

Jay, G.D. and K.A. Waller (2014) The biology of Lubricin: Near frictionless joint motion *Matrix Biology*, **39** 17-24.

Jeon, O., C. Powell, S.M. Ahmed, and E. Alsberg (2010) Biodegradable, photocrosslinked alginate hydrogels with independently tailorable physical properties and cell adhesivity *Tissue Engineering - Part A*, **16** 2915-2925.

Jeon, O., J.-Y. Shin, R. Marks, M. Hopkins, T.-H. Kim, H.-H. Park, and E. Alsberg (2017a) Highly Elastic and Tough Interpenetrating Polymer Network-Structured Hybrid Hydrogels for Cyclic Mechanical Loading-Enhanced Tissue Engineering *Chem Mater*, **29** 8425-8432.

Jeon, O., J.Y. Shin, R. Marks, M. Hopkins, T.H. Kim, H.H. Park, and E. Alsberg (2017b) Highly elastic and tough interpenetrating polymer network-structured hybrid hydrogels for cyclic mechanical loading-enhanced tissue engineering *Chemistry of Materials*, **29** 8425-8432.

Jiang, J., A. Tang, G.A. Ateshian, X. Edward Guo, C.T. Hung, and H.H. Lu (2010) Bioactive stratified polymer ceramic-hydrogel scaffold for integrative osteochondral repair *Annals of Biomedical Engineering*, **38** 2183-2196.

Jiao, Z., B. Luo, S. Xiang, H. Ma, Y. Yu, and W. Yang (2019) 3D printing of HA / PCL composite tissue engineering scaffolds *Advanced Industrial and Engineering Polymer Research*, **2** 196-202.

Johnson, V.L. and D.J. Hunter (2014) The epidemiology of osteoarthritis *Best Practice and Research: Clinical Rheumatology*, **28** 5-15.

Johnstone, B., M. Alini, M. Cucchiarini, G. Dodge, D. Eglin, F. Guilak, H. Madry, A. Mata, R. Mauck, C. Semino, and M. Stoddart (2013) Tissue engineering for articular cartilage repair – the state of the art *Eur Cells Mater*, **25** 248-267.

Johnstone, B., T.M. Hering, A.I. Caplan, V.M. Goldberg, and J.U. Yoo (1998) In vitro chondrogenesis of bone marrow-derived mesenchymal progenitor cells *Experimental Cell Research*, **238** 265-272.

Jukes, J.M., S.K. Both, A. Leusink, L.M.T. Sterk, C.a. van Blitterswijk, and J. de Boer (2008) Endochondral bone tissue engineering using embryonic stem cells. *Proceedings of the National Academy of Sciences of the United States of America*, **105** 6840-6845.

Jung, Y., S.H. Kim, Y.H. Kim, and S.H. Kim (2010) The effect of hybridization of hydrogels and poly(L-lactide-co-ε- caprolactone) scaffolds on cartilage tissue engineering *Journal of Biomaterials Science, Polymer Edition*, **21** 581-592.

Jurvelin, J.S., M.D. Buschmann, and E.B. Hunziker (1997) Optical and mechanical determination of Poisson's ratio of adult bovine humeral articular cartilage *Journal of Biomechanics*, **30** 235-241.

Kalson, N.S., P.D. Gikas, and T.W.R. Briggs (2010) Current strategies for knee cartilage repair *International Journal of Clinical Practice*, **64** 1444-1452.

Kanczler, J.M., P.J. Ginty, L. White, N.M.P. Clarke, S.M. Howdle, K.M. Shakesheff, and R.O.C. Oreffo (2010) The effect of the delivery of vascular endothelial growth factor and bone morphogenic protein-2 to osteoprogenitor cell populations on bone formation *Biomaterials*, **31** 1242-1250.

Kang, H.-W., S.J. Lee, I.K. Ko, C. Kengla, J.J. Yoo, and A. Atala (2016) A 3D bioprinting system to produce human-scale tissue constructs with structural integrity *Nature Biotechnology*, **34** 312-319.

Kang, N., X. Liu, Y. Guan, J. Wang, F. Gong, X. Yang, L. Yan, Q. Wang, X. Fu, Y. Cao, and R. Xiao (2012) Effects of co-culturing BMSCs and auricular chondrocytes on the elastic modulus and hypertrophy of tissue engineered cartilage *Biomaterials*, **33** 4535-4544.

Karamooz Ravari, M.R., M. Kadkhodaei, M. Badrossamay, and R. Rezaei (2014) Numerical investigation on mechanical properties of cellular lattice structures fabricated by fused deposition modeling *International Journal of Mechanical Sciences*, **88** 154-161.

Katta, J., T. Stapleton, E. Ingham, Z.M. Jin, and J. Fisher (2008) The effect of glycosaminoglycan depletion on the friction and deformation of articular cartilage. *Proceedings of the Institution of Mechanical Engineers. Part H, Journal of engineering in medicine*, **222** 1-11.

Keeney, J.A., S. Eunice, G. Pashos, R.W. Wright, and J.C. Clohisy (2011) What is the evidence for total knee arthroplasty in young patients?: A systematic review of the literature *Clinical Orthopaedics and Related Research*, **469** 574-583.

Kempen, D.H.R., L. Lu, A. Heijink, T.E. Hefferan, L.B. Creemers, A. Maran, M.J. Yaszemski, and W.J.A. Dhert (2009) Effect of local sequential VEGF and BMP-2 delivery on ectopic and orthotopic bone regeneration *Biomaterials*, **30** 2816-2825.

Kempson, G.E., M.A. Freeman, and S.A. Swanson (1968) Tensile properties of articular cartilage. *Nature*, **220** 1127-8.

Kempson, G.E., H. Muir, C. Pollard, and M. Tuke (1973) The tensile properties of the cartilage of human femoral condyles related to the content of collagen and glycosaminoglycans *BBA - General Subjects*, **297** 456-472.

Kempson, G.E., H. Muir, S.A.V. Swanson, and M.A.R. Freeman (1970) Correlations between stiffness and the chemical constituents of cartilage on the human femoral head *BBA - General Subjects*, **215** 70-77.

Kim, B.S., H. Kim, G. Gao, J. Jang, and D.W. Cho (2017) Decellularized extracellular matrix: A step towards the next generation source for bioink manufacturing *Biofabrication*, **9**.

Kinnunen, J., S. Saarakkala, M. Hauta-Kasari, P. Vahimaa, and J.S. Jurvelin (2011) Optical spectral reflectance of human articular cartilage – relationships with tissue structure, composition and mechanical properties *Biomedical Optics Express*, **2** 1394.

Kisiday, J.D., D.D. Frisbie, C.W. McIlwraith, and A.J. Grodzinsky (2009) Dynamic compression stimulates proteoglycan synthesis by mesenchymal stem cells in the absence of chondrogenic cytokines *Tissue Engineering - Part A*, **15** 2817-2824.

Klotz, B.J., D. Gawlitta, A.J.W.P. Rosenberg, J. Malda, and P.W. Melchels (2018) Europe PMC Funders Group Gelatin-Methacryloyl Hydrogels : Towards Biofabrication-Based Tissue Repair, **34** 394-407.

Kock, L., C.C. Van Donkelaar, and K. Ito (2012) Tissue engineering of functional articular cartilage: The current status *Cell and Tissue Research*, **347** 613-627.

Kon, E., M. Delcogliano, G. Filardo, D. Pressato, M. Busacca, B. Grigolo, G. Desando, and M. Marcacci (2010) A novel nano-composite multi-layered biomaterial for treatment of osteochondral lesions: Technique note and an early stability pilot clinical trial *Injury*, **41** 693-701.

Kong, H.-J., K.Y. Lee, and D.J. Mooney (2002) Decoupling the dependence of rheological/mechanical properties of hydrogels from solids concentration *Polymer*, **43** 6239-6246.

Kong, H.J., D. Kaigler, K. Kim, and D.J. Mooney (2004) Controlling rigidity and degradation of alginate hydrogels via molecular weight distribution *Biomacromolecules*, **5** 1720-1727.

Koyama, E., Y. Shibukawa, M. Nagayama, H. Sugito, B. Young, T. Yuasa, T. Okabe, T. Ochiai, N. Kamiya, R.B. Rountree, D.M. Kingsley, M. Iwamoto, M. Enomoto-Iwamoto, and M. Pacifici (2008) A distinct cohort of progenitor cells participates in synovial joint and articular cartilage formation during mouse limb skeletogenesis. *Developmental biology*, **316** 62-73.

Krishnan, R., M. Kopacz, and G.A. Ateshian (2010) Experimental Verification of the Role of Interstitial *J Orthop Res*, **22** 565-570.

Kronenberg, H.M. (2003) Developmental regulation of the growth plate *Nature*, **423** 332-6.

Kundu, J., J.-H.H. Shim, J. Jang, S.-W.W. Kim, and D.-W.W. Cho (2015) An additive manufacturing-based PCL-alginate-chondrocyte bioprinted scaffold for cartilage tissue engineering. *Journal of tissue engineering and regenerative medicine*, **9** 1286-97.

Kuyinu, E.L., G. Narayanan, L.S. Nair, and C.T. Laurencin (2016) Animal models of osteoarthritis: Classification, update, and measurement of outcomes *Journal of Orthopaedic Surgery and Research*, **11** 1-27.

Kwon, H., W.E. Brown, C.A. Lee, D. Wang, N. Paschos, J.C. Hu, and K.A. Athanasiou (2019) Surgical and tissue engineering strategies for articular cartilage and meniscus repair *Nature Reviews Rheumatology*.

Lacroix, D., J.A. Planell, and P.J. Prendergast (2009) Computer-aided design and finite-element modelling of biomaterial scaffolds for bone tissue engineering *Philosophical Transactions of the Royal Society A: Mathematical, Physical and Engineering Sciences*, **367** 1993-2009.

Lakin, B.A., D.J. Grasso, S.S. Shah, R.C. Stewart, P.N. Bansal, J.D. Freedman, M.W. Grinstaff, and B.D. Snyder (2013) Cationic agent contrast-enhanced computed tomography imaging of cartilage correlates with the compressive modulus and coefficient of friction. *Osteoarthritis and cartilage*, **21** 60-8.

Lakin, B.A., B.D. Snyder, and M.W. Grinstaff (2017) Assessing Cartilage Biomechanical Properties: Techniques for Evaluating the Functional Performance of Cartilage in Health and Disease *Annual Review of Biomedical Engineering*, **19** 27-55.

Lamb, K.J., J.C. Lewthwaite, E.R. Bastow, and A.A. Pitsillides (2003) Defining boundaries during joint cavity formation: Going out on a limb *International Journal of Experimental Pathology*, **84** 55-67.

Laupattarakasem, W., M. Laopaiboon, P. Laupattarakasem, and C. Sumananont (2008) Arthroscopic debridement for knee osteoarthritis *Cochrane Database of Systematic Reviews*.

Lee, C.H., J.L. Cook, A. Mendelson, E.K. Moioli, H. Yao, and J.J. Mao (2010) Regeneration of the articular surface of the rabbit synovial joint by cell homing: a proof of concept study. *Lancet (London, England)*, **376** 440-8.

Lee, C.H., S.A. Rodeo, L.A. Fortier, C. Lu, C. Erisken, and J.J. Mao (2014) Protein-releasing polymeric scaffolds induce fibrochondrocytic differentiation of endogenous cells for knee meniscus regeneration in sheep. *Science translational medicine*, **6** 266ra171.

Lee, D.W., W.S. Choi, M.W. Byun, H.J. Park, Y.M. Yu, and C.M. Lee (2003) Effect of γ-irradiation on degradation of alginate *J Agric Food Chem*, **51** 4819-4823.

Lee, H.J., Y.B. Kim, S.H. Ahn, J.S. Lee, C.H. Jang, H. Yoon, W. Chun, and G.H. Kim (2015) A New Approach for Fabricating Collagen/ECM-Based Bioinks Using Preosteoblasts and Human Adipose Stem Cells *Advanced Healthcare Materials*, **4** 1359-1368.

Lee, K.Y. and D.J. Mooney (2012) Alginate: Properties and biomedical applications *Progress in Polymer Science (Oxford)*, **37** 106-126.

Lepage, S.I.M., N. Robson, H. Gilmore, O. Davis, A. Hooper, S. St John, V. Kamesan, P. Gelis, D. Carvajal, M. Hurtig, and T.G. Koch (2019) Beyond Cartilage Repair: The Role of the Osteochondral Unit in Joint Health and Disease *Tissue Engineering - Part B: Reviews*, **25** 114-125.

Levato, R., W.R. Webb, I.A. Otto, A. Mensinga, Y. Zhang, M. van Rijen, R. van Weeren, I.M. Khan, and J. Malda (2017) The bio in the ink: cartilage regeneration with bioprintable hydrogels and articular cartilage-derived progenitor cells *Acta Biomaterialia*, **61** 41-53.

Levett, P.A., F.P.W. Melchels, K. Schrobback, D.W. Hutmacher, J. Malda, and T.J. Klein (2014a) Chondrocyte redifferentiation and construct mechanical property development in single-component photocrosslinkable hydrogels *Journal of Biomedical Materials Research - Part A*, **102** 2544-2553.

Levett, P.A., F.P.W. Melchels, K. Schrobback, D.W. Hutmacher, J. Malda, and T.J. Klein (2014b) A biomimetic extracellular matrix for cartilage tissue engineering centered on photocurable gelatin, hyaluronic acid and chondroitin sulfate *Acta Biomaterialia*, **10** 214-223.

Levingstone, T.J., A. Ramesh, R.T. Brady, P.A.J. Brama, C. Kearney, J.P. Gleeson, and F.J. O'Brien (2016) Cell-free multi-layered collagen-based scaffolds demonstrate layer specific regeneration of functional osteochondral tissue in caprine joints *Biomaterials*, **87** 69-81.

Li, L., F. Yu, L. Zheng, R. Wang, W. Yan, Z. Wang, J. Xu, J. Wu, D. Shi, L. Zhu, X. Wang, and Q. Jiang (2019) Natural hydrogels for cartilage regeneration: Modification, preparation and application *Journal of Orthopaedic Translation*, **17** 26-41.

Li, W.J., Y.J. Jiang, and R.S. Tuan (2008) Cell-nanofiber-based cartilage tissue engineering using improved cell seeding, growth factor, and bioreactor technologies *Tissue Engineering - Part A.*, **14** 639-648.

Li, X., S. Chen, J. Li, X. Wang, J. Zhang, N. Kawazoe, and G. Chen (2016) 3D culture of chondrocytes in gelatin hydrogels with different stiffness *Polymers*, **8**.

Li, Z., S. Huang, Y. Liu, Y. Bin, T. Hu, H. Shi, and J. Xie (2018) Tuning Alginate-Gelatin Bioink Properties by Varying Solvent and Their Impact on Stem Cell Behavior 1-8.

Liao, I.-C., F.T. Moutos, B.T. Estes, X. Zhao, and F. Guilak (2013a) Composite Three-Dimensional Woven Scaffolds with Interpenetrating Network Hydrogels to Create Functional Synthetic Articular Cartilage *Advanced Functional Materials*, **23** 5833-5839.

Liao, I.C., F.T. Moutos, B.T. Estes, X. Zhao, and F. Guilak (2013b) Composite three-dimensional woven scaffolds with interpenetrating network hydrogels to create functional synthetic articular cartilage *Adv Funct Mater*, **23** 5833-5839.

Lieberman, J.R., A. Daluiski, and T.A. Einhorn (2002) The role of growth factors in the repair of bone biology and clinical applications *Journal of Bone and Joint Surgery - Series A*, **84** 1032-1044.

Lipowiecki, M. and D. Brabazon (2010) Design of bone scaffolds structures for rapid prototyping with increased strength and osteoconductivity *Advanced Materials Research*, **83-86** 914-922.

Little, C.J., N.K. Bawolin, and X. Chen (2011) Mechanical Properties of Natural Cartilage and Tissue-Engineered Constructs *Tissue Engineering Part B: Reviews*, **17** 213-227.

Liu, M., X. Yu, F. Huang, S. Cen, G. Zhong, and Z. Xiang (2013) Tissue engineering stratified scaffolds for articular cartilage and subchondral bone defects repair. *Orthopedics*, **36** 868-73.

Liu, X., H. Sun, D. Yan, L. Zhang, X. Lv, T. Liu, W. Zhang, W. Liu, Y. Cao, and G. Zhou (2010) In vivo ectopic chondrogenesis of BMSCs directed by mature chondrocytes *Biomaterials*, **31** 9406-9414.

Loeser, R.F. (2017) the Role of Aging in the Development *Transactions of the American Clinical and Climatological Association*, **128** 44-54.

Lohfeld, S., S. Cahill, H. Doyle, and P.E. McHugh (2015) Improving the finite element model accuracy of tissue engineering scaffolds produced by selective laser sintering *Journal of materials science. Materials in medicine*, **26** 5376.

Loibl, M., A. Binder, M. Herrmann, F. Duttenhoefer, R.G. Richards, M. Nerlich, M. Alini, and S. Verrier (2014) Direct cell-cell contact between mesenchymal stem cells and endothelial

progenitor cells induces a pericyte-like phenotype in vitro. *BioMed research international*, **2014** 395781.

Long, F. and T.F. Linsenmayer (1995) Tissue-specific Regulation of the Type X Collagen Gene *Journal of Biological Chemistry*, **270** 31310-31314.

Longoni, A., L. Knežević, K. Schepers, H. Weinans, A.J.W.P. Rosenberg, and D. Gawlitta (2018) The impact of immune response on endochondral bone regeneration *npj Regenerative Medicine*, **3** 1-11.

Lu, X.L. and V.C. Mow (2008) Biomechanics of articular cartilage and determination of material properties *Med Sci Sports Exerc*, **40** 193-9.

Lyyra-Laitinen, T., M. Niinimäki, J. Töyräs, R. Lindgren, I. Kiviranta, and J.S. Jurvelin (1999) Optimization of the arthroscopic indentation instrument for the measurement of thin cartilage stiffness. *Physics in medicine and biology*, **44** 2511-24.

Lyyra, T., I. Kiviranta, U. Väätäinen, H.J. Helminen, and J.S. Jurvelin (1999) In vivo characterization of indentation stiffness of articular cartilage in the normal human knee *Journal of Biomedical Materials Research*, **48** 482-487.

Mackie, E.J., Y.A. Ahmed, L. Tatarczuch, K.S. Chen, and M. Mirams (2008) Endochondral ossification: How cartilage is converted into bone in the developing skeleton *International Journal of Biochemistry and Cell Biology*, **40** 46-62.

Madry, H., E. Kon, V. Condello, G.M. Peretti, M. Steinwachs, R. Seil, M. Berruto, L. Engebretsen, G. Filardo, and P. Angele (2016) Early osteoarthritis of the knee *Knee Surgery, Sports Traumatology, Arthroscopy*, **24** 1753-1762.

Madry, H., C.N. van Dijk, and M. Mueller-Gerbl (2010) The basic science of the subchondral bone *Knee Surgery, Sports Traumatology, Arthroscopy*, **18** 419-433.

Maes, C., P. Carmeliet, K. Moermans, I. Stockmans, N. Smets, D. Collen, R. Bouillon, and G. Carmeliet (2002) Impaired angiogenesis and endochondral bone formation in mice lacking the vascular endothelial growth factor isoforms VEGF164 and VEGF188 *Mechanisms of Development*, **111** 61-73.

Magill, P., D.P. Byrne, J.F. Baker, and K.J. Mulhall (2011) Review article: Osteochondral reconstruction and grafting. *Journal of orthopaedic surgery (Hong Kong)*, **19** 93-8.

Malda, J., J. Visser, F.P. Melchels, T. Jüngst, W.E. Hennink, W.J.A. Dhert, J. Groll, and D.W. Hutmacher (2013) 25th anniversary article: Engineering hydrogels for biofabrication *Advanced Materials*, **25** 5011-5028.

Mano, J.F. and R.L. Reis (2008) Osteochondral defects: present situation and tissue engineering approaches. *Journal of tissue engineering and regenerative medicine*, **1** 261-73.

Mariani, E., G. Lisignoli, R.M. Borzì, and L. Pulsatelli (2019) Biomaterials: Foreign bodies or tuners for the immune response? *International Journal of Molecular Sciences*, **20**.

Marijnissen, W.J.C.M., G.J.V.M. Van Osch, J. Aigner, S.W. Van Der Veen, A.P. Hollander, H.L. Verwoerd-Verhoef, and J.A.N. Verhaar (2002) Alginate as a chondrocyte-delivery substance in combination with a non-woven scaffold for cartilage tissue engineering *Biomaterials*, **23** 1511-1517.

Marlovits, S., M. Hombauer, M. Truppe, V. Vècsei, and W. Schlegel (2004) Changes in the ratio of type-I and type-II collagen expression during monolayer culture of human chondrocytes *Journal of Bone and Joint Surgery - Series B*, **86** 286-295.

Matricali, G.A., G.P.E. Dereymaeker, and F.P. Luvten (2010) Donor site morbidity after articular cartilage repair procedures: A review *Acta Orthopaedica Belgica*, **76** 669-674.

Mauck, R.L., B.A. Byers, X. Yuan, and R.S. Tuan (2007) Regulation of cartilaginous ECM gene transcription by chondrocytes and MSCs in 3D culture in response to dynamic loading *Biomechanics and Modeling in Mechanobiology*, **6** 113-125.

Mauck, R.L., C.T. Hung, and G.A. Ateshian (2003) Modeling of neutral solute transport in a dynamically loaded porous permeable gel: implications for articular cartilage biosynthesis and tissue engineering. *Journal of biomechanical engineering*, **125** 602-14.

Mauck, R.L., S.L. Seyhan, G.A. Ateshian, and C.T. Hung (2002) Influence of seeding density and dynamic deformational loading on the developing structure/function relationships of chondrocyte-seeded agarose hydrogels *Annals of Biomedical Engineering*, **30** 1046-1056.

Mauck, R.L., M.A. Soltz, C.C.B. Wang, D.D. Wong, P.H.G. Chao, W.B. Valhmu, C.T. Hung, and G.A. Ateshian (2000) Functional tissue engineering of articular cartilage through dynamic loading of chondrocyte-seeded agarose gels *Journal of Biomechanical Engineering*, **122** 252-260.

McCormack, T. and J.M. Mansour (1997) Reduction in tensile strength of cartilage precedes surface damage under repeated compressive loading in vitro *Journal of Biomechanics*, **31** 55-61.

Melancon, D., Z.S. Bagheri, R.B. Johnston, L. Liu, M. Tanzer, and D. Pasini (2017) Mechanical characterization of structurally porous biomaterials built via additive manufacturing: experiments, predictive models, and design maps for load-bearing bone replacement implants. *Acta biomaterialia*, **63** 350-368.

Melchels, F.P.W., K. Bertoldi, R. Gabbrielli, A.H. Velders, J. Feijen, and D.W. Grijpma (2010) Mathematically defined tissue engineering scaffold architectures prepared by stereolithography *Biomaterials*, **31** 6909-6916.

Melchels, F.P.W., W.J.A. Dhert, D.W. Hutmacher, and J. Malda (2014) Development and characterisation of a new bioink for additive tissue manufacturing *Journal of Materials Chemistry B*, **2** 2282-2289.

Melchels, F.P.W., B. Tonnarelli, A.L. Olivares, I. Martin, D. Lacroix, J. Feijen, D.J. Wendt, and D.W. Grijpma (2011) The influence of the scaffold design on the distribution of adhering cells after perfusion cell seeding. *Biomaterials*, **32** 2878-84.

Mente, P.L. and J.L. Lewis (1994) Elastic modulus of calcified cartilage is an order of magnitude less than that of subchondral bone *Journal of Orthopaedic Research*, **12** 637-647.

Meretoja, V.V., R.L. Dahlin, F.K. Kasper, and A.G. Mikos (2012) Enhanced chondrogenesis in co-cultures with articular chondrocytes and mesenchymal stem cells. *Biomaterials*, **33** 6362-9.

Mesallati, T., C.T. Buckley, and D.J. Kelly (2017) Engineering cartilaginous grafts using chondrocyte-laden hydrogels supported by a superficial layer of stem cells *Journal of Tissue Engineering and Regenerative Medicine*, **11** 1343-1353.

Mesallati, T., E.J. Sheehy, T. Vinardell, C.T. Buckley, and D.J. Kelly (2015) Tissue engineering scaled-up, anatomically shaped osteochondral constructs for joint resurfacing *Eur Cells Mater*, **30** 163-186.

Metzger, T.A., S.A. Schwaner, A.J. LaNeve, T.C. Kreipke, and G.L. Niebur (2015) Pressure and shear stress in trabecular bone marrow during whole bone loading *J Biomech*, **48** 3035-43.

Mhanna, R., A. Kashyap, G. Palazzolo, Q. Vallmajo-Martin, J. Becher, S. Möller, M. Schnabelrauch, and M. Zenobi-Wong (2014) Chondrocyte culture in three dimensional alginate sulfate hydrogels promotes proliferation while maintaining expression of chondrogenic markers *Tissue Engineering - Part A*, **20** 1454-1464.

Milan, J.L., J.A. Planell, and D. Lacroix (2009) Computational modelling of the mechanical environment of osteogenesis within a polylactic acid-calcium phosphate glass scaffold *Biomaterials*, **30** 4219-4226.

Minas, T., A.H. Gomoll, R. Rosenberger, R.O. Royce, and T. Bryant (2009) Increased failure rate of autologous chondrocyte implantation after previous treatment with marrow stimulation techniques *American Journal of Sports Medicine*, **37** 902-908.

Mithoefer, K., T. Mcadams, R.J. Williams, P.C. Kreuz, and B.R. Mandelbaum (2009) Clinical efficacy of the microfracture technique for articular cartilage repair in the knee: An evidence-based systematic analysis *American Journal of Sports Medicine*, **37** 2053-2063.

Mo, X.t., S.c. Guo, H.q. Xie, L. Deng, W. Zhi, Z. Xiang, X.q. Li, and Z.m. Yang (2009) Variations in the ratios of co-cultured mesenchymal stem cells and chondrocytes regulate the expression of cartilaginous and osseous phenotype in alginate constructs *Bone*, **45** 42-51.

Moffat, K.L., K. Goon, F.T. Moutos, B.T. Estes, S.J. Oswald, X. Zhao, and F. Guilak (2018) Composite Cellularized Structures Created from an Interpenetrating Polymer Network Hydrogel Reinforced by a 3D Woven Scaffold *Macromolecular Bioscience*, **1800140** 1800140.

Moroni, L., J.R. De Wijn, and C.A. Van Blitterswijk (2006) 3D fiber-deposited scaffolds for tissue engineering: Influence of pores geometry and architecture on dynamic mechanical properties *Biomaterials*, **27** 974-985.

Moroni, L., F.M. Lambers, W. Wilson, C.C. van Donkelaar, J.R. de Wijn, R. Huiskesb, and C.a. van Blitterswijk (2007) Finite Element Analysis of Meniscal Anatomical 3D Scaffolds: Implications for Tissue Engineering. *The open biomedical engineering journal*, **1** 23-34.

Mouser, V.H.M., F.P.W. Melchels, J. Visser, W.J.A. Dhert, D. Gawlitta, and J. Malda (2016) Yield stress determines bioprintability of hydrogels based on gelatin-methacryloyl and gellan gum for cartilage bioprinting *Biofabrication*, **8**.

Moutos, F.T., L.E. Freed, and F. Guilak (2007a) A biomimetic three-dimensional woven composite scaffold for functional tissue engineering of cartilage *Nature Materials*, **6** 162-167.

Moutos, F.T., L.E. Freed, and F. Guilak (2007b) A biomimetic three-dimensional woven composite scaffold for functional tissue engineering of cartilage *Nat Mater*, **6** 162-7.

Moutos, F.T. and F. Guilak (2010) Functional properties of cell-seeded three-dimensionally woven poly(ε-Caprolactone) scaffolds for cartilage tissue engineering *Tissue Engineering - Part A*, **16** 1291-1301.

Moutos, F.T. and F. Guilak (2008) Composite scaffolds for cartilage tissue engineering. *Biorheology*, **45** 501-12.

Mouw, J.K., J.T. Connelly, C.G. Wilson, K.E. Michael, and M.E. Levenston (2007) Dynamic compression regulates the expression and synthesis of chondrocyte-specific matrix molecules in bone marrow stromal cells. *Stem cells (Dayton, Ohio)*, **25** 655-63.

Mow, V.C., G.A. Ateshian, and R.L. Spilker (1993) Biomechanics of diarthrodial joints: A review of twenty years of progress *Journal of Biomechanical Engineering*, **115** 460-467.

Mow, V.C. and X.E. Guo (2002) Mechano-Electrochemical Properties Of Articular Cartilage: Their Inhomogeneities and Anisotropies *Annual Review of Biomedical Engineering*, **4** 175-209.

Mow, V.C., M.H. Holmes, and W. Michael Lai (1984) Fluid transport and mechanical properties of articular cartilage: A review *Journal of Biomechanics*, **17** 377-394.

Mow, V.C., S.C. Kuei, W.M. Lai, and C.G. Armstrong (1980) Biphasic creep and stress relaxation of articular cartilage in compression? Theory and experiments. *Journal of biomechanical engineering*, **102** 73-84.

Mow, V.C., A. Ratcliffe, and A. Robin Poole (1992) Cartilage and diarthrodial joints as paradigms for hierarchical materials and structures *Biomaterials*, **13** 67-97.

Murphy, S.V. and A. Atala (2014a) 3D bioprinting of tissues and organs *Nature Biotechnology*, **32** 773-785.

Murphy, S.V. and A. Atala (2014b) 3D bioprinting of tissues and organs *Nat Biotechnol*, **32** 773-85.

Musumeci, G. (2016) The Effect of Mechanical Loading on Articular Cartilage *Journal of Functional Morphology and Kinesiology*, **1** 154-161.

Naghieh, S., M.R. Karamooz Ravari, M. Badrossamay, E. Foroozmehr, and M. Kadkhodaei (2016) Numerical investigation of the mechanical properties of the additive manufactured bone scaffolds fabricated by FDM: The effect of layer penetration and post-heating *Journal of the Mechanical Behavior of Biomedical Materials*, **59** 241-250.

Naghieh, S., M. Sarker, M. Karamooz-Ravari, A. McInnes, X. Chen, S. Naghieh, M.D. Sarker, M.R. Karamooz-Ravari, A.D. McInnes, and X. Chen (2018) Modeling of the Mechanical Behavior of 3D

Bioplotted Scaffolds Considering the Penetration in Interlocked Strands *Applied Sciences*, **8** 1422.

Nazempour, A., C.R. Quisenberry, N.I. Abu-Lail, and B.J. Van Wie (2017) Combined effects of oscillating hydrostatic pressure, perfusion and encapsulation in a novel bioreactor for enhancing extracellular matrix synthesis by bovine chondrocytes *Cell and Tissue Research*, **370** 179-193.

Nehrer, S., M. Spector, and T. Minas, *Histologic analysis of tissue after failed cartilage repair procedures*, in *Clinical Orthopaedics and Related Research*. 1999. p. 149-162.

Neumann, A.J., T. Quinn, and S.J. Bryant (2016) Nondestructive evaluation of a new hydrolytically degradable and photo-clickable PEG hydrogel for cartilage tissue engineering *Acta Biomaterialia*, **39** 1-11.

Nguyen, Q.T., Y. Hwang, A.C. Chen, S. Varghese, and R.L. Sah (2012) Cartilage-like mechanical properties of poly (ethylene glycol)-diacrylate hydrogels *Biomaterials*, **33** 6682-6690.

Nooeaid, P., V. Salih, J.P. Beier, and A.R. Boccaccini (2012) Osteochondral tissue engineering: Scaffolds, stem cells and applications *Journal of Cellular and Molecular Medicine*, **16** 2247-2270.

Nyberg, E., C. Holmes, T. Witham, and W.L. Grayson (2016) Growth factor-eluting technologies for bone tissue engineering *Drug Delivery and Translational Research*, **6** 184-194.

O'Brien, F.J. (2011) Biomaterials & scaffolds for tissue engineering *Materials Today*, **14** 88-95.

O'Conor, C.J., N. Case, and F. Guilak (2013) Mechanical regulation of chondrogenesis *Stem Cell Research and Therapy*, **4** 1.

O'Reilly, A. and D.J. Kelly (2016) A Computational Model of Osteochondral Defect Repair Following Implantation of Stem Cell-Laden Multiphase Scaffolds *Tissue Engineering Part A*, **23** 30-42.

Ofek, G., C.M. Revell, J.C. Hu, D.D. Allison, K.J. Grande-Allen, and K.A. Athanasiou (2008) Matrix development in self-assembly of articular cartilage *PLoS ONE*, **3**.

Okulov, A.V., A.S. Volegov, J. Weissmüller, J. Markmann, and I.V. Okulov (2018) Dealloying-based metal-polymer composites for biomedical applications *Scripta Materialia*, **146** 290-294.

Olivares, A.L., È. Marsal, J.A. Planell, and D. Lacroix (2009) Finite element study of scaffold architecture design and culture conditions for tissue engineering *Biomaterials*, **30** 6142-6149.

Olubamiji, A.D., Z. Izadifar, J.L. Si, D.M.L. Cooper, B.F. Eames, and D.X.B. Chen (2016) Modulating mechanical behaviour of 3D-printed cartilage-mimetic PCL scaffolds: influence of molecular weight and pore geometry. *Biofabrication*, **8** 025020.

Ouyang, L., R. Yao, Y. Zhao, and W. Sun (2016) Effect of bioink properties on printability and cell viability for 3D bioplotting of embryonic stem cells *Biofabrication*, **8**.

Pacifici, M., E. Koyama, Y. Shibukawa, C. Wu, Y. Tamamura, M. Enomoto-Iwamoto, and M. Iwamoto (2006) Cellular and molecular mechanisms of synovial joint and articular cartilage formation. *Annals of the New York Academy of Sciences*, **1068** 74-86.

Park, H., J.S. Kim, E.J. Oh, T.J. Kim, H.M. Kim, J.H. Shim, W.S. Yoon, J.B. Huh, S.H. Moon, S.S. Kang, and H.Y. Chung (2018) Effects of three-dimensionally printed polycaprolactone/β-tricalcium phosphate scaffold on osteogenic differentiation of adipose tissue- and bone marrow-derived stem cells *Archives of Craniofacial Surgery*, **19** 181-189.

Park, J.S., J.S. Chu, A.D. Tsou, R. Diop, Z. Tang, A. Wang, and S. Li (2011) The effect of matrix stiffness on the differentiation of mesenchymal stem cells in response to TGF-β. *Biomaterials*, **32** 3921-30.

Park, J.Y., J.-H.H. Shim, S.-A.A. Choi, J. Jang, M. Kim, S.H. Lee, and D.-W.W. Cho (2015) 3D printing technology to control BMP-2 and VEGF delivery spatially and temporally to promote large-volume bone regeneration *Journal of Materials Chemistry B*, **3** 5415-5425.

Park, S., C.T. Hung, and G.A. Ateshian (2004) Mechanical response of bovine articular cartilage under dynamic unconfined compression loading at physiological stress levels *Osteoarthritis and Cartilage*, **12** 65-73.

Park, S., R. Krishnan, S.B. Nicoll, and G.A. Ateshian (2003) Cartilage interstitial fluid load support in unconfined compression *Journal of Biomechanics*, **36** 1785-1796.

Pastrama, M.-I., A.C. Ortiz, L. Zevenbergen, N. Famaey, W. Gsell, C.P. Neu, U. Himmelreich, and I. Jonkers (2019) Combined enzymatic degradation of proteoglycans and collagen significantly alters intratissue strains in articular cartilage during cyclic compression *Journal of the Mechanical Behavior of Biomedical Materials*, **98** 383-394.

Patel, Z.S., S. Young, Y. Tabata, J.A. Jansen, M.E.K. Wong, and A.G. Mikos (2008) Dual delivery of an angiogenic and an osteogenic growth factor for bone regeneration in a critical size defect model. *Bone*, **43** 931-40.

Pati, F., J. Jang, D.-H.H. Ha, S. Won Kim, J.-W.W. Rhie, J.-H.H. Shim, D.-H.H. Kim, and D.-W.W. Cho (2014) Printing three-dimensional tissue analogues with decellularized extracellular matrix bioink *Nature Communications*, **5** 1-11.

Pek, Y.S., A.C.A. Wan, and J.Y. Ying (2010) The effect of matrix stiffness on mesenchymal stem cell differentiation in a 3D thixotropic gel. *Biomaterials*, **31** 385-91.

Peng, H., V. Wright, A. Usas, B. Gearhart, H.-C. Shen, J. Cummins, and J. Huard (2002) Synergistic enhancement of bone formation and healing by stem cell–expressed VEGF and bone morphogenetic protein-4 *Journal of Clinical Investigation*, **110** 751-759.

Plunkett, N. and F.J. O'Brien (2011) Biomaterials and Tissue Engineering: Bioreactors in tissue engineering. *Technology and Health Care*, **19** 55-69.

Poldervaart, M.T., H. Gremmels, K. Van Deventer, J.O. Fledderus, F.C. Öner, M.C. Verhaar, W.J.A. Dhert, and J. Alblas (2014) Prolonged presence of VEGF promotes vascularization in 3D bioprinted scaffolds with defined architecture *J Control Release*, **184** 58-66.

Priddy, L.B., O. Chaudhuri, H.Y. Stevens, L. Krishnan, B.A. Uhrig, N.J. Willett, and R.E. Guldberg (2014) Oxidized alginate hydrogels for bone morphogenetic protein-2 delivery in long bone defects. *Acta biomaterialia*, **10** 4390-9.

Pritzker, K.P.H., S. Gay, S.A. Jimenez, K. Ostergaard, J.P. Pelletier, K. Revell, D. Salter, and W.B. van den Berg (2006) Osteoarthritis cartilage histopathology: Grading and staging *Osteoarthritis and Cartilage*, **14** 13-29.

Provot, S. and E. Schipani (2005) Molecular mechanisms of endochondral bone development *Biochemical and Biophysical Research Communications*, **328** 658-665.

Qu, D., J. Li, Y. Li, A. Khadka, Y. Zuo, H. Wang, Y. Liu, and L. Cheng (2011) Ectopic osteochondral formation of biomimetic porous PVA-n-HA/PA6 bilayered scaffold and BMSCs construct in rabbit *Journal of Biomedical Materials Research - Part B Applied Biomaterials*, **96 B** 9-15.

Ragaert, K. and L. Cardon (2009) Bulk mechanical properties of thermoplastic poly- ε -caprolactone .

Raggatt, L.J. and N.C. Partridge (2010) Cellular and molecular mechanisms of bone remodeling *Journal of Biological Chemistry*, **285** 25103-25108.

Ren, X., F. Wang, C. Chen, X. Gong, L. Yin, and L. Yang (2016) Engineering zonal cartilage through bioprinting collagen type II hydrogel constructs with biomimetic chondrocyte density gradient *BMC Musculoskeletal Disorders*, **17**.

Rhee, S., J.L. Puetzer, B.N. Mason, C.A. Reinhart-King, and L.J. Bonassar (2016) 3D Bioprinting of Spatially Heterogeneous Collagen Constructs for Cartilage Tissue Engineering *ACS Biomaterials Science & Engineering* acsbiomaterials.6b00288.

Ribeiro, J.F.M., S.M. Oliveira, J.L. Alves, A.J. Pedro, R.L. Reis, E.M. Fernandes, and J.F. Mano (2017) Structural monitoring and modeling of the mechanical deformation of three-dimensional printed poly(ε-caprolactone) scaffolds. *Biofabrication*, **9** 025015.

Rodrigues, M.T., M.E. Gomes, and R.L. Reis (2011) Current strategies for osteochondral regeneration: From stem cells to pre-clinical approaches *Current Opinion in Biotechnology*, **22** 726-733.

Roohani-Esfahani, S.-I., P. Newman, and H. Zreiqat (2016) Design and Fabrication of 3D printed Scaffolds with a Mechanical Strength Comparable to Cortical Bone to Repair Large Bone Defects. *Scientific reports*, **6** 19468.

Roos, E.M. (2005) Joint injury causes knee osteoarthritis in young adults *Current Opinion in Rheumatology*, **17** 195-200.

Rosa, D.S., I.C. Neto, M.R. Calil, A.G. Pedroso, C.P. Fonseca, and S. Neves (2004) Evaluation of the Thermal and Mechanical Properties of and Their Blends *Journal of Applied Polymer Science*, **91** 3909-3914.

Rowley, J.A., G. Madlambayan, and D.J. Mooney (1999) Alginate hydrogels as synthetic extracellular matrix materials *Biomaterials*, **20** 45-53.

Sabatino, M.A., R. Santoro, S. Gueven, C. Jaquiery, D.J. Wendt, I. Martin, M. Moretti, and A. Barbero (2015) Cartilage graft engineering by co-culturing primary human articular chondrocytes with human bone marrow stromal cells. *Journal of tissue engineering and regenerative medicine*, **9** 1394-403.

Sachlos, E., J.T. Czernuszka, S. Gogolewski, and M. Dalby (2003) Making tissue engineering scaffolds work. Review on the application ofsolid freeform fabrication technology to the production of tissue engineeringscaffolds *European Cells and Materials*, **5** 29-40.

Salerno, A., M. Oliviero, E. Di Maio, S. Iannace, and P.A. Netti (2009) Design of porous polymeric scaffolds by gas foaming of heterogeneous blends *Journal of Materials Science: Materials in Medicine*, **20** 2043-2051.

Santo, V.E., M.E. Gomes, J.F. Mano, and R.L. Reis (2013) Controlled release strategies for bone, cartilage, and osteochondral engineering-part i: Recapitulation of native tissue healing and variables for the design of delivery systems *Tissue Engineering - Part B: Reviews*, **19** 308-326.

Schaefer, L. and R.M. Schaefer (2010) Proteoglycans: From structural compounds to signaling molecules *Cell and Tissue Research*, **339** 237-246.

Schiavone Panni, A., S. Cerciello, M. Vasso, and M. Tartarone (2009) Stiffness in total knee arthroplasty *Journal of Orthopaedics and Traumatology*, **10** 111-118.

Schipani, R., D.R. Nolan, C. Lally, D.J. Kelly, R. Schipani, D.R. Nolan, C. Lally, and D.J. Kelly (2019) Integrating finite element modelling and 3D printing to engineer biomimetic polymeric scaffolds for tissue engineering, **8207**.

Schlichting, K., H. Schell, R.U. Kleemann, A. Schill, A. Weiler, G.N. Duda, and D.R. Epari (2008) Influence of scaffold stiffness on subchondral bone and subsequent cartilage regeneration in an ovine model of osteochondral defect healing *Am J Sports Med*, **36** 2379-2391.

Schmidt, M.B., V.C. Mow, L.E. Chun, and D.R. Eyre (1990) Effects of proteoglycan extraction on the tensile behavior of articular cartilage *Journal of Orthopaedic Research*, **8** 353-363.

Schmidt, T.A., N.S. Gastelum, Q.T. Nguyen, B.L. Schumacher, and R.L. Sah (2007a) Boundary lubrication of articular cartilage: Role of synovial fluid constituents *Arthritis and Rheumatism*, **56** 882-891.

Schmidt, T.A. and R.L. Sah (2007b) Effect of synovial fluid on boundary lubrication of articular cartilage *Osteoarthritis and Cartilage*, **15** 35-47.

Schnabel, M., S. Marlovits, G. Eckhoff, I. Fichtel, L. Gotzen, V. Vécsei, and J. Schlegel (2002) Dedifferentiation-associated changes in morphology and gene expression in primary human articular chondrocytes in cell culture *Osteoarthritis and Cartilage*, **10** 62-70.

Schon, B.S., G.J. Hooper, and T.B.F. Woodfield (2016) Modular Tissue Assembly Strategies for Biofabrication of Engineered Cartilage *Annals of Biomedical Engineering*, **45** 1-15.

Schulz, R.M. and A. Bader (2007) Cartilage tissue engineering and bioreactor systems for the cultivation and stimulation of chondrocytes *European Biophysics Journal*, **36** 539-568.

Schumacher, B.L., J.A. Block, T.M. Schmid, M.B. Aydelotte, and K.E. Kuettner, *A novel proteoglycan synthesized and secreted by chondrocytes of the superficial zone of articular cartilage*, in *Archives of Biochemistry and Biophysics*. 1994. p. 144-152.

Schuurman, W., V. Khristov, M.W. Pot, P.R. Van Weeren, W.J.A. Dhert, and J. Malda (2011) Bioprinting of hybrid tissue constructs with tailorable mechanical properties *Biofabrication*, **3**.

Schuurman, W., P.a. Levett, M.W. Pot, P.R. van Weeren, W.J.a. Dhert, D.W. Hutmacher, F.P.W. Melchels, T.J. Klein, and J. Malda (2013) Gelatin-methacrylamide hydrogels as potential biomaterials for fabrication of tissue-engineered cartilage constructs. *Macromolecular bioscience*, **13** 551-61.

Scotti, C., B. Tonnarelli, A. Papadimitropoulos, A. Scherberich, S. Schaeren, A. Schauerte, J. Lopez-Rios, R. Zeller, A. Barbero, and I. Martin (2010) Recapitulation of endochondral bone formation using human adult mesenchymal stem cells as a paradigm for developmental engineering *Proceedings of the National Academy of Sciences*, **107** 7251-7256.

Seil, R. and D. Pape (2011) Causes of failure and etiology of painful primary total knee arthroplasty *Knee Surgery, Sports Traumatology, Arthroscopy*, **19** 1418-1432.

Seo, S.-J., C. Mahapatra, R.K. Singh, J.C. Knowles, and H.-W. Kim (2014) Strategies for osteochondral repair: Focus on scaffolds *Journal of tissue engineering*, **5** 2041731414541850.

Shafiee, A., M. Soleimani, G.A. Chamheidari, E. Seyedjafari, M. Dodel, A. Atashi, and Y. Gheisari (2011) Electrospun nanofiber-based regeneration of cartilage enhanced by mesenchymal stem cells *Journal of Biomedical Materials Research - Part A*, **99 A** 467-478.

Sheehy, E.J., D.J. Kelly, and F.J. O'Brien (2019) Biomaterial-based endochondral bone regeneration: a shift from traditional tissue engineering paradigms to developmentally inspired strategies *Materials Today Bio*, **3** 100009.

Sheehy, E.J., T. Vinardell, C.T. Buckley, and D.J. Kelly (2013) Engineering osteochondral constructs through spatial regulation of endochondral ossification *Acta Biomaterialia*, **9** 5484-5492.

Shen, G. (2005) The role of type X collagen in facilitating and regulating endochondral ossification of articular cartilage *Orthodontics and Craniofacial Research*, **8** 11-17.

Shepherd, D.E.T. and B.B. Seedhom (1997) The compressive modulus of human articular cartilage in joints of the lower limb determined under physiological loading conditions *Rheumatology*, **38** 124-132.

Shim, J.-H., K.-M. Jang, S.K. Hahn, J.Y. Park, H. Jung, K. Oh, K.M. Park, J. Yeom, S.H. Park, S.W. Kim, J.H. Wang, K. Kim, and D.-W. Cho (2016) Three-dimensional bioprinting of multilayered constructs containing human mesenchymal stromal cells for osteochondral tissue regeneration in the rabbit knee joint *Biofabrication*, **8** 014102.

Simmons, C.A., E. Alsberg, S. Hsiong, W.J. Kim, and D.J. Mooney (2004) Dual growth factor delivery and controlled scaffold degradation enhance in vivo bone formation by transplanted bone marrow stromal cells *Bone*, **35** 562-569.

Sivashankari, P.R. and M. Prabaharan (2016) Prospects of chitosan-based scaffolds for growth factor release in tissue engineering *International Journal of Biological Macromolecules*, **93** 1382-1389.

Soltz, M.A. and G.A. Ateshian (2000) Interstitial Fluid Pressurization during Confined Compression Cyclical Loading of Articular Cartilage *Annals of Biomedical Engineering*, **28** 150-159.

Soltz, M.A. and G.A. Ateshian (1998) Experimental verification and theoretical prediction of cartilage interstitial fluid pressurization at an impermeable contact interface in confined compression *Journal of Biomechanics*, **31** 927-934.

Sommerfeldt, D. and C. Rubin (2001) Biology of bone and how it orchestrates the form and function of the skeleton *European Spine Journal*, **10** 86-95.

Spiller, K.L., S.A. Maher, and A.M. Lowman (2011) Hydrogels for the repair of articular cartilage defects *Tissue Engineering - Part B: Reviews*, **17** 281-299.

Srikumar, K., Z. Zhengyi, and C. Xu (2017) Biofabrication of Interpenetrating Polymer Network Hydrogels.

Stok, K. and A. Oloyede (2007) Conceptual fracture parameters for articular cartilage *Clinical Biomechanics*, **22** 725-735.

Street, J., M. Bao, L. DeGuzman, S. Bunting, F.V. Peale, N. Ferrara, H. Steinmetz, J. Hoeffel, J.L. Cleland, A. Daugherty, N. Van Bruggen, H.P. Redmond, R.A.D. Carano, and E.H. Filvaroff (2002) Vascular endothelial growth factor stimulates bone repair by promoting angiogenesis and bone turnover *Proceedings of the National Academy of Sciences of the United States of America*, **99** 9656-9661.

Sukegawa, A., N. Iwasaki, Y. Kasahara, T. Onodera, T. Igarashi, and A. Minami (2012) Repair of rabbit osteochondral defects by an acellular technique with an ultrapurified alginate gel containing stromal cell-derived factor-1 *Tissue Engineering - Part A*, **18** 934-945.

Sun, A.X., H. Lin, M.R. Fritch, H. Shen, P.G. Alexander, M. DeHart, and R.S. Tuan (2017) Chondrogenesis of human bone marrow mesenchymal stem cells in 3-dimensional, photocrosslinked hydrogel constructs: Effect of cell seeding density and material stiffness. *Acta biomaterialia*, **58** 302-311.

Sun, W., B. Starly, A. Darling, and C. Gomez (2004) Computer-aided tissue engineering: application to biomimetic modelling and design of tissue scaffolds. *Biotechnology and applied biochemistry*, **39** 49-58.

Swieszkowski, W., B.H.S. Tuan, K.J. Kurzydlowski, and D.W. Hutmacher (2007) Repair and regeneration of osteochondral defects in the articular joints *Biomolecular Engineering*, **24** 489-495.

Tamaddon, M., L. Wang, Z. Liu, and C. Liu (2018) Osteochondral tissue repair in osteoarthritic joints: clinical challenges and opportunities in tissue engineering *Bio-Design and Manufacturing*, **1** 101-114.

Tampieri, A., S. Sprio, M. Sandri, and F. Valentini (2011) Mimicking natural bio-mineralization processes: A new tool for osteochondral scaffold development *Trends in Biotechnology*, **29** 526-535.

Taylor, D., N. O'Mara, E. Ryan, M. Takaza, and C. Simms (2012) The fracture toughness of soft tissues *Journal of the Mechanical Behavior of Biomedical Materials*, **6** 139-147.

Tellis, B.C., J.A. Szivek, C.L. Bliss, D.S. Margolis, R.K. Vaidyanathan, and P. Calvert (2008) Trabecular scaffolds created using micro CT guided fused deposition modeling *Materials Science and Engineering C*, **28** 171-178.

Temenoff, J.S. and A.G. Mikos (2000) Review: Tissue engineering for regeneration of articular cartilage *Biomaterials*, **21** 431-440.

Terraciano, V., N. Hwang, L. Moroni, H.B. Park, Z. Zhang, J. Mizrahi, D. Seliktar, and J. Elisseeff (2007) Differential Response of Adult and Embryonic Mesenchymal Progenitor Cells to Mechanical Compression in Hydrogels *Stem Cells*, **25** 2730-2738.

Thorpe, S.D., C.T. Buckley, T. Vinardell, F.J. O'Brien, V.A. Campbell, and D.J. Kelly (2010) The response of bone marrow-derived mesenchymal stem cells to dynamic compression following tgf-β3 induced chondrogenic differentiation *Annals of Biomedical Engineering*, **38** 2896-2909.

Thorpe, S.D., C.T. Buckley, T. Vinardell, F.J. O'Brien, V.A. Campbell, and D.J. Kelly (2008) Dynamic compression can inhibit chondrogenesis of mesenchymal stem cells *Biochemical and Biophysical Research Communications*, **377** 458-462.

Thorpe, S.D., T. Nagel, S.F. Carroll, and D.J. Kelly (2013a) Modulating Gradients in Regulatory Signals within Mesenchymal Stem Cell Seeded Hydrogels: A Novel Strategy to Engineer Zonal Articular Cartilage *PLoS ONE*, **8**.

Thorpe, S.D., T. Nagel, S.F. Carroll, and D.J. Kelly (2013b) Modulating gradients in regulatory signals within mesenchymal stem cell seeded hydrogels: a novel strategy to engineer zonal articular cartilage *PLoS One*, **8** e60764.

Tse, J.R. and A.J. Engler (2011) Stiffness gradients mimicking in vivo tissue variation regulate mesenchymal stem cell fate *PLoS ONE*, **6**.

Valonen, P.K., F.T. Moutos, A. Kusanagi, M.G. Moretti, B.O. Diekman, J.F. Welter, A.I. Caplan, F. Guilak, and L.E. Freed (2010) In vitro generation of mechanically functional cartilage grafts based on adult human stem cells and 3D-woven poly(epsilon-caprolactone) scaffolds. *Biomaterials*, **31** 2193-200.

Van Den Bulcke, A.I., B. Bogdanov, N. De Rooze, E.H. Schacht, M. Cornelissen, and H. Berghmans (2000a) Structural and Rheological Properties of Methacrylamide Modified Gelatin Hydrogels *Biomacromolecules*, **1** 31-38.

Van Den Bulcke, A.I., B. Bogdanov, N. De Rooze, E.H. Schacht, M. Cornelissen, and H. Berghmans (2000b) Structural and rheological properties of methacrylamide modified gelatin hydrogels *Biomacromolecules*, **1** 31-38.

Vanlauwe, J., D.B.F. Saris, J. Victor, K.F. Almqvist, J. Bellemans, and F.P. Luyten (2011) Five-year outcome of characterized chondrocyte implantation versus microfracture for symptomatic cartilage defects of the knee: early treatment matters *American Journal of Sports Medicine*, **39** 2566-2574.

Vinardell, T., E.J. Sheehy, C.T. Buckley, and D.J. Kelly (2012) A comparison of the functionality and in vivo phenotypic stability of cartilaginous tissues engineered from different stem cell sources *Tissue Engineering - Part A*, **18** 1161-1170.

Visser, J., F.P.W. Melchels, J.E. Jeon, E.M. van Bussel, L.S. Kimpton, H.M. Byrne, W.J.a. Dhert, P.D. Dalton, D.W. Hutmacher, and J. Malda (2015) Reinforcement of hydrogels using three-dimensionally printed microfibres. *Nature communications*, **6** 6933.

Walsh, D.A., C.S. Bonnet, E.L. Turner, D. Wilson, M. Situ, and D.F. McWilliams (2007) Angiogenesis in the synovium and at the osteochondral junction in osteoarthritis *Osteoarthritis and Cartilage*, **15** 743-751.

Wang, H. and G.A. Ateshian (1997) The normal stress effect and equilibrium friction coefficient of articular cartilage under steady frictional shear *Journal of Biomechanics*, **30** 771-776.

Wang, H., S. Vijayavenkataraman, Y. Wu, Z. Shu, J. Sun, and J. Fuh Ying Hsi (2016) Investigation of process parameters of electrohydro-dynamic jetting for 3D printed PCL fibrous scaffolds with complex geometries *International Journal of Bioprinting*, **2**.

Williamson, A.K., A.C. Chen, K. Masuda, E.J.M.A. Thonar, and R.L. Sah (2003) Tensile mechanical properties of bovine articular cartilage: Variations with growth and relationships to collagen network components *Journal of Orthopaedic Research*, **21** 872-880.

Wise, J.K., A.L. Yarin, C.M. Megaridis, and M. Cho (2009) Chondrogenic differentiation of human mesenchymal stem cells on oriented nanofibrous scaffolds: Engineering the superficial zone of articular cartilage *Tissue Engineering - Part A*, **15** 913-921.

Wolfram, U. and J. Schwiedrzik (2016) Post-yield and failure properties of cortical bone *BoneKEy Reports*, **5** 1-10.

Woo Jung, J., H.-G. Yi, T.-Y. Kang, W.-J. Yong, S. Jin, W.-S. Yun, and D.-W. Cho (2013) Evaluation of the Effective Diffusivity of a Freeform Fabricated Scaffold Using Computational Simulation *Journal of Biomechanical Engineering*, **135** 084501.

Woo, S.L.Y., W.H. Akeson, and G.F. Jemmott (1976) Measurements of nonhomogeneous, directional mechanical properties of articular cartilage in tension *Journal of Biomechanics*, **9** 785-791.

Woodfield, T.B.F., M. Guggenheim, B. Von Rechenberg, J. Riesle, C.A. Van Blitterswijk, and V. Wedler (2009) Rapid prototyping of anatomically shaped, tissue-engineered implants for restoring congruent articulating surfaces in small joints *Cell Proliferation*, **42** 485-497.

Woodfield, T.B.F., J. Malda, J. De Wijn, F. Péters, J. Riesle, and C.A. Van Blitterswijk (2004) Design of porous scaffolds for cartilage tissue engineering using a three-dimensional fiber-deposition technique *Biomaterials*, **25** 4149-4161.

Woodfield, T.B.F., C.A. Van Blitterswijk, J. De Wijn, T.J. Sims, A.P. Hollander, and J. Riesle (2005) Polymer scaffolds fabricated with pore-size gradients as a model for studying the zonal organization within tissue-engineered cartilage constructs *Tissue Engineering*, **11** 1297-1311.

Woodruff, M.A. and D.W. Hutmacher (2010) The return of a forgotten polymer - Polycaprolactone in the 21st century *Progress in Polymer Science (Oxford)*, **35** 1217-1256.

Wu, L., J. Leijten, C.A. Van Blitterswijk, and M. Karperien (2013) Fibroblast growth factor-1 is a mesenchymal stromal cell-secreted factor stimulating proliferation of osteoarthritic chondrocytes in co-culture *Stem Cells and Development*, **22** 2356-2367.

Wu, L., J.C.H. Leijten, N. Georgi, J.N. Post, C.A. Van Blitterswijk, and M. Karperien (2011) Trophic effects of mesenchymal stem cells increase chondrocyte proliferation and matrix formation *Tissue Engineering - Part A*, **17** 1425-1436.

Xiao, Y., E.A. Friis, S.H. Gehrke, and M.S. Detamore (2013) Mechanical testing of Hydrogels in cartilage tissue engineering: Beyond the compressive modulus *Tissue Engineering - Part B: Reviews*, **19** 403-412.

Xu, C., G. Dai, and Y. Hong (2019) Recent advances in high-strength and elastic hydrogels for 3D printing in biomedical applications *Acta Biomaterialia*, **95** 50-59.

Yan, K.C., K. Nair, and W. Sun (2010) Three dimensional multi-scale modelling and analysis of cell damage in cell-encapsulated alginate constructs. *Journal of biomechanics*, **43** 1031-8.

Yang, J., Y.S. Zhang, K. Yue, and A. Khademhosseini (2017) Cell-laden hydrogels for osteochondral and cartilage tissue engineering *Acta Biomaterialia*, **57** 1-25.

Yang, X., Z. Lu, H. Wu, W. Li, L. Zheng, and J. Zhao (2018) Collagen-alginate as bioink for three-dimensional (3D) cell printing based cartilage tissue engineering *Materials Science and Engineering: C*, **83** 195-201.

Yeung, T., P.C. Georges, L.A. Flanagan, B. Marg, M. Ortiz, M. Funaki, N. Zahir, W. Ming, V. Weaver, and P.A. Janmey (2005) Effects of substrate stiffness on cell morphology, cytoskeletal structure, and adhesion *Cell Motility and the Cytoskeleton*, **60** 24-34.

Yousefi, A.M., M.E. Hoque, R.G.S.V. Prasad, and N. Uth (2015) Current strategies in multiphasic scaffold design for osteochondral tissue engineering: A review *Journal of Biomedical Materials Research - Part A*, **103** 2460-2481.

Zein, I., D.W. Hutmacher, K.C. Tan, and S.H. Teoh (2002) Fused deposition modeling of novel scaffold architectures for tissue engineering applications *Biomaterials*, **23** 1169-1185.

Zhang, S., S. Vijayavenkataraman, W.F. Lu, and J.Y.H. Fuh (2019) A review on the use of computational methods to characterize, design, and optimize tissue engineering scaffolds, with a potential in 3D printing fabrication *Journal of Biomedical Materials Research - Part B Applied Biomaterials*, **107** 1329-1351.

Zhao, X., N. Huebsch, D.J. Mooney, and Z. Suo (2010) Stress-relaxation behavior in gels with ionic and covalent crosslinks *J Appl Phys*, **107** 63509.

Zhou, S., T.S. Thornhill, F. Meng, L. Xie, J. Wright, and J. Glowacki (2016) Influence of osteoarthritis grade on molecular signature of human cartilage *Journal of Orthopaedic Research*, **34** 454-462.

Zhou, X., M. Nowicki, H. Cui, W. Zhu, X. Fang, S. Miao, S.J. Lee, M. Keidar, and L.G. Zhang (2017) 3D bioprinted graphene oxide-incorporated matrix for promoting chondrogenic differentiation of human bone marrow mesenchymal stem cells *Carbon*, **116** 615-624.

Zhu, D., X. Tong, P. Trinh, and F. Yang (2018) Mimicking Cartilage Tissue Zonal Organization by Engineering Tissue-Scale Gradient Hydrogels as 3D Cell Niche *Tissue Engineering - Part A*, **24** 1-10.

Supplementary Figures

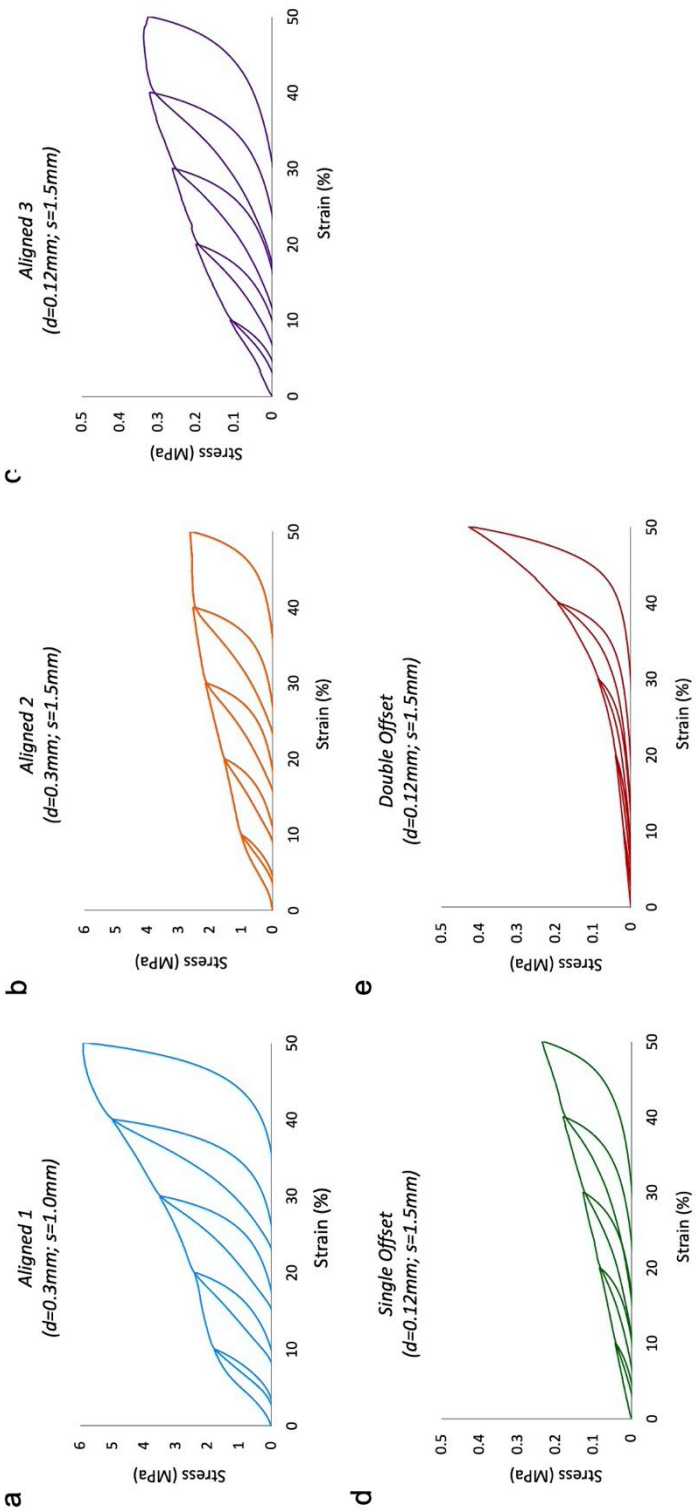

Supplementary Figure 1 Representative cyclic compression stress-strain plots for (a) *Aligned 1* (d=0.3mm; s=1.0mm), (b) *Aligned 2* (d=0.3mm; s=1.5mm), (c) *Aligned 3* (d=0.12mm; s=1.5mm), (d) *Single Offset* (d=0.12mm; s=1.5mm) and (e) *Double Offset* (d=0.12mm; s=1.5mm) scaffold geometries.

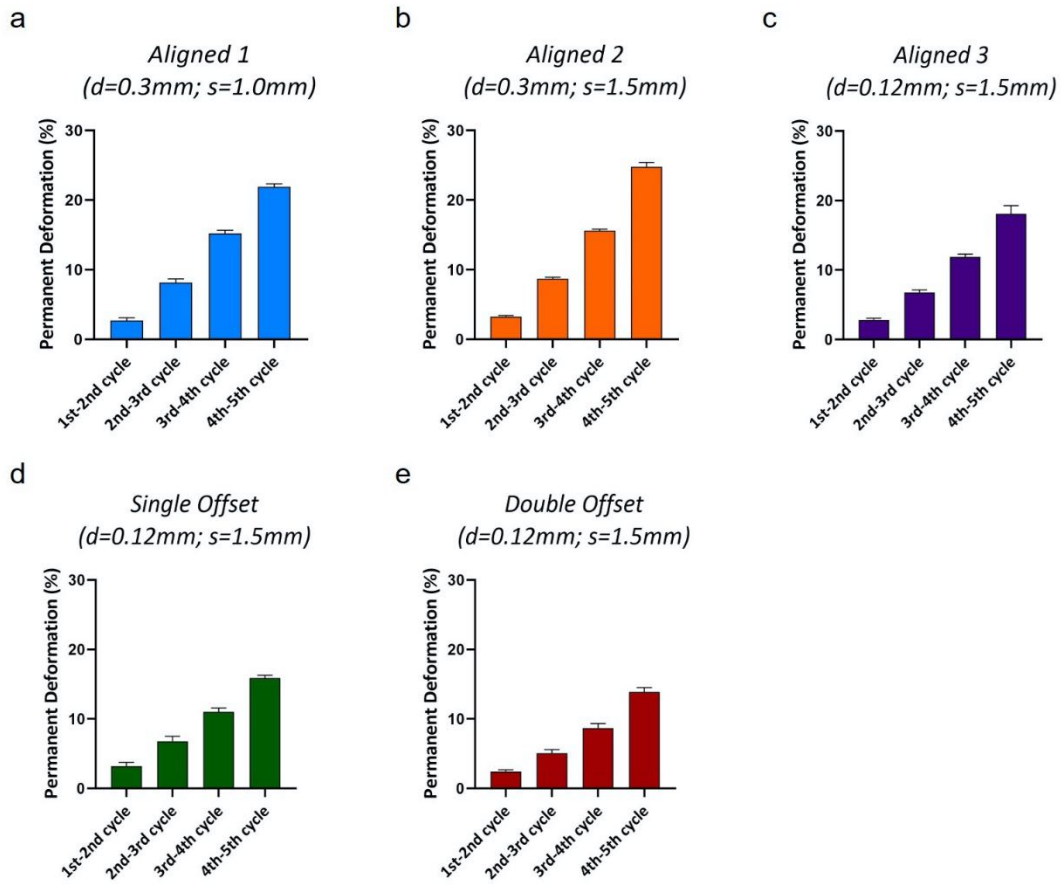

Supplementary Figure 2 Permanent deformation at each applied compressive strain amplitude for (a) *Aligned 1* (*d*=0.3mm; *s*=1.0mm), (b) *Aligned 2* (*d*=0.3mm; *s*=1.5mm), (c) *Aligned 3* (*d*=0.12mm; *s*=1.5mm), (d) *Single Offset* (*d*=0.12mm; *s*=1.5mm) and (e) *Double Offset* (*d*=0.12mm; *s*=1.5mm) scaffold geometries.

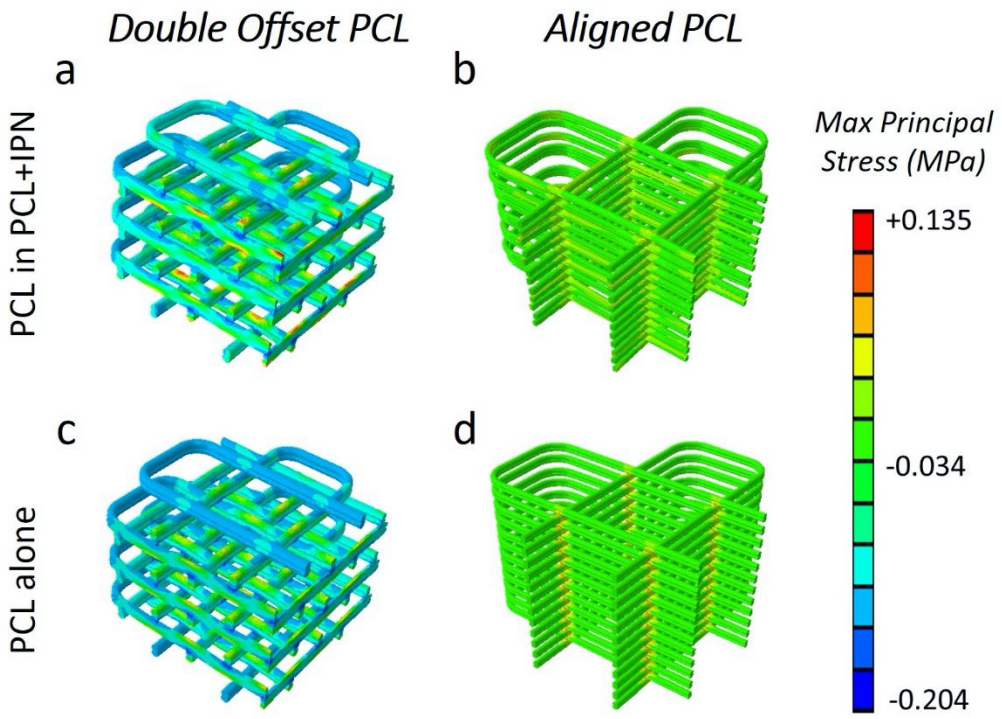

Supplementary Figure 3 Max Principal Stress contour plots for (a, c) *Double Offset* PCL and (b, d) *Aligned* PCL structures in (a, b) PCL+IPN and (c, d) PCL alone constructs.

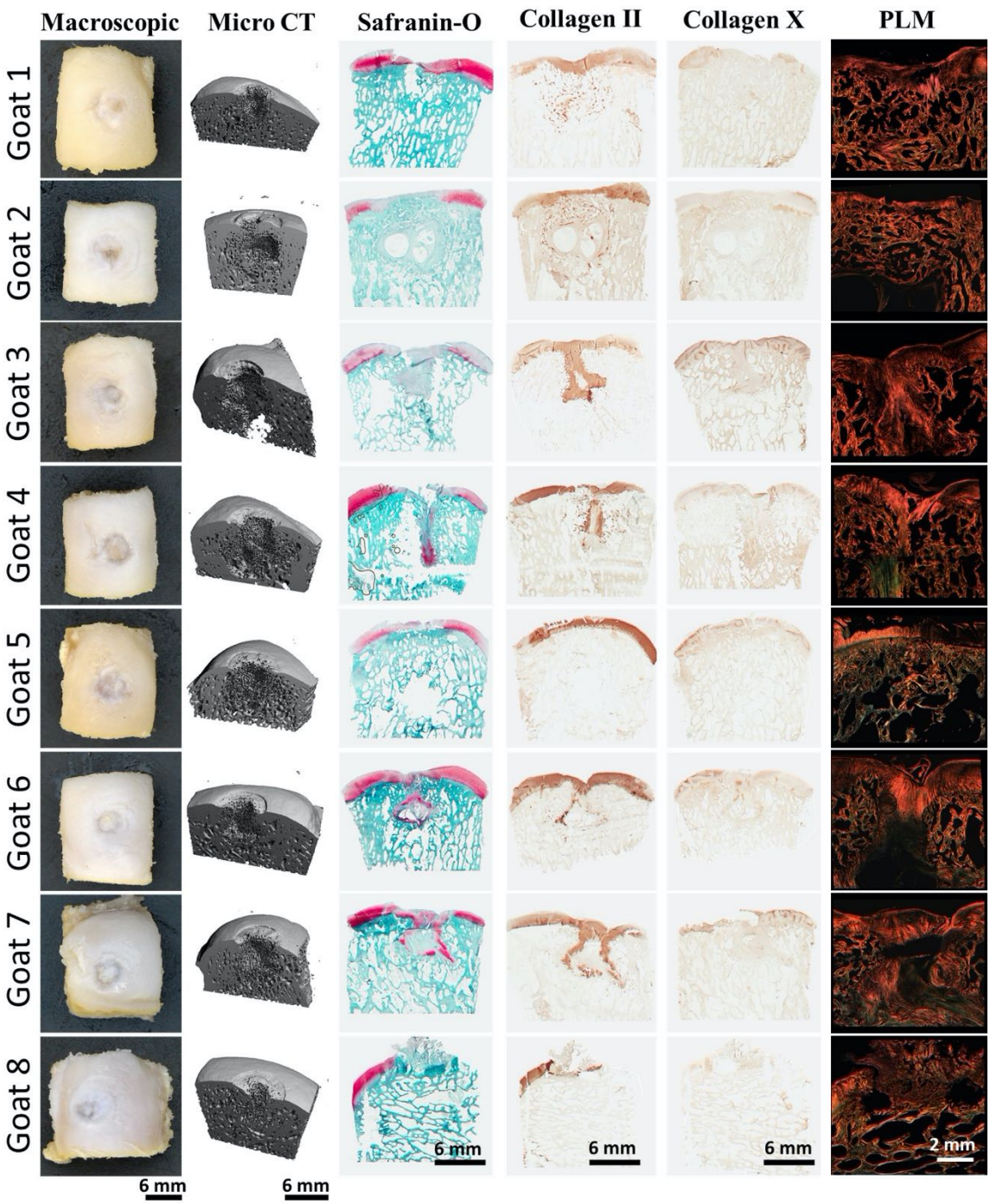

Supplementary Figure 4 Macroscopic, micro CT, Safranin-O, collagen type II, collagen type X and PLM images of the empty control group (n = 8).

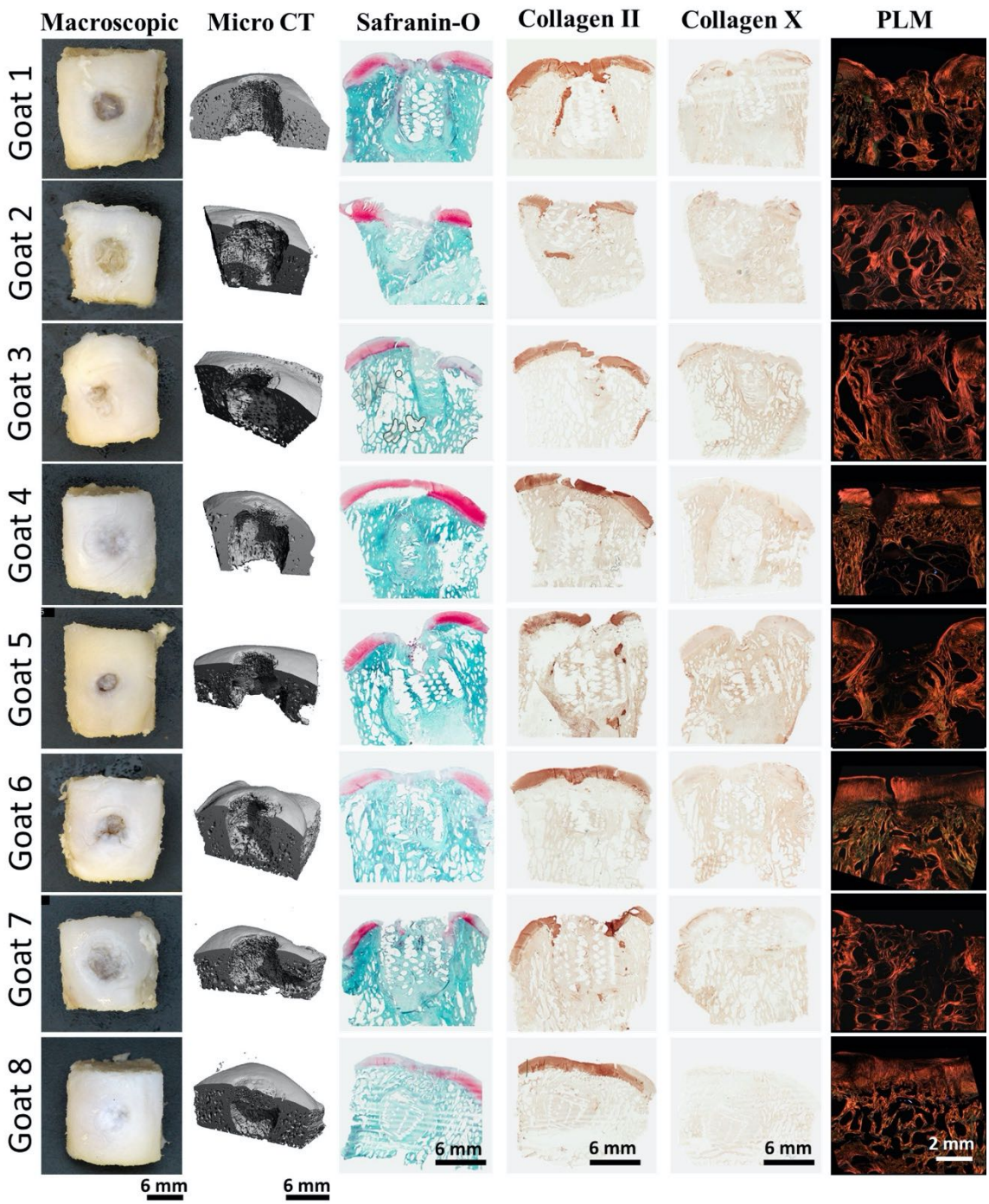

Supplementary Figure 5 Macroscopic, micro CT, Safranin-O, collagen type II, collagen type X and PLM images of the 3DP bi-layered scaffold treated group (n = 8).